Characterisation of Residual Stresses using Neutron Diffraction and Finite Element Simulation

Doctoral Thesis

submitted by

Dipl.-Ing. Ulrike Cihak

Department Physical Metallurgy and Materials Testing
Montanuniversität Leoben

Leoben, Mai 2007

Declaration

The author declares that this thesis is his own work and that, to the best of his knowledge and belief, it contains no material previously published or written by any other person, nor material which to a substantial extent has been accepted for the award of any other degree or diploma, except where acknowledgement or reference has been made in the text.

Leoben, Mai 2007

Acknowledgements

First of all, I would like to thank my supervisor Prof. Helmut Clemens, Head of the Department Metallkunde and Werkstoffprüfung, Leoben, Austria, for his vital encouragement and support throughout this work. I also truly appreciate his personal support during the eventful final year of my PhD thesis.

Special thanks should be given to my supervisor Dr. Peter Staron from GKSS, Geestacht, Germany, for his constant guidance and support throughout the dissertation. He did not only teach me how to use the diffractometer ARES at GKSS, which showed me the work on a large scale research facility, but did always did spare some time for fruitful discussions.

I would like to acknowledge the company Bohler Schmiedetechnik GmbH & Co KG, who enabled this thesis and provided the studied samples. Particularly, I want to thank Dr. Wilfried Marketz, who motivated this work and encouraged me with challenging discussions, and Dr. Martin Stockinger for his support concerning DEFORM and his review of the articles.

My thank also goes to the research center GKSS for the financial support and the provision of the research facilities. The author is grateful to Prof. Heinz-Günter Brokmeier, Inst. für Werkstoffkunde und Werkstofftechnik, TU Clausthal, Germany, for the provision of the tensile test device. Special thank goes to Sangbong Yi and H.-U. Ruhnau for assistance with the tensile tests.

The tensile tests would not have been possible without the active support of Dr. Jens Homeyer, who supervised the measurements at BW5 at HASYLAB, DESY, Germany.

Furthermore, special thanks go to Dr. Michael Panzenböck for his fruitful support with the tensile test at BW5 and for his personal encouragement during my time at the Department for Metallkunde and Werkstoffprüfung in Leoben.

I would like to thank the Material Center Leoben MCL for the provision of the DEFORM software.

I would like to acknowledge the assistance with the DEFORM software of Dr. Erwin Reiss, S&I Technologies DI Erwin Reiss GmbH, Aflenz, Austria.

Furthermore, this thesis has partly been supported by the European Commission under the 6th Framework Program through the Key Action: Strengthening the European Research Area, Research Infrastructures. Contract n°: RII3-CT-2003-505925. Financial support was also granted WPO Werkstoffcluster GmbH.

I would like to thank technical staff of the Department of Metallkunde and Werkstoffprüfung for their assistance.

Thanks go to the members of the Department of Metallkunde and Werkstoffprüfung as well as of GeNeSYS, GKSS for the friendly working atmosphere.

Most especially, I would like to extend my heartfelt gratitude to my parents. Without their support and encouragement this work would not have been possible. I am especially grateful to my mother, who unfortunately did not life to see the end of this thesis. I also want to say thank you to my partner Florian Bayr, who was a vital support due to his cheerful manner and his believe in me. Last but not least, I acknowledge my farther and Amanda Bowles for their review of the work.

Abstract

The aim of the present thesis is the experimental verification of the simulated residual stresses within forged, large scale components. Neutron diffraction was used to asses the residual stresses within a forged and water-quenched turbine disc with a thickness of up to 25 mm. During machining, residual stresses within the disc can cause a physical distortion of the component. This can lead to failure of the finished component if the dimensional tolerances are not met. Therefore, a finite element model is required to determine the residual stress state within the as-forged component prior to machining and minimize the distortion during a machining process. In order to avoid any cross-couplings, the experimental and the finite element approach for residual stresses analysis are treated strictly independently. A detailed parameter study shows that the heat transfer coefficient is a key parameter of the finite element model and has to be defined as a function of the surface temperature. The experimental part of the work focuses on the homogeneity of the residual stress states and the repeatability of the neutron diffraction measurements. Furthermore, the potential of an "up-sizing" of the finite element model to larger components is investigated. The comparison of experimentally determined stress results for a small model plate and the results obtained on the relatively large turbine disc show, that the finite element model correctly simulates the residual stress state in both samples.

Zusammenfassung

Das Ziel der vorliegenden Arbeit ist die Verifikation von simulierten Eigenspannungen in großen, wasserabgeschreckten Schmiedeteilen. Für die experimentelle Bestimmung der Eigenspannungen in einer geschmiedeten und wasserabgeschreckten Turbinenscheibe, mit einer Dicke von bis zu 25 mm, wurde die Methode der Neutronenstreuung gewählt. Bei der Bearbeitung können die Eigenspannungen zu einem Verzug der Scheibe führen. Wenn infolgedessen die Toleranzen nicht eingehalten werden können, führt dies zum Ausschuss des Bauteils. Aus diesem Grund wird ein finite Elemente Model benötigt, das die Eigenspannungen in geschmiedetem Bauteilen vor der Bearbeitung korrekt simuliert. Die zwei Methoden zur Bestimmung der Eigenspannungen werden komplett unabhängig behandelt, um etwaige gegenseitige Beeinflussungen auszuschließen. Eine detaillierte Parameterstudie zeigt, dass der Wärmeübergangskoeffizient ein Schlüsselparameter des finite Elemente Models ist und dass er von der Oberflächentemperatur des Bauteils abhängt. Der experimentelle Teil der Arbeit beschäftigt sich mit der Homogenität der Eigenspannungsverteilungen und mit der Wiederholbarkeit der Neutronenmessungen. In weiterer Folge wird das Potential des finiten Elemente Models bezüglich eines „up-sizing" überprüft. Der Vergleich zwischen den experimentell bestimmten Eigenspannungswerten in einer kleinen Modellplatte und denen in der großen Turbinenscheibe mit den entsprechenden simulierten Spannungen zeigt, dass das finite Elemente Model die Eigenspannungen in beiden Proben korrekt simuliert.

Contents

1 Introduction

Finite element simulations have become more and more popular in recent times to optimise processing parameters and predict properties of components [1 - 7]. For critical rotating parts in turbine applications made of nickel-based superalloys finite element simulations of various production steps are particularly relevant due to the rigorous specifications for aeroengines and the high material costs of superalloys [5, 8]. The production of nickel-based superalloy forgings like turbine discs is a complex process involving numerous forging and heat treatment steps, followed by sophisticated machining sequences [9]. During machining, residual stresses within the disc due to quenching can redistribute and cause a physical distortion of the component. This can lead to failure of the finished component if the dimensional tolerances are not met. Practical experience has shown that even after annealing treatments residual stresses are rarely relaxed completely. In the worst case, these stresses cause distortion and the component cracks. In order to avoid or at least minimize the distortion an optimised machining sequence is necessary. For the determination of such an improved machining process, it is essential to know the residual stress distribution within the component. Therefore, a finite element model that correctly simulates the quenching residual stresses in a turbine disc has to be evaluated. From an engineering point of view, the aim is to apply a finite element model to various heat treated forgings and thus provide detailed information on the residual stress distribution in a component prior to machining as an added value for the customer.

Before the finite element model can be employed to predict quenching residual stresses in various geometries, the simulated stresses have to be verified experimentally. Thus, from a scientific point of view, the aim of the current work is to apply two completely independent approaches for residual stress analysis: finite element modelling and experimental determination. Most of the available experimental techniques for residual stress analysis such as x-ray or hole drilling are limited to near-surface stresses [10, 11]. Therefore, neutron diffraction has been chosen, as it enables the measurement of tri-axial stresses to great depths [12, 13]. Any deviations between the two approaches have been clarified by appraising the repeatability of the experimental values and by evaluating the numerous influencing factors. Partly these investigations have been conducted on a small, cuboid model plate to simplify the matter. The reduction of the sample geometry also served as a test for the up-sizing of the finite element model. As most commercial forgings are even larger than the studied turbine disc, it is essential to verify if the same finite element model successfully reflects the residual stresses in two different sample geometries. Then, it can be assumed that the model correctly simulates residual quenching stresses in larger discs or differently shaped components that cannot be measured by neutron diffraction due to large thicknesses.

2 Production of the Studied Turbine Disc

Critical rotating aeroengine parts like turbine discs have to pass through multiple production steps to meet the high standards regarding mechanical properties, microstructure and defect content. Up to now, nickel based alloys are still the most prominent alloy group in aeroengine turbines. Typically nickel based alloys are produced by casting in several steps to obtain the highest cleanliness. The ingot starting material for the turbine disc used in this thesis was produced by the so-called "triple-melt" process, combining VIM (vacuum induction melting), ESR (electron slag refining), and VAR (vacuum arc remelting), which are described in more detail in Refs. [2, 14]. After casting, the ingot was given a homogenisation treatment at approximately 1100°C, followed by air-cooling. The homogenisation treatment reduces any remaining segregations. The cast structure is then broken down by open-die forging. The next step in the process is to produce the turbine disc pre-forms by closed-die forging on a screw press [15]. The discs studied in this work were formed by a two-step closed-die forging process employing a screw press, where large deformations can be realized and thus fine grained microstructures can be achieved. Additionally, careful attention has to be paid to the forging temperature to avoid partial melting or undesired precipitation. Forging nickel-based alloys is very sophisticated due to the small available temperature range. Before the components are machined to their final geometry, multi-stage heat treatment processes have to be performed to obtain the required microstructure. Practical experience has shown that after these heat treatment steps residual stresses still remain in the discs and the stresses are high enough to cause detrimental distortions during machining to the final shape.

The basic steps of the production after the primary forging process are illustrated in Figure 1. First, the heated pre-form is forged by closed-die forging at a forging temperature of 960 °C. After the final forging step, the discs are removed from the die and directly quenched in water with a temperature of 20 °C. This is called the "Direct Aging" route [16]. The standard heat treatment route cools the disc in air and then adds a solution annealing step [14]. In both cases, the discs are machined to the final geometry after a two-step annealing procedure. The machining is not depicted because it is a separate step usually performed by the customer. The studied discs are representative of components produced under actual large-scale commercial conditions; the discs were taken from the commercial production directly after water quenching.

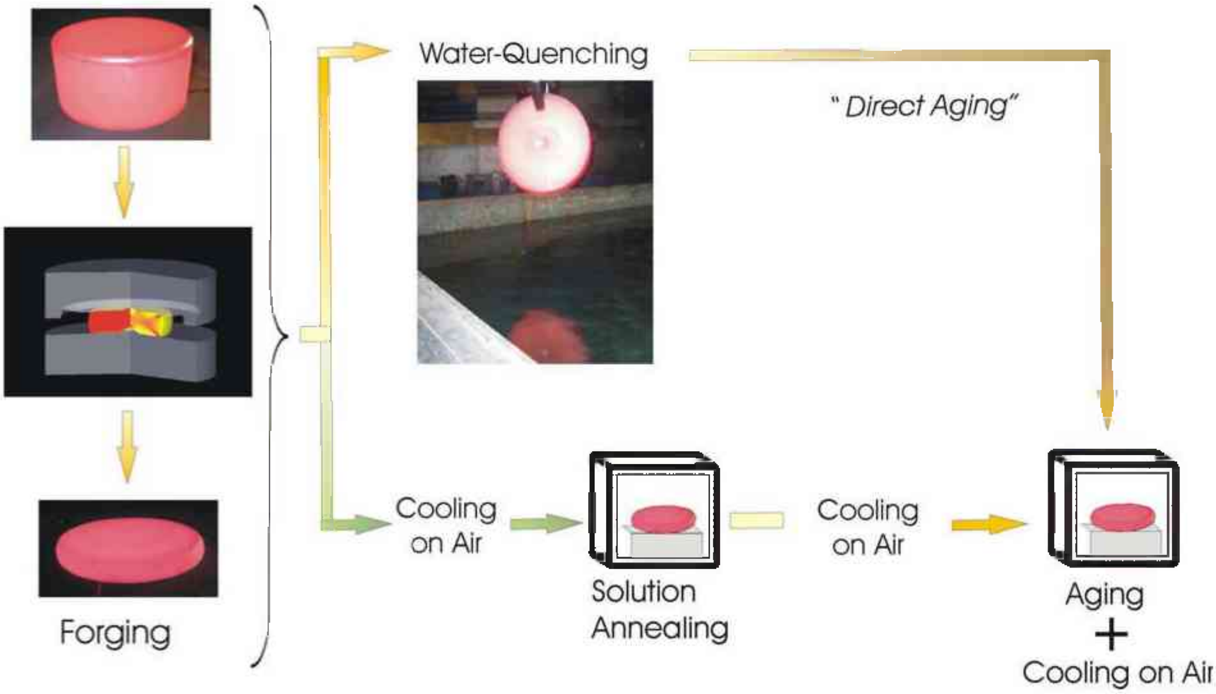

Figure 1: Production of the turbine disc.

3 Material

3.1 Chemical Composition

Inconel 718 exists since the 1950′s and is still the most prominent nickel-based alloy in aeroengine turbines, although new nickel-based alloys and other alloy groups with lower specific weight and excellent high temperature strengths have been developed. In major parts of a turbine aeroengine, nickel-based alloys are still irreplaceable because they can be tailored for very different applications. They can either be optimised for high creep properties (turbine blades) or for high temperature strength and high fatigue resistance (turbine discs). In any case, all nickel-based alloys offer high oxidation resistance and good corrosion properties. IN718 in particular was designed for an excellent combination of high fatigue resistance and high strength at the working temperature of a turbine and additionally offers superior weldability. All these properties are achieved by the highest cleanliness and by specialised heat treatments [17, 18]. The continuous development of Ni-based alloys has involved improved cleanliness and reduced segregation by more and more sophisticated remelting processes [14]. The heat treatment procedures have also been improved to meet the raising demands concerning fatigue and high temperature strength. Lately, a process called direct aging has been developed which enables even higher strength without reducing the good fatigue properties [16, 19]. Thus, IN718 is still widely in use today whenever a combination of high toughness and high temperature strength is required; for example, in the compressor unit or the rear part of the turbine where temperatures are constantly around 600 °C or even higher. Song *et al* [20] measured the ultimate tensile strength and yield strength of IN718 between room temperature and 600°; the values were found to range form 1400 MPa to 1000 MPa for the ultimate tensile strength and from 1100 MPa to 900 MPa for the yield strength. This determines the limit of 650 °C for the typical temperature range for the application of IN718.

Table 1 gives the chemical composition of the IN718 alloy examined in the current work. Generally, nickel-based superalloys obtain their maximum strength from the precipitation of γ' and γ'' in the γ matrix. In alloy IN718 the Al and Ti content is limited by their detrimental effects on weldability and Nb by its propensity for segregation [21]. The smaller ratio of the combined Al and Ti content results in IN718 and other Nb bearing superalloys hardened mainly by γ'' precipitates [22]. Niobium-strengthened alloys exhibit delayed responses to precipitation-hardening temperatures and so the weldability is enhanced, because the heat of welding does not induce hardening and the weld stresses can be relieved by annealing.

Table 1: Nominal chemical composition of IN718 according to AMS 5662-5664 (EN 2.4856).

	m%		**m%**
Ni	50-55	C	max. 0.08
Cr	17-21	Mn	max. 0.35
Fe	Balance	Si	max. 0.35
Nb	4.75-5.50	P	max. 0.015
Mo	2.80-3.30	S	max. 0.015
Ti	0.65-1.15	B	max. 0.006
Al	0.20-0.80	Cu	max. 0.30
Co	max. 1.0		

3.2 Microstructure

Apart from the chemical composition and the precipitation morphology, the grain size is a key parameter for the outstanding properties of IN718. The fine grain size required for good fatigue properties is achieved by high effective strains during the thermomechanical processing on a screw press combined with a well chosen forging temperature [15]. Figure 2 illustrates the resulting microstructure of a water-quenched turbine disc showing the δ phase, which appears as white particles after an electrolytic etch with oxalic acid.

The grain size is also relevant for the neutron diffraction study, because too large grains result in bad measurement statistics and thus the obtained lattice distance is not a representative mean value. A detailed study of the microstructure showed no significant differences of the grain sizes over the cross section of the turbine disc but a fully recrystallised, homogeneous, fine-grained microstructure. This is a result of the high deformation during closed-die forging and the relatively thin geometry of the disc. Additionally, the δ particles pin the γ grain boundaries and therefore prevent excessive grain growth during forging as long as the forging temperature is beneath the δ solvus temperature. As the material recrystallised, the grain size or shape did not reflect the material flow during forging. The flow direction of the material during forging was visible to the naked eye after an electrolytic etch with oxalic acid because the δ phase particles were not fully dissolved during forging and could act as a tracer for the material flow. In some parts a localized depletion of the δ phase was observed, which resulted in locally larger grains because the grain boundaries were no longer pinned by δ particles.

Large grain size differences were observed for the as-forged and the pre-forged material. Figure 3a shows the pre-forged material with a grain size of 15 - 20 µm and Figure 3b is representative for the forged microstructure with a grain size of 5 µm. A further annealing at 960 °C followed by water quenching did not change the grain size of the pre-forged material (Figure 4), but the δ particles are more obvious.

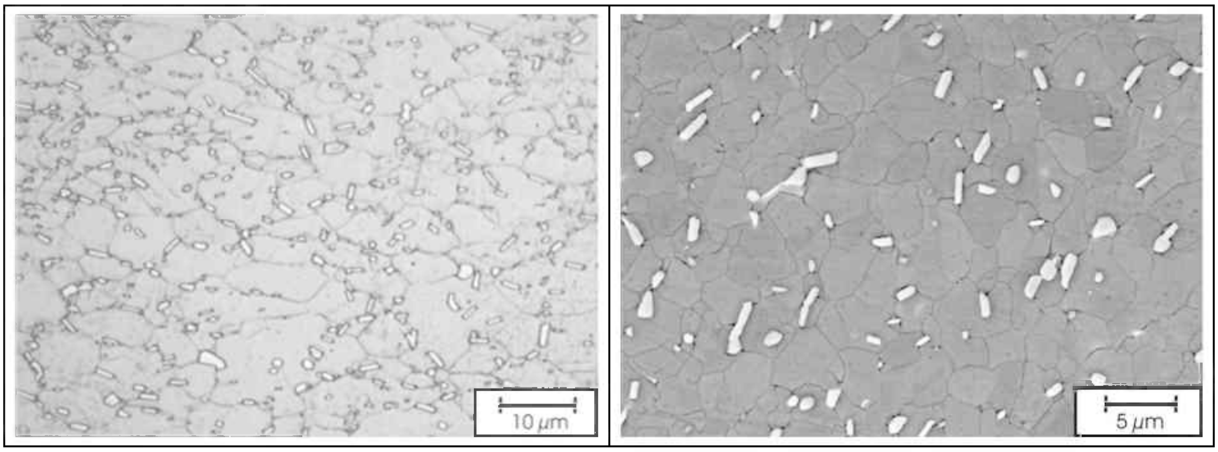

Figure 2: Microstructure of IN718 after forging and water quenching. (a) A light microscopy picture showing the grain boundaries as well as the δ precipitates which are not dissolved during the forging process. (b) A SEM picture where the δ precipitates appear as bright particles.

The appearance of the δ precipitates and the grain boundaries depends to a great extend on the employed etching solution. The oxalic acid did not dissolve the δ particles contrary to the etchant (see Appendix A) used to produce the micrograph in Figure 3b, where the δ precipitates are dissolved and can only be displayed by interference light. Generally, it was very difficult to elaborate the grain boundaries with a high quality to allow grain size analyses. The etchants used to produce the micrographs in Figures 2 - 4 are given in Appendix A.

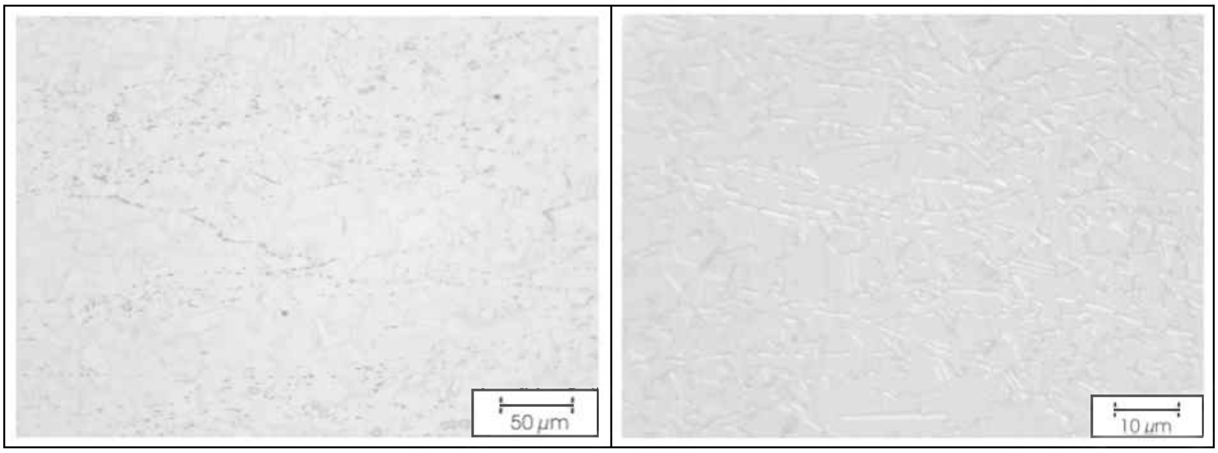

Figure 3: Light optical micrographs of the IN718 model plate (a) machined from the pre-forged material (b) machined from the forged turbine disc.

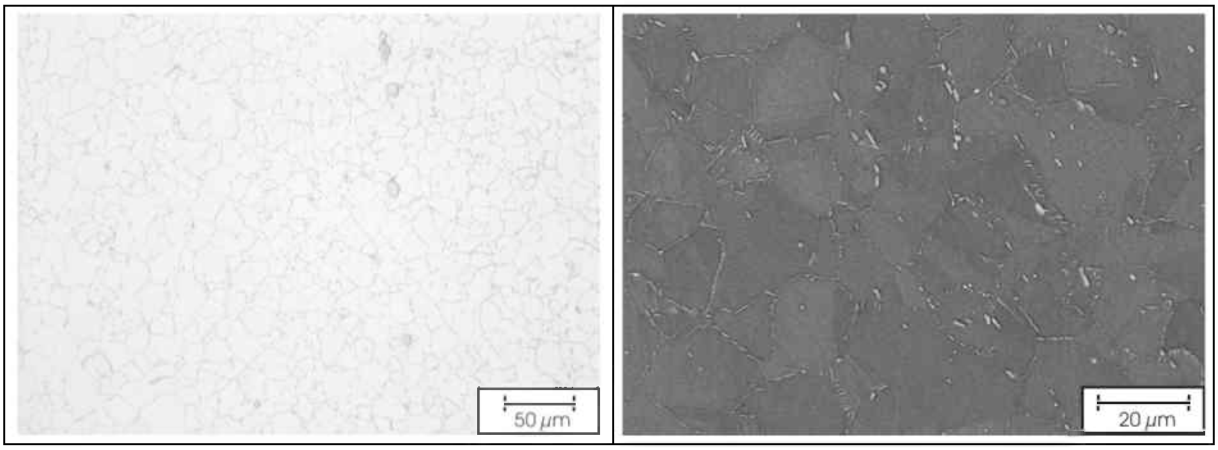

Figure 4: Microstructure of the IN718 model plate cut from the pre-forged material solution annealed at 960 °C/WQ and subsequently annealed 718 °C/8h with furnace cooling 621 °C/10h/WQ (a) A light microscope picture showing the grain boundaries as well as the δ precipitates and some carbides (large particles). (b) A SEM picture of the same heat treatment condition showing the δ precipitates and indicating annealing twins within the γ grains.

3.3 Phases

The main phases in the alloy IN718 are the coherent γ' phase, the partially coherent γ'' phase and the thermodynamically stable phase δ. Furthermore, M(C,N) and $M_{23}C_6$ carbides can be found in the matrix, but due to the small carbon content (0.004 m%) their volume fraction is very small [23]. TCP phases (**t**etragonal **c**losed **p**acked) and the α-Cr phase as well as oxides and nitrides can also form, but their formation is avoided, as they deteriorate the forgeability [17]. The morphology, the kinetics and the effects on the mechanical properties of the carbides, nitrides, γ'-, γ''-, and δ-phases are the focus of multiple publications in literature, e.g. [24 - 31]. These subjects were not within the focus of the current work, because only the water-quenched condition of IN718 was studied. The effect of different aging times on the precipitates was not examined. Therefore, only a basic characterization of the coherent and partially coherent precipitates is given as they have a potential influence on the lattice distances which are the basis for strain and stress determinations. The mismatch of their lattice parameters to the lattice parameter of the matrix unit cell is an indication for the strengthening effect. Generally, the mismatch δ^* is defined as the normalised difference in lattice parameter between matrix and the precipitation, given by:

$$\delta^* = \frac{(a-a')}{0.5(a+a')}, \tag{1}$$

where a is the lattice parameter of the γ matrix and a' is the lattice parameter of the γ' or γ'' phases [x]. Neutron diffraction does not distinguish between the matrix and the precipitates as long as the crystal structure is equal. Thus, the measured lattice parameter is a sum of γ and γ' or γ''.

3.3.1 Ni_3Al - Gamma Prime γ'

The intermetallic phase γ' ($Ni_3(Al,Ti)$) is a fully coherent precipitate. Its crystal structure is $L1_2$, which is cubic, similar to an fcc lattice and represents an ordered A_3B type compound as shown in Figure 5a: the Al atoms are placed at the corners and Ni atoms at the centres of the planes. The phase γ' occurs as spheres at 0 - 0.2% mismatch to the matrix, then becomes cubic around 0.5% - 1.0% mismatch, and finally forms plates at mismatches above 1.25% [14]. In IN718 after conventional heat treatments, the volume fraction of γ' is only about 4 m% and the lattice misfit is 0.407% [22]. Therefore, the contribution of γ' to the precipitation hardening in IN718 much lower than that of γ'' [32].

The phase is not strictly stoichiometric, as the atoms in the unit cell of γ' (Figure 5a) can be substituted by other elements and so the lattice constant is variable. The lattice constant was examined for a γ' single crystal at 23 °C with X-ray diffraction by Kayser *et al.* [33], who determined $a_0 = 0.35677 \pm 0.00001$ nm and C_{11}=224 GPa, C_{12}=148 GPa, C_{44}=125 GPa for the elastic constants of the single crystal. Muhkeji *et al.* [24] studied the γ' particles in a bulk IN706 sample and found: $a_{\gamma'} = 0.3605 - 0.3608$ nm. A study performed by Slama *et al.* [32] extracted γ' precipitates chemically from bulk IN718 samples after different annealing times and temperatures. After 4 h at 680 °C they found $a_{\gamma'} = 0.3592$ nm and after 4 h at 750 °C $a_{\gamma'} = 0.3593$ nm. Additionally, Durrand [34] published an empirical formula to estimate the lattice parameter from the overall phase composition.

The volume fraction of γ' largely depends on the aging time and temperature as well as on the sum of Al+Ti+Nb fractions in atomic percent. In the literature the phase fraction of γ' is often not given as a singular value, but as a combined value for $\gamma' + \gamma''$. For example, in Refs. [35, 36] vol ($\gamma' + \gamma''$) = 14 - 16 m% in the as heat-treated condition and after 500h aging at 760 °C vol ($\gamma' + \gamma''$) = 8 m%. In IN718 there are generally not many γ' precipitates, because the alloy is designed to primarily form γ''. Therefore, γ' can only be characterised by high resolution TEM studies after aging treatments [37] and not in the water-quenched condition, which is the focus of the current work. Besides, the difference between the lattice constants of γ' and γ is small and the single crystal elastic constants are also similar (see Chapter 6.2). Consequently, the relevance of the homogenously distributed γ' particles for the determination of the residual stress state should be small. Therefore, the phase fraction of γ' in the turbine disc was not considered in the present diffraction study.

3.3.2 Ni_3Nb - Gamma Double Prime γ''

The γ'' phase is a body centred tetragonal precipitate with a DO_{22} crystal structure (Figure 5b). In its stoichiometric form (Ni_3Nb), the unit cell contains six nickel atoms in the centre of the planes and two niobium atoms at the corners. However, similar to γ' the substitution of the atoms in the unit cell by other alloying elements is possible. Therefore, the lattice constant will vary as a function of the alloy content. Data given in literature can act as guidance. For example, Sims *et al.* [14] measured $a_{\gamma''} = 0.3624$ nm and $c_{\gamma''} = 0.7406$ nm and Muhkeji *et at.* [24] studied bulk IN706 and found $a_{\gamma''} = 0.3625\text{-}0.3629$ nm, $c_{\gamma} = 0.7410 - 0.7422$ nm and the ratio $c/a \approx 2.04$.

The phase γ'' is partially coherent and consists of long disc-shaped particles that lie parallel to the {100} planes of the matrix with the c-axis perpendicular to the disc plane. Thus, the crystalline structures of the γ'' precipitates and the γ matrix form the following orientation relationship [32]:

$$(001)\gamma'' \parallel (001)\gamma \quad \text{and} \quad [100]\gamma'' \parallel [100]\gamma.$$

As a consequence, three variants of the γ'' phase can form [38].

The coherency strains between γ and γ'' have been measured to be 2.86% [22], this gives rise to the effective hardening by Ni_3Nb in Ni-based alloys. In IN718, γ'' is the main strengthening phase as the volume fraction of γ'' (15%) has been reported to be four times higher than that of γ' (4%) [22, 32].

After conventional aging treatments, TEM examinations [19] revealed that the γ'' precipitates had a thickness of 5 - 15 nm and a diameter of 20 - 40 nm , or according to Sims *et al.* [14] a diameter of 60 nm. With decreasing cooling rates, the size of the γ'' phase increases while a maximum volume fraction appears at a cooling rate of 2 °C/min [21]. Between 843 °C and 870 °C the γ'' phase begins to dissolve [19].

As the γ'' phase is thermodynamically metastable, the particle size decreases rapidly at temperatures equal to or higher than 750 °C, and the precipitates dissolve at the advantage of a stable orthorhombic phase with the same stoichiometric composition: δ - Ni_3Nb. As a result, IN718 looses stability and the strengthening effect of the γ'' (and γ' to some extent) phase.

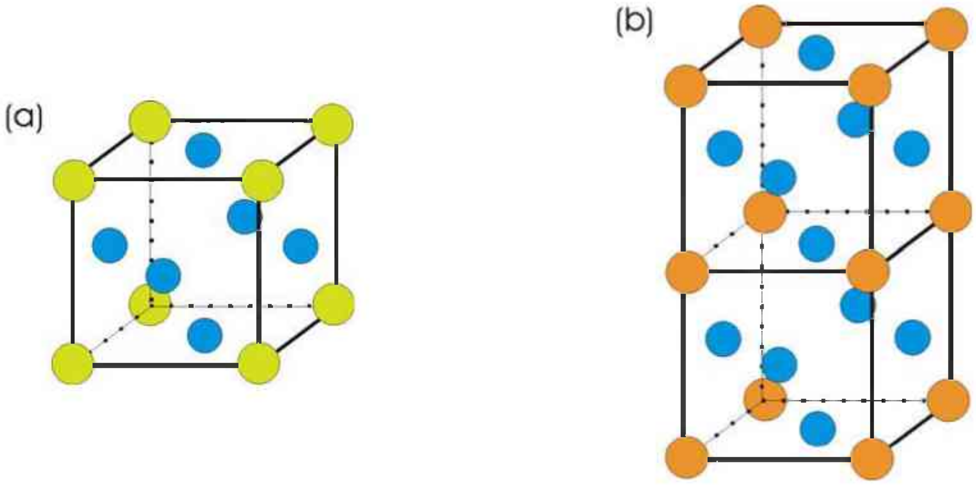

Figure 5: (a) Crystal structure of the γ' unit cell. The Ni atoms are illustrated in blue, the Al atoms in green. (b) Crystal structure of the unit cell of γ''. Ni atoms are illustrated in blue, Nb atoms in orange.

At the forging temperature of the turbine disc of 960 °C, the γ'' precipitates are in solution and are formed only during the subsequent two-step aging treatment [19]. The γ'' particles do not form very quickly; in fact the sluggishness of the γ'' precipitation is well recognized in the literature, with a maximum 16 vol% present after 20 h at 900 °C and only 8 vol% after 20 h at 950 °C [25]. Geng *et al.* [21] merely observed clusters with a few nm in size by transmission electron microscopy in the as-quenched condition (after a solution heat treatment to dissolve the γ'/γ'' that formed during hot-extrusion). However, using TEM Renhof *et al.* [38] have observed the main strengthening phases, the coherent γ' and the partially coherent γ'' in the as-quenched condition despite the high cooling rate. The γ'' particles were found to have a diameter of only 1 nm and so the γ'' particles are considered as negligible in the water-quenched condition.

Figure 6 shows the precipitation behaviour of the main phases in IN718 as given in Ref [14]. The precipitation sequence of γ' and γ'' are the subject of debate, but according to [35] the reason for contradictory results can most likely be attributed to a variation in the amount of Ti, Al and Nb. Another explanation for the different precipitation sequences was presented by Geng *et al.* [21], who observed that in continuous cooling, the γ'' precipitation precedes the γ' precipitation, but claims that the sequence is likely to be reversed for isothermal treatments.

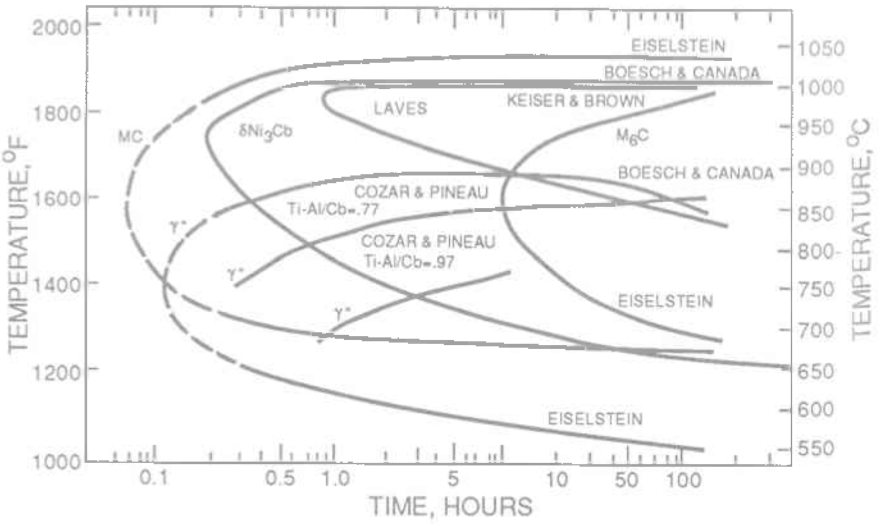

Figure 6: TTT Diagram of IN718 showing the kinetics of γ'' and γ' as well as MC, M_6C, Laves, and δ in IN718 according to Ref. [14].

3.3.3 δ Phase

The thermodynamically stable δ phase has a DO_a structure with the same nominal composition Ni_3Nb as γ'' and forms over the temperature range 650 – 980 °C [14]. According to Li *et al.* [39] $a_\delta = 0.5106$ nm, $b_\delta = 0.4251$ nm, $c_\delta = 0.4556$ nm (X-ray diffractometer using Co radiation); the δ particles were extracted from IN718 by anode selective electrolysis.

The δ phase forms as intragranular laths along the (111) planes of the matrix or by a cellular reaction at the grain boundaries or at primary MC carbides [19]. Relative to the matrix a matching of closed packed planes occurs between δ and γ with the following relationship [14]:

$$(010)\delta \parallel \{111\}\gamma \text{ and } \quad [100]\delta \parallel [100]\gamma.$$

According to Krueger [19] the precipitation of the δ phase is most pronounced in the 927 °C -954 °C temperature range, but the precipitation kinetics and morphology can be dramatically altered as a result of forging below the δ solvus temperature (T^{sol}_δ = 995 °C) [16]. If sufficient forging deformation is introduced, nucleation of δ will be rapidly accelerated and will occur intragranularly in a uniform manner rather than preferentially at the grain boundaries.

In wrought IN718 alloys the δ phase particles play an important role in the control of the grain size because they pin the grain boundaries during hot deformation. Therefore, forging is usually performed below the δ solvus temperature. During long-term exposure below the forging temperature and above 650 °C the δ phase dissolves γ'' particles. This limits the range of application range of IN718, because without the δ particles a coarsening of the matrix grains will occur and will deteriorate the fatigue properties [20].

The size of the δ phase is inversely proportional to the cooling rate [21]. For the forged disc the δ size was typically between 2 - 5 µm and neither the size nor the volume fraction changed significantly as all annealing steps were performed below the δ solvus temperature (Figures 2 - 4). A quantitative phase analysis performed on SEM images (Figure 2b, 3) of the as-quenched condition revealed a volume fraction of only 3 - 4%. This was considered to be too low to influence the neutron strain measurements. Furthermore, no diffraction peaks corresponding to the orthorhombic δ phase could be identified neither in neutron or in X-ray diffractogramms. Additionally, Krueger [19] also found negligible amounts of δ in IN718 after a comparable heat treatment of 982 °C/2 h.

3.3.4 Matrix

The γ matrix is the most important phase for the diffraction measurements in water quenched IN718 as no diffraction peaks referring to any of the precipitates could be resolved and superlattice reflections were not measured. Small peak broadening due to the presence of fine, coherent γ' or γ'' precipitates could be observed for the annealed condition, but not for the water-quenched material.

There are few diffraction studies on the contents of γ', γ'' and δ because of the difficulties in their measurement. Quantitative chemical analysis is complicated as all three phases are of the A_3B type and moreover γ'' and δ have the same nominal composition. Wenchang *et al.* [23] determined the content of γ', γ'' and δ in IN718 as δ = 4.02 m%, γ'' = 7.80 m%, γ' = 1.95 m% for a heat treatment condition after cold rolling at 970 °C/0.5 h followed by air cooling before the usual double ageing at 720 °C and 620 °C, which is very similar to the condition of the turbine discs studied here. Therefore, a single phase approach was considered as justified for the studied heat treatment condition of IN718.

Due to the high nickel content of the alloy, the matrix consists of a solid solution fcc lattice. Empirical formulas to calculate the lattice constant of the matrix as a function of the alloy elements can be found in literature [26]:

$$a = 0.35234 + 0.0119X_{Fe} + 0.0130X_{Cr} + 0.0183X_{Al} + 0.0360X_{Ti} + 0.0421X_{Mo} + 0.0624X_{Nb}\ , \qquad (2)$$

where a is given in nm and X denotes the amounts of the alloying elements in at%. According to equ. (2) the lattice constant of pure Ni is 0.35234 nm. However, the lattice constant does not only depend on the alloying elements but also on the amount and composition of the precipitates. Therefore, Liu *et al.* [26] calculate the lattice constant as:

$$a = a_0 - \frac{n_1 p_1 W_\delta + n_2 p_2 W_{\gamma''} + n_3 p_3 W_{\gamma'}}{m\left(m - n_1 W_\delta - n_2 W_{\gamma''} - n_3 W_{\gamma'}\right)}, \qquad (3)$$

where a_0 is the lattice constant of the γ matrix before the δ phase precipitation; n and p are constants which depend on the compositions of the phases δ, γ'', and γ'; and W_δ, $W_{\gamma''}$, and $W_{\gamma'}$, refer to the mass percentage of the δ, the γ'' and the γ' phases.

These empirical calculations as well as the measured data given in literature, for example, a = 0.359691 nm [23] can only act as approximate values. However, for strain measurements absolute values of lattice parameters are not required.

3.4 Heat treatment

The outstanding material properties of IN718 regarding the high yield and ultimate tensile strength together with the high creep resistance up to 650 °C are a result of the optimised microstructure. Apart from the forging techniques, the heat treatment steps play a major role in determining the final material properties. The annealing of IN718 was tailored to precipitate the optimum amount and size of the γ', γ'' and δ precipitates. Due to the extended lifetimes of critical parts and longer intervals between part overhauls, the thermal stability of IN718 is very important.

Nowadays, two main heat treatment routes are applied on IN718 materials: the well established, so-called standard heat treatment STD and the more recent variation termed "direct aging" DA, both are illustrated in Figure 7.

The standard heat treatment (STD) consists of air cooling from the forging temperature followed by an solution annealing step at 980 °C for 1h and air cooling. Subsequently, the part is aged with the following two-step aging treatment: annealing for 8 h at 718 °C, followed by furnace cooling to 621 °C (50 °C/2 h), holding for 10 h, and finally air cooling .

The direct aging (DA) route was developed in order to further increase the high temperature strength by an increased fraction of γ'' precipitates with a decreased particle size [16, 19]. Then IN718 is often referred to as DA718. First the γ'' precipitation is suppressed by a water-quench from the forging temperature; because γ'' precipitates are known to appear only at cooling rates of less then 20 °C/min. The high quenching rate freezes a higher amount of dislocations which act as nucleation sites for the γ'' particles during the subsequent two-step annealing process. The solution annealing step is omitted and the parts are directly annealed after forging and subsequently water quenched. According to Krueger [19], DA718 materials show peak hardening in the 680 °C - 700 °C temperature range and the ultimate tensile strength and yield strength properties are about 10% and 20% higher respectively, than in the range between room temperature and 650 °C, while creep and LCF properties were at least equivalent. Horvath *et al.* [16] observed an increase of the yield strength by 4.7% and an increase of the ultimate tensile strength of 3.7%.

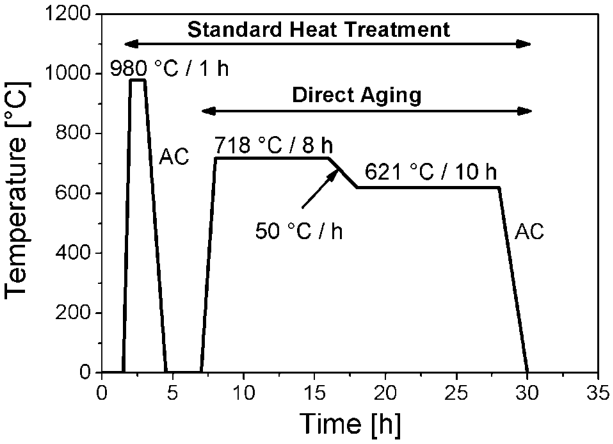

Figure 7: The basics of the two main heat treatment routes for IN718: The standard route (STD) and the direct aging route (DA). "AC" stands for air cooling.

The main focus of the current study was on the direct aging heat treatment route as it is more prone to cause large distortions of the disc and thus was more interesting in industry. Practical experience showed that water-quenching from the forging temperature did produce larger residual stresses even in the final condition after the annealing step. Therefore, the initial residual stress state in the water-quenched condition of the as-forged geometry was the basis for a verification of a finite element model that simulates the residual stresses throughout the production. From an experimental point of view it made sense to examine high residual stresses, because a lateral variation of very low stresses probably does not exceed the magnitude of the measurement uncertainty and thus cannot be interpreted. Therefore, mainly water-quenched discs were examined and this condition was compared to the FE simulation.

4 Geometry of Studied Samples & Measurement Locations

4.1 Turbine Disc

The turbine discs studied in this work are components of aeroengine turbines from the turbine family named CF34 produced by GE and were all taken from the commercial production at the company Bohler Schmiedetechnik GmbH&Co KG (Kapfenberg, Austria).

All turbine discs were forged with the same forging die (nr. 8068) and were taken out of two charges. Figure 8 illustrates the final geometry of the turbine discs which had a diameter of 320 mm and a maximum thickness of 25 mm at the rim. Directly after the final forging step, the discs were removed from the die and quenched in water. This was done at Bohler Schmiedetechnik where the parts experienced no further treatment or machining, thus, the studied discs are representative for the components produced under real large-scale conditions. The outer contour of all the discs were the same to within the typical tolerances of hot-forged components; e.g. sometimes flashed due caused by forging could be found at the outer edge.

Apart from water-quenched discs, solution treated and machined discs were also examined. Table 2 lists all the turbine discs that were measured in the course of this work, as well as their sample names referring to the respective heat-treatment conditions: “B” for water-quenched, “D” for solution annealed, “E” for machined.

Table 2: Turbine disc samples and their heat-treatment conditions as studied in this work.

Disc - Name	Condition	Remarks
B3	As Forged - WQ	
B4	As Forged - WQ	
B5	As Forged - WQ	
D4	Aged - AC	Disc B4 aged
E3	Machined	Disc B3 machined

First, the residual stress state was examined at 5 locations along a line parallel to the radius of the disc as shown in Figure 9. The disc B3 was measured along three radii that were set 120° apart to clarify the angular homogeneity of the residual stress state within one disc (Figure 8). The disc B4 was only measured along one radius to study the homogeneity of the residual stress state within one lot. More detailed measurements along the thickness were conducted in the disc B5 along the scan lines A, B and C (Figure 9); three measurement points along the thickness of the disc proved to be insufficient to describe the residual stress state and compare it to the simulations.

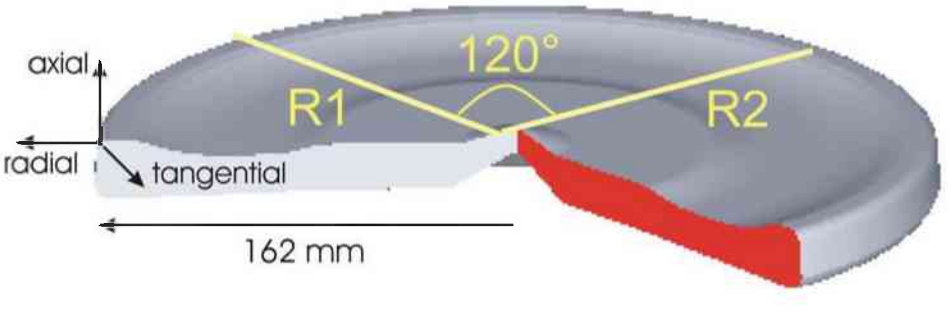

Figure 8: 3-dimensional sketch of the turbine disc showing the position of the three cross sections that were set apart 120° to study the angular homogeneity of the residual stress state.

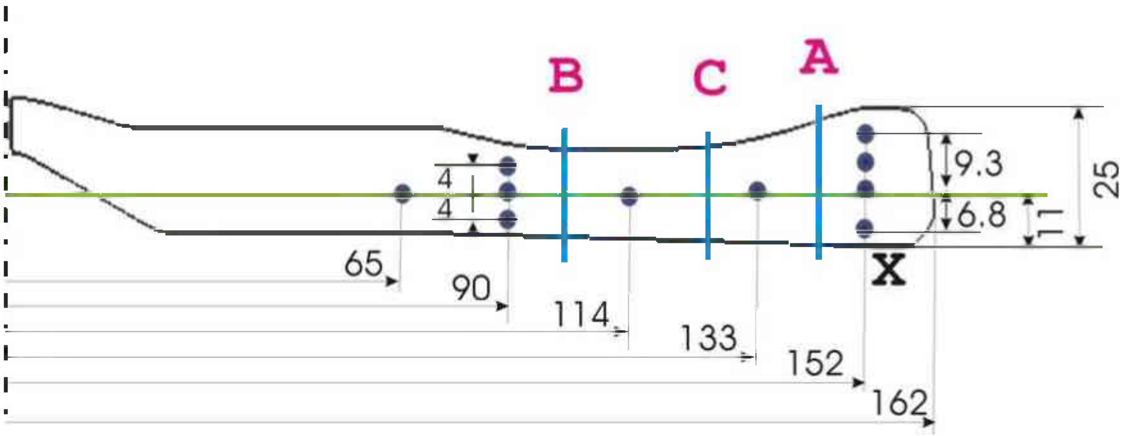

Figure 9: Cross section of the studied turbine disc showing the forging contour and the measurement locations indicated by the filled circles. The measurements along the three scan lines parallel to the axis of the disc are referred to as "A" for a disc radius of R = 146 mm, "B" for R = 123 mm, and "C" for R = 100 mm. All numbers are given in mm. The location near the rim indicated by "X" denotes the reference point for the relative positioning of the sample in the neutron beam, as described in chapter 6.4.1.

The aged disc D4 was examined at the same positions as disc B3 (Figure 9). The machined disc E3 was only measured at a very few locations shown in Figure 10 and furthermore, the d_0 value could not be measured, due to limited measurement time

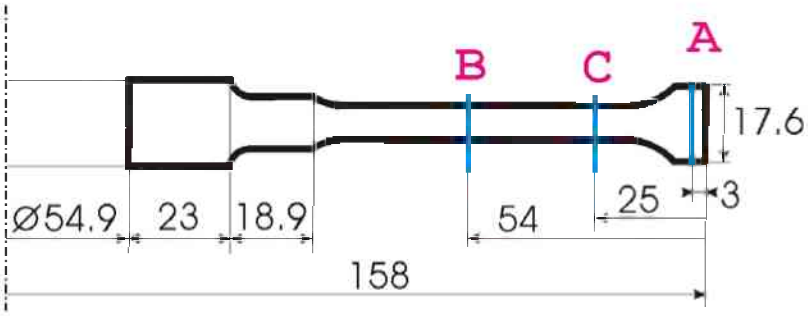

Figure 10: Measurement points in the machined disc E3 indicated by the scan lines parallel to the axis of the disc which were referred to as "A", "B", and "C". All numbers are given in mm.

4.2 Model Plate

Two thin model plates of the size of 100 × 50 × 6 mm^3 were cut from pre-forged material as shown in Figure 11a. These plates were given an annealing treatment at the forging temperature of the disc (960 °C) and subsequently quenched in water to simulate the production conditions of the water-quenched discs. One plate was examined in the water-quenched condition, and was then further exposed to the two-step annealing treatment shown in Figure 7. The other plate was used to cut a reference sample from the middle. The third model plate with the same dimension was cut directly from a disc (Figure 11b) by electron discharge machining and was solution annealed at 960 °C and subsequently quenched in water. A cubic reference sample was cut from the middle of a plate, which was machined parallel to the actual plate. Subsequently, a cube was machined directly from the edge of the model plate itself and cut further into small cuboids to test if the size of 4x4x4 mm^3 was small enough for the present sample and residual stress state.

All model plates were examined along a line parallel to the longitudinal direction in the centre of the plate shown in Figure 12. The residual stresses along the thickness of the disc could not be properly resolved due to the thin dimension of the plates.

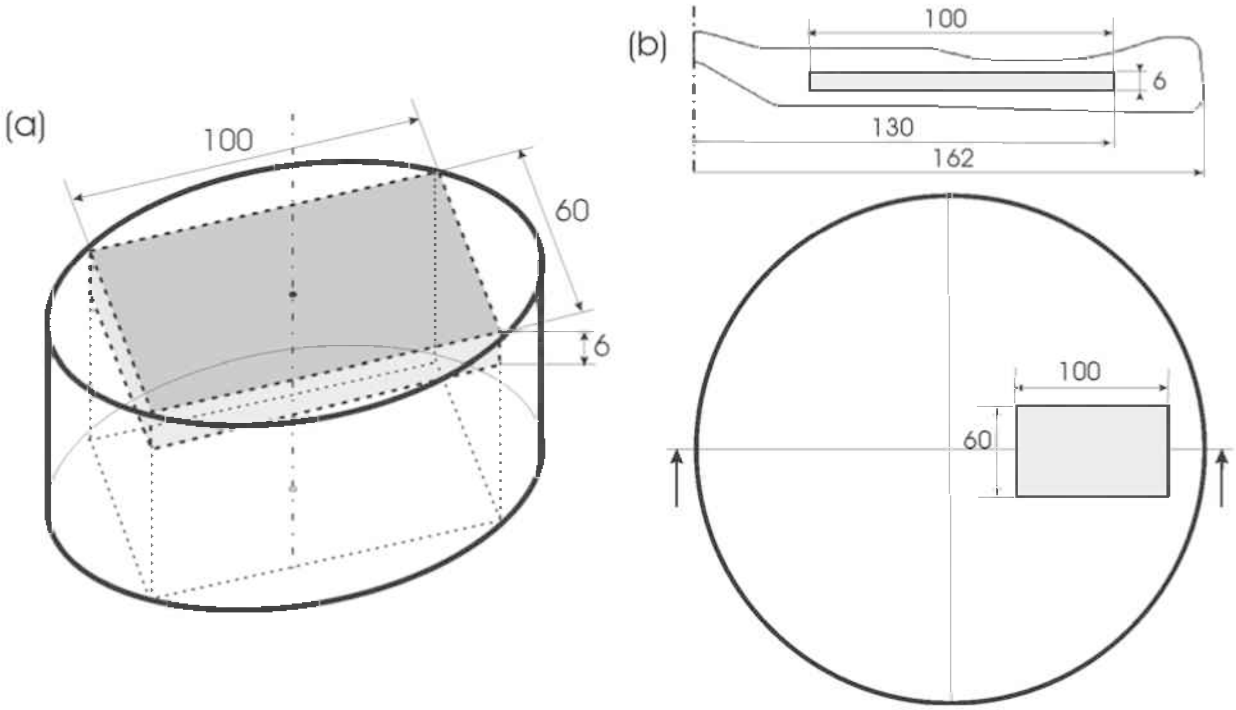

Figure 11: Sketch of the (a) turbine disc and (b) the pre-forged material cylinder showing where the model plates were machined. All numbers are given in mm.

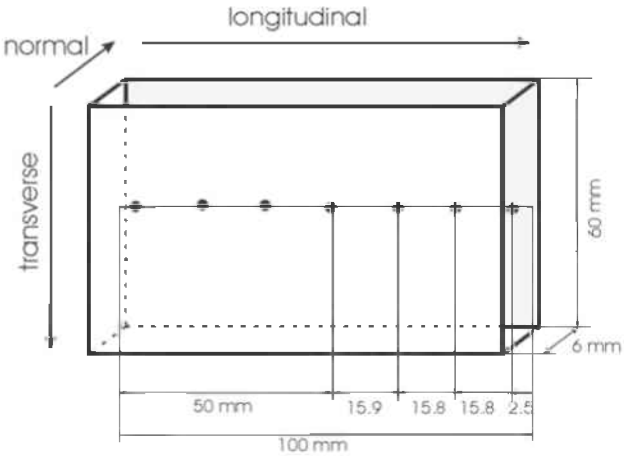

Figure 12: Measurement locations within the model plates. The numbers are given in mm.

4.3 Tensile Samples

Round dog-bone shaped tensile test samples with a diameter of 5 mm and a gauge length of 25 mm were machined out of the forged and water-quenched discs, according to DIN 50125, as illustrated in Figure 13 and were mechanically polished. The tensile samples received no further heat treatments as annealing would potentially change the precipitation condition. In this case, the tensile tests were not representative of the water-quenched turbine disc. It was believed that machining itself would only introduce stresses in the very outer shell of the samples, thus having no influence on the diffraction measurements, because the gauge volumes are situated in the centre of the samples.

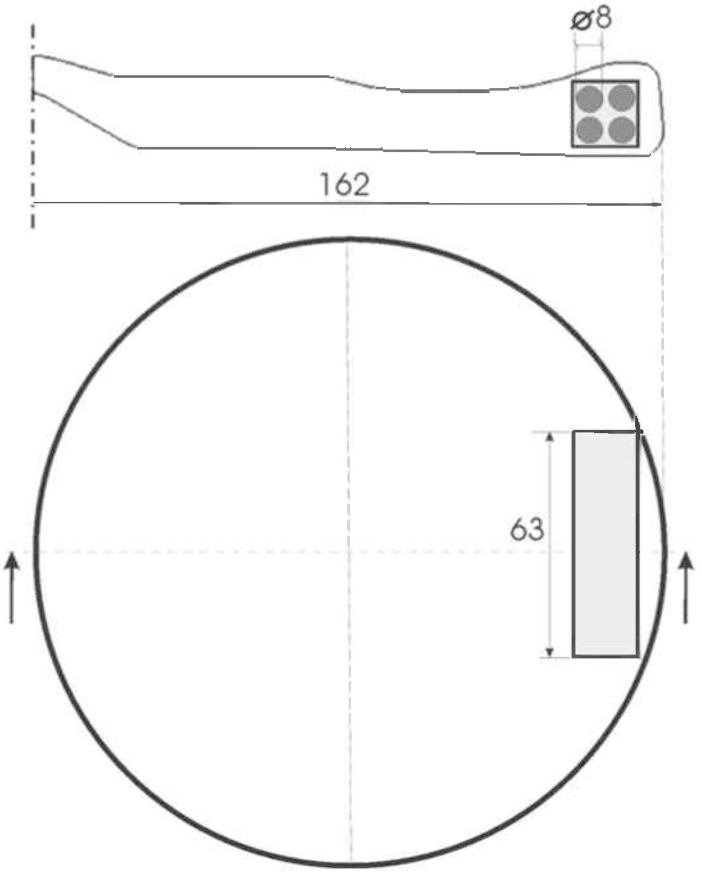

Figure 13: Sketch of a turbine disc showing the location were the tensile samples were machined out of the disc. The distances are given in mm

5 Finite Element Simulation

5.1 Simulations with DEFORM

The special purpose finite element (FEM) code DEFORM is nowadays an established tool to simulate forming processes like forging. In industrial research the number of expensive trial forgings for new part geometries or for new materials could considerably be reduced due to the successful application of finite element codes like DEFORM [40]. The company Bohler Schmiedetechnik GmbH & CoKG employs DEFORM for the design of the forging steps and would like to employ it for an integrated simulation of the whole production including all forging steps as well as heat treatments and machining processes. Previous studies have focused on modelling of the evolution of the grain size during closed-die forging [2] and during cogging [3]. The present work carries on in the production line and examines the evolution of residual stresses during the heat treatment steps succeeding the forging process. These residual stresses proved to be very crucial, as practical experience showed that even within annealed components they can give rise to massive distortions during the machining to the final geometry.

DEFORM was originally designed to model large plastic deformations as these deformations prevail during hot temperature forming processes like forging. However, cooling processes involve small deformations and the elastic properties as well as the starting point for yielding are highly important. Nowadays, DEFORM has implemented elasto-plastic materials models, which are appropriate to simulate processes dominated by small deformations. Consequently, DEFORM is expected to be a valid tool for cooling simulations, but the results have to be confirmed by experimental data. Furthermore, the correct simulation input parameter for the cooling process has to be verified.

Like many other finite element codes DEFORM consists of three main parts:

- **Pre-Processor**

  Enables the user to specify the geometry of the components, the finite element net, the material input data, and the material model. Furthermore, the simulation parameters as well as the thermal and geometric boundary conditions are defined. All of these parameters are written into a so-called keyword file, which can be read by the DEFORM simulation unit. The following input parameters are equal for all simulations:

Starting Temperature:	960 °C
Environment Temperature:	20 °C
Material:	IN718 (s. "Input Parameter")
Remeshing:	suppressed
Type of Object (=Material Model):	elasto-plastic
Type of Elements (3D):	brick
Process Duration:	120 s

  The length of the time step and the number of steps are adopted for the performed parameter variations.

- **Simulation Unit**

  Performs the finite element simulation itself. The cooling simulation involves a thermal and a mechanical problem, which are coupled with each other. For each simulation step DEFORM first solves the thermal problem and then the mechanical one.

- **Post-Processor**

  Permits the analysis and description of the simulation results. The feature called "Point tracking" was used to evaluate the temperature during the cooling process at given sample locations. For the description of the residual stresses along a defined line in the part the feature "State variable between two points" is employed. In both cases DEFORM calculates the average of the neighbouring finite element nodes if the coordinates do not coincide with the element nodes. For a smooth curve of the extracted stress components along the thickness of the simulated parts the high number of finite elements proved to be necessary.

In the present work two sample geometries are simulated: a commercial turbine disc and a rectangular model plate. The DEFORM code offers a two-dimensional version DEFORM2D and a three-dimensional version DEFORM3D, which are both employed. The axi-symmetric shape of the disc suggested that a 2D simulation is sufficient to describe the whole disc, but for the sake of comparison 3D simulations of the disc were performed as well. The model plate, however, had to be simulated with DEFORM3D. In order to reduce the simulation to a 2D problem it is necessary to assume either axial symmetry or plane stress conditions, but none of the two simplifications are applicable to the model plate.

5.2 Turbine Disc

The geometry of the modelled turbine disc is identical to the contour of the forged component at the end of the closed-die forging process. The investigated turbine disc was forged using dies with the number 8068 and Bohler Schmiedetechnik supplied the geometry data corresponding to these forging dies. In Figure 14 the 3D simulation model is illustrated. It only consists of a sector of 3° in order to reduce the simulation time. The red cross section of the disc in Figure 14 marks the 2D model. The number of finite elements was chosen to be high in order to be able to extract the state variables as a function of position in the disc without any kinks. Figure 15 shows the finite element net, which was generated by the automatic mesh generator provided by DEFORM. The 2D version consists of 9838 elements and the 3D version of 29514 elements.

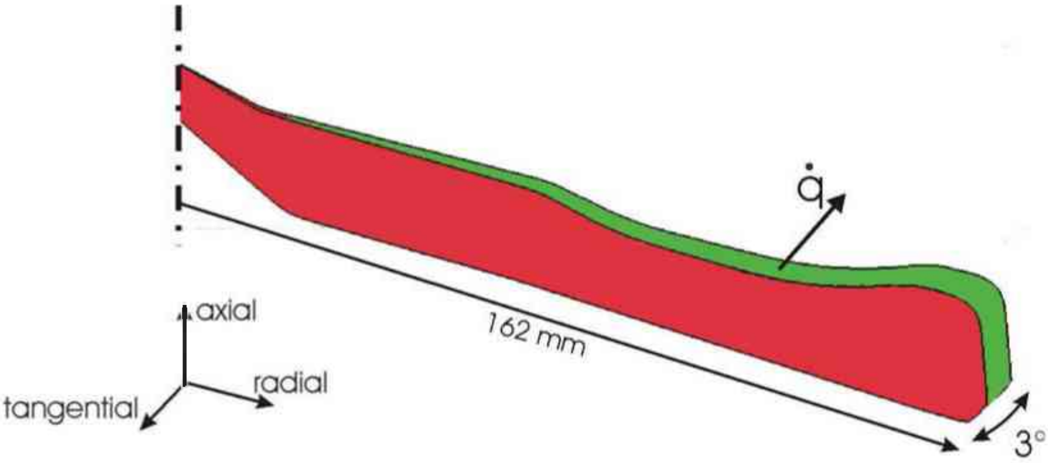

Figure 14: 3D simulation model of the turbine disc, which is reduced to a sector of 3°. The thermal boundary condition are illustrated the by the green surface, where the flux of the extracted heat is indicated by the vector $\dot{q}$.

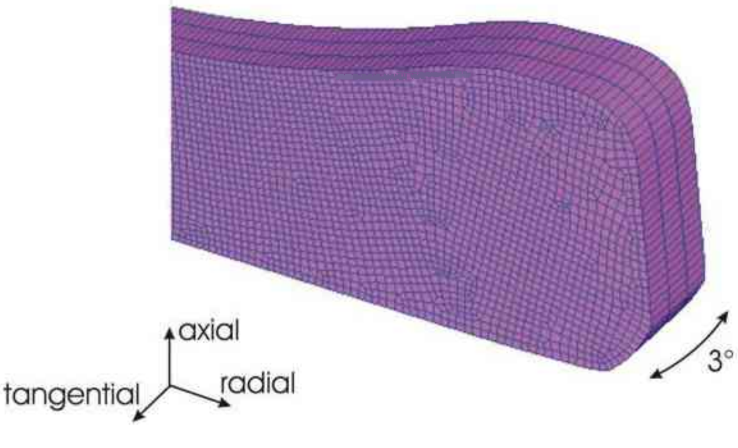

Figure 15: The finite element net employed for the 3D simulation of the turbine disc. The sketch only shows the rim of the disc, as the finite elements in the middle and central region are all rectangular and evenly distributed. The element net in the cross section is equal for the 2D and 3D model; the 3D version is build up by 3 layers of the cross section with a thickness of 1°.

The axi-symmetric shape of the disc and one fixed node in the radial direction defined the mechanical boundary conditions. The thermal boundary conditions were applied on all contour nodes and on all surface nodes illustrated by the green surface in Figure 15. Consequently, the simulation models the fictitious case, where each point on the surface of the disc experiences exactly the same cooling history. However, in reality the discs are always immersed vertically into the water and not all the points on the surface come in contact with the cooling water at the same time. Nevertheless, the immersion into the water was done as quickly as possible. Therefore, the temperature gradient that builds up during the immersion is regarded as not significant and so the thermal boundary condition seemed justified.

The axi-symetric shape of the turbine disc suggested that the directions of the principal stresses $\sigma_1 = \sigma_{axi}$, $\sigma_2 = \sigma_{rad}$ and $\sigma_3 = \sigma_{tan}$ coincide with the axial, the radial and the tangential direction of the disc geometry. In this case the shear stresses are zero $\sigma_{12} = \sigma_{13} = \sigma_{23} = 0$ and the complete stress tensor is given by σ_{axi}, σ_{rad} and σ_{tan}.

5.3 Model Plate

The model plate was simulated in addition to the commercial turbine disc. Its small dimensions facilitated the neutron diffraction measurements and any effects of the turbine disc shape onto the residual stress state could be excluded. Despite the simple shape of the model plate Deform3D had to be employed for the simulation as neither axi-symmetric conditions nor plain strain could be assumed. The simulation time could be reduced due to the threefold symmetry of the part, which allowed simulating one-eighth of the plate with the dimensions: 50 × 30 × 3 mm^3. Figure 16 shows the simulated part of the plate together with the finite element net. Along the thickness of the plate the finite elements were chosen to be very thin which cannot be resolved in Figure 16. Altogether 11832 brick elements were used, which resulted in a considerably longer simulation time compared to tetrahedral elements, which are produced by the automatic mesh generator. Yet, tetrahedral elements could not be used because they produced uneven stress patterns and for this reason automatic re-meshing was suppressed.

The mechanical boundary conditions were given by the definition of the three symmetry planes in the plate, which means that all nodes on these planes are fixed in either of the three directions x, y or z. Thermal boundary conditions are applied only on the open surfaces, but again the heat transfer is equal on all faces like in the disc. The green planes in Figure 16 illustrate the surfaces that are simulated to be in contact with the quenching water.

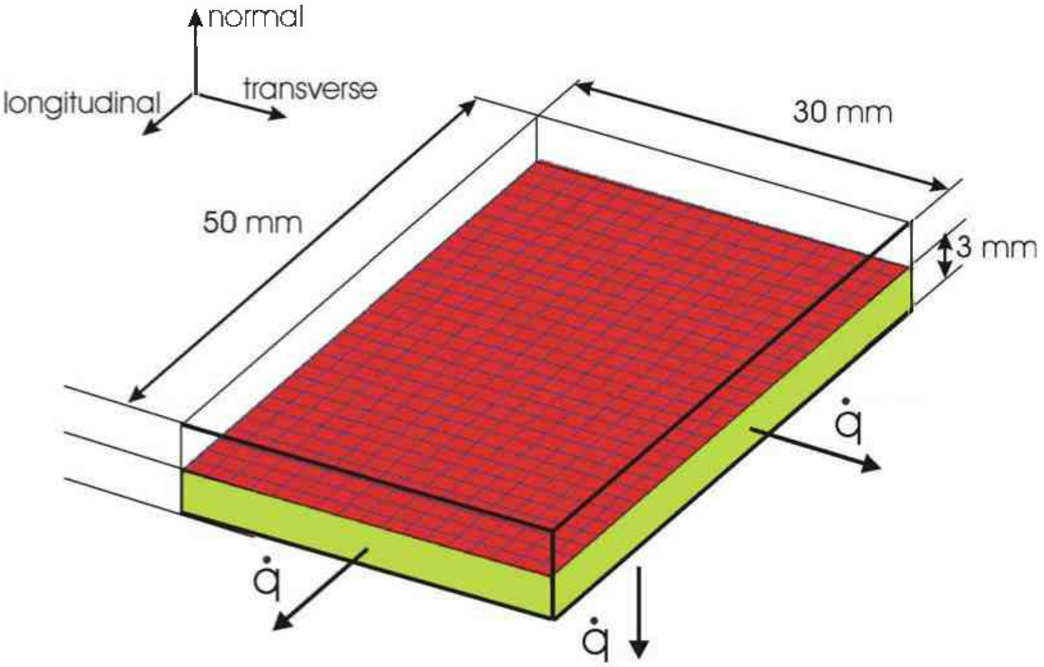

Figure 16: Sketch of the finite element model, which equals one-eighth of the real model plate. The red cross section shows the finite element net and also illustrated one of the three symmetry planes. At green surfaces the thermal boundaries conditions are applied, which is indicated by the vector $\dot{q}$.

Comparable to the turbine disc, the directions of the principal stresses are assumed to coincide with the normal, the longitudinal and the transverse direction of the geometry of the model plate. Thus, the stress tensor is given by σ_{norm}, σ_{long} and σ_{trans} and the shear stresses are believed to be zero.

5.4 Input Parameter to FEM Simulation

The material input parameters for IN718 were provided by Bohler Schmiedetechnik. Figure 17a shows the stress-strain curves for solution annealed IN718 which were determined by Bohler Schmiedetechnik (Bohler) via compression tests at a constant strain rate of 0.1 s^{-1}. Before the measured stress-strain curves could be applied as input data in DEFORM, they had to be corrected for dissipation heat. The combined influence of the strain rate and the temperature was taken into account by the Zener - Hollomon parameter Z. As the stress-strain curves were supplied by Bohler already in the corrected form, the reader is referred to Karhausen *et al.* [6] and Brand *et al.* [41] as well as to Appendix **B** for further details on the calculation of Z. The selection of the data in Figure 17b gives a better illustration of the temperature dependent flow stress. Different interpolation methods are offered by DEFORM for strain and temperature values in between the measurement points. In the end linear interpolation was chosen for all simulations, because using other interpolation methods did not lead to significantly different stress results.

The temperature dependence of the Young's Modulus and the Poisson ratio was taken into account as depicted in Figures 18a and 18b. These values are also a result of measurements performed on solution annealed IN718 [42].

The measured yield stress values could not be compared directly to other studies published in literature, because simulations of residual stresses were either based on assumption of a hardening law [43] or no mechanical material data were given at all [1, 4]. Dye *et al.* [43] employed a rate-independent, isotropic linear-hardening model with a hardening coefficient of $d\sigma_y/d\varepsilon_{pl} = 0.01$. The temperature dependence of the yield strength was fit to the data of solution heat-treated IN718 using the following equation [43]:

$$\sigma_y(T) = \frac{\sigma_y(RT) - \sigma_y(HT)}{1 + \exp((T-b)/c)} + \sigma_y(HT), \qquad (4)$$

where: $\sigma_y(RT)$ = 300 MPa is the room temperature yield strength
$\sigma_y(HT)$ = 30 MPa is the yield strength at high temperatures, above the γ' and γ'' solvii.
b = 910 °C and
c = 75 °C.

As no strain rate data was given, the yield stress values are compared to the lowest strain rate of the measured data in the current work, which are slightly above Dye's yield stress values.

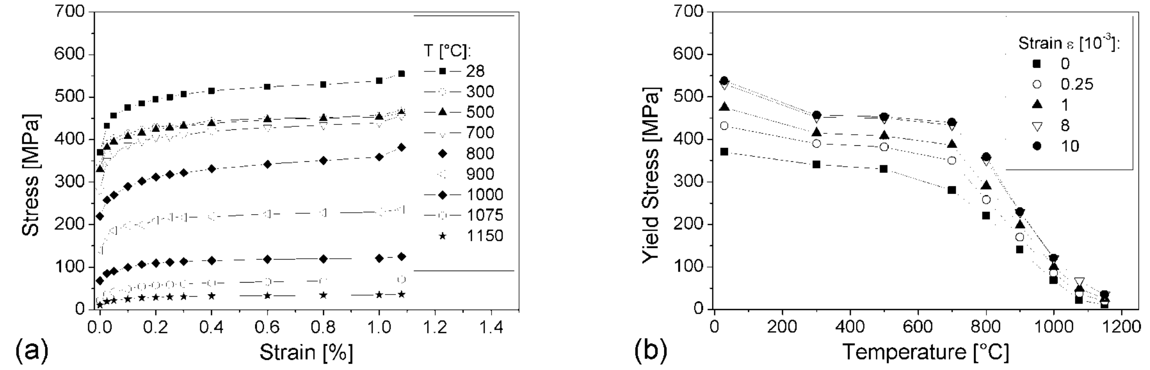

Figure 17: Measured yield stresses as a function of applied strain, determined in compression tests of solution treated IN718 cylinders at Bohler Schmiedetechnik. The strain rate was constant at 0.1 s^{-1}. (a) Stress-strain curves corrected for dissipation heat taking the Zener-Hollomon parameter Z into account. (b) A selection of the data in (a) illustrating the yield stresses as a function of temperature for different strains.

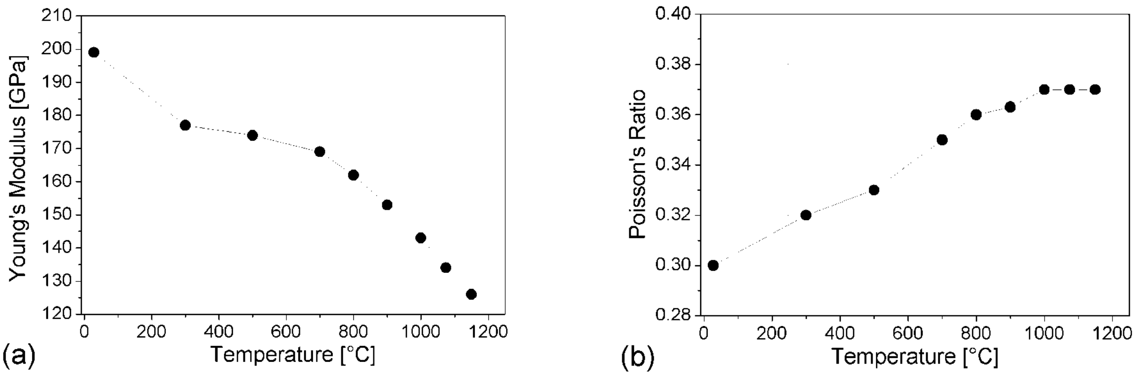

Figure 18: Temperature dependence of (a) Young's Modulus and (b) Poisson's ratio for IN718 as they were implemented in DEFORM. The data were measured by Bohler Schmiedetechnik.

The Young's modulus and the Poisson's ratio as well as the thermo-physical values are comparable to data published in literature [43]. The thermo-physical values for IN718 depicted in Figure 19 were taken from literature [11, 44, 45] and are similar to the data in [43]. The only pronounced difference could be observed for the heat capacity. In Figure 19b the precipitation of the γ'' and γ' phase is well indicated by the two peaks, but the heat capacity data published by Dye *et al.* [43] increases steadily.

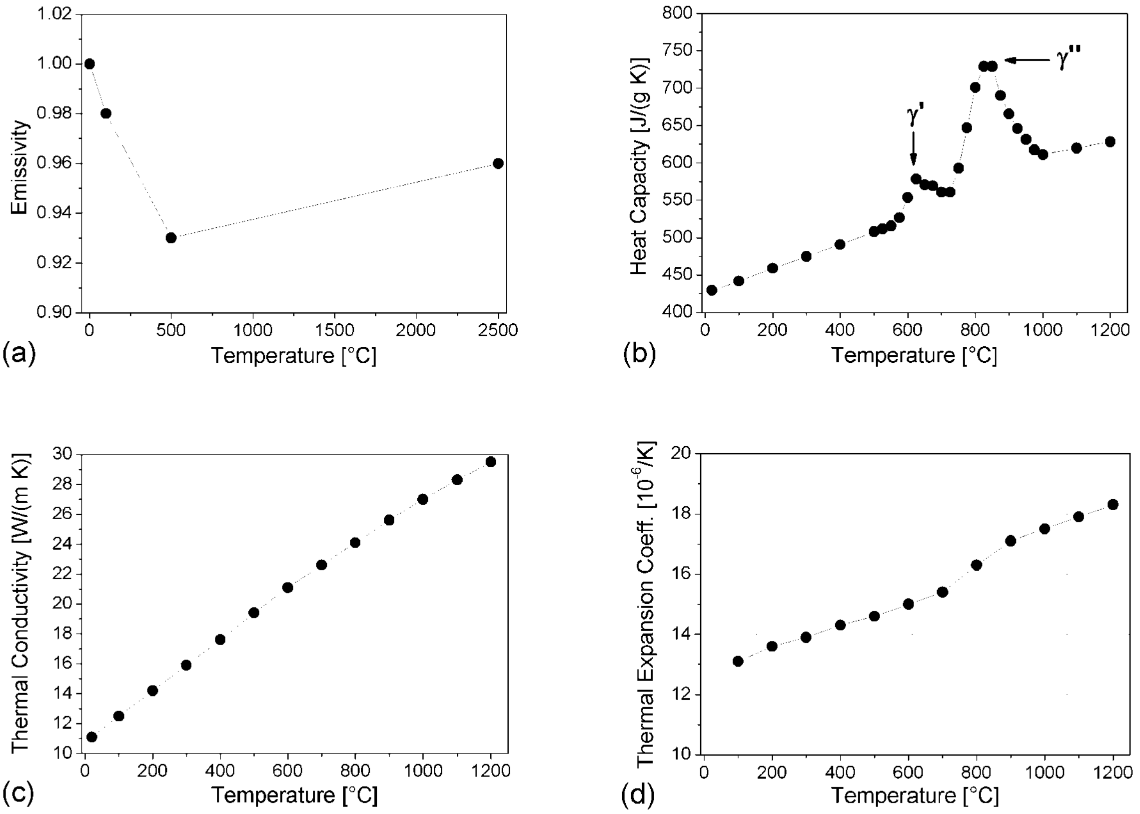

Figure 19: Thermo-physical data of IN718 given as a function of temperature according to [11, 44, 45]. The peaks in (b) correspond to the γ' and γ'' precipitation. emissivity

Finally, the temperature distribution within the sample is not only influenced by the thermal properties of the material, but also by the quenching severity that is characterized by the convective heat transfer as a function of temperature at the specimen surface.

5.5 The Heat Transfer Coefficient

Initially, the FEM simulation of the turbine disc was performed with different element numbers and in the 2D and 3D version as well as with different thermal material properties to evaluate the influences on the final stress result. All these calculations have shown that only the heat transfer coefficient has a strong influence on the stress results. Besides, the other input values as for example the yield strength, the thermal expansion, and the heat capacity are approved by other data published in literature for IN718 [43, 45]. These parameters could only affect the residual stress state if changes in the values were well above their measurement uncertainties.

Contrary to other input data, the heat transfer coefficient cannot be measured directly, which results in a relatively low number of published data in literature [46 - 49]. Actually, many authors simply assume a constant value without giving any references for it [50, 51]. Some authors have attempted to calculate it for a specific cooling experiment using model parts like cylinders [47, 48, 52] or spheres [51, 53]. However, the present work concentrates on an industrial part, directly taken from commercial production. Heat transfer data from other experiments cannot be employed here, as the influences of modified quenching conditions cannot be neglected. It is important to mention that especially water-quenching is very sensitive to the specific quenching conditions. Water temperature, agitation, immersion velocity, etc. directly influence the vapour film caused by the Leidenfrost effect and thus change the quenching kinetics. Therefore, temperature measurements were undertaken within the turbine disc as well as within the model plate to gain information of the prevailing quenching condition of the quenching of commercial turbine discs studied in this work.

Some authors [43, 54] refer to temperature measurements directly at the surface and use these temperature curves as a boundary condition for their finite element simulations. As nickel-based alloys do not tend to exhibit large scaling this procedure can perhaps be appropriate for air cooling, but during water cooling the formation of vapour bubbles will change the conditions at every single point along the surface. Consequently, the author of this work believes that such a measurement cannot be representative for the average temperature during the cooling period of a whole part. Authors like [55, 56] share this appraisal and state that surface measurements cannot give representative temperature values when quenching is done in liquid media.

5.5.1 Temperature Measurements

In order to avoid surface effects the thermocouples were placed in blind holes as illustrated in Figure 20. The tip of the thermocouples were placed at the bottom of the holes, which had a distance of 1 to 3 mm to the surface. In order to prevent any infiltration of water, the diameter of the holes had to be equal to the diameter of the thermocouples (1.5 mm). As nickel-based alloys are not easily machinable, the holes in the turbine disc were produced by electro-discharge machining. In the model plate, it was possible to drill the holes with hard metal drill bits, because the holes were not as long as in the disc (Figure 21).

Mineral insulated NiCr-Ni (type "K") thermocouples (Sensotec [57]) were used to measure the temperature drop. In order to have low reaction times very thin thermocouples were used. The diameter of the outer shell was 1.5 mm and the reaction time was 0.90 s according to Sensotec. K-Type thermocouples were used as the quenching always started at 960 °C, which is within the optimum measurement range for K-Type elements of -200 °C to 1100 °C.

The industrial quenching process was reproduced by heating the disc up to the forging temperature of 960 °C and quenching it in cold water (20 °C). Contrary to the disc, the model plate was not heated up in a furnace at Bohler Schmiedetechnik, but in a small laboratory furnace at the Department Metallkunde und Werkstoffprüfung (Montanuniversität Leoben, Austria). However, the procedure was equal for both parts. After the parts reached temperature, they were taken out of the furnace by hand and submerged vertically into the water as quickly as possible. The time between the extraction from the furnace and the full submersion was less than 5 s. In the experiments external agitation did not govern the heat transfer, as the parts were not moved in the water once they were fully submerged. Therefore, the formation and the break-down of the vapour bubbles as well as the velocity of the immersion were regarded as the main influencing factors for the heat transfer.

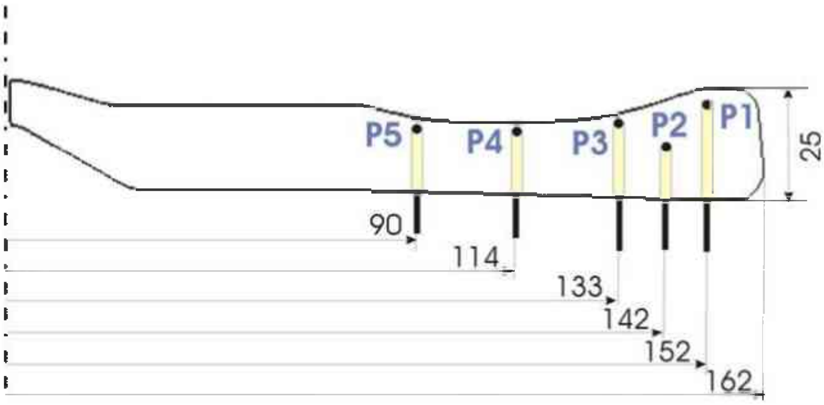

Figure 20: Cross section of the turbine disc showing the location of the temperature measurements at the bottom of the blind holes referred to as P1, P2, P3, P4, and P5.

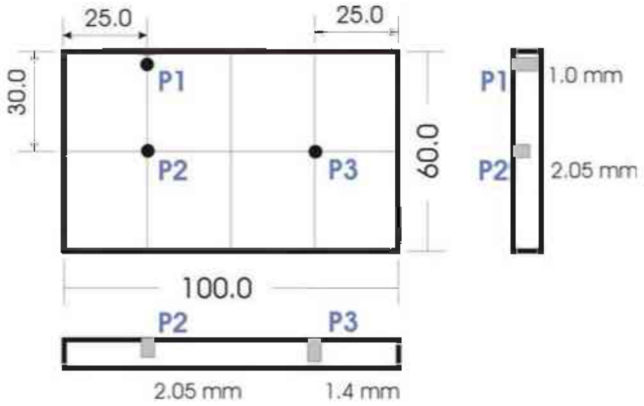

Figure 21: Model plate with its location of the temperature measurements at the bottom of the blind holes referred to as P1, P2, and P3.

Figures 22 - 23 show the recorded temperatures within the turbine disc and the model plate as a function of time. As can be seen the parts cool down to 100 °C very quickly. The disc reaches 100 °C after approximately 60 s, the thin model plate after only about 15 s. The further cooling down to RT needs considerably longer for both parts.

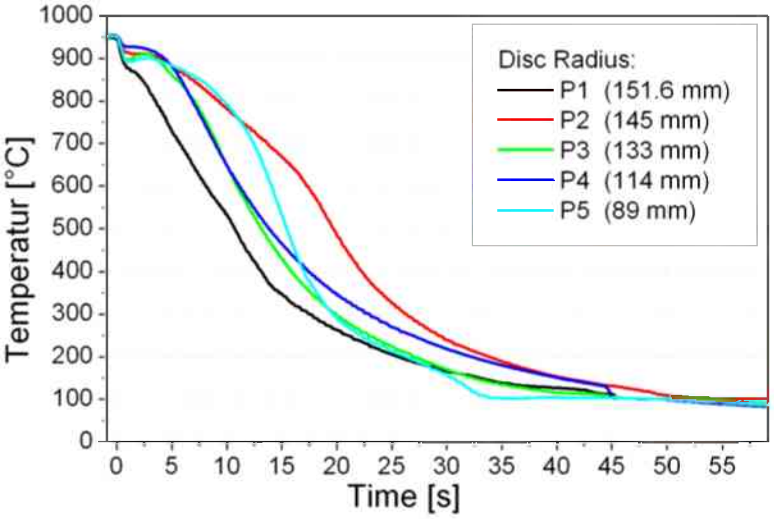

Figure 22: Measured temperatures in the turbine disc as a function of cooling time.

The temperatures recorded within the disc showed that the measurement location P2 in the thicker region close to the rim (Figure 20) cools down much slower than the rest. No big differences could be recorded for the measurement locations along the disc radius. Therefore, the distance from the disc's top surface seems to be more important than the radial position, although the disc was submerged vertically into the cooling water with the points P1, P3, P4, and P5 successively submerged. In the thin section of the disc the measurement points P3 and P4 are identical within the estimated measurement uncertainty. The fact, that the temperature at P1 decreases slightly quicker than at P3 and P4 is attributed to its position in the rim area. For the first 3 - 4 s the temperatures at P2 - P5 show nearly constant values, which most likely can be attributed to the presence of a vapour film or vapour bubbles that retard the heat transfer. During the experiment massive formation of vapour bubbles could be observed for the disc as well as for the model plate.

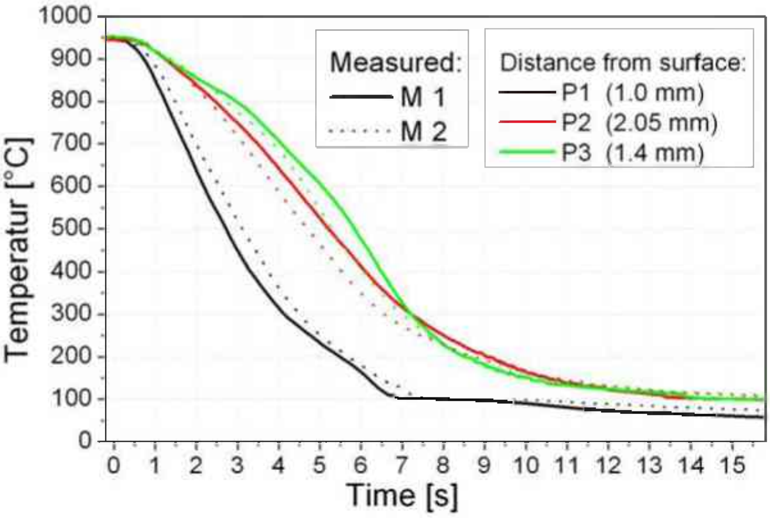

Figure 23: Measured temperatures in the model plate as a function of cooling time. Continuous lines depict the first measurement M1; dotted lines show the second measurement M2 at the same positions with identical thermocouples.

In the 6 mm thick model plate the temperature measurement was performed two times. After the plate was cooled down to room temperature it was heated and quenched again. Thus, the temperature was measured at the same positions with identical thermocouples. Differences of up to 50 °C were recorded for the two measurements and so the results of the measurement positions P2 and P3 could be regarded as identical, despite their different distances from the plate's surface (Figure 23). The difference of 0.4 mm between P1 and P3 proved to be significant as the temperature at P1 decreases to 100 °C within 6 s, which is about half the time for the other locations. Between 100 °C and RT the temperature decreases very slowly in the plate as well as in the disc, but this temperature range was not important for the residual stress development.

5.5.2 Heat Transfer Coefficients in Literature

Despite much research and many experimental and theoretical investigations, boiling and cooling phenomena are not fully understood. It is generally accepted that quenching involves complex processes like vapour film formation followed by subsequent break-down and generation of vapour bubbles that lead to agitation of the surrounding liquid and enhance the transport of heat. There is no doubt that full contact between the quenchant and the surface is only taking place after the liquid has ceased boiling and that the vapour film causes a decrease in the heat transfer. However, there seems to be a lack of expertise how this knowledge can be used for finite element quenching simulations, because a FE model requires well defined numbers for the heat transfer coefficient. There are several experimental as well as analytical approaches to this problem published in literature [46 - 53, 55, 56], but the results are sometimes contradictory or not well founded.

Among the first systematic experiments Nukiyama's study of a heated plate with a boiling liquid on top of it has to be mentioned [58]. Nukiyama determined the heat flux rate as a function of the difference between the surface and the coolant temperature, which is shown in Figure 24a and is often referred to as Nukiyama curve. On the basis of this heat transfer curve it is possible to separate different boiling stages of a quenching experiment and correlate them, at least qualitatively to a certain heat flux. There are three main stages: the film boiling, the nucleate boiling, and the liquid cooling stage, also referred to as convection phase. The maximum heat flux occurs at the so-called transition boiling stage, which separates film and nucleate boiling. Often it is just referred to as the temperature T_{DNB} (**d**eparture from **n**ucleate **b**oiling) as the phase is too short to be detected. Nucleate boiling and the liquid cooling stages are separated by the Leidenforst temperature T_{Le}, which is also defined as the temperature where rewetting occurs. T_{Le} typically lies between 300 °C and 850 °C [59]. The main stages of quenching can also be found in a so-called "cooling curve" (Figure 24b), which represents the sample temperature recorded as a function of time.

The quenching process is influenced by numerous parameters and their correlation to the key figures of the heat transfer curve: T_{Le}, T_{DNB} and $h_{max;}$ are difficult to interpret as none of the parameters change independently. Figure 25 presents a schematic illustration of the vapour film and its break-down.

A schematic function for h(T) is given in Figure 25, the figure illustrates the vapour film and its break-down for immersion and film cooling. According to Liscic [53] the location of the Leidenforst temperature is most important, as it is very sensitive to changes in the system, for example: bath temperature, surface roughness, size, and diameter of the sample as well as the type and velocity of the liquid. Increasing T_{Le} results in an increased cooling time as the vapour film collapses earlier and the phase of the highest heat transfer is shortened. This can be provoked by: a lower bath temperature, an increased velocity of the quenchant and by external agitation. The quicker the vapour film is destroyed the sooner the vapour bubbles will be transported away from the surface of the component. Obstructions by geometrically sophisticated parts hinder the movement of the quenchant and so the vapour blanket can be locally more stable. Yet, even at the smooth surface of a geometrically simple part like a cylinder, T_{Le} is not a single value as during immersion quenching the film collapses successively along the length which results in different Leidenfrost temperatures. The boiling point of the quenchant also strongly influences the T_{Le}, but the two temperatures are not identical [53].

The temperature between film boiling and nucleate boiling T_{DNB} is strongly linked with T_{Le}. The mutual dependency was studied for spheres and cylinders and is described by empirical equations [53], but cannot be applied for other geometries like the model plate or the turbine disc.

The level of the maximum heat transfer h_{max} is reported to be influenced only by the type of metal [Lisc]. Above T_{Le} the heat transfer coefficient h is determined by the presence of an external agitation and the properties of the liquid. Significant differences are reported for oil or polymer quenchants and for cooling water with impurities [53].

In the current study only water was employed as a quenchant and thus different levels of h above T_{Le} in the FEM simulation can be interpreted as a modification of the agitation rate. The change of the Leidenfrost temperature itself can be recognized as an adjustment to the prevailing water temperature and to the water flow velocity during the immersing of the sample. Influences of the shape of the samples and the surface roughness are indirectly included in the T_{Le} as well. The liquid properties and the prevailing agitation rate are also reflected in the temperature of maximum heat transfer and in the slope ($\Delta h/\Delta T$) between T_{Le} and T_{max}, because both describe once more the stability of the vapour film

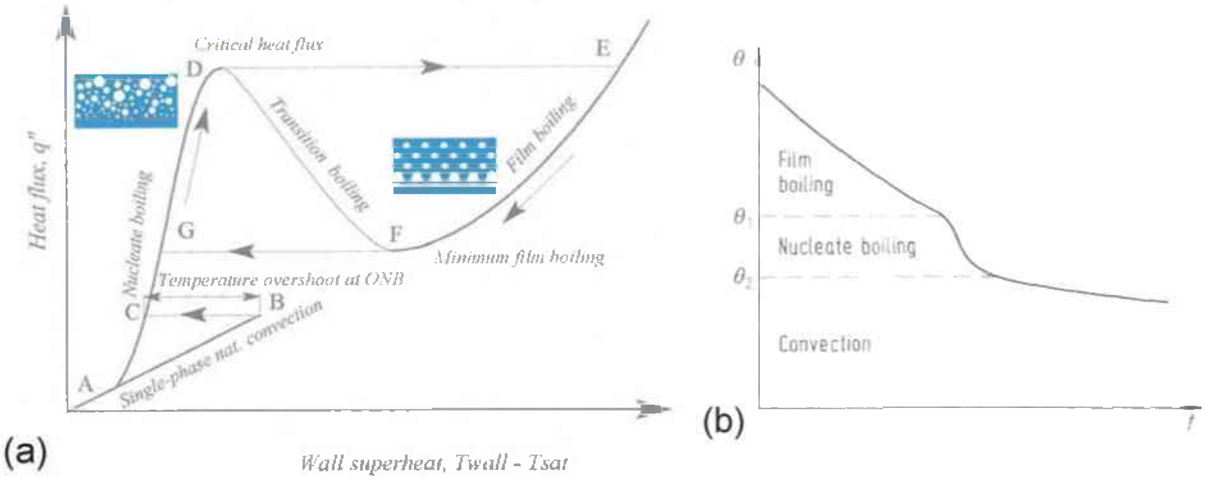

Figure 24: (a) Nukiyama curve for boiling showing the main phases: free convection, nucleate boiling, and film boiling. The figure was extracted from [60] (b) Cooling curve showing the transition temperature between film and nucleate boiling θ_1 (T_{DNB}) and temperature at the beginning of natural convection θ_2 (T_{Le}).

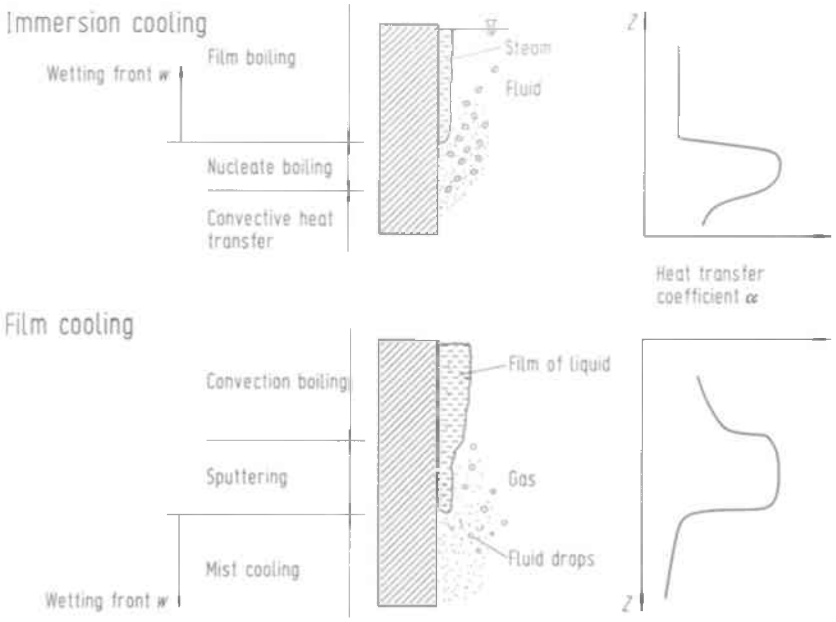

Figure 25: Immersion and film cooling with the assigned functions for the heat transfer coefficient. The figure was extracted from [53]

The majority of the studies published in literature that focus on cooling simulations [51, 61] or on the measurement of thermal residual stresses [54, 62] assume a constant heat transfer coefficient or a constant heat flux. This means most studies neglect the boiling phenomena described above or regard them as negligible. On the other hand there are detailed investigations that describe various influences on the heat flux for simple sample geometries like spheres or cylinders [53] as a function of the immersion velocity, the degree of contamination of the quenchant or other factors that cannot be measured for commercial processes or for components like the turbine disc.

Often the use of constant heat transfer values is justified by the good fit between measured and calculated cooling curves or the corresponding simulated residual stresses. Some studies lack any comparison to measured data and present FEM results only [50]. Table 3 shows examples for constant heat transfer coefficients or heat fluxes that can be found in literature.

Table 3: Heat transfer coefficients used in literature for quenching simulations.

	Author	*h* [W/(m²K)]	Sample	Quenchant	Type of Quenching
(1)	Rist [54]	20000 – 2000	Ni – cylinder turbine disc	water	immersion
(2)	Sen [50]	16742.2	steel cylinder & tube	water	immersion
(3)	Hossain [51]	7000 and 16740 based on [Sen2000]	stainless steel spheres	water	spray water quenching
(4)	Hossain [61]	16700 2000 7000 based on [Gür] 200	steel sphere & cylinder	water	spray water quenching
(5)	Becker [64]	100	Al bar	water	immersion

Another group of studies published in literature concentrate on the analytical calculation of the heat transfer coefficient by solving the inverse heat transfer equation using different mathematical methods. Conjugate gradient: [48, 52], Broyden-Fletcher-Goldfarb: [47] and inverse conduction algorithm: [55, 56]. Figure 26 shows a selection of the obtained functions of the heat transfer coefficient or heat flux. However, none of them employed these curves for quenching simulations. Le Masson *et al.* [48] calculated the heat transfer coefficient for water at the bottom face of a Jominy sample made of steel with the conjugate gradient method, making it necessary to assume a function for *h* first. Based on this assumed function Le Masson *et al.* calculated complex 2-dimensional curves for *h* that start at 10000 W/(m²K) and reach up to 60000 W/(m²K). But the quenching process of a Jominy sample is substantially different to the quenching by immersion of a hot part like a disc. In contrast to an immersion quenching experiment the high water pressure on the surface of the Jominy sample detains the formation of a continuous vapour film and is in fact a spray water quenching experiment. Oliveria *et al.* [64] performed spray water quenching as well and presented very different data (Figure 26b) from the previously mentioned authors. These differences illustrate that employing published data is very questionable as even similar experimental conditions can lead to different heat transfer results.

All curves in Figure 26, except for the one determined by Buczek [47], have one maximum only. Buczek *et al.* studied the effect of different angles between the blind hole of the thermocouple and the sample surface and found heat transfer curves with two maxima (Figure 26f). For the rest of the studies the location of this maximum varies between 150 °C and 300 °C, which is in any case well above the boiling temperature for water. The height of the maximum heat transfer differs significantly, which can partly be attributed to different experimental conditions. Considerable differences regarding the Leidenfrost temperature are observed in Figure 26, which in any case would lead to large differences in the residual stress state. Yet, none of these authors performed finite element simulations or measurements of residual stresses.

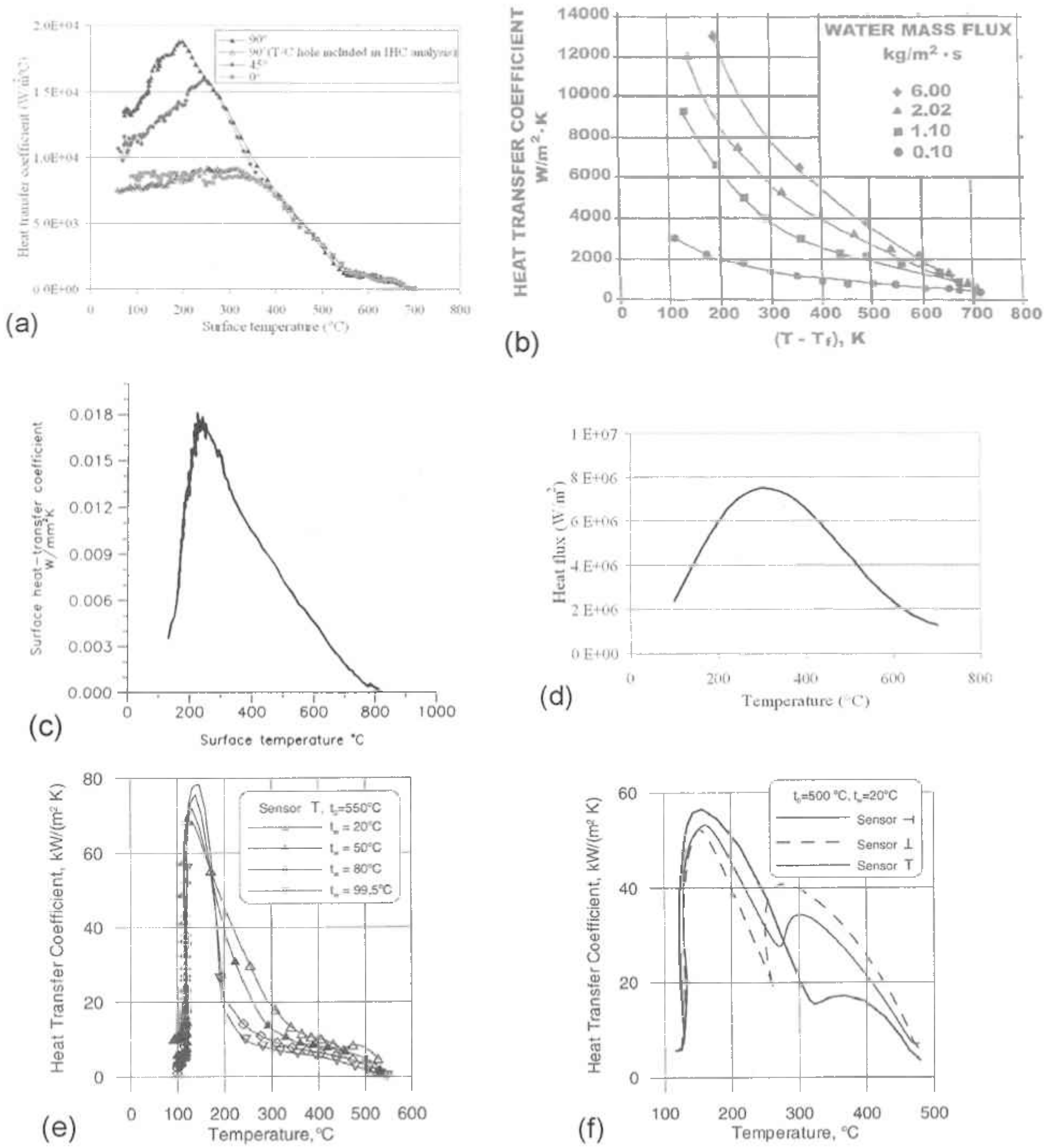

Figure 26: Temperature dependent heat transfer coefficients for water quenching determined by analytical calculations based on temperature measurements (a) [48], (b) [64], (c) [49], (d) [55], (e)-(f) [47].

The general shape of the curves in Figure 26 confirms the shape of the heat transfer coefficient as function of temperature. As all curves started at 500 °C or 700 °C, they could not be employed for the quenching simulation of IN718, which requires data up to 1000 °C. Actually, the temperature range between 1000 °C and 500 °C proved to be crucial for the residual stresses in the studies parts and thus extrapolations of the literature data presented above is problematic.

Apart from the numerous publications that state no heat transfer data at all, some authors give the heat transfer data as a function of time not of temperature [56]. Then these data are useless for the simulation of other quenching experiments, because the cooling time is directly linked to the dimension of the sample and the position of the thermocouple.

Another group of publications employ analytic calculations and transfer the thermal and material input data into dimensionless numbers [65]. This procedure can be very useful to examine the effect of different material models, but it does not offer definite numbers for real quenching experiments, either.

5.5.3 Heat Transfer Coefficients in the Current Work

During quenching small variation in the experimental conditions have a great influence upon the residual stress state within the sample. The obtained FE results proved to be especially sensitive to the presumed surface heat transfer coefficient, which cannot be measured directly. Due to the high importance of this parameter and the partly contradictory numbers given in literature, the heat transfer conditions of the current quenching process were investigated. To do this the measured cooling curves and residual stresses were compared to the corresponding values determined with DEFORM.

Initially, the model plate was used to simulate the different quenching conditions. The model plate was chosen as variations of the heat transfer condition had more pronounced effects on the cooling curve and the residual stresses within the small plate. To begin with, the heat transfer coefficient was chosen to be constant with temperature, which can be regarded as a first approximation. With reference to the literature values between 4000 W/(m²K) [Wärmeatlas] and 20000 W/(m²K) [54] were tested.

The real conditions during quenching involve the above-mentioned boiling and nucleate stage followed by a break-down of the vapour film, the wetting of the surface and finally the convection phase. In terms of simulation input parameters this complex process can only be taken into account by a temperature dependent heat transfer coefficient.

The function h_s shown in Figure 27 was used as the basis for further variations of h. A specialized DEFORM module enabled the calculation of h_s based on temperature measurements during a different quenching experiment [66]. Yet, this specialized module was not available for the current study.

Table 4 shows the variations of h that were investigated by finite element simulations. The key parameters of the curve: T_{Le}, T_{max} and h_{max} were changed independently of each other as far as possible to study their influences separately. Of course, in reality variations of the quenching conditions would cause mutual changes of these key parameters. The curves of the heat transfer coefficient themselves are shown in the next chapter.

Despite the different dimensions of the turbine disc and the plate it was believed that the same heat transfer curve h (T) could be employed for a quenching simulation. First of all the basic shapes of the two parts are similar, because they are thin compared to their diametrical extension. Secondly, both samples were immersed vertically and that should lead to equal cooling conditions.

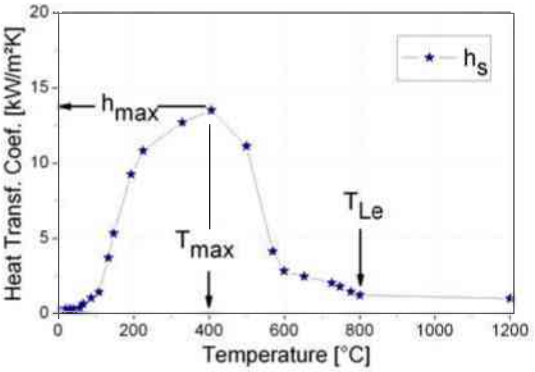

Figure 27: The function h_s for the temperature dependent heat transfer coefficient that was used as a basis for further empirical variations of h. T_{Le} typically lies between 300 °C and 850 °C [59].

Table 4: Variations of a temperature dependent heat transfer coefficient *h* employed as input data for the simulation of the model plate.

Variation of	Figure
1. Location of T_{Le}	31a 31c
2. Location of T_{max}	32
3. Modification of h_{max}	33
4. Modification of the slope ($\Delta h/\Delta T$)	34a 34c

For a comparison some heat transfer coefficients given in literature were used as input data. As mentioned above, the available data is very limited and partly contradictory. Surprisingly, many authors claim to achieve good fits even with constant values for *h* or partly constant values (see for example Refs. [50, 54, 61]), which could not be confirmed. Yet, these studies never perform a complete comparison between simulated and measured data involving residual stresses as well as cooling curves.

5.6 Simulation Results of the Model Plate

For a profound analysis of the FEM simulations the calculated residual stresses as well as the cooling curves at the locations P1, P2, and P3 (Figure 21) were investigated. For a correct simulation of the real process, the FE model has to fit the measured cooling curves as well as the experimentally determined residual stresses. First, the simulated cooling curves for different assumptions of the heat transfer coefficients are compared to the measured temperatures at P1 and P2. This gives an indication for the limits but also points at legitimate assumptions for *h*.

5.6.1 Evolution of Stress and Strain with Time

All finite element calculations simulated a real time of 120 s. This ensured that the entire component cooled down to the water temperature independently of the employed input parameters. In the model plate the final stress values were reached much earlier, which is demonstrated by the stress evolution of one representative simulation in Figure 28. The development of the internal stresses and the plastic strains at the locations P1 and P2 (Figure 21) as a function of the cooling time illustrate that 12 s is sufficient to describe the whole cooling behaviour of the model plate.

The value of the single stress components gradually increase during the initial cooling period above T_{Le}. Afterwards, the stresses reach the yield limit and plastic deformation takes place during the period of highest heat transfer between the quenchant and the surface. Then, the stresses change gradually until they reach their final values at the end of the quenching process, when the whole part has cooled down to the cooling water temperature.

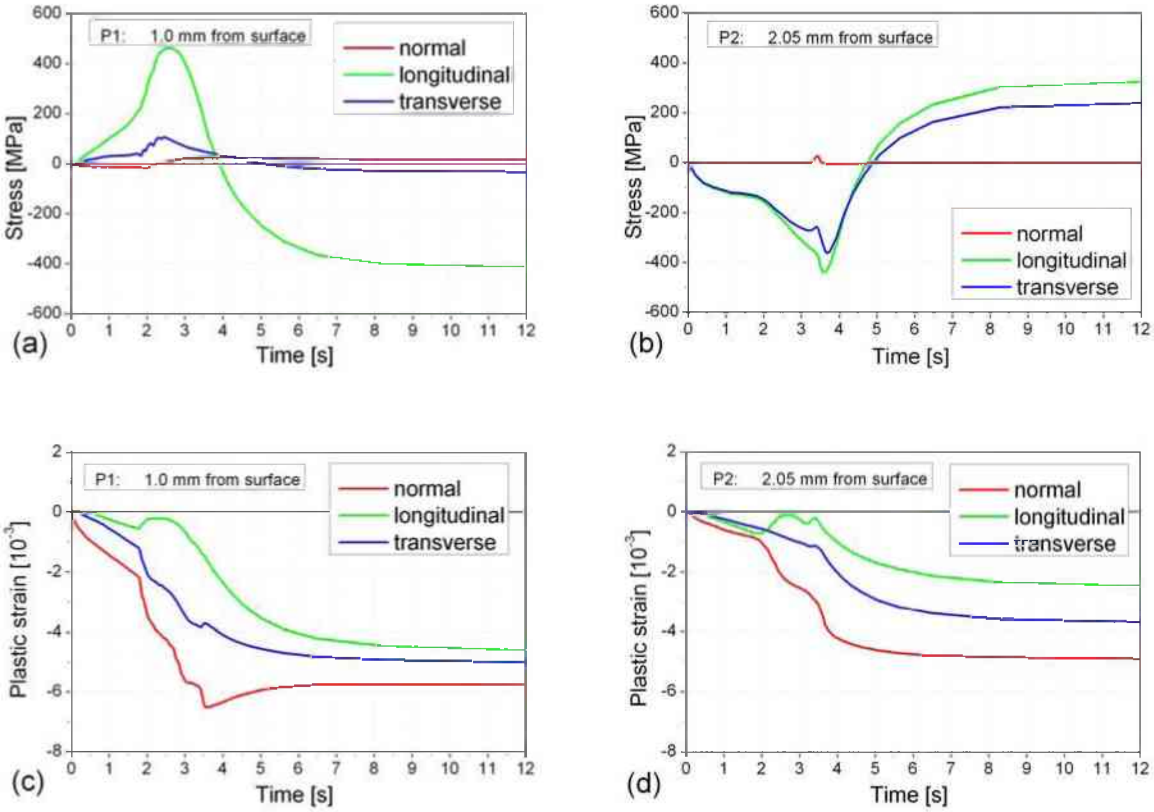

Figure 28: The evolution of residual stress and plastic strain within the model plate as a function of cooling time at two measurement positions located 1 mm and 2.5 mm away from the surface.

5.6.2 Cooling Curves: Comparison of Literature Values and the Parameters Studied in this Work

5.6.2.1 Constant Heat Transfer Coefficients

In classical textbooks like [67] constant values ranging between 3000 and 4000 W/(m²K) are often reported for water quenching. Therefore, the initial simulation was performed with h = 4000 W/(m²K). In order to draw a comparison to studies that used much higher values like h = 16742 W/(m²K) [61] the simulations were conducted with different heat transfer coefficients from h = 4000 W/(m²K) up to 20000 W/(m²K). The results are shown in Figure 29. Obviously, none of the simulated cooling curves fit the measured temperatures, all of the calculated temperatures drop much quicker than the values recorded with the thermocouples. Lower heat transfer coefficients of course result in milder cooling but any values below 3000 W/(m²K) would simulate oil quenching or air cooling and are thus inappropriate for the water-quenching of turbine discs. Besides, even though literature values for h diverge considerably, all studies at least state values above 4000 W/(m²K).

As the temperature measurements were not performed directly at the sample's surface, there is a certain contribution from the heat conduction properties of the material. For a comparison, calculations with different values of the thermal conductivity λ were performed. Yet, within a range $\lambda \pm 10\%$, no significant differences of the simulated results could be observed. Any larger variations of λ did not make sense as this would exceed the measurement uncertainty of the laser flash method, which was used to determine the heat conduction properties [11]. Besides, the values employed for λ in this work are consistent with [11, 43]. As a consequence the thermal conductivity was not regarded as a major parameter for the residual stress state in the quenched samples.

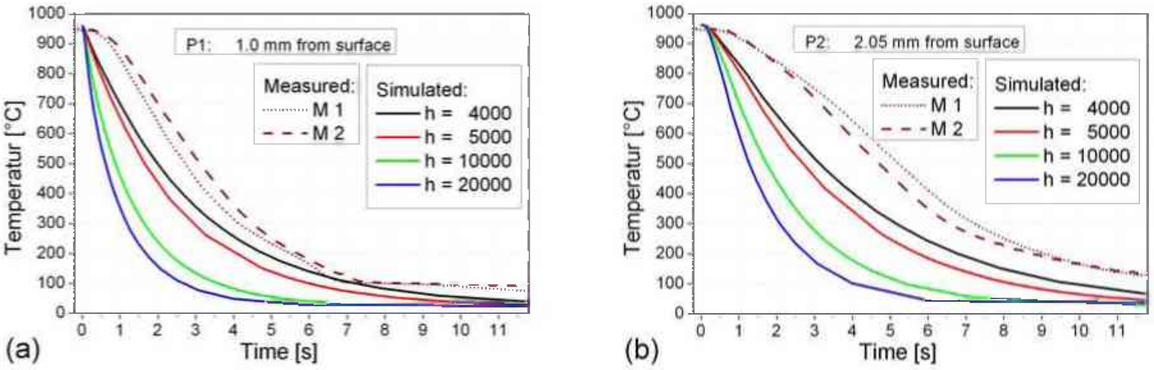

Figure 29: Simulated cooling curves at the locations corresponding to (a) point P1 and (b) point P2 in Figure 21, using heat transfer coefficients that are independent of the surface temperature. M1 and M2 represent the measured temperatures at P1 and P2 (see Figure 23). h given in [W/(m^{2}K)].

5.6.2.2 Temperature Dependent Heat Transfer Coefficients

Due to the insufficient correlation between the measured and the simulated cooling curves, the assumption of a constant heat transfer coefficient proved to be an oversimplification. Obviously, it is necessary to retard the cooling velocity in the beginning but after the initial boiling period, high heat transfer conditions have to be assumed. For a start, the function h_s (Figure 27) was employed to simulate water quenching. The obtained temperatures at the locations P1 and P2 are given in Figure 30. As described above h_s was acquired in another experiment and was used as a basis for empirical variations of the heat transfer function. Figure 30 shows that at point P1 the cooling curve simulated with the function h_s does follow the measured cooling curve better than the cooling curves simulated with constant heat transfer coefficients. Nevertheless, significant deviations of more than 100 °C in the first 4 s of the cooling process cannot be ignored as the residual stresses mainly build up in the beginning (Figure 28). Moreover, the simulated residual stresses predicted with h_s were well below the measured stresses, which will be described in more detail in Chapter 5.6.3.2. In order to model more severe quenching conditions the function h_s was varied as depicted in Table 4. The Figures 31 - 34 show all the functions h (T) that were investigated.

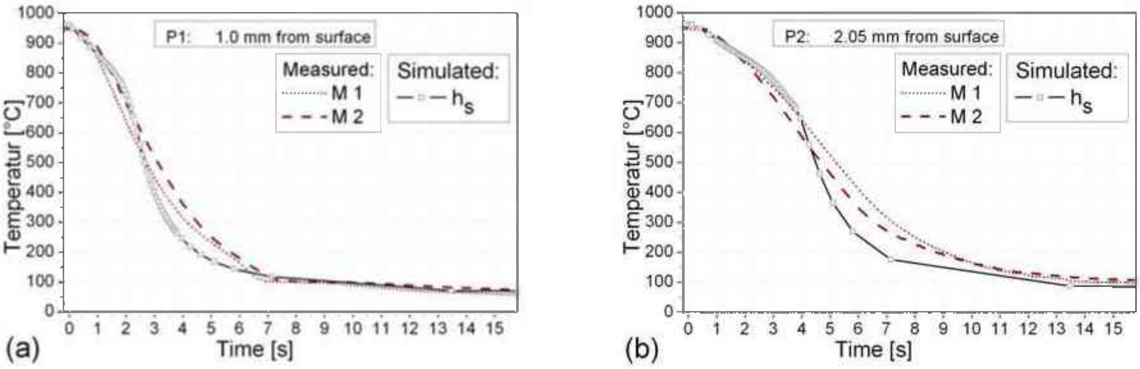

Figure 30: Temperature curves (a) at point P1 and (b) at point P2 calculated with the heat transfer function h_s. M1 and M2 represent the measured temperatures at P1 and P2 (see Figure 23).

First the Leidenfrost temperature T_{Le} was varied, leaving the value and temperature of the maximum heat transfer unchanged. Figure 31 shows the heat transfer functions h_1 - h_4 and the resulting cooling curves. As T_{Le} is increased the cooling time decreases, because higher T_{Le} temperatures are equivalent to a reduction of the film boiling phase and earlier wetting of the plate's surface. In the case of water, this can be interpreted as an increased velocity of the quenchant, because the water temperature remains constant. In any case, a change of the T_{Le} temperature proved to have a significant effect on the temperature gradient of the simulated cooling curves.

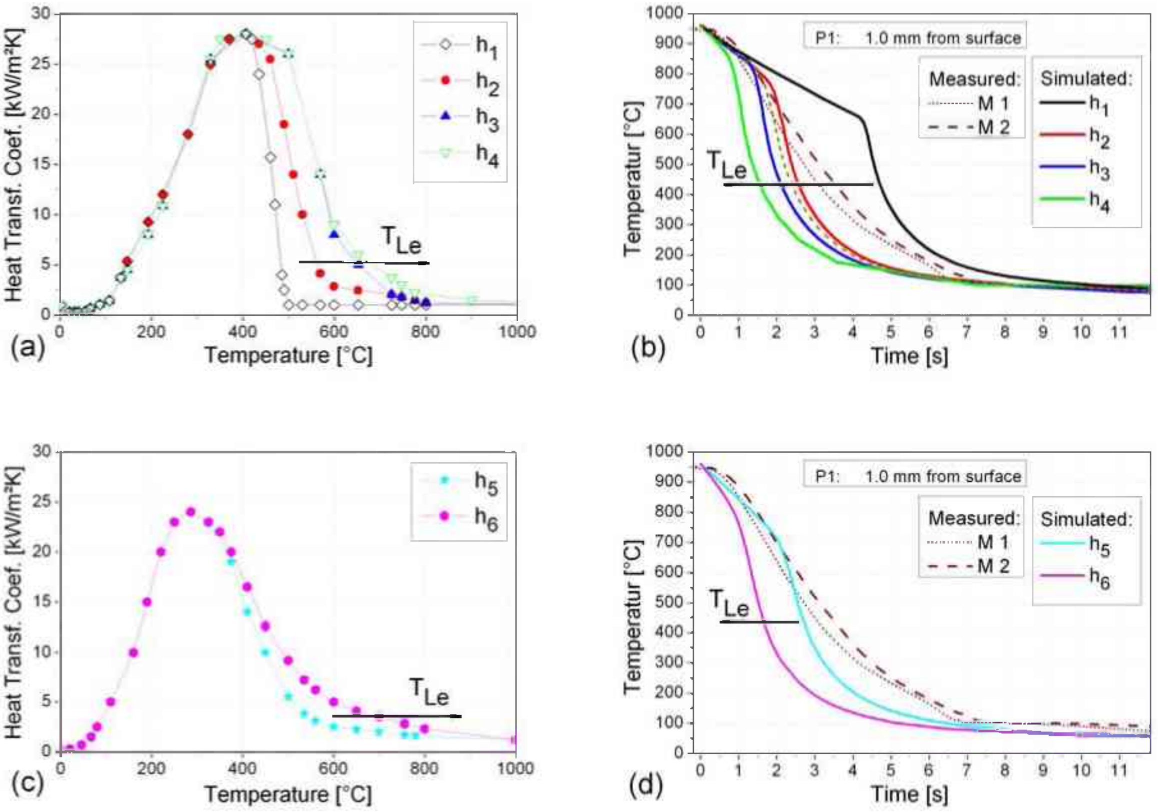

Figure 31: Increase of the Leidenfrost temperature. (a) Heat transfer functions with T_{max} = 400 °C, h_{max} = 28000 W/(m²K), T_{Le} increases from h_1 to h_4. (b) Cooling curves at point P1 resulting from h(T) in (a). (c) Heat transfer functions with T_{max} = 300 °C, h_{max} = 25000 W/(m²K), T_{Le} increases from h_5 to h_6. (d) Cooling curves at point P1 resulting from h(T) in (c). M1 and M2 represent the measured temperatures at P1 (s. Figure 23).

Figure 32 shows the influence of a variation of the temperature for maximum heat transfer T_{max}. The general shape of the heat transfer function was not changed and therefore a shift of T_{max} is accompanied with a shift of the Leidenfrost temperature. A variation of both temperatures does not affect the initial slope of the cooling curves up to the point where the gradient of the cooling curves exhibits a rapid change. However, significant changes are observed regarding the time and temperature of this point of discontinuity. With increasing T_{max} the point of discontinuity is shifted to higher temperatures and lower times. As the initial period with a low gradient can be interpreted as the film boiling phase, a variation of T_{max} proved to affect only the subsequent break-down of the film and the convection phase.

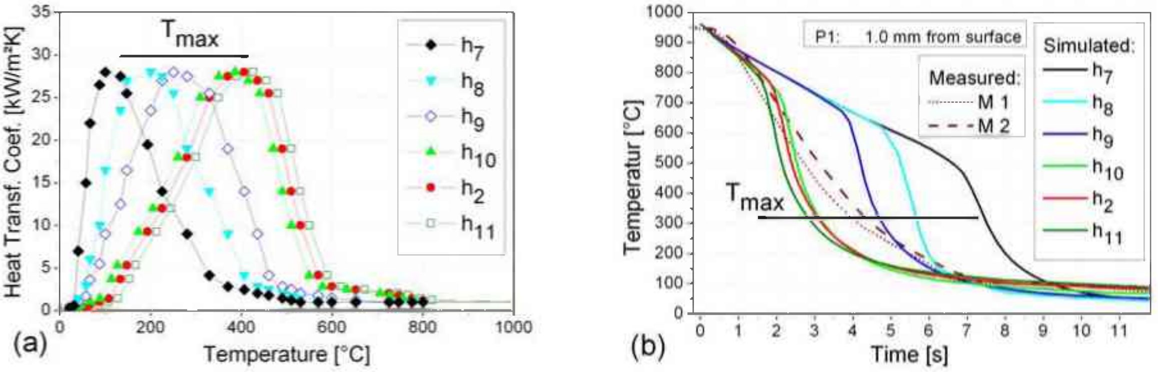

Figure 32: Variations of the temperature at maximum heat transfer, which increases from h_7 to h_{10}, h_2, and h_{11}. (a) Heat transfer functions with h_{max} = 28000 W/(m²K). (b) Cooling curves at point P1 resulting from h(T) in (a). M1 and M2 represent the measured temperatures at P1 (see Figure 23).

A variation of the maximum level of the heat transfer coefficient h_{max} is illustrated in Figure 33. In the case of immersion quenching the maximum heat transfer value is largely determined by the position of the Leidenfrost temperature according to textbooks (see for example Liscic [Lisc,p85]). Nevertheless, these parameters were changed independently in the simulations in order to verify the correct values for the present quenching experiment. Again the duration of the initial cooling phase was not affected. This can be explained by the fact that the heat transfer conditions above T_{Le} were not changed. For the rest of the cooling curves the observed differences were too small to allow a profound interpretation. Obviously, the value of the maximum heat transfer is not a key figure as long as all other parameters are identical.

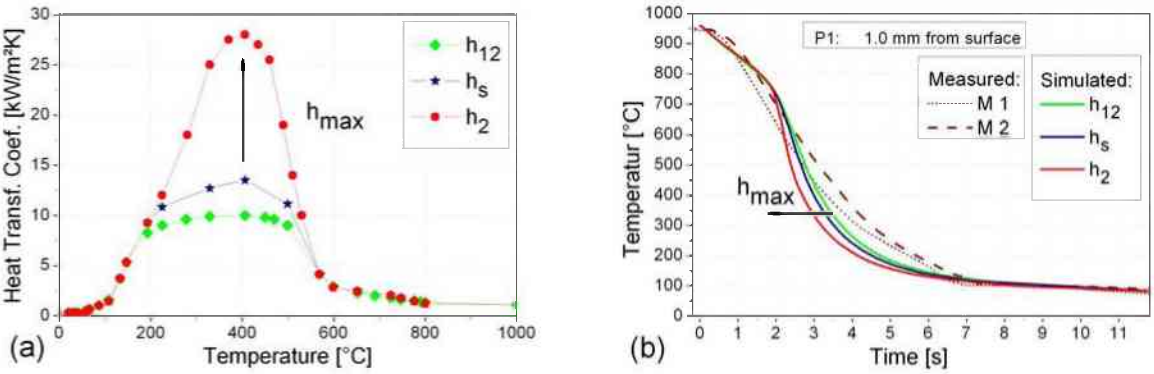

Figure 33: Variations of the maximum level of the heat transfer, which increases from h_{12} to h_s, and h_2. (a) Heat transfer functions with T_{Le} ~ 700 °C. (b) Cooling curves at point P1 resulting from $h(T)$ in (a). M1 and M2 represent the measured temperatures at P1 (s. Figure 23).

As in reality the parameters T_{Le} and h_{max} are linked and a single variation of h_{max} did not result in significant changes, both parameters were changed as shown in Figure 34. The simultaneous variation of T_{Le} and h_{max} also changes the slope of the heat transfer function ($\Delta h/\Delta T$) between T_{Le} and T_{max}. The functions h_{12} and h_{13} in Figure 34a illustrate the effects of a steeper increase of h with constant temperatures for T_{Le} and T_{max}. In this case h_{13}, with the higher heat transfer value h_{max} leads to faster cooling. However, a comparison with the function h_{14} shows that the level of h above the Leidenfrost temperature together with the position of T_{Le} are in fact much more crucial. The reduced heat transfer for h_{14} above T_{Le} initially delays the cooling but in the end, the steep increase to h_{max} at relatively high temperatures (700 - 500 °C) results in a rapid drop of the simulated temperatures.

Increasing this slope ($\Delta h/\Delta T$) results in an increased gradient of the cooling curves (h_5 and h_{15} in Figure 34c) and the point of discontinuity becomes more pronounced. The measured cooling curves do not show such a well-defined point where the gradient changes abruptly. Therefore, a smooth increase of h from T_{Le} to T_{max}, demonstrated by the function h_{15}, seems to be more appropriate to reflect the measured curves. Yet, the quenching of h_{15} is still too impetuous.

The results of the simulated cooling curves can be summarized as follows:

- An exact determination of the $\boldsymbol{T_{Le}}$ was not possible due to the numerous influencing factors and mutual dependencies of the different key parameters. The performed simulations can only narrow down the temperature range for T_{Le} that applies to the studied quenching process. The temperature curves in Figure 31b indicate that the Leidenfrost temperature is located between 500 °C (h_1) and 900 °C (h_4).

- Strong impacts on the cooling curves are observed by the location of $\boldsymbol{T_{max}}$, but this parameter variation could not be separated from a variation of T_{Le}. In any case the T_{max} of the functions h_7, h_8, and h_9 ranging from 100 °C to 250 °C was definitely too low to describe the quenching of the model plate.

- Furthermore, the value of $\boldsymbol{h}$ **above** $\boldsymbol{T_{Le}}$ proved to be of high importance for the cooling curves. It determines the duration and the slope of the initial cooling phase, which was identified as the film boiling phase (Figure 34b, 21a, b). As many heat transfer functions were not chosen to be constant above T_{Le}, the upper and lower bounds for h had to be estimated. A value of h = 1000 W/(m²K) seems reasonable for temperatures down to 800 °C but at 500 °C it is definitely too low. The functions h_2 and h_{12} suggest that h should be below 3000 W/(m²K) for surface temperatures above 600 °C.

- The correct level of the maximum heat transfer h_{max} coefficient could not be narrowed down, but seems to be no key parameter.
- Finally, the **slope ($\Delta h/\Delta T$)** between T_{Le} and T_{max} is another key parameter. It correlates with the break-down of the vapour film, and describes the stability of the vapour phase. The parameter variations showed that a more gentle increase in the coefficient h produces a smother drop of the temperatures. However, all the slopes ($\Delta h/\Delta T$) of the studied heat transfer functions h_1 and h_{15} were too high to fit exactly the smooth drop of the measured temperatures. Still it was possible to define ($\Delta h/\Delta T$) = 70 W/(m²K)² as the upper bound for the slope.

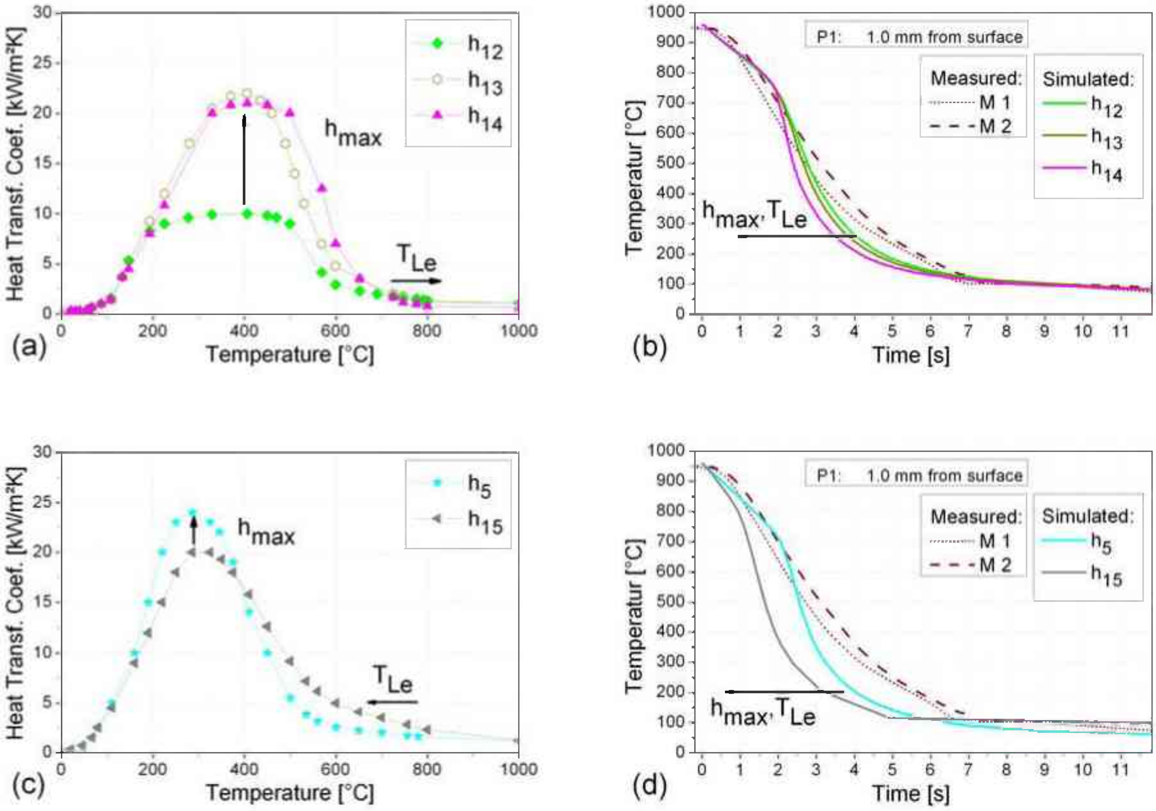

Figure 34: Variations of the maximum level of the heat transfer and of T_{Le}. (a) Heat transfer functions with T_{max} = 400 °C and increasing h_{max} and **increasing** T_{Le} from h_{12} to h_{13}, and h_{14}. (b) Cooling curves at point P1 resulting from h(T) in (a). (c) Heat transfer functions with T_{max} = 300 °C and increasing h_{max} and **decreasing** T_{Le} from h_{15} to h_5. (d) Cooling curves at point P1 resulting from h(T) in (c). M1 and M2 represent the measured temperatures at P1 (see Figure 23).

5.6.2.3 Heat Transfer Data Taken From the Literature

As mentioned above (Chapter 3.2), the number of available heat transfer data is limited. Figure 35 presents a selection of the functions published in literature that resulted from the investigation of different sample shapes: cylinders [gür2001, Mass2002, Buczek, LiWells], plates [nuki] and spheres [Hossain2006]. The findings of these studies are not fully comparable as they are often based on materials other than IN718 and therefore the observed temperature range diverges from the one of the current study.

There are only two publications investigating the cooling process of nickel-based alloys that disclose the functions for the heat transfer coefficient [Rist,Oli2002]. Rist *et al.* [rist] examined the residual stresses within an IN718 cylinder and used a constant value of h = 20000 W/(m²K) for temperatures up to 600 °C and then assumed a linear decline of h down to 2000 W/(m²K) at 20 °C (Figure 35). This function for h was not derived from experimental measurements or analytic calculations and, unfortunately, no motivation for the presented function was given. Rist *et al.* [rist] claim to achieve good correlations between the measured surface temperature and the simulated value for a IN718 cylinder For the sake of comparison, Rist's function for the heat transfer coefficient was implemented in the finite element simulation of the model plate. Figure 36 shows that the cooling curves, simulated with Rist's function, the figure shows a far too impetuous quenching process, which is in fact identical to the thermal gradient of a constant heat transfer coefficient h = 20000 W/(m^{2}K). Consequently, it is not clear why Rist *et al.* included a linear decline of h for lower temperatures, as no influence of a reduced heat transfer could be observed for the DEFORM simulations. The calculated cooling curves of the present work indicate quite the contrary, namely a high significance of the values of h between 600 °C and 1000 °C.

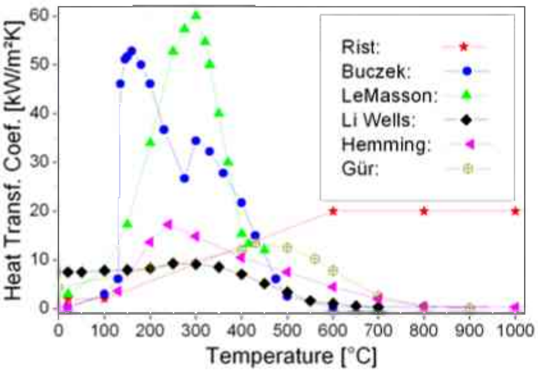

Figure 35: Heat transfer coefficients as a function of temperature given in literature [Rist, Buczek, Masson, LiWells, Hemming, Gür].

Despite all the differences concerning the maximum values of the heat transfer coefficient and the shape of the curves, all studies, except for [Rist], present functions h (T) with much lower heat transfer values at the beginning of the quenching process than at intermediate temperatures. The curves given by Hemming and LeMasson show a maximum of the heat transfer function at 350 °C and 250 °C, respectively. The only work that found two maxima for the heat transfer coefficient studied the influence of different geometries of the blind hole for the thermocouples [Buczek]. For certain angles between the thermocouple holes and the immersion direction Buczek *et al.* found two maxima as given in Figure 35. Finally, the function published by LiWells *et al.* [LiWellls] rises up to a maximum value for h and then remains fairly constant.

The main problem of transferring these literature data to the current work is the temperature range. For instance LeMasson, *et al.* [Mass2002] examined a copper cylinder and thus started the quenching process at a maximum temperature of 500 °C. Buczek's [Buczek] studies on steel cylinder samples started only at 600 °C. In order to employ these results for nickel-based alloys it is necessary to extrapolate the curves to higher temperatures, which is of course debatable. As none of the curves derived from the function h_s, given in Figure 27, exhibit two maxima, one of Buczek's functions for h was chosen for a parameter simulation. For temperatures above 600 °C the heat transfer values had to be extrapolated from the highest value, which was 300 W/(m^{2}K). However, these conditions proved to be far too mild and the simulated temperatures did not at all follow the measured curves (Figure 36). Any effect of the two maxima was superposed by the inadequately low heat transfer above 500 °C. This finding fortifies the presumption that the level of h above T_{Le} is highly important for the cooling characteristics. For all heat transfer functions published in literature just this value would have to be extrapolated for the quenching of the model plate and turbine disc. For this reason no other function from Figure 35 was implemented in the finite element model.

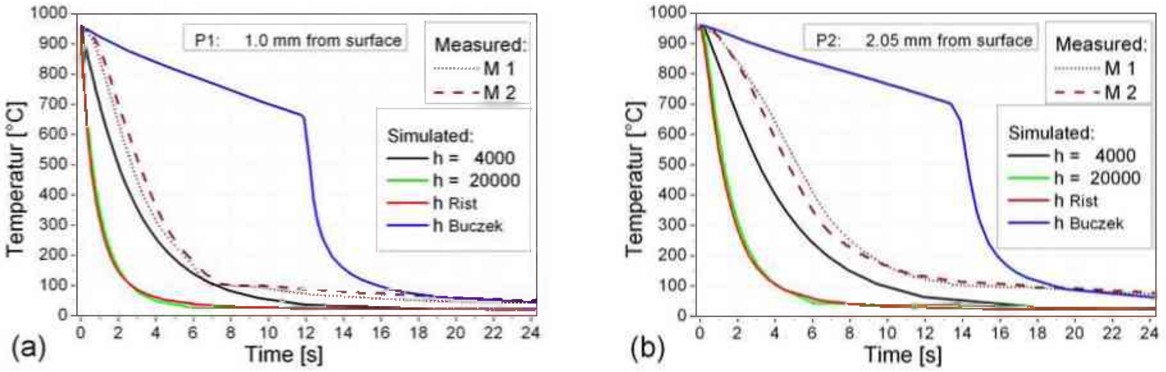

Figure 36: Cooling curves based on the literature data for *h*: *h* Rist [Rist] and *h* Buczek [Buczek]. M1 and M2 represent the measured temperatures at P1 and P2 (s. Figure 23). *h* for the constant values is given in [W/(m²K)].

5.6.3 Residual Stress as a Function of Different Heat Transfer Coefficients

The residual stress components were extracted from the middle of the simulated model plate, parallel to the long edge with a length of 100 mm in reality and 50 mm in the model. The position of this line correlates to the locations of the centre of the neutron measurement volumes.

5.6.3.1 Constant Heat Transfer Coefficients

The first simulations performed with the model plate are based on the assumption of a constant heat transfer coefficient ranging from *h* = 4000 W/(m²K) up to 20000 W/(m²K). As can be seen in Figure 37 the values of the resulting longitudinal as well as the transverse stress components are fairly constant over the majority of the plate's length. Both stress components show a pronounced decline near the rim. Surprisingly, the range of this decline seems to be independent of the chosen heat transfer value, as it never extends past 10 mm. For the longitudinal component a small local maximum can be observed just before it declines to zero at the surface. Towards the centre of the plate the transverse component declines to a minimum, but the decline is not very pronounced. The normal component is only shown once in Figure 38 (*h* = 4000 W/(m²K)), as it is zero for all simulations independent of the chosen heat transfer value. Only in the rim region, the normal stress component exhibits positive stresses as illustrated in Figure 38a. Even for *h* = 20000 W/(m²K) the normal stress only reaches up to 150 MPa.

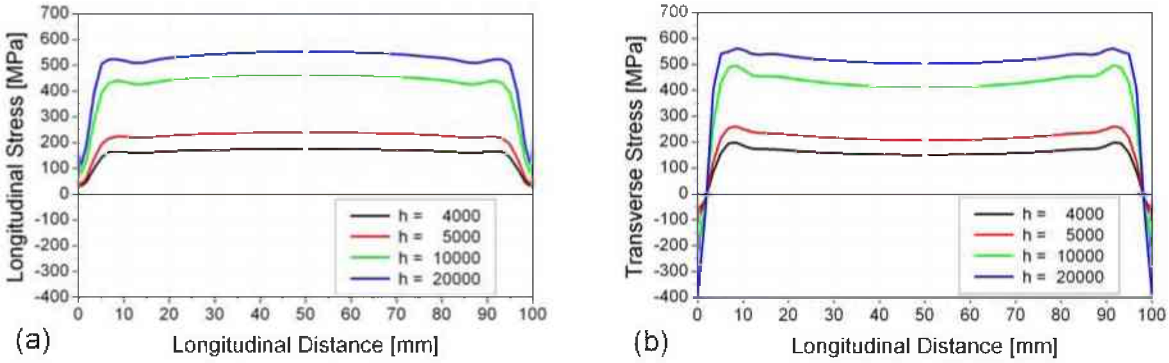

Figure 37: (a) Longitudinal and (b) transverse residual stresses calculated with constant heat transfer coefficients (given in W/(m²K)) along the central line in the model plate.

The simulation results based on a constant heat transfer coefficient did not at all fit the residual stress state determined by neutron measurements. First of all, the absolute value of the simulated stresses is much lower than the measured stress values and secondly, the amount of the longitudinal and transverse components should differ considerably in the middle of the plate according to the neutron measurements. A further increase of the heat transfer coefficient above *h* = 20000 W/(m²K) did not make sense, as a comparison of measured and simulated cooling curves revealed that this quenching condition was already too severe.

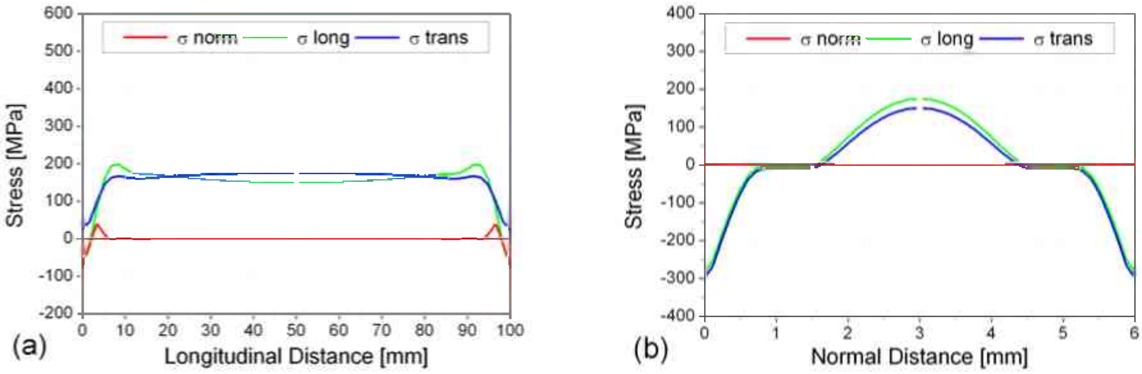

Figure 38: Calculated stress tensor for h = 4000 W/(m^{2}K) (a) along the central line of the model plate and (b) along a scan through the thickness of the plate.

5.6.3.2 Temperature Dependent Heat Transfer Coefficients

All simulations based on a constant heat transfer coefficient proved to be inadequate to reflect the measured residual stresses. Only the implementation of a temperature dependent heat transfer coefficient led to substantially different shapes of the residual stresses, which resembled the non-plateau like shape determined by neutron diffraction. All temperature dependent heat transfer coefficients given in Figures 31 - 34 were implemented in the simulations of the model plate and the resulting stress states are presented below in Figures 39 - 43. Again, the normal stress component is not illustrated separately, as it is zero except for the small rim region; a result that correlates to the simulations with constant h values.

Figure 39 shows the complete stress tensor that evolved from simulations choosing the primary function h_s (Figure 27) for the heat transfer conditions. Basically, the shape of this stress state is representative for all simulations with a temperature dependent heat transfer coefficient. The transverse component always exhibits a pronounced minimum at the centre of the plate and the longitudinal component steadily increases towards the middle. Both components begin to drop rapidly in a distance of 10 mm from the edge.

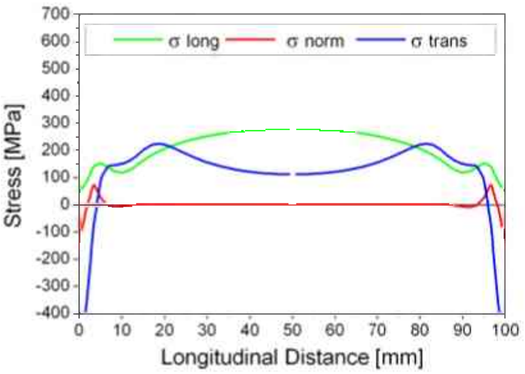

Figure 39: Residual stress tensor at the central line of the model plate simulated with the temperature dependent heat transfer coefficient h_s shown in Figure 27.

Although the stress state in Figure 39 does resemble the measured stresses better than the simulations based on constant h values, the stress level is much too low. The real plate seems to experience higher plastic deformations during cooling and therefore the residual stresses are higher in the end. Consequently, the variations of h_s are aimed at a higher temperature gradient along the thickness of the plate, because this provokes higher plastic deformation. Together with the analysis of the cooling curves this observation implies that the slope ($\Delta h/\Delta T$) between T_{Le} and T_{max} should be increased as well as the maximum heat transfer value h_{max}. Additionally, the value of h above T_{Le} and the temperature of T_{Le} itself might require a reduction to improve the simulation model.

The effect of an increase of T_{Le} is illustrated in Figure 40. The maximum value of the longitudinal component increases as well as the values of the minimum of the transverse component in the middle of the plate. For the functions h_3 and h_4 the longitudinal stress raises steadily from the edge to the middle, whereas h_1 and h_2 provoke an increase that is interrupted by a short shoulder at 200 MPa. This parameter study shows that the residual stress level for all components increases with increasing values for the temperature T_{Le}. An opposing trend for the longitudinal and transverse stress could be provoked by h_5 and h_6. Although the Leidenforst temperature of h_5 was below that of h_6 the maximum level of the longitudinal stress was higher and the minimum of the transverse one was lower. Besides, the simulation employing h_5 led to a small shoulder of both stress components. These two observations were attributed to the higher slope ($\Delta h/\Delta T$) between T_{Le} and T_{max} for h_5, which seems to superimpose the effect of the location of T_{Le}.

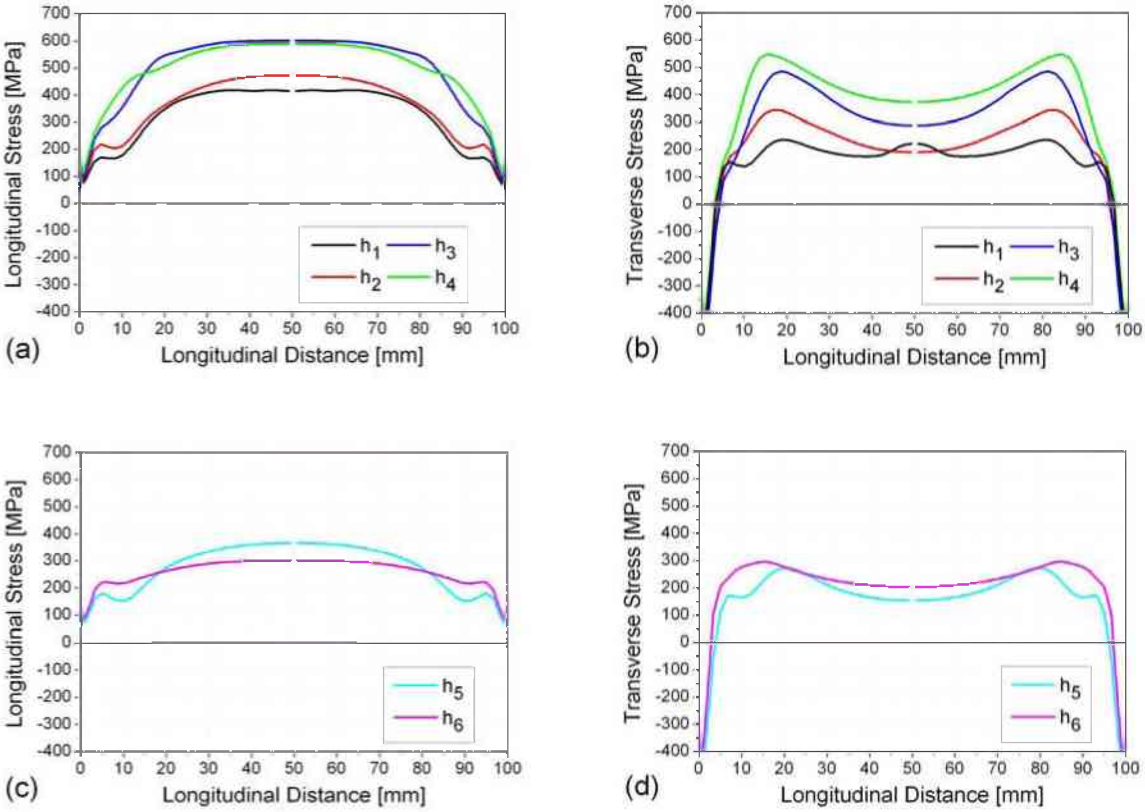

Figure 40: Simulated longitudinal and transverse residual stresses calculated with temperature dependent heat transfer coefficients with increasing T_{Le} (Figure 31). (a - b) T_{max} = 400 °C, h_{max} = 28000 W/(m²K), T_{Le} increases from h_1 to h_4. (c - d) T_{max} = 300 °C, h_{max} = 25000 W/(m²K), T_{Le} increases from h_5 to h_6.

Figure 41 depicts the parameter variations with different temperatures of the maximum heat transfer T_{max}. This parameter could not be changed independently from the position of T_{Le} and consequently, there is a combined influence of the two temperatures. The functions h_7, h_8 and h_9 indicate that an increase of T_{max} and T_{Le} increases the level of all residual stress components, but these results are overlapped by the effect of a small increase between T_{Le} and T_{max}. This slope ($\Delta h/\Delta T$) was unchanged for h_2, h_{10} and h_{11} but the difference of ± 20 °C proved to be too small to give rise to significant changes of the residual stress state.

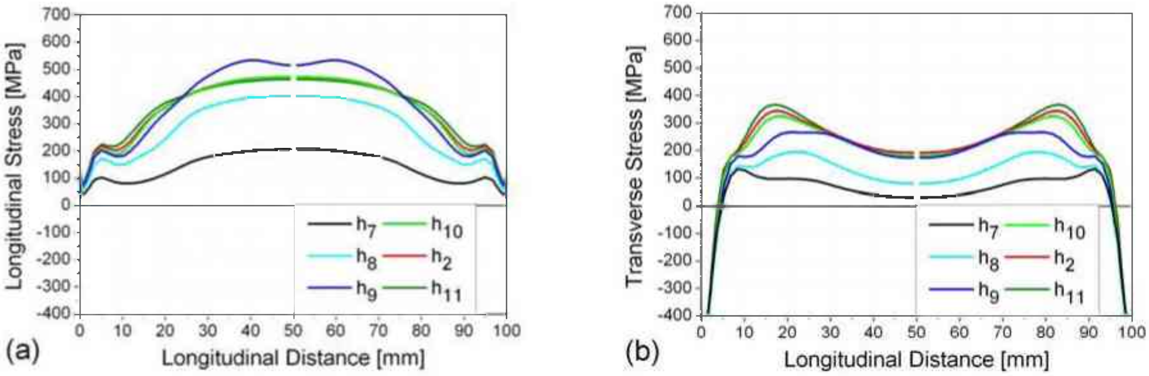

Figure 41: Simulated (a) longitudinal and (b) transverse residual stresses calculated with temperature dependent heat transfer coefficients with T_{max} increasing from h_7 to h_{10}, h_2 and h_{11} (Figure 32) and h_{max} = 28000 W/(m²K).

Variations of the level of h_{max} (Figure 42) showed that high heat transfer coefficients can increase the residual stress level, which is consistent with the observation of the constant h values. But as long as all other parameters are fixed, no opposing trend for the transverse and longitudinal stress component can be observed.

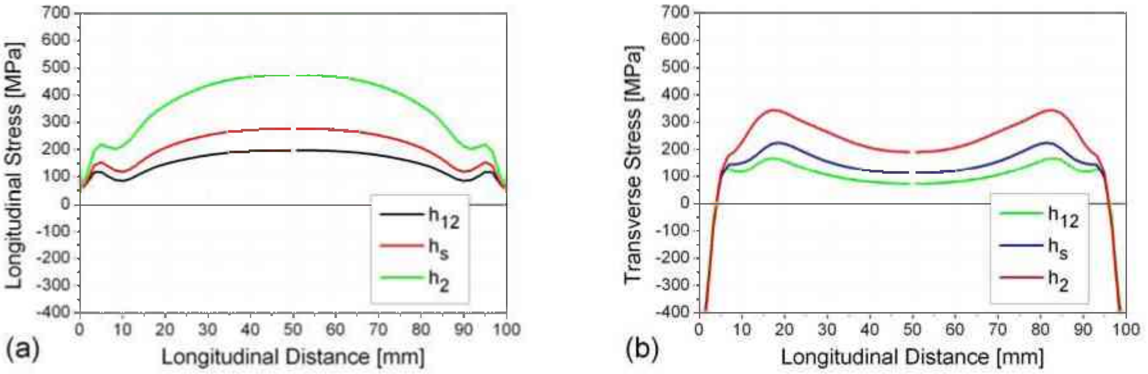

Figure 42: Simulated (a) longitudinal and (b) transverse residual stresses calculated with temperature dependent heat transfer coefficients with h_{max} increasing from h_{12} to h_5 and h_2. (Figure 33) with T_{max} = 400 °C and T_{Le} ~ 700 °C.

Finally, the parameters T_{Le} and h_{max} were changed simultaneously (cf. Figure 43), this is because they are linked in real quenching processes. The function h_{12}, with the lowest maximum heat transfer and lowest Leidenfrost temperature also resulted in the lowest residual stresses. A substantial increase of all stress level was observed for h_{13} and h_{14}, which exhibit the same h_{max} value. A further increase in the longitudinal component could be effected with h_{14} by a reduction of the h level above T_{Le} and a steeper increase between T_{Le} and T_{max} (Figure 34a).

The functions h_5 and h_{15} illustrate that the effect of the chosen slope ($\Delta h/\Delta T$) overlaps the influence of the maximum value for the heat transfer, because the residual stress results are equal in magnitude. The two simulations verify the assumption that a steeper slope ($\Delta h/\Delta T$) between T_{Le} and T_{max} (Figure 34c) leads to more pronounced differences of the longitudinal and transverse components in the middle of the plate. The smoother h increases the closer are the levels of the two stress components in the centre of the plate. If the heat transfer value increases smoothly as in the function h_{15}, but then reaches the same h_{max} value as in function h_{14} then the final residual stress levels are still much below the those for h_{14}.

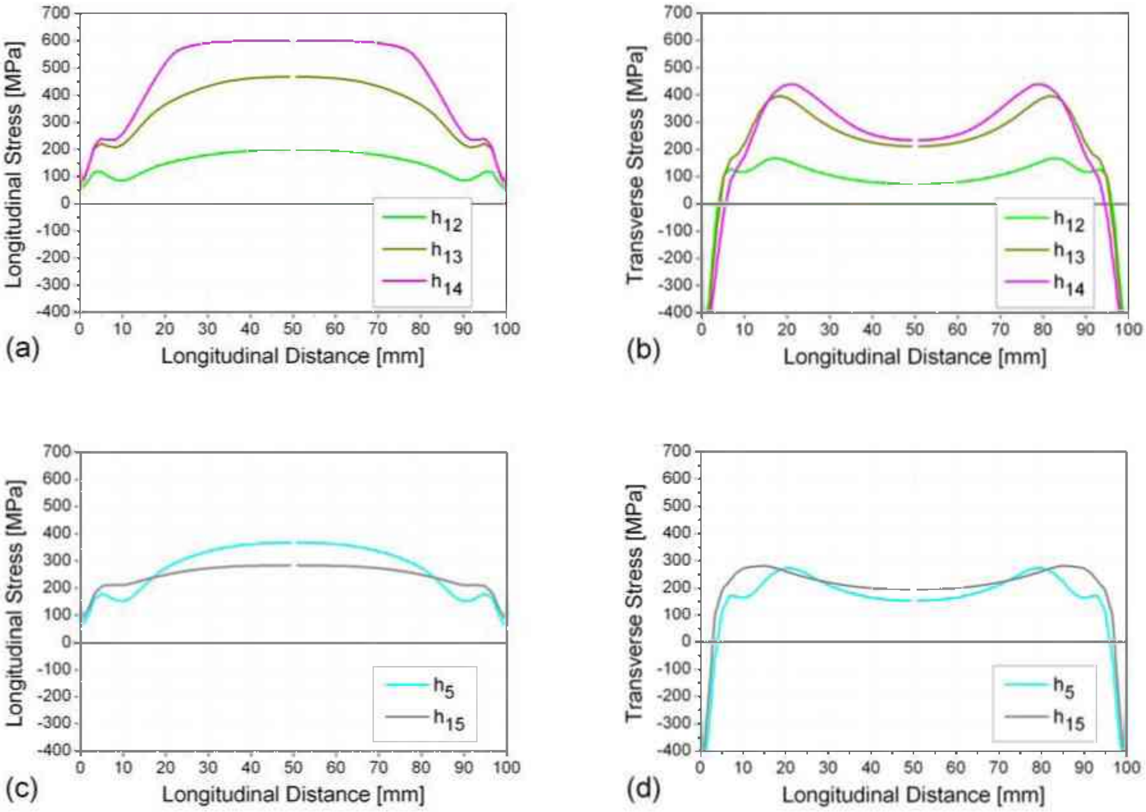

Figure 43: Simulated longitudinal and transverse residual stresses calculated with temperature dependent heat transfer coefficients with increasing T_{Le} and increasing h_{max} (Figure 34). (a - b) T_{max} = 400 °C, h_{max} and T_{Le} **increase** from h_{12} to $h_{13,}$ and h_{14}. (c - d) T_{max} = 300 °C, h_{max} **increases** and T_{Le} **decreases** from h_{15} to h_5.

5.7 Simulation Results of the Turbine Disc

The turbine disc was simulated with different constant heat transfer coefficients and a selection of the temperature dependent functions h (T) given in the Figures 31 - 34.

5.7.1 Cooling Curves

5.7.1.1 Constant Heat Transfer Coefficient

Initially, the simulations of the turbine disc were performed with heat transfer coefficients that were assumed to be independent of the temperature. The simulated temperatures were extracted at the five points correlating to the locations of the temperature measurement. For the sake of clarity Figure 44 only shows the results at the locations P1, P2, and P4 for h values ranging from 4000 W/(m²K) to 20000 W/(m²K). The temperature curves at the points P3 and P5 are very similar to P4, and so P4 is a good representation. The course of the temperature in P2 differs significantly from the rest, as the point is located much further inside the sample.

Consistent with the results of the model plate the simulation with h = 4000 W/(m²K) does not fit the measured curves nor do higher values of h. In fact, 4000 W/(m²K) appears to be too high already, but lower values would simulate oil quenching or air-cooling. Additionally, the experimental cooling curves (expect for P1) exhibit a slow decrease of the temperature at the beginning, followed by a period of very rapid quenching. These changing cooling velocities cannot be modelled with a constant heat transfer coefficient as the temperatures always drop steadily. Furthermore, the measured temperatures decrease extremely slowly from 100 °C to 20 °C and the simulated temperatures drop rather quickly.

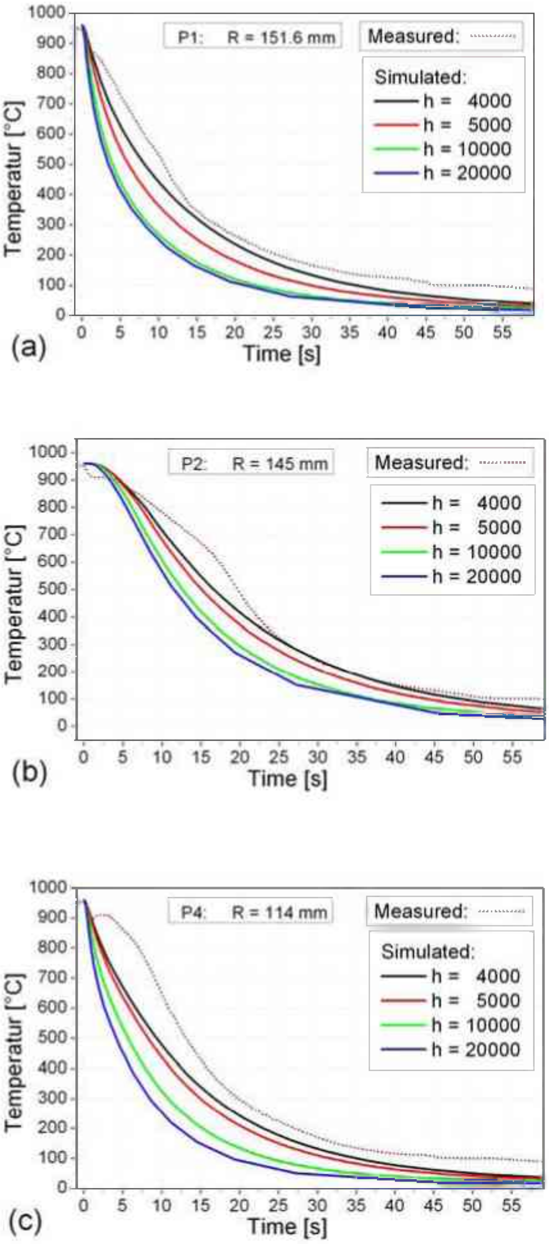

Figure 44: Cooling curves resulting from simulations with constant heat transfer coefficients (given in W/(m²K)) compared to the equivalent measured temperatures at the positions (a) P1, (b) P2 and (c) P4 (see Figure 20).

5.7.1.2 Temperature Dependent Heat Transfer Coefficient

The assumption of a constant heat transfer coefficient also proved to be an oversimplification for the turbine disc, because the temperatures do not drop steadily in reality. Temperature dependent heat transfer coefficients led to simulated cooling curves, shown in Figure 31 - 34, with non-constant cooling velocities during the quenching process. This was regarded as the first improvement of the simulation model.

The effect of a variation of the Leidenforst temperature is shown in Figure 45a-c. For higher T_{Le}, the part cools down quicker, as the initial cooling stage characterized by the vapour film ends earlier. This is in accordance with the same parameter variation on the model plate, although the differences are less pronounced for the disc geometry. The cooling curves resulting from the functions h_2 and h_3 diverge little as the corresponding T_{Le} temperatures lay very close together. The functions h_2 and h_3 differ more in respect of the slope ($\Delta h/\Delta T$) between T_{Le} and T_{max} which, seems to result in nearly identical temperature paths for the turbine disc.

Changing the temperature of the maximum heat transfer coefficient by only ± 20 °C (functions h_{10} and h_{11}) does not cause significant changes in the cooling curves as illustrated in Figure 45d-f. For the simulation of the model plate distinct changes were observed for ΔT_{max} = ± 100 °C to ± 200 °C, but then the quenching was much too mild to follow the measured temperatures. These results did not encourage the use of values for T_{max} below 300 °C. Higher values for T_{max} were also considered as inappropriate as the function h_2 with T_{max} = 400 °C does already cause slightly too severe quenching conditions.

The heat transfer functions h_s and h_2 demonstrate a variation of the maximum heat transfer values only (Figure 46a-c). The corresponding cooling curves indicate that an increase of h_{max} from 18000 W/(m²K) to 28000 W/(m²K) alone is irrelevant for the cooling curves, which in accordance to the results of the model plate.

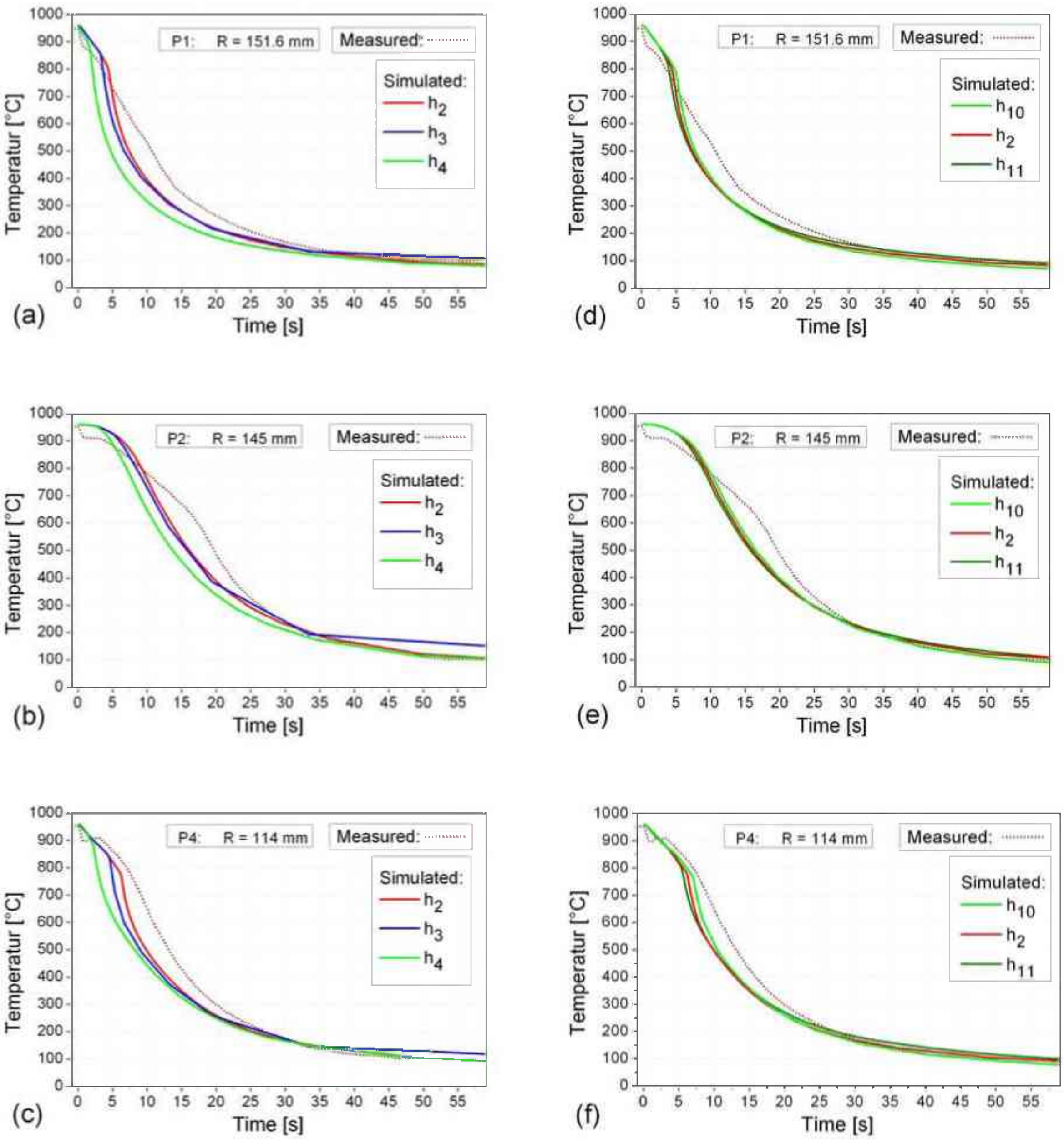

Figure 45: Simulated and measured cooling curves at the locations P1, P2 and P4 calculated with temperature dependent heat transfer coefficients with (a - c) T_{Le} increasing from h_2 to h_4 (Figure 31a) and (d - f) T_{max} increasing from h_{10} to h_2 and h_{11} (Figure 32). The value for h_{max} = 28000 W/(m²K) was unchanged.

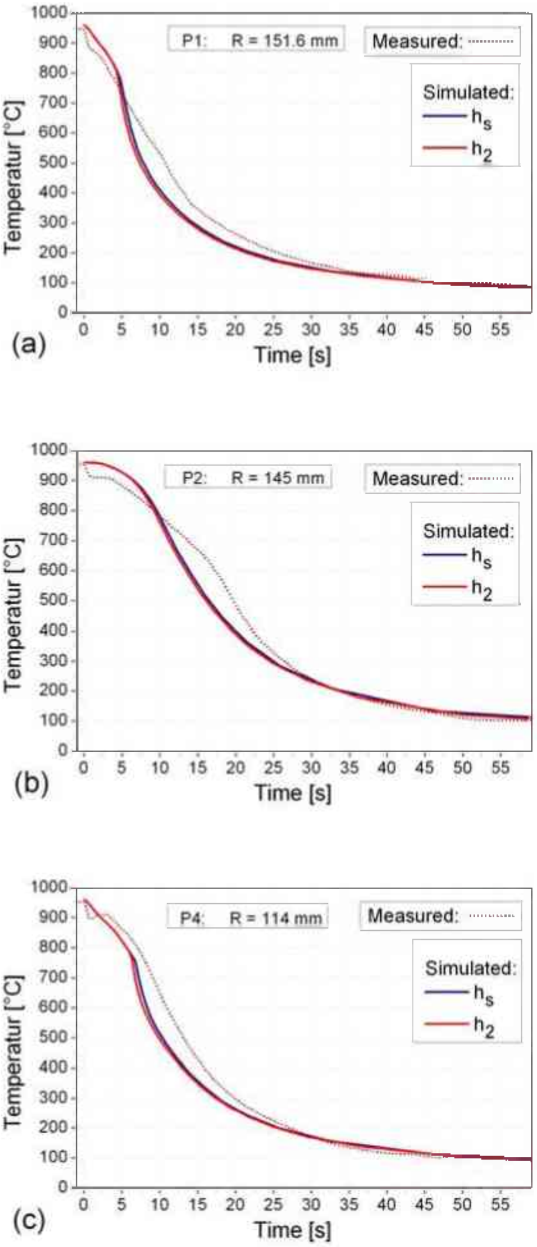

Figure 46: Simulated and measured cooling curves at the locations P1, P2 and P4 calculated with temperature dependent heat transfer coefficients with (a - c) increasing h_{ma} from h_s to h_2. The temperature T_{max} = 400 °C was unchanged (Figure 33).

5.7.2 Residual Stress as a Function of Different Heat Transfer Coefficients

Figure 47 shows a 2D picture illustrating the general shape of the simulated residual stresses in the turbine disc for all three main stress components. The residual stress components were extracted along a horizontal line parallel to the disc radius as depicted in Figure 9. Additionally, several scans parallel to the disc axis at different radii were analysed. Here, only the simulated residual stresses at the thinnest section of the disc, at a radius of R = 100 mm, are shown. Again, the position of these lines correlate to the centre of the neutron measurement volumes.

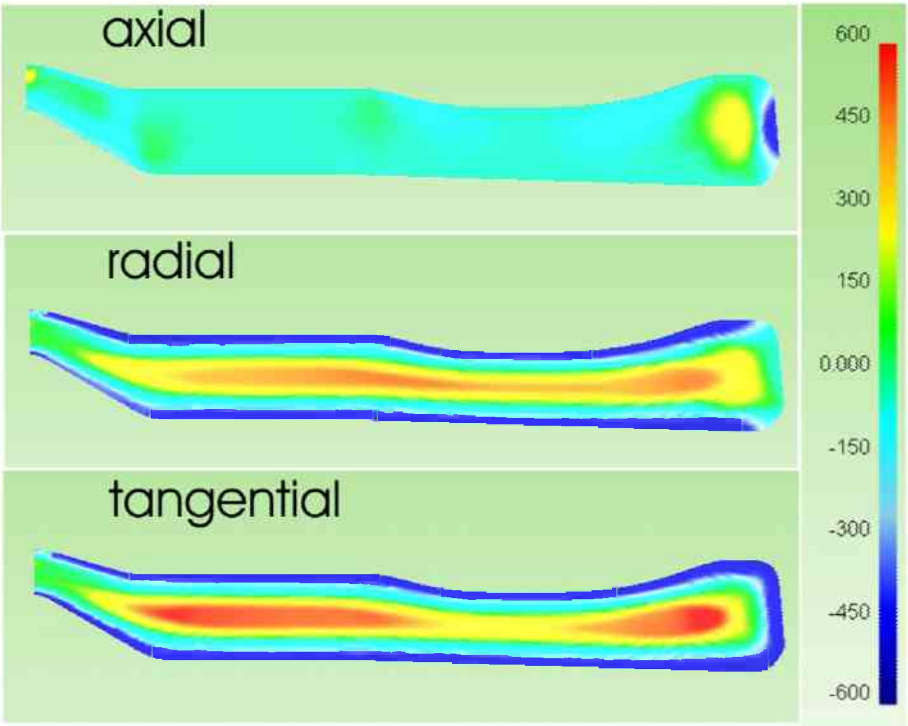

Figure 47: 2 -dimensional illustration of the simulated residual stresses in the turbine disc. The values are given in MPa.

5.7.2.1 Constant Heat Transfer Coefficient

Figure 48 shows the complete stress tensor for *h* = 4000 W/(m^{2}K) along a horizontal scan. Naturally higher heat transfer coefficients lead to higher residual stresses within the turbine disc, but values above *h* = 20000 W/(m^{2}K) did not significantly increase the residual stresses. Between *h* = 4000 W/(m^{2}K) and *h* = 20000 W/(m^{2}K) not only the maximum stress level raises, but also the stress gradient becomes steeper.

Along the horizontal line (Figure 49) the changes are most obvious in the thin section of the disc between a disc radius of R= 90 mm and R = 120 mm. However, in this section the increase of the stress level is not equivalent with the increase of the stress maximum, because the horizontal scan line is not located at the same position as the stress maximum. Near the rim, at a disc radius of R ≥ 147 mm, the residual stresses correspond to the stress maximum in this region. The use of different heat transfer coefficients basically changes the radial and tangential component in the thin section of the disc. Near the rim, the effect on the radial stress is minimal and only a small increase can be observed for the tangential stress. The axial stress increases too in the rim region, but is effectively zero for all other locations inside the disc independent of the chosen value for *h*. Therefore, the simulated axial stresses are omitted in the figures below.

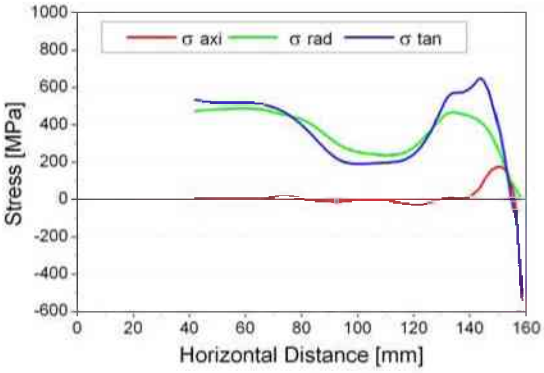

Figure 48: Simulated residual stress state along the horizontal line assuming a constant heat transfer coefficient of *h* = 4000 W/(m²K).

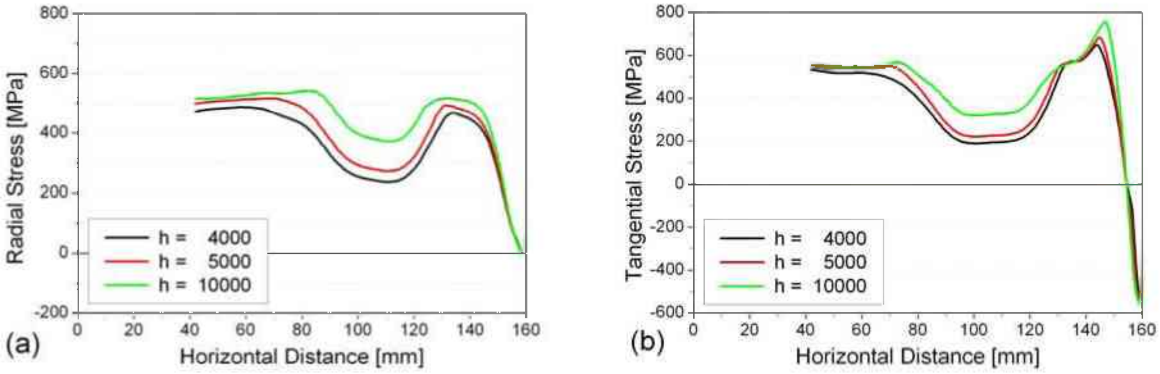

Figure 49: (a) Radial and (b) tangential residual stresses along a horizontal line parallel to the disc radius and at a distance of 11 mm to the bottom side of the disc calculated with constant heat transfer coefficients (given in W/(m²K)).

Along the vertical scan parallel to the disc axis, the radial and tangential stress component follow a parabolic shaped curve, which is depicted in Figure 50 (together with the position of the horizontal scan line). The stress maxima of both components are not exactly in the middle of the disc, but are shifted 1.25 mm towards the topside and also the horizontal scan line is closer to the top than the stress maximum. The value of the heat transfer coefficient does not seem to affect the location of zero stress for either of the two stress components, but the shape of the stress curves changes. There is a small region where the stress gradient is much lower and nearly zero, which will be referred to as the stress "shoulder". The lateral extension of this shoulder decreases for higher values of *h* and it is shifter closer to zero stress.

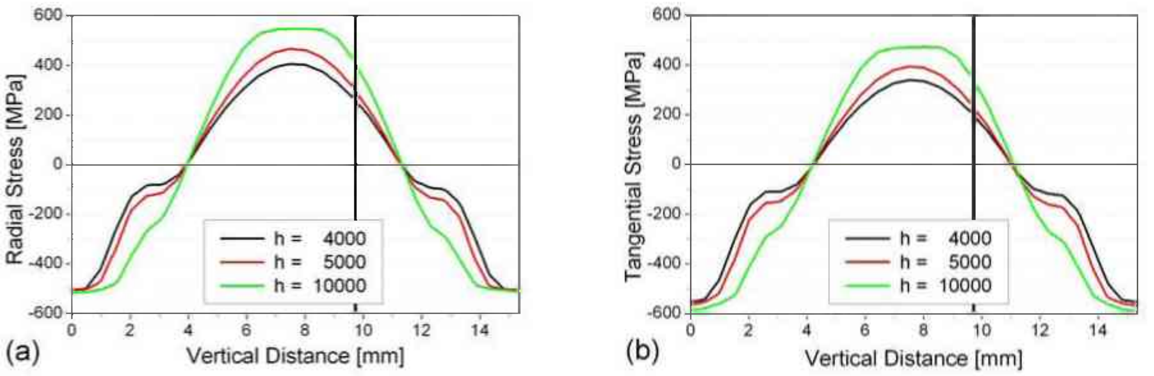

Figure 50: (a) Radial and (b) tangential residual stresses calculated with constant heat transfer coefficients at a disc radius of R = 100 mm (thin section), parallel to the disc axis, calculated with constant heat transfer coefficients (given in W/(m²K)). The vertical line shows the position of the horizontal measurement line.

5.7.2.2 Temperature Dependent Heat Transfer Coefficients

Contrary to the model plate, the general shape of the residual stress curves does not change if heat transfer conditions are modified. Yet, the level of the maximum stress depends heavily on the cooling conditions. In order to increase the stress level significantly, temperature dependent heat transfer coefficients had to be employed because the neutron measurements indicated high residual stress levels. For a limited time span it is possible to assume much higher heat transfer values than h = 10000 W/(m^{2}K), which was much too high to fit the measured temperatures if a constant heat transfer coefficient was assumed. As discussed previously, such temperature dependent conditions do depict the real conditions better. Yet, compared to the model plate the residual stress state within the disc experiences only small changes for the different parameter variations. In fact, the changes are most evident in the thin section for scans parallel to the disc axis. There, the stress gradient and thus the widths of the parabolic shaped curves are modified. This causes large changes in the horizontal scan line, because the horizontal scan is not located at the position of the stress maximum. Near the rim all the stress components are virtually independent of the heat transfer coefficient as the stress gradients are extremely steep and thus changes are not resolvable.

The discussion of the parameter variations are focused on the scan parallel to the disc axis at R = 100 mm, because there the effects are clearer than along the horizontal line. The tangential stresses are not given due to their similarity to the radial component, which is illustrated in Figure 51 that shows the complete stress tensor along the horizontal line and along the vertical scan calculated with the function h_s.

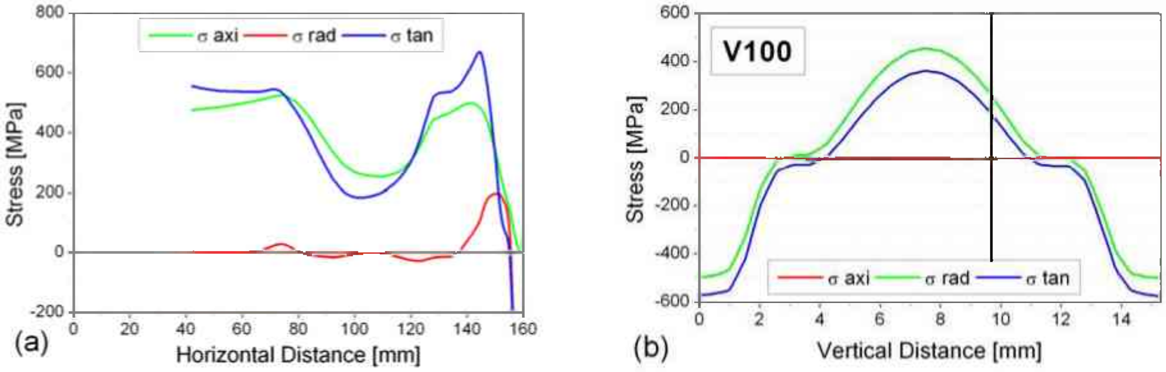

Figure 51: The simulated residual stress state (a) along a horizontal line parallel to the disc radius (b) at a disc radius of R = 100 mm, parallel to the disc axis. The heat transfer coefficient was assumed to follow the function h_s given in Figure 27.

Increasing the Leidenfrost temperature of the function h (T), increases the level of the stress maximum as well as the stress gradient. Figure 52 shows the corresponding residual stresses resulting from a simulation with the heat transfer functions h_2, h_3, and h_4, which are depicted in the previous chapter (Figure 31a). Again the location of zero stress seems to be unaffected by this variation, which is in accordance with the simulations with constant heat transfer coefficients. The region where the stress gradient is very low decreases for increasing T_{Le} values and can be observed at lower, negative stress levels. The same applies for an increase in the temperature of maximum heat transfer T_{max}, which was not surprising due to the strong linkage of T_{Le} and T_{max}. The influence of a modified T_{max} temperature is shown in Figure 53.

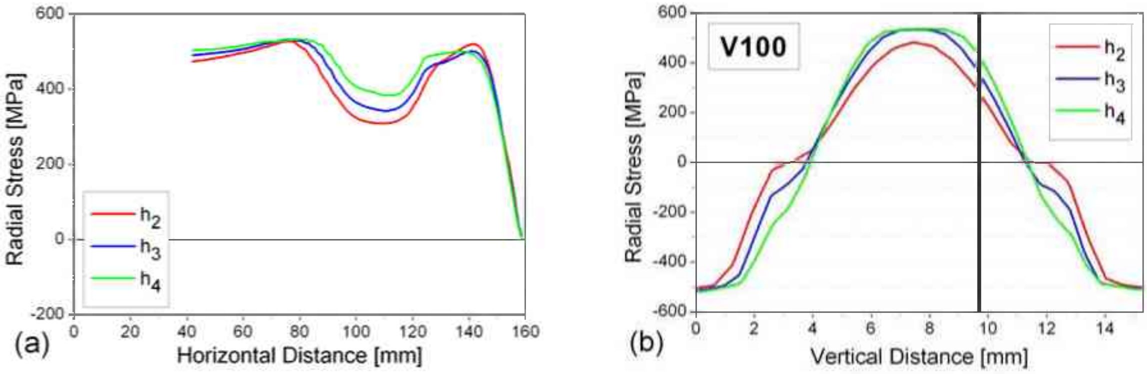

Figure 52: Simulated radial residual stress (a) along a horizontal line parallel to the disc radius and (b) at a disc radius of R = 100 mm, parallel to the disc axis. The simulations were performed employing temperature dependent heat transfer coefficients with T_{Lf} increasing from h_2 to h_4 (Figure 31a). The vertical line shows the position of the horizontal measurement line.

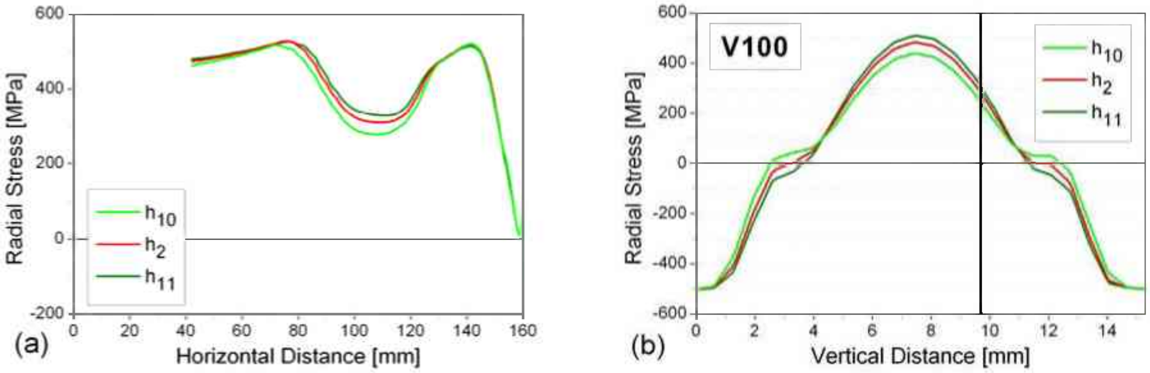

Figure 53: Simulated radial residual stress (a) along a horizontal line parallel to the disc radius and (b) at a disc radius of R = 100 mm, parallel to the disc axis. The simulations were performed employing temperature dependent heat transfer coefficients with T_{max} increasing from h_{10} to h_2 and h_{11} (Figure 32). The vertical line shows the position of the horizontal measurement line.

The effect of different slopes ($\Delta h/\Delta T$) between T_{Lf} and T_{max} is as well indicated in Figure 52. For a steeper slope ($\Delta h/\Delta T$), displayed by h_3, the stress maximum seems to be unaffected, but the parabolic stress curve at R = 100 mm is slightly broader, which is reflected in higher stress values along the horizontal scan line. However, the effect of the slope ($\Delta h/\Delta T$) was not studied in detail for the turbine disc.

No influence could be observed if the maximum heat transfer h_{max} is increased alone, leaving the temperatures T_{Lf} and T_{max} unchanged (Figure 54).

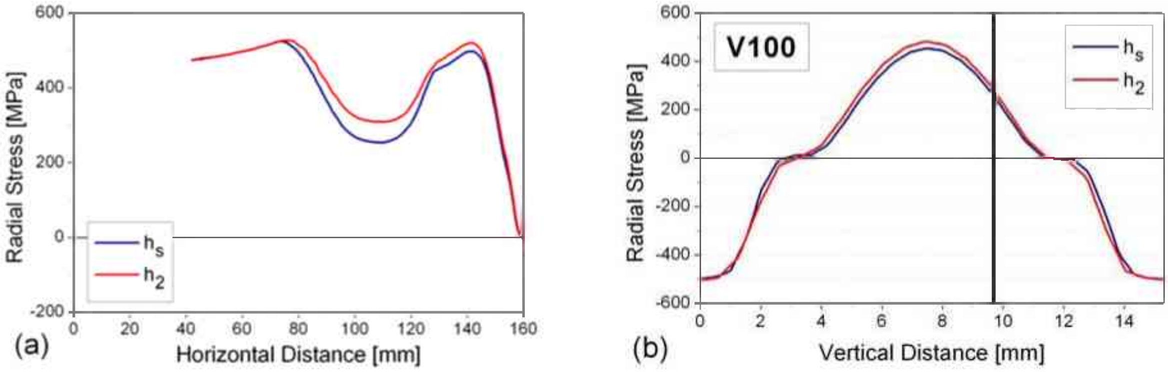

Figure 54: Simulated radial residual stress (a) along a horizontal line parallel to the disc radius and (b) at a disc radius of R = 100 mm, parallel to the disc axis. The simulations were performed employing temperature dependent heat transfer coefficients with h_{max} increasing from h_s to h_2 (Figure 33). The vertical line shows the position of the horizontal measurement line.

6 Residual Stress Analysis with Neutron Diffraction

The principles of neutron and X-ray diffraction are the same, only the type of radiation differs, and so the basics of the measurement and the evaluation are equal [68 - 72]. The main advantage of neutrons compared to X-ray is that that stresses deep within a sample can be evaluated with high accuracy. X-rays are limited to the surface region because they interact with the electronic shells of the atoms and are consequently attenuated much quicker than neutrons, which interact with the atomic nucleus. However, the degree of interaction of the neutrons with different atomic kernels is not proportional to the atomic weight. Thus, the actual penetration depth can vary largely for different alloy compositions [73]. For Ni-based superalloys stresses up to a depth of a few cm are accessible at a medium-flux neutron source [73].

6.1 Determination of Stress

The evaluation of residual stresses by diffraction methods is based on the measurement of lattice distances. According to Bragg's Law (1) a shift $\Delta\theta_{hkl}$ of the Bragg peak can be correlated to a change Δd of the corresponding lattice plane *(hkl)*, provided the wavelength λ is constant.

$$d_{(hkl)} = \frac{\lambda}{2\sin\Theta_{(hkl)}} \tag{5}$$

Subsequently, the strain ε_{hkl} in the direction normal to the reflecting lattice plane *(hkl)* was calculated by:

$$\varepsilon_{hkl} = \frac{d_{hkl} - d_0}{d_0}, \tag{6}$$

where d_0 is the lattice parameter of the unstrained lattice. For a calculation of the residual stress state, the principal strains (ε_{11}, ε_{22}, ε_{33}) had to be determined in three perpendicular directions. The axial symmetry of the turbine disc suggested that the direction of the principal stresses and strains coincided with the coordinate system of the disc. The same applied for the rectangular model plate. Hence, the strains were determined in the axial (ε_a), radial (ε_r), and tangential (ε_t) direction in the disc (Figure 8) and in the normal (ε_n), longitudinal (ε_l), and transverse (ε_t) direction in the model plate (Figure 12). Then, the residual stresses in these directions could be calculated. Tri-axial residual stresses were calculated from the measured strains according to Hook's law [10, 74]:

$$\sigma_i = \frac{E_{hkl}}{(1+\nu_{hkl})}\left[\varepsilon_i + \frac{\nu_{hkl}}{(1-2\nu_{hkl})}(\varepsilon_{11}+\varepsilon_{22}+\varepsilon_{33})\right], \tag{7}$$

where i = r, t, a. E_{hkl} and ν_{hkl} represent the diffractometric elastic constants (DEC), which depend on the reflection *(hkl)* selected for the strain measurement and are usually different from the bulk values. For certain alloys the values for E_{hkl} and ν_{hkl} are published in literature, e.g. [75 - 80].

Fewer measurements are necessary if plane stress conditions are present at the measurement locations. In this case two strain measurements and a reference value d_0 are sufficient to determine the stress state. If data for the third strain direction are available, then they can be employed to calculate the unstrained lattice parameter d_0 and no reference sample has to be cut from the component [10, 81].

Alternatively, the stress differences can be determined according to equ. (8), because they are equal to the longitudinal and the transverse component, if the normal stress component is zero (plane stress conditions). This, for example, applies for a very thin and infinite plane. As the reference value d_0

cancels out in equ. (8), it is not necessary to cut a reference cube from the sample. Initially, plane stress conditions were also assumed for the turbine disc, which is described in more detail in Appendix **B**.

$$\sigma_{\mathrm{r/t}} - \sigma_{\mathrm{a}} = \frac{E}{1+\nu}\left(\varepsilon_{\mathrm{r/t}} - \varepsilon_{\mathrm{a}}\right) \tag{8}$$

After having determined the stress state, the stress tensor can be split up into a hydrostatic stress, which involves only pure tension or compression, and deviatoric stresses, according to equ. (9) and (10) [81]. The hydrostatic component is very sensitive to the reference value d_0, thus a wrong or erroneous d_0 value is reflected in an erroneous hydrostatic stress, but the deviatoric component is not affected. Therefore, deviatoric stresses can be used to compare tri-axial stress states when the unstrained lattice parameter cannot be determined or is questionable.

$$\sigma_{hydro} = \frac{\left(\sigma_{11} + \sigma_{22} + \sigma_{33}\right)}{3} \tag{9}$$

$$\sigma_i^{dev} = \sigma - \sigma_i^{hydro} \tag{10}$$

6.2 Determination of the Diffraction Elastic Constants - DEC

The diffraction elastic constants can either be measured for a certain alloy and the desired lattice planes, or they can be calculated. The basis for a calculation of E_{hkl} and ν_{hkl} of a polycrystal are the single crystal elastic compliances C_{11}, C_{12}, C_{44} or stiffnesses S_{11}, S_{12}, S_{44}. In fact, the elastic compliance or stiffness is described by a fourth-rank tensor. Due to the symmetry of cubic crystals these three tensor components are sufficient to describe the elastic behaviour, as all other tensor components are zero [10, 82]. Three main models are available in the literature to determine the behaviour of a polycrystal on the basis of single crystal elasticity values C_{11}, C_{12}, C_{44} and S_{11}, S_{12}, S_{44} [10, 13, 73, 83]. The models differ concerning the concepts of how the single grains in a material are linked together. The Reuss model assumes uniform stress in all grains; the Voigt model presumes uniform strain. Nowadays the Kröner model is usually applied as it incorporates grain-grain interactions utilizing Elshelby's theory of inclusions. It is generally regarded as the most accurate [13] and is therefore employed for the current study on IN718. According to Refs. [82, 83] the elastic behaviour of a single crystal was transformed to the elastic behaviour of a polycrystal.

Before the Kröner model can be applied, the appropriate single crystal values for IN718 have to be defined. Single crystal data are available for pure Ni [83, 84] and some simple Ni-alloys (like Ni-Fe) [84] as well as for Ni_3Al [33], but not for IN718 or other nickel-based superalloys. There are different strategies published in literature for an estimation of the single crystal values of IN718. Holden *et al.* [85] refer to the fact that S_{11}^{-1}, $(S_{11}-S_{12})^{-1}$, and S_{44}^{-1} vary linearly with the Fe concentration in a binary Ni-Fe system [84]. Therefore, they assume that these quantities also vary linearly with the alloy content for a multi-component system like a nickel-based superalloy and thus interpolate the data. On the other hand, Dye *et al.* [86] calculated the average of the C_{11}, C_{12}, and C_{44} values of single crystal γ (pure Ni) [84] and single crystal γ' [33] and scaled the obtained average by the value of the elastic bulk modulus for solutioned heat-treated IN718 (204 GPa). The γ'' precipitates were not taken into account, as no data for this phase is available in literature. Table 5 shows single crystal elasticity values for IN718 than can be found in literature [86, 87].

Table 5: Literature values for the single crystal elastic constants used to calculate the diffractometric elastic constants for IN718.

IN718	**C_{11}** [GPa]	**C_{12}** [GPa]	**C_{44}** [GPa]
[86] scaled values	224	142	119
[86]	248	152	125
[87]	266.4	171.6	154.7

Based on the Kröner model, Behnken and Hauk [82] developed an algorithm to calculate the tensor $\boldsymbol{T}$, which describes the interaction of the single grain with the matrix. Assuming an isotropic material with a cubic lattice and globular grains a third order equation for the shear modulus $\boldsymbol{G}$ can be formulated:

$$f(G) = G^3 + \alpha G^2 + \beta G + \gamma, \tag{11}$$

where α, β, and γ are given by the tensor invariants K_e, μ, and ν as follows:

$$\begin{aligned} K_e &= \frac{1}{3}(C_{11} + 2C_{12}) = \frac{1}{3(S_{11} + 2S_{12})} & \qquad \alpha &= \frac{(9K + 4\nu)}{8} \\ \mu &= C_{44} = \frac{1}{S_{44}} & \beta &= -\frac{(3K + 12\nu)\mu}{8} \\ \nu &= \frac{1}{2}(C_{11} - C_{12}) & \gamma &= -\frac{3K\mu\nu}{4} \end{aligned} \tag{12}$$

Then the coefficients of the interaction tensor $\boldsymbol{T}$ can be calculated with its tensor invariants K_e, μ, ν and with the shear modulus $\boldsymbol{G}$, as $K_e = K_m$ for cubic systems:

$$A = T_{11} + 2T_{12} = \frac{K_m - K_e}{K_m(3K_e + 4G)} \tag{13}$$

$$B = T_{11} - T_{12} = \frac{(G - \nu)(3K_m + 6G)}{G[8G^2 + G(9K_m + 12\nu) + 6\nu K_m]} \tag{14}$$

$$C = 2T_{44} = \frac{(G - \mu)(3K_m + 6G)}{G[8G^2 + G(9K_m + 12\mu) + 6K_m\mu]} \tag{15}$$

and so T_{11}, T_{12}, T_{44}, and T_0 are given by:

$$T_{11} = \frac{A + 2B}{3} \tag{16}$$

$$T_{12} = \frac{A - B}{3} \tag{17}$$

$$T_{44} = \frac{C}{2} \tag{18}$$

$$T_0 = T_{11} - T_{12} - 2T_{44} \tag{19}$$

Introducing orientation parameter Γ completes the calculation of the diffraction elastic constants s_1 and s_2.

$$\Gamma = \frac{h^2k^2 + k^2l^2 + l^2h^2}{(h^2 + k^2 + l^2)^2} \tag{20}$$

$$s_1 = S_{12} + T_{12} + \Gamma T_0 \tag{21}$$

$$s_2 = 2(S_{11} - S_{12} + T_{11} - T_{12} - 3\Gamma T_0) \tag{22}$$

where S_{11} and S_{12} are the single crystal elastic compliances.

Finally, E_{hkl} and ν_{hkl} can be determined with:

$$E_{hkl} = \frac{1}{s_1 + \frac{1}{2}s_2} \qquad \text{and} \qquad \nu_{hkl} = -\frac{s_1}{s_1 + \frac{1}{2}s_2} \tag{23}$$

According to Dye *et al.* [86], the following DEC were determined for a mixture of the γ matrix and Ni_3Al precipitates:

$$hkl = \begin{pmatrix} 311 \\ 220 \\ 200 \\ 111 \end{pmatrix} \quad E_{hkl} = \begin{pmatrix} 195 \\ 215 \\ 168 \\ 237 \end{pmatrix} \quad \nu_{hkl} = \begin{pmatrix} 0.309 \\ 0.289 \\ 0.335 \\ 0.267 \end{pmatrix} \qquad \text{[86] not scaled}$$

$$hkl = \begin{pmatrix} 311 \\ 220 \\ 200 \\ 111 \end{pmatrix} \quad E_{hkl} = \begin{pmatrix} 193 \\ 218 \\ 163 \\ 246 \end{pmatrix} \quad \nu_{hkl} = \begin{pmatrix} 0.310 \\ 0.286 \\ 0.341 \\ 0.259 \end{pmatrix} \qquad \text{[86] scaled}$$

According to Schröder *et al.* [87] the obtained DEC values were only slightly different:

$$hkl = \begin{pmatrix} 311 \\ 220 \\ 200 \\ 111 \end{pmatrix} \quad E_{hkl} = \begin{pmatrix} 195 \\ 216 \\ 167 \\ 239 \end{pmatrix} \quad \nu_{hkl} = \begin{pmatrix} 0.309 \\ 0.288 \\ 0.336 \\ 0.266 \end{pmatrix} \qquad \text{[87]}$$

These values differ considerably from the corresponding values for other superalloys, which shows that this calculation has to be performed anew for each alloy composition. For example Waspaloy: E_{311} = 206 GPa, ν_{311} = 0.26 and E_{111} = 257 GPa, ν_{111} = 0.25. For IN718 some authors [88] give slightly different values for selected DECs, as for example: E_{311} = 209 GPa and ν_{311} = 0.290. This result was not taken into account because Dye *et al.* [88] did not discuss the basis for their results.

6.3 Peak Fit

The lattice distances d_{hkl} are given by the centre of the diffraction peaks recorded for a certain location in the sample. Figure 55a shows the typical shape of the (311) peak recorded for the quenched samples and the peak in Figure 55b is representative of diffraction peaks in an aged sample. The Gaussian function was chosen to fit all the peaks of the quenched samples and the Voigt function was chosen for the samples in the aged condition. In the aged samples the presence of an increased amount of precipitates was well reflected in the broader shape of the diffraction peak, which could not be modelled by a Gaussian function. For all recorded peaks, the fitting procedure assumed a linear background. In the current work, the uncertainty of the peak position was defined by the standard deviation u_x of the peak fitting process.

The diffraction peaks in Fig 55a and 55b are representative for all measurements on the studied turbine disc and the model plate because the material was homogenous concerning grain size and texture. The texture was examined by EBSD at various locations in the disc and proved to be random (Chapter 8). Single large grains could lead to strain results that are not representative for the whole sample, but the grain size was homogeneously small and so the chosen gauge volumes captured enough grains to guarantee good statistics. The typical gauge volume of $3 \times 3 \times 3$ mm^3 contained about $413 \cdot 10^6$ grains, and therefore the measured lattice distances can be regarded as a representative mean value for the whole region covered by the gauge volume.

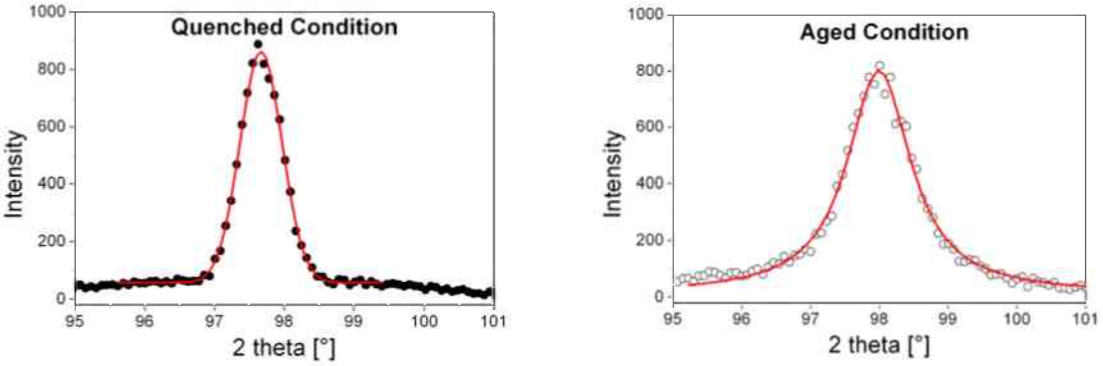

Figure 55: Examples of typical (311) peak profiles measured within the turbine disc material IN718 fitted with (a) a Gaussian function for the water quenched condition and (b) with a pseudo-Voigt function for the aged condition.

Diffraction methods are sensitive to macro and microstresses, which is illustrated by the change of the peak shape in the aged condition where coherent precipitates are present and thus lattice distortions add up to any macrostrains inside the sample. Generally it is assumed that macro and microstresses add up linearly according to:

$$\sigma = \sigma^{I} + \sigma^{II} + \sigma^{III}, \qquad (24)$$

where σ^{I} represents the macrostress, σ^{II} the intergranular stress and σ^{III} the intragranular stress.

As microstresses do not only change the peak shape, and thus the **f**ull **w**idth at **h**alf-**m**aximum value (FWHM), but can also influence the location of the peak centre, it is not possible to measure macrostresses selectively if microstresses are present. It can be necessary to separate microstresses from the measured result to obtain only the macrostresses. Holden *et al.* [79] successfully performed such a separation for the strains determined in a severely bent tube made of Inconel 600.

6.4 ARES

The neutron measurements were performed on the diffractometer *ARES* (**A**nalysis of **Re**sidual **S**tresses) at GKSS (Geesthacht, Germany) [89]. Thermal neutrons were obtained from the steady-state nuclear fission reactor FGR-1 at GKSS, and a silicon (311) monochromator filtered the neutrons with equal velocity and thus equal wavelengths. Hence, a neutron beam with a fixed wavelength of λ = 0.16379 - 0.16396 nm was used for the strain measurements. A shift of the Bragg peak $\Delta\theta$ can be linked directly to a change of the lattice parameter Δd_{hkl} according to equ. (5). Using an area detector with an active area of 30 cm × 30 cm, it was possible to measure at diffraction angles from $2\theta = 0°$ up to about 100° with an angular resolution of approximately 0.12°. The repeatability of the strain measurements was guaranteed by the use of a reference sample (Ni-powder) that was measured after each scan. Absolute values of lattice parameters were not determined as they are not required for strain measurements.

The detector distance (d = 958 mm) was kept constant for all measurements and the channel slope (mm/channel) was determined together with the neutron wavelength once, after each restart of the reactor. With this information the detected curves of the intensity versus the channels could be transferred to curves of intensity versus diffraction angle 2θ. The measurement of the Ni powder was performed after each scan of a disc or plate. In this way, slight changes of the set-up at ARES caused by the manipulation between the measurements, like changing of the slits, could not cause systematic errors in the measurement.

At a diffractometer like ARES a single reflection has to be chosen to determine the lattice distances. At ARES, typical measurement times varied between 30 min and 5 h for the disc and between 15 min and 30 min for the model plate for the (311) reflection. Of course, the measurement times depend largely on the beam path inside the sample. For this reason, the axial direction required the longest measurement times for locations on the opposite side of the entry of the neutron beam if the same accuracy was achieved. Naturally, the measurement times also varied largely for different gauge volume sizes used in the course of the work ($2 \times 2 \times 2$ mm^3 up to $3 \times 3 \times 30$ mm^3).

Figures 56a and 56b show how the model plate and the Ni-powder were positioned on the x-y-z table at ARES during a measurement. The position of the gauge volume was fixed and so the sample had to be moved through the neutron beam with the "x-y-z" table.

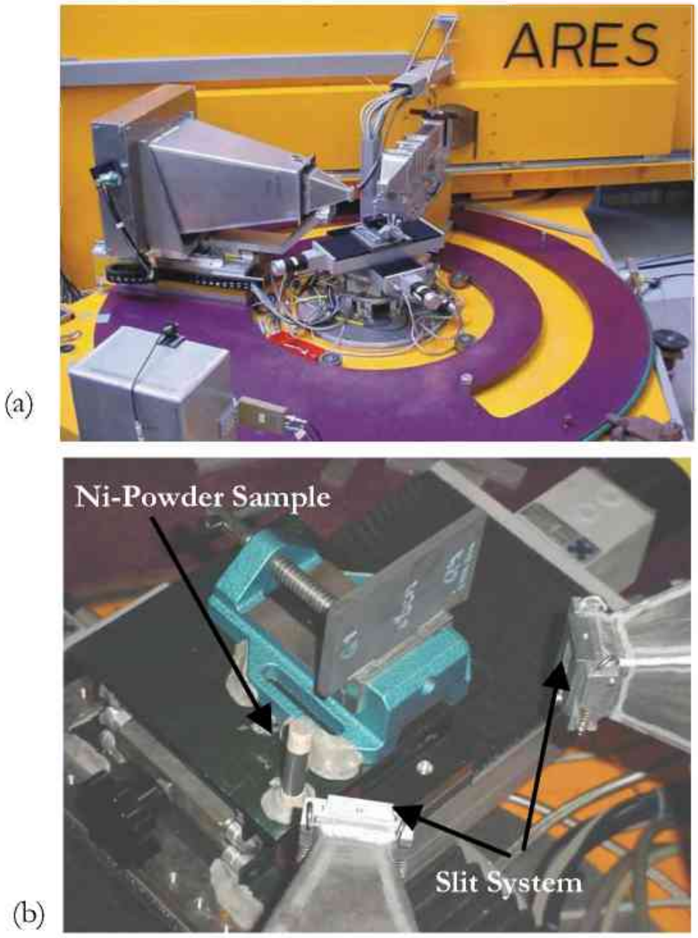

Figure 56: (a) The diffractometer ARES at GKSS which was used for all the neutron measurements. (b) A model plate positioned in the neutron beam configured to measure longitudinal lattice distances. On the left hand side the Ni-power sample can be seen as well.

6.4.1 Positioning

As mentioned above three independent strain measurements are necessary to determine the stress tensor. Therefore, the samples have to be positioned anew three times at ARES. Care has to be taken to locate the gauge volume at exactly the same position within the sample for the three measurements. Otherwise the determined strains would not be related to the same location inside the sample.

Scanning a well defined edge of the sample through the gauge volume and recording the intensity versus position is regarded as the most accurate technique to position the sample, because it uses the neutron beam itself [13, 73]. Here, the chosen step size was usually 0.5 mm. The intensity first increases due to the increasing amount of diffracting material inside the gauge volume (= sampled gauge volume) and due to an extending length of the diffraction path. Moving the sample further along the scan line, the intensity decreases because the absorption of neutrons starts to prevail, once the gauge volume is fully immersed in the sample. If the intensity is recorded for a sample movement parallel to the diffraction vector $\boldsymbol{q}$, it is necessary to correct the translator reading. Compared to a sample movement normal to $\boldsymbol{q}$, the length of the diffraction path inside the sample increases quicker and so the proportion of the adsorption increases quicker as well. Consequently, the location of the half maximum intensity is located slightly outside the sample. The required correction for the attenuation of the recorded intensity depends on the size of the gauge volume and on the diffraction angle. The formulas to calculate the intensity profile as given in Figures 57a, b as well as the relation between the centroid of the sampled gauge volume and the translator reading are described in detail in Ref. [73]. For the γ-(311) reflection ($2\theta \cong 98°$) the correction of the translator reading was calculated to be between 0.2 mm and 0.3 mm for the different cross sections of the gauge volumes. Finally, the position of the half-height intensity gave the wall position with an accuracy of about ± 0.1 mm. This value results from an estimation based on the steep rise and fall of the intensity curves near the sample edge.

For the turbine disc the intensity curve was initially determined at the bottom side near the rim, as illustrated by the point **X** in Figure 9. This point **X** served as a reference point for all measurement locations inside the disc. With the help of a "x-y-z" table the sample was translated in three mutually perpendicular directions relative to the incident beam. One single reference point is sufficient, as long as the axial, radial, and tangential directions of the disc are exactly parallel to the x, y, and z axis of the instrument coordinate system. However, in the course of the work this proved to be an improper assumption. As a consequence, the edge of disc B5 was determined separately for each radius of the scan lines parallel to the disc axis. For the model plate the intensity curves were always determined at three separate positions to locate the middle of the plate in the x as well as y direction.

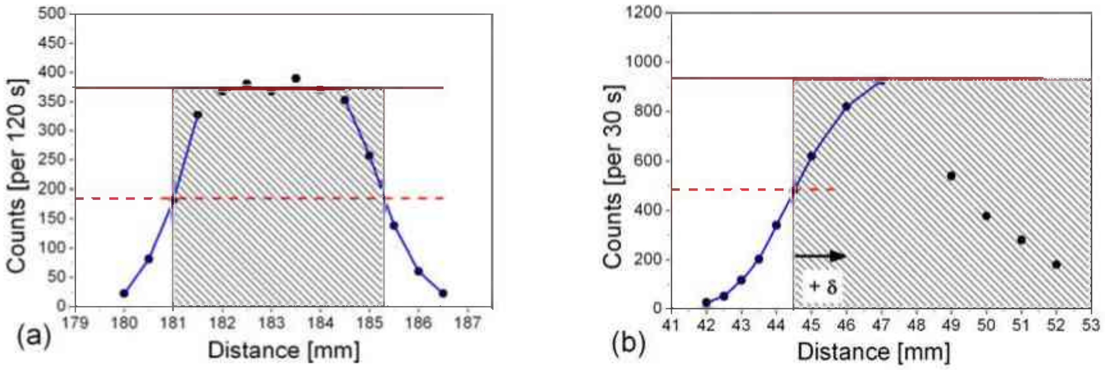

Figure 57: Intensity curves as a function of the lateral position of the gauge volume. The location of the half intensity gave the position of the sample edge, which was used as a reference line for the positioning of the measurement locations. (a) Scan through a reference cube perpendicular to the scattering vector *q*. The employed slit sizes were 2×14 mm² and 2×30 mm² for the incoming and the diffracted beam. (b) Scan into the disc in the axial direction (parallel to *q*) using a slit size of 3×30 mm² for the incoming as well as the diffracted beam. Here, the location of the edge had to be corrected by δ depending on the size of the gauge volume.

6.4.2 Gauge Volumes

The gauge volume was defined by Cd diaphragms (Figure 58), which reduce the incoming and diffracted beam to a rectangular column and form a matchstick-like or cubic gauge volume with a quadratic cross section if the diffraction angle is 90°. By moving the specimen through the beam, the gauge volume could be positioned at different locations in the sample. Figure 59 illustrates the alignment of the gauge volumes inside the turbine disc.

For the first neutron measurements a nominal gauge volume of $3 \times 3 \times 30$ mm³ was chosen for the radial and axial directions and $3 \times 3 \times 14$ mm³ for the tangential direction. A matchstick-like gauge volume was used to increase the intensity and save beam time. As the strains were assumed to be fairly constant along the circumference of the disc and transverse to the longitudinal direction of the model plate, the elongation of the gauge volume was expected to have no effect on the determined strain results.

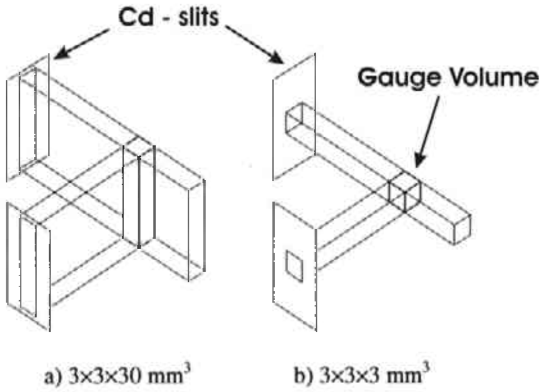

Figure 58: Sketch of the matchstick-like gauge volumes defined by the Cd slits, which produce (a) a matchstick-like gauge volume or (b) a cubic gauge volume.

The counting times were chosen in such a way that peak heights of approximately 500 - 1000 counts could be obtained and high measurement accuracies could be achieved. Naturally, the counting times vary considerably, especially for the axial direction, due to large differences in the length of the beam paths within the disc. For the tangential direction the background was much higher than for the axial and radial direction, which resulted in a lower peak-to-background ratio. This of course could not be improved by increased measurement times and thus the tangential strain components of the disc exhibited larger measurement uncertainties.

In order to make sure the statistics of the measurement are good, the number of grains within the gauge volume was determined for the different gauge volume sizes. For this calculation a grain size of 5 µm was employed. As the IN718 material of the disc had a nearly random texture the numbers given in Table 6 ensure good statistics.

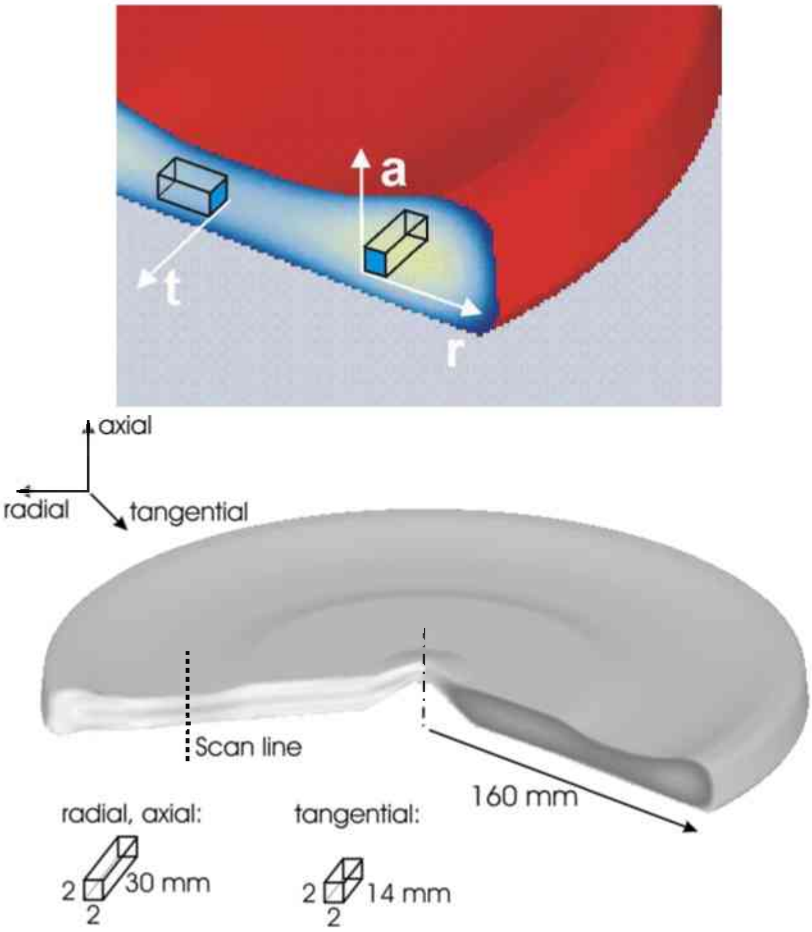

Figure 59: Sketch of the matchstick-like gauge volume in the turbine disc.

Table 6: Number of grains captured by the different gauge volume sizes that were employed to measure the lattice strains in the turbine disc and the model plate as well as their reference cubes.

Gauge Volume [mm³]	**Number of grains** (grain size: 5 μm)
$3 \times 3 \times 30$	$4125 \cdot 10^6$
$2 \times 2 \times 14$	$856 \cdot 10^6$
$3 \times 3 \times 3$	$413 \cdot 10^6$
$2 \times 2 \times 2$	$122 \cdot 10^6$

6.5 Determination of the Reference Values

6.5.1 Measurement of the Reference Cube

One possibility to obtain a reference value d_0 is to cut a small cube from the sample by electron discharge machining. The basic idea is that the lattice distance in the cube is equivalent to the unstrained lattice parameter, because the macrostress field is destroyed due to the cutting [13, 43, 90]. The chemistry or any intergranular effects stay intact since these parameters vary on the scale of the grain size. In order to serve as a stress-free sample the cube has to be small in size compared to the variation of the stress field in the investigated part. In the current work, sizes of $4 \times 5 \times 6$ mm^3 and $4.0 \times 4.1 \times 4.2$ mm^3 were chosen for the cubes cut from the disc. For the model plates the cubes' sizes were always $4.0 \times 4.1 \times 4.2$ mm^3. Holden *et al.* [91] suggested to further cut the cube in small slices or smaller cubes to ensure complete relaxation of macrostresses. For the sake of comparison, this was done once for the reference cube of a model plate, but the final results appeared to be unaffected by a further reduction of the cube's size.

Figure 60 shows where the reference samples were cut from the discs. The cubes from the disc were initially cut at the rim (cube indicated by "R"). Later on, 20 cubes were once cut directly at the measurement locations all over the cross section of the disc for a verification of small chemical or texture differences along the cross section of the disc. Figure 60 depicts the five radial positions of these reference cubes.

No annealing was performed on the reference cubes, because the microstructure of IN718 was very sensitive to further heat treatments and annealing could have caused significant precipitation of γ' and γ'' particles. This would have resulted in different microstress states and thus different lattice distances.

Figure 61 illustrates that the reference samples were measured with a gauge volume that captured as much of the cube as possible. In the course of the work, the different slit sizes were used and sometimes the gauge volume was chosen to be matchstick-like to increase the neutron intensity e.g.:

3 mm × 10 mm and 3 mm ×30 mm or
3 mm × 30 mm and 3 mm ×30 mm or
2 mm × 10 mm and 2 mm ×30 mm or
2 mm × 30 mm and 2 mm ×30 mm.

For the sake of simplification the single slit sizes of the reference measurements are not stated hereafter, but the gauge volumes are only referred to as $3 \times 3 \times 3$ mm^3 or $2 \times 2 \times 2$ mm^3, independent of the matchstick-like shape. Of course, a nominal gauge volume with a matchstick-like shape can never exceed the size of the sample.

The reference cubes were measured in three orthogonal directions with the scattering vector lying normal to the faces of the cubes, which were parallel to the axial, radial, and tangential direction of the disc or the normal, longitudinal, and transverse direction respectively of the model plate (Figure 61). This procedure enabled monitoring any directional differences due to texture influences or due to remaining residual stresses. Table 7 shows that the measured lattice distances only exhibited minor differences in the three directions. Nevertheless, the average of the three directions was used as a reference d_0 for the residual strain calculation in order to balance any potential statistical errors of the d_0 measurement.

The analysis of the 20 cubes showed no major variation of the lattice distance neither along the disc radius nor across the thickness of the disc. The results are illustrated in detail in Figure 62. In the axial directions no tendency can be observed at all. In the radial and tangential there are small variations of the d_0-value. In fact only the values at a disc radius of 151.6 mm are set apart from the rest, but up to a radius of R = 132.9 mm the d_0-values in all directions are equal within the measurement error. At R = 151.9 mm the lattice distances are slightly higher for the radial direction and slightly lower for the tangential direction. Close to the bottom side, 2 mm from the edge, the lattice distances in the tangential direction were a little higher, but no systematic variation could be observed for the other directions. Most likely these differences reflect the deformation history of the disc, as the final compression is highest for the rim region and the bottom side according to FE simulations. As the observed differences were too small to significantly affect the residual stress result, an average value of all 20 cubes and all three directions was calculated and employed as a reference d_0. This was further justified by independently performed chemical analyses along the cross section that did not reveal any chemical differences. Finally, one cube was considered as sufficient for an accurate determination of the unstrained lattice parameter.

The same applied for the model plate, as the insertion direction into the quenching water was not reflected in the unstrained lattice parameter of the three cubes cut along the longitudinal direction of the plate. Consequently, the strains in the model plate were also calculated with the average d_0 value of the three cubes.

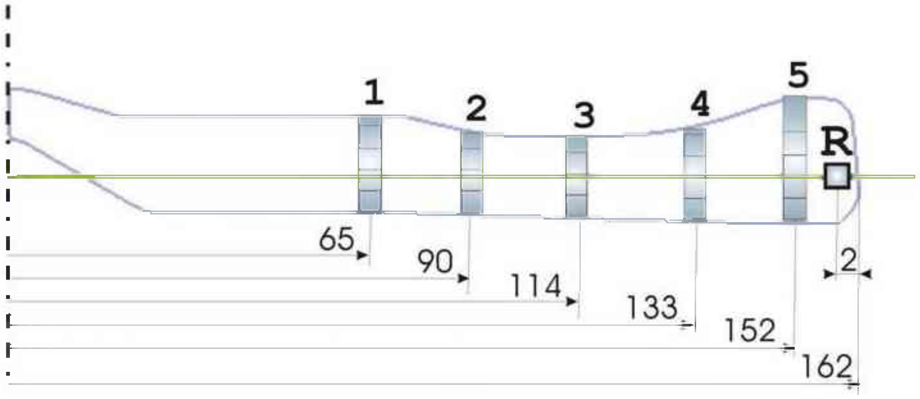

Figure 60: Location of the reference cubes in the turbine disc which were taken out by electro-discharge machining.

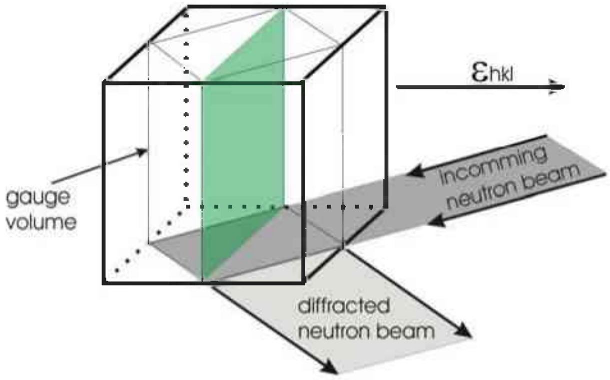

Figure 61: Cuboid reference sample shown with a cubic gauge volume that captured as much of the reference sample as possible while still being completely filled with the examined material. This was the case for a reference sample size of 4.0 × 4.1 × 4.2 mm^3 and a gauge volume size of 3 × 3 × 3 mm^3.

Table 7 shows the reference values determined on the different cubes which were cut from the disc in order to illustrate the small magnitude of the differences between the three directions. The values of different measurements cannot be compared, because the values are not absolute values. As mentioned above, the measurement at ARES is relative and so the lattice data of different measurement series cannot be compared to each other or to X-ray data.

For gauge volume sizes which capture nearly the entire volume of the reference cube, the alignment has to be very accurate to ensure that the gauge volume is completely filled with the examined cube. Minor misalignments cannot totally be excluded as the intensity curves sometimes indicated minor irregularities of the microstructure, e.g. very localized textures. Despite all efforts this can result in slightly erroneous d_0 values.

Table 7: Measured d_0 -values determined with the (311) reflection of the reference cubes machined from the water-quenched discs B3 and B5. The measured d_0 values are plotted together with the measurement uncertainty Δd generated from the standard deviation u_x of the peak fitting procedure given in brackets.

Sample	**λ** [nm]	**Cube size** [mm³]	**Gauge volume** [mm³]	d_0^{axial} [nm]	d_0^{radial} [nm]	$d_0^{\text{tangential}}$ [nm]	$\overline{d_0}$ [nm]
B3 rim	0.16396	4 × 5 × 6	2 × 2 × 30	0.108 647 (5)	0.108 638 (8)	0.108 621 (5)	0.108 635 (6)
B5 rim	0.16391	4 × 5 × 6	3 × 3 × 30	0.108 624 (5)	0.108 564 (7)	-	0.108 594 (6)
B5 rim	0.16394	4 × 5 × 6	2 × 2 × 30	0.108 593 (9)	0.108 592 (5)	0.108 581 (8)	0.108 589 (7)
B5 21 cubes	0.16394	4 × 5 × 6	2 × 2 × 30	0.108 602 (15)	0.108 625 (16)	0.108 617 (18)	0.108 615 (16)
B5 R = 102 mm	0.16379	4.0 × 4.1 × 4.2	2 × 2 × 14	0.108 609 (5)	0.108 612 (6)	0.108 622 (6)	0.108 614 (5)

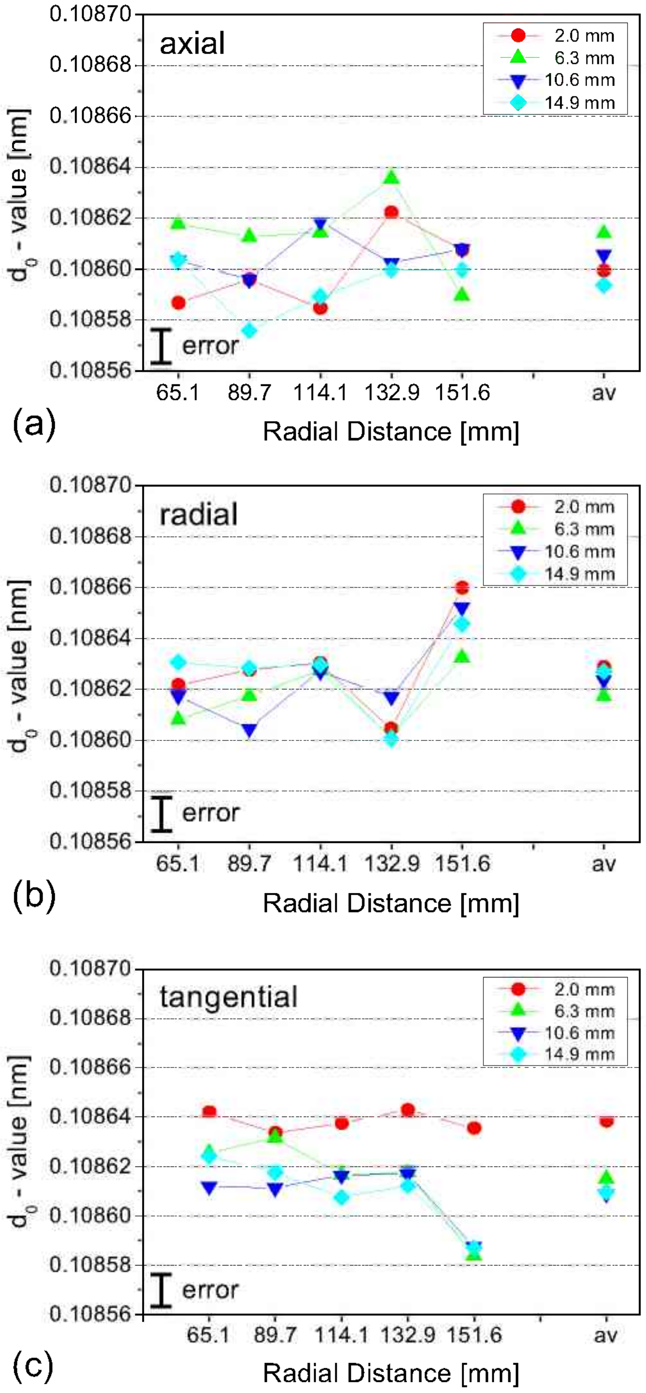

Figure 62: Stress-free lattice parameters d_0 determined with the reflection (311) on 20 cubes, each having a size of 4 × 5 × 6 mm³ and cut from the water-quenched disc B5 made of IN718. "av" denotes the average value of the d_0 values measured at a given distance from the bottom edge of the turbine disc.

6.5.2 Plane Stress Conditions

In order to obviate the destruction of the sample by cutting a reference cube, it is possible to use the information that a 2-axial stress state prevails in the sample. In very thin and very elongated plates, plane stress conditions can be assumed as this shape is close to an infinite plate, which has no normal stress component. According to the finite element simulations plane stress conditions prevail in the model plate, except for the rim region, as well as in major parts of the turbine disc. For plane stress conditions a notional reference value d_0^* can be calculated using [10, 69, 81]:

$$d_0^* = \frac{1-\nu_{hkl}}{1+\nu_{hkl}} d_{a/n} + \frac{\nu_{hkl}}{1+\nu_{hkl}} \left(d_{r/l} + d_t\right), \tag{25}$$

where $d_{a/n}$ is either the lattice distance in the axial direction or normal direction. Similarly, $d_{r/l}$ is either the lattice distances in the radial or the longitudinal direction and d_t is either the lattice distances in the tangential or transverse direction.

This method is extensively used in laboratory-based X-ray investigations of near-surface stress fields, as the stress component normal to the surface of the sample must be zero in all cases [10, 69].

6.6 Measurement Error

The measurement error of neutron diffraction experiments is largely associated with the statistical nature of the diffraction process itself. The detector records single neutrons that hit the detector and so the raw data is obtained in terms of counts at successive angular positions. The intensity distribution versus the diffraction angle, also referred to as diffraction peak, has to be fitted by an appropriate profile function. In this work a non-linear least square fit of a Gaussian or a Voigt function has been performed. The uncertainty of the obtained peak centre is defined by the standard deviation u_x and by the ratio H/B of the peak height H and the background B.

Apart form the uncertainties in the peak fitting, the strain measurement may be affected by many possible systematic effects. These include instrument resolution, non-homogeneous material properties, an off-centre centroid of the sampled volume due to attenuation or texture effects, or a partially filled gauge volume and uncertainties in positioning of the sample – especially in the case of steep strain gradients. It is only possible to estimate these systematic uncertainties by testing different configurations of the sample and the instrument. This was done by varying the size of the gauge volumes for an examination of the reference cubes, which were also changed in size from their initial dimensions of $4 \times 5 \times 6$ mm^3 to $4.0 \times 4.1 \times 4.2$ mm^3.

Furthermore, the uncertainties of the neutron wavelength and of the distance of the detector as well as a modification of the slit system influenced the conversion of the detector channels to an angular value and consequently the residual stress result. These parameters have not been considered separately, but were indirectly taken into account by a reference measurement of a Ni powder sample. It was measured after each scan to give the accurate diffraction angle for the current set-up. The neutron wavelength, the detector distance and its slope were unchanged and thus only determined once after each restart of the reactor.

Thus, only the statistical error of the peak position is considered in the calculation of the uncertainty of the residual stresses in the current work. According to Pyzalla [71] the measurement error can be determined using the Gaussian law of error propagation:

$$\Delta\sigma_r = \frac{1}{(1/2)s_2}\cot\theta_0 \left[\left(1-\frac{3s_1}{(1/2)s_2+3s_1}\right)^2 (\Delta\theta_0)^2 + \left(1-\frac{s_1}{(1/2)s_2+3s_1}\right)^2 (\Delta\theta_r)^2 + \left(\frac{s_1}{(1/2)s_2+3s_1}\right)^2 \left(\Delta\theta_a{}^2 + \Delta\theta_t{}^2\right)\right]^{1/2}, \tag{26}$$

where $s_1 = E/(1+\nu)$ and $s_2 = \nu/(1-2\nu)$ are the diffractometric elastic constants, $\Delta\theta_0$, $\Delta\theta_r$, $\Delta\theta_a$, and $\Delta\theta_t$ are the measurement uncertainties of the Bragg peaks corresponding to the radial (r), the axial (a), the tangential (t) direction and to the reference θ_0. The measurement uncertainties of the Bragg angles used in equ. (26) were set equal to the standard deviations u_x of the fitting functions, which was always the Gaussian function for the water-quenched condition.

For all measurements great attention was paid to a proper peak-to-background ratio. Generally, the ratio was approximately $H/B = 7$, but for some strain directions the background was unavoidably high. For example, the tangential direction in the disc involves long beam paths and thus results in high background signals ($H/B = 2.5$). Of course, increased beam times could not improve the H/B ratio, but the peak shape was more well defined and this reduced the standard deviations u_x, of the fit.

According to equ. (26), the average measurement uncertainty of the different directions was calculated to be $5 \cdot 10^{-6}$ nm for the lattice distances which led to an uncertainty of the strain of 10^{-4} and resulted in an error of the residual stresses of $\Delta\sigma_{max}$ = ± 55 MPa for the water quenched turbine disc and the model plate.

In addition to the uncertainty of the peak centre, the positioning of the sample had a major influence on the obtained stress results. Great care has to be taken to position the gauge volume at exactly the same location inside the sample for each of the three stress directions. Despite all efforts, misalignments cannot be excluded and even though they might be very small, they proved to be significant. First of all, the samples had to be readjusted completely for each strain component, which adds up the single positioning errors. Secondly, a non-perfect vertical alignment will cause a modification of the scan line and thus different locations in the sample will be measured. The positioning error was estimated to be ± 0.1 mm, but the additional uncertainty due to a vertical inclination as illustrated in Figure 63 cannot properly be quantified as the inclination angle was unknown.

Finally, the diffraction elastic constants are also a potential source for erroneous stress values. However, there are very few publications giving E_{hkl} and ν_{hkl} data for IN718 [86, 87] and they do not state any measurement uncertainties. Most of the DEC data published in the literature are calculated values and do not result from a least square fit of the measured elastic response to a macroscopic uniaxial load. Calculations of DEC values are always based on single crystal constants, but they are not available for commercial alloys like IN718. Actually, only a limited number of publications on pure Nickel [83] and simple binary [92] or ternary alloy systems [84] exist. Therefore, single crystal constants for complex alloys have to be estimated. Currently, all studies on IN718 refer to the same publication [86], which uses the average of pure Nickel data and single crystal values for γ'.

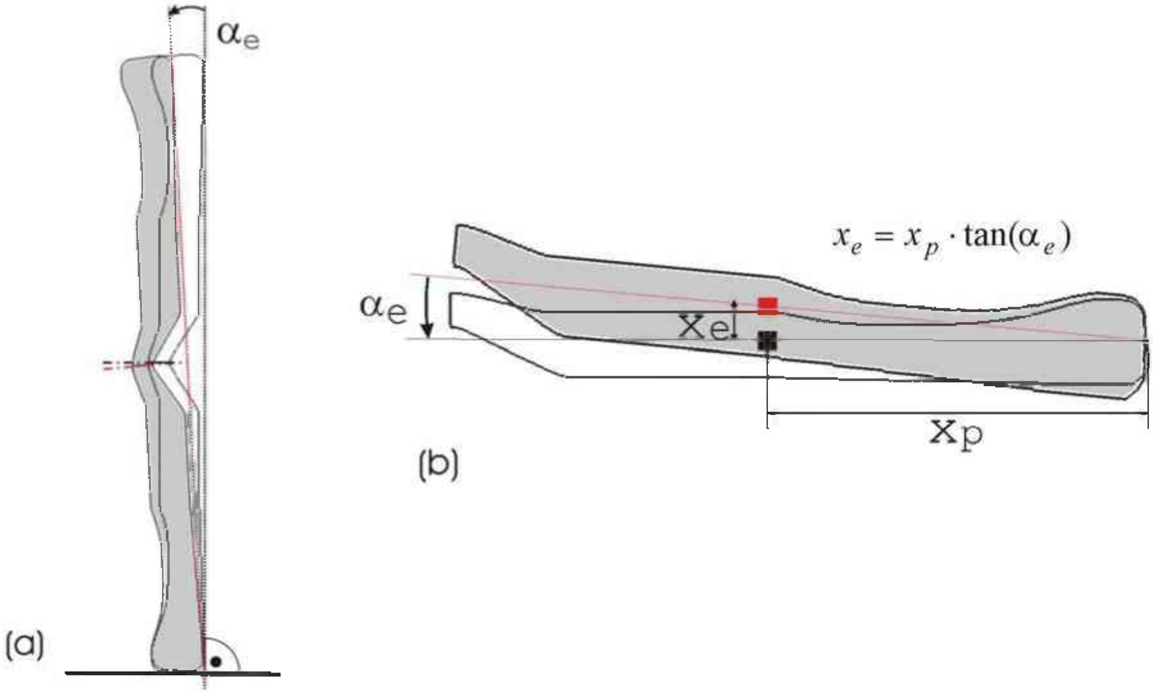

Figure 63: Sketch of the turbine disc showing how it was mounted on the x-y-z table and illustrating the possible deviation from the vertical position, which results in a misalignment x_e given by the angle α_e.

6.7 Results and Discussion of the Neutron Measurements

6.7.1 Model Plates

The basic idea was to measure a thin plate made of the same material as the turbine disc because it allowed to test the influence of the disc geometry of the residual stress state. The same thermal history was applied to this model plate in order to make sure any differences regarding the precipitation conditions have no impact on the stress result. Two plates were investigated: one cut from pre-forged material (plate **A**) and one cut from a forged and water-quenched turbine disc (plate **B**). Both had the same dimensions: 100 × 60 × 6 mm^3 and both were measured along a central line parallel to the longitudinal direction of the plate (see Figure 12). The low thickness enabled lower measurement times compared to the turbine disc and thus also the other reflections: (220), (200) and (111) could be investigated for comparison.

6.7.1.1 Model Plate **A** Cut from the Pre-forged Material – Quenched Condition

The strains were determined with the help of a reference cube cut from the middle of an identical plate, which was also cut from the pre-forged material and annealed at the forging temperature of 960 °C for 1 h, to ensure the whole plate is fully heated up. Subsequently, the plate was water-quenched. The cube, which had a size of 4.0 × 4.1 × 4.2 mm^3, was measured in one main direction only, using a 3 × × 3 mm^3 gauge volume. The same procedure was performed for all four peaks.

Figure 64 illustrates the residual stresses determined with the reflection (311), which was regarded as the most appropriate to study macrostresses [75, 94]. The longitudinal component reaches a maximum level of 300 MPa in the middle of the disc, where the transverse component shows a minimum close to zero stress. The axial stress is close to zero except for the rim region, where stresses up to 100 MPa are reached. All components are fairly symmetric. The difference between the longitudinal and transverse component is most prominent in the middle. Along the whole length of the plate, the calculated normal stresses are non-zero, which provoked the investigation of the residual stress state with the other reflections (220), (200) and (111).

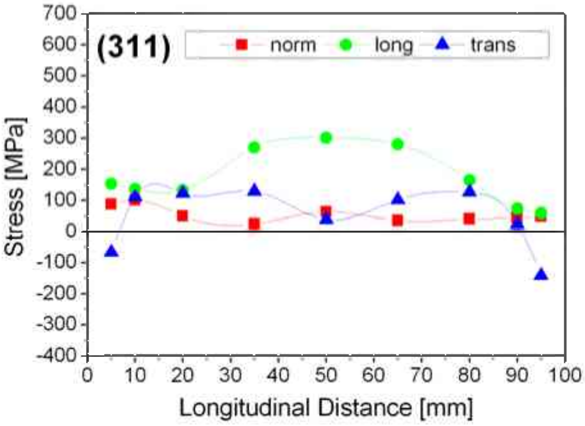

Figure 64: Residual stresses within a water-quenched model plate (100 × 60 × 6 mm^3) cut from pre-forged material (plate "A") determined with the (311) reflection. The reference cube had a size of 4.0 × 4.1 × 4.2 mm^3 was measured with a 3 × × 3 mm^3 gauge volume

The results of the other reflections (Figure 65) show essentially the same picture as the (311) reflection: The longitudinal component is the highest and steadily increased towards the middle, whereas the transverse component shows a minimum in the middle of the plate and strongly decreases towards the edge. The normal component is the lowest and fairly constant over the whole cross section of the plate. The result of the peak (200) evidently differs from the others, which is in accordance to literature, where it is generally declared as highly sensitive to microstresses. The peak (111) is also often recommended for macrostress analysis, but in the present case the measurement error is unacceptably high due to the low diffraction angle 2θ. Nevertheless, the result suggests that (111) is reflecting the macrostress better than (311) because the normal stress component is closer to zero. As none of the single stress results were completely satisfying, the average of the four peaks was calculated in order to obtain a Rietveld type analysis, which is often applied in the literature for the stress determination [51, 54, 62]. This analysis resulted in virtually zero normal stress, which corresponds to the simulation results. The longitudinal component reaches up to 300 MPa and the transverse component reaches 150 MPa with a local minimum of 50 MPa in the middle.

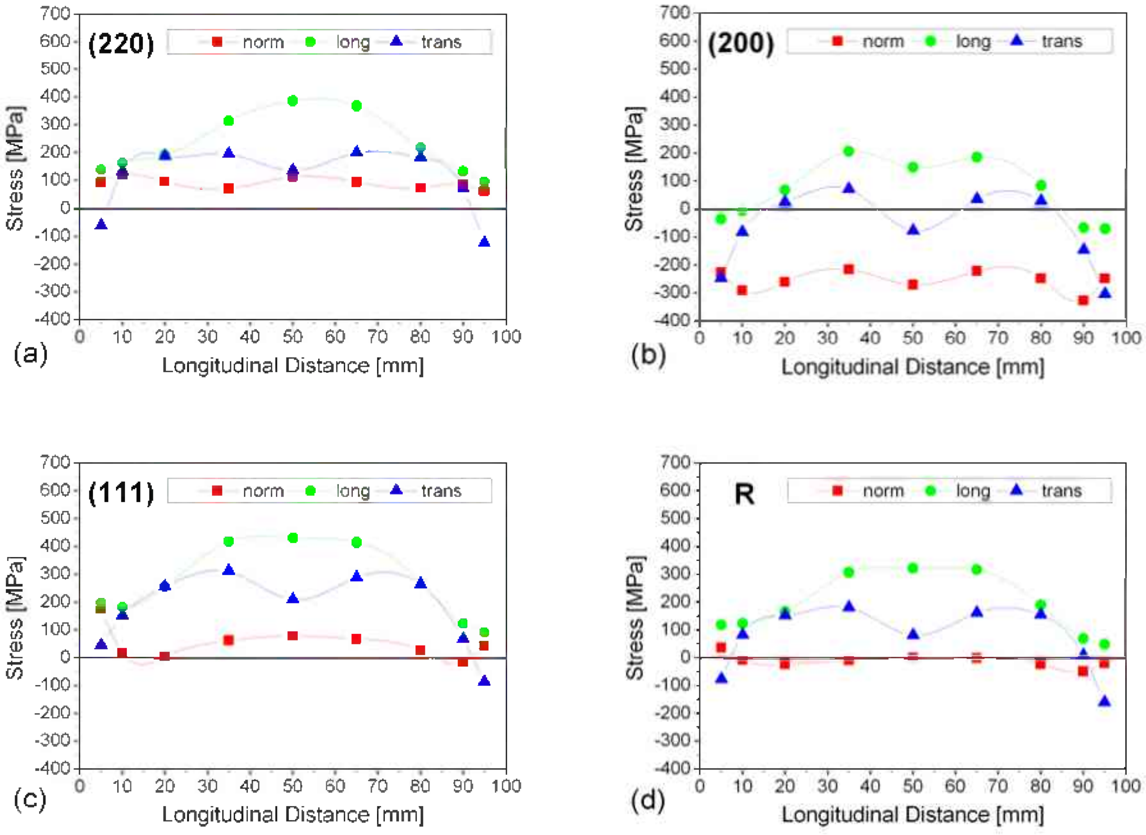

Figure 65: Residual stresses within a water-quenched model plate (100 × 60 × 6 mm^3) cut from pre-forged material (plate "A") determined with the following reflections (a) (220), (b) (200), (c) (111), and (d) Rietveld type analysis of all four reflections. The reference cube had a size of 4.0 × 4.1 × 4.2 mm^3 and was measured with a 3 × × 3 mm^3 gauge volume.

6.7.1.2 Model Plate **B** Cut from the Turbine Disc – Quenched Condition

The deformation history of the model plate cut from the pre-forged material and of the turbine disc was not identical and, as a consequence, the microstructures were different. Especially the grain size of the material before forging was considerably larger (10 - 15 µm) than the gain size after forging and subsequent water quenching (5 µm). Regarding the amount and size of the γ'' particles no differences between the two microstructures (forged and pre-forged) could be observed. In both cases the particles were too small to be resolved with the available SEM and the texture measured with EBSD was random. Consequently, another model plate with the same dimensions (100 × 60 × 6 mm^3) was machined directly from a quenched turbine disc and will be referred to as "Plate **B**". The large difference in the grain size suggested that the residual stresses in the pre-forged material were not representative for the residual stresses in the forged turbine disc because the yield stress is well known to be a function of the grain size as depicted by the Hall-Patch relation. This new model plate was reheated again to 960 °C and subsequently quenched in water. A second plate with the same dimensions was cut parallel to the plate **B** and received the same annealing and quenching treatment. The reference cube, which had a size of 4.0 × 4.1 × 4.2 mm^3, was cut from the middle of this dummy plate and was measured once with each of the four available reflections. For the sake of comparison the reference measurement was performed with a gauge volume of 3 × 3 × 3 mm^3 as well as with a gauge volume of 2 × 2 × 2 mm^3. The results of the obtained residual stress values were not equal as can be seen in Figures 66 - 67, where the full symbols refer to the 3 × 3 × 3 mm^3 gauge volume and the open symbols to the 2 × 2 × 2 mm^3 measurement.

Compared to the model plate **A** cut from the pre-forged material, the reflection (311) leads to significantly higher residual stresses, but in general the trend of the stress components was equal. The longitudinal component had a maximum in the middle of the plate at about 500 MPa. The transverse component was again lower than the longitudinal component and varied between 50 MPa and 150 MPa. For the 3 × 3 × 3 mm^3 reference, the normal stress component was zero, which was in accordance to continuum mechanics (simulation results). Yet, using the 2 × 2 × 2 mm^3 reference values led to normal stresses of about 100 MPa and about 100 MPa higher longitudinal and transverse stresses.

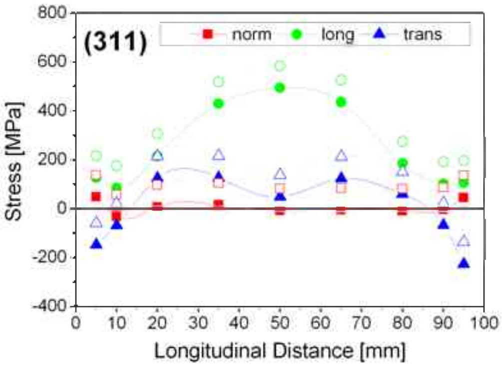

Figure 66: Residual stresses within a water-quenched model plate (100 × 60 × 6 mm^3) cut from the turbine disc (plate "B") determined with the (311) reflection. The reference cube had a size of 4.0 × 4.1 × 4.2 mm^3, and was measured with a 3 × 3 × 3 mm^3 gauge volume (filled symbols) as well as with a 2 × 2 × 2 mm^3 gauge volume (open symbols).

The results of the reflections (220), (200) and (111) for the model plate **B** are given in Figure 67. Contrary to model plate **A**, the longitudinal and transverse stress components obtained with (311) and (220) were nearly identical, only the normal component was slightly negative for (220). Thus, the (200) and the (220) normal stresses did not exhibit opposing algebraic signs like in plate **A**. The normal stresses of (200) varied between –100 MPa and –200 MPa, which was significantly closer to zero than the normal stresses in the model plate **A**. The level of the longitudinal and transverse component for (200) were just slightly below the corresponding levels of the (311) and (220) reflections. Using a 3 × 3 × 3 mm^3 gauge volume for the d_0 measurement, the residual stress state obtained with the (111) reflection did only correspond qualitatively to the one determined with the (311) reflection as shown in Figures 66, 67c. Both reflections are commonly regarded as appropriate to reflect macrostresses and thus the obtained stresses should also agree quantitatively. For the (111) reflection the normal stresses were –200 MPa and the longitudinal and transverse components were about 100 MPa below the stresses obtained with (311).

Looking at the stress results based on the 2 × 2 × 2 mm^3 d_0 value presents a somewhat modified image. The (111) and (311) results were still not alike, but now the (111) normal stresses were nearly perfectly zero and the (311) reflection showed non-plane stress conditions with positive normal stresses. The normal component derived from the (200) and (220) reflections were also unlike the ones that were calculated with the 3 × 3 × 3 mm^3 d_0 value. The (200) normal stress was about zero and the (220) normal stress was about 100 MPa. For all four reflections the longitudinal and transverse stress components were shifted by about 100 MPa to higher values for the d_0 value obtained with a 2 × 2 × 2 mm^3 gauge volume. Altogether, these results of the model plate **B** did support the idea of an influence of type II microstrains on the determined residual stress values.

Consequently, the results did not clearly point out which gauge volume was more appropriate for the measurements. The average of all 8 reference measurements was not considered as appropriate either, because the normal stresses were increased even more, but according to simulation results they should be zero at least for (311) and (111).

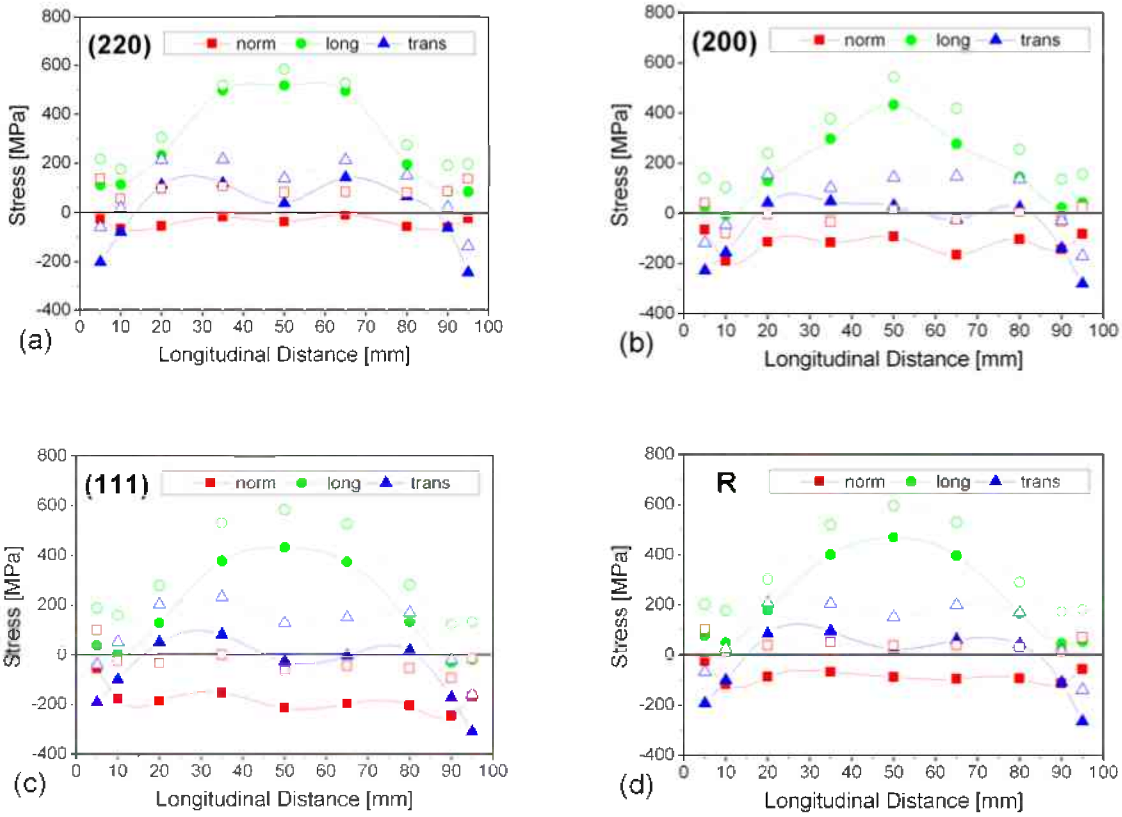

Figure 67: Residual stresses within a water-quenched model plate (100 × 60 × 6 mm³) cut from the turbine disc (plate "B") determined with the (a) (220), (b) (200), and (c) (111) reflection and (d) Rietveld type analysis of all four reflections The reference cube had a size of 4.0 × 4.1 × 4.2 mm³, and was measured with a 3 × 3 × 3 mm³ gauge volume (filled symbols) as well as with a 2 × 2 × 2 mm³ gauge volume (open symbols).

A second measurement of plate **B** was performed with another reference cube to check for the significance of the cube size. It was cut form the edge of the model plate **B** and was divided further into small cuboids to ensure the relaxation of all macrostresses. The lattice parameter was determined along the three main directions and the average of these measurements was used as a d_0^{hkl} for the strain calculations. The plate itself was measured with a gauge volume of 3 × 3 × 3 mm³ in order to capture as much of the thickness as possible still ensuring the whole gauge volume was inside the sample. The obtained stress results are shown in Figures 68 - 69.

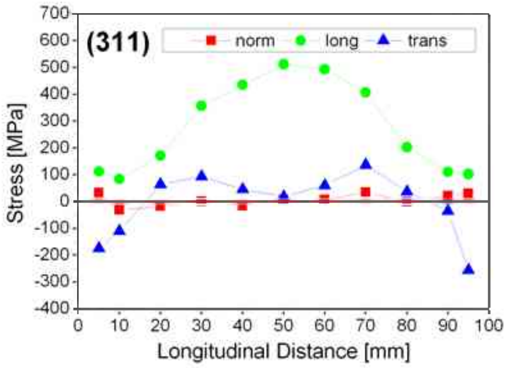

Figure 68: Residual stresses within a water-quenched model plate (100 × 60 × 6 mm³) cut from the turbine disc (plate "B") determined with the (311) reflection. The reference cube, which was split up further into small cupons, had a size of 4.0 × 4.1 × 4.2 mm³, and was measured with a 3 × 3 × 3 mm³ gauge volume.

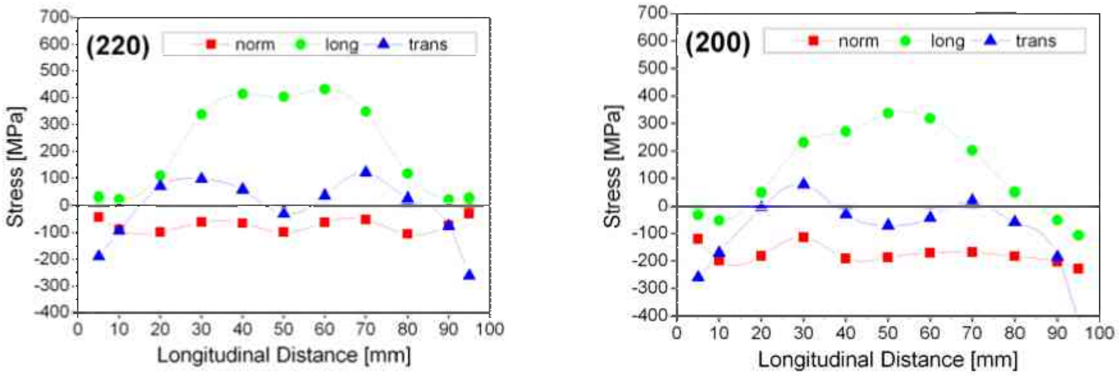

Figure 69: Residual stresses within a water-quenched model plate ($100 \times 60 \times 6$ mm^3) cut from the turbine disc (plate "B") determined with the (220) and (200) reflection. The reference cube, which was split up further into small cupons, had a size of $4.0 \times 4.1 \times 4.2$ mm^3, and was measured with a $3 \times 3 \times 3$ mm^3 gauge volume.

The normal and longitudinal component for the (311) stress state are identical to the results obtained with the undivided reference cube using the large gauge volume, with zero normal stresses and longitudinal stresses up to 500 MPa. This gives an indication that the initial results for (311) determined with the $3 \times 3 \times 3$ mm^3 gauge volume were correct. Only the transverse component was slightly (50 MPa) lower for the divided cube. Again, both the (220) reflection and the (200) reflection led to negative normal stresses. The transverse stresses are close to zero for (200) and maximal 100 MPa for (220).

Altogether the stress states obtained for the divided cube were similar to the initial results. This fact was taken as a proof that the initial size of the reference cube was already small enough and that a further reduction did not significantly change the stress results.

6.7.1.3 Comparison and Discussion of the Results for the Quenched Model Plates

The measurements on plate **A** and **B** showed that the different microstructures led to different residual stresses, although the geometrical dimensions as well as the heat treatment and thus the thermal gradient were identical for the two plates. The differences were most obvious for the longitudinal component, where the model plate **B** showed about 150 to 200 MPa higher stresses than the pre-forged material. In both cases the level of the normal and the transverse component was much lower than σ_l and did not show large changes. No differences could be observed in the general trend of the stress components neither for the two plates nor for the different measurements on plate **B**. The longitudinal component was always the highest, and increased steadily from the edge towards the middle following a nearly parabolic line. The level and algebraic sign of the normal component was very different for the individual measurements, but it was reasonably constant except for the rim region of 10 mm. The level of the transverse component was between that of the longitudinal and normal component for all measurements and always showed a minimum in the middle of the plate and a pronounced decrease to negative values close to the rim.

In all cases the shape of the residual stress components were symmetric, which legitimised a finite element model that was reduced to an eighth ($3 \times 30 \times 50$ mm^3) of the original size. The symmetry of the residual stress state in all model plates showed that the direction of the insertion into the quenching water did not influence the residual stresses. Thus, the cooling procedure could be regarded as homogeneous all over the plate.

Despite the different results of the four reflections, it was clear that the model plate **A** could not be regarded as representative for the forged turbine disc and so the neutron measurements on plate **B** had to be employed to fine tune the simulation model. Yet, these results demanded further investigations as two individual measurements on plate **B** did not lead to identical results for the observed reflections. Additionally, the fact that different gauge volume sizes for the reference cube measurement resulted in different stress results using the same lattice measurements of the plate shows that further research is needed to check the influence of gauge volume size on the measured diffraction angle in materials with stronger absorption than e.g. Al or Fe. Such an influence could also be responsible for the fact that the two reflections (311) and (111) with significantly different diffraction angles, which are both considered as appropriate to reflect macrostresses [75, 94, 95], did not lead to similar stress results. This inconsistency was especially obvious for the normal stress component, which was expected to be zero, but was partly around –200 MPa and partly around +100 MPa. As none of the three stress results of plate **B** coincide for the four reflections, possible measurement errors had to be examined. First of all, a slight variation of the alignment of the plate in the neutron beam cannot fully be excluded, because for different measurement series the residual strain components determined with the same lattice reflection did not fully match to each other. Furthermore, a misalignment of the reference cube had to be taken into consideration. Despite all efforts, the $3 \times 3 \times 3$ mm^3 gauge volume might sometimes not be filled completely with the cube material and then cause erroneous lattice values. The reason for this could be small microstructure variations, like larger grains or localized textures that influence the intensity curves and thus the determination of the sample centre. The $2 \times 2 \times 2$ mm^3 gauge volume did not capture the whole volume of the reference cube like the larger gauge volume and this could result in even worse statistics for the grains. Nevertheless, the $2 \times 2 \times 2$ mm^3 results seem to follow the expectations from continuum mechanics closer for some reflections, e.g. (111). Consequently, the obtained d_0 values seem to represent the statistical variation of the measurement, which unfortunately had a large influence on the stress results and even led to different algebraic signs. Of course microstrains could also influence the stress results. This is definitely the case for (200), which was found to accumulate large microstrains in the plastic regime. However, the inconsistency of the three results for a single reflection strongly supports the idea of a misalignment of the reference cube and maybe small misalignments of the plate itself did add up to the inaccuracy of the reference measurement.

An erroneous d_0 value is known to be reflected in the hydrostatical stress component only. The deviatoric stresses are insensitive to the chosen reference value. Therefore, the deviatoric and hydrostatic stress components were determined for the three measurements on plate **B**. As can be seen in Figure 70, the deviatoric stresses are nearly identical for the different measurements. The longitudinal deviatoric stress was additionally reasonably identical for all four reflections with a maximum level of 300 MPa. Major differences can only be observed for the normal deviatoric stress of the (111) reflection, which can most likely be attributed to the large measurement error connected with (111) for the used wavelength. The hydrostatic stress for the two individual measurements with a $3 \times 3 \times 3$ mm^3 gauge volume were identical (Figure 71), which strongly indicates that the (311) measurement with the large d_0 gauge volume offer the smallest measurement uncertainty and can thus be used for a comparison with simulation results.

The measurements on plate A and B showed that the different microstructures led to different residual stresses, although the geometrical dimensions and the heat treatment, and thus the thermal gradient were identical for the two plates. The model plate **B**, machined from the forged turbine disc showed about 150 to 200 MPa higher stresses than the pre-forged material, but the general trend of the residual stress components was the same. The longitudinal component was always the highest and increased from the edge towards the middle following a nearly parabolic line. The level and algebraic sign of the normal component was very different for the individual measurements, but it was always fairly constant except for the rim region of 10 mm. The level of the transverse component was between the level of the longitudinal and normal component for all measurements and always showed a minimum in the middle of the plate.

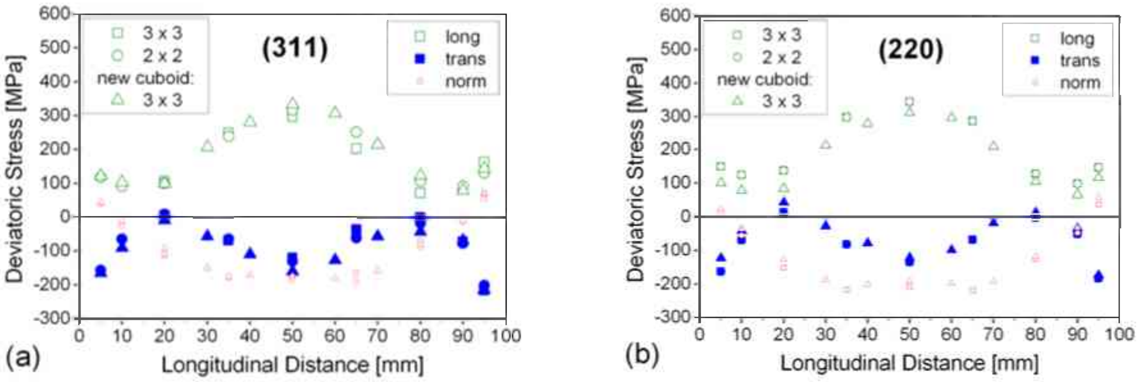

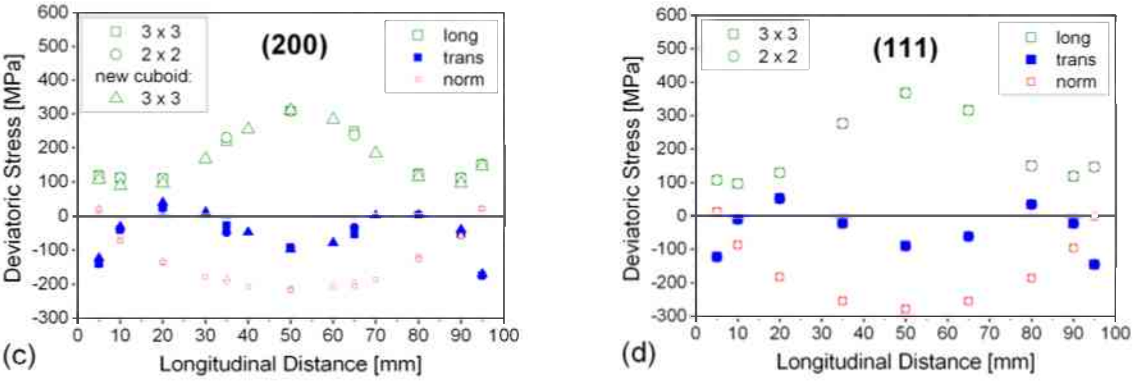

Figure 70: Deviatoric stresses within a water-quenched model plate (100 × 60 × 6 mm³) cut from the turbine disc (plate "B") determined with the (a) (311), (b) (220), (c) (200), and (d) (111) reflection. Two different measurements with three different reference measurements are depicted: For □ the reference cuboid was measured with a 3 × 3 × 3 mm³ gauge volume, for ○ the reference cuboid was measured with a 2 × 2 × 2 mm³ gauge volume, and for △ the reference cuboid was machined directly from the plate and further split up into small cubes measured with a 3 × 3 × 3 mm³ gauge volume.

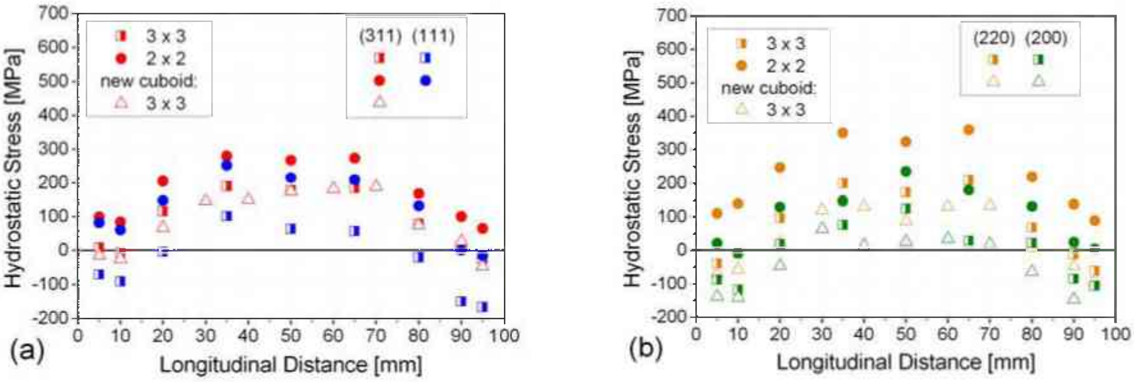

Figure 71: Hydrostatic stress determined in the model plate "B" determined with the (a) (311) and (111), (b) (220) and (200) reflection. Two different measurements with three different reference measurements are depicted: For ◨ the reference cuboid was measured with a 3 × 3 × 3 mm³ gauge volume, for ● the reference cuboid was measured with a 2 × 2 × 2 mm³ gauge volume, and for △ the reference cuboid was machined directly from the plate and further split up into small cubes measured with a 3 × 3 × 3 mm³ gauge volume.

6.7.1.4 Residual Stresses in the Model Plate - Aged Condition

The model plate **A** was annealed after the neutron measurement and examined again with the four reflections (311), (220), (200), and (111). As SANS (Small Angle Neutron Scattering) measurements suggested the presence of a small amount of precipitates of a size of 6 nm even in the water-quenched condition, a possible influence of the particles on the residual strain measurement could not be excluded. If the deviation of the normal component from zero stress was at least partly caused by the presence of coherent particles, then this effect would increase in the annealed condition. As the partly coherent γ'' precipitates have a defined orientation relationship to the matrix, it is possible that they influence the microstrains.

A gauge volume of $2 \times 2 \times 2$ mm^3 was chosen to examine the annealed model plate and its reference sample. The reference cube with a size of $4 \times 5 \times 6$ mm^3 was cut from a dummy plate that was annealed and subsequently quenched together with the model plate.

Figures 72 - 73 illustrate that the results show no enhancement of the deviation for the normal stresses for (311). In fact the residual stresses were all negative for each of the four reflections. Consequently, the average of all four reflections, which corresponds roughly to a Rietveld analysis, did not fulfil the demands for a mechanical equilibrium either, as all stress components were negative. Yet, this is in accordance to the very first measurements on an annealed turbine disc, where all stress components of the reflection (311) were negative too. Nevertheless, the stress state determined with the (311) reflection was very debatable, because the normal strain exceeded the longitudinal and transverse strain component, which was not the case for any other analysis of the model plates. The reason for these results could not be clarified and consequently, the residual stress determined with (311) in the annealed model plate was not further considered in this work.

The (220), the (200) and the (111) reflection showed that the magnitude of the residual stresses in the annealed plate (quenched from 620 °C) was much lower than the magnitude of the residual stresses in the as-forged plate that was quenched from 960 °C. The same applied for the deviatoric stresses, which did not exceed +150 MPa or –150 MPa. However, only the transverse deviatoric stresses were approximately uniform for all four reflections.

Although the stress results of the annealed plate were not completely satisfying, the following conclusions can be drawn:

- The presence of a considerably higher amount of partially coherent precipitates did not introduce significant type II microstrains. If considerable microstrains would be present, then the two reflections (220) and (200) that are sensitive to microstrains would show opposing trends and would clearly vary from the (311) and (111) results.
- The residual stresses in the annealed plate seem to be much smaller than the stresses in the as-forged plate. Obviously, the difference of the starting temperature (ΔT = 960 °C - 620 °C = 340 °C) has a pronounced effect on the generated residual stresses.

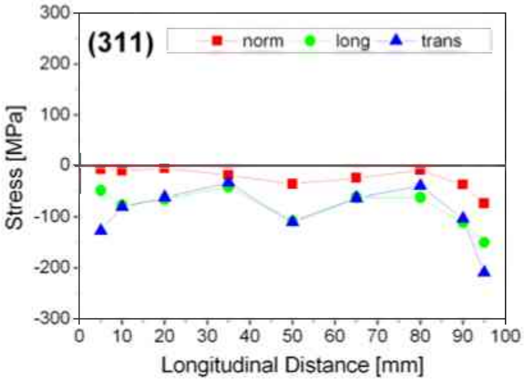

Figure 72: Residual stresses within an aged model plate ($100 \times 60 \times 6$ mm^3) cut from pre-forged material determined with the (311) reflection. The reference cube had a size of $4 \times 5 \times 6$ mm^3, and was measured with a $2 \times 2 \times 2$ mm^3 gauge volume.

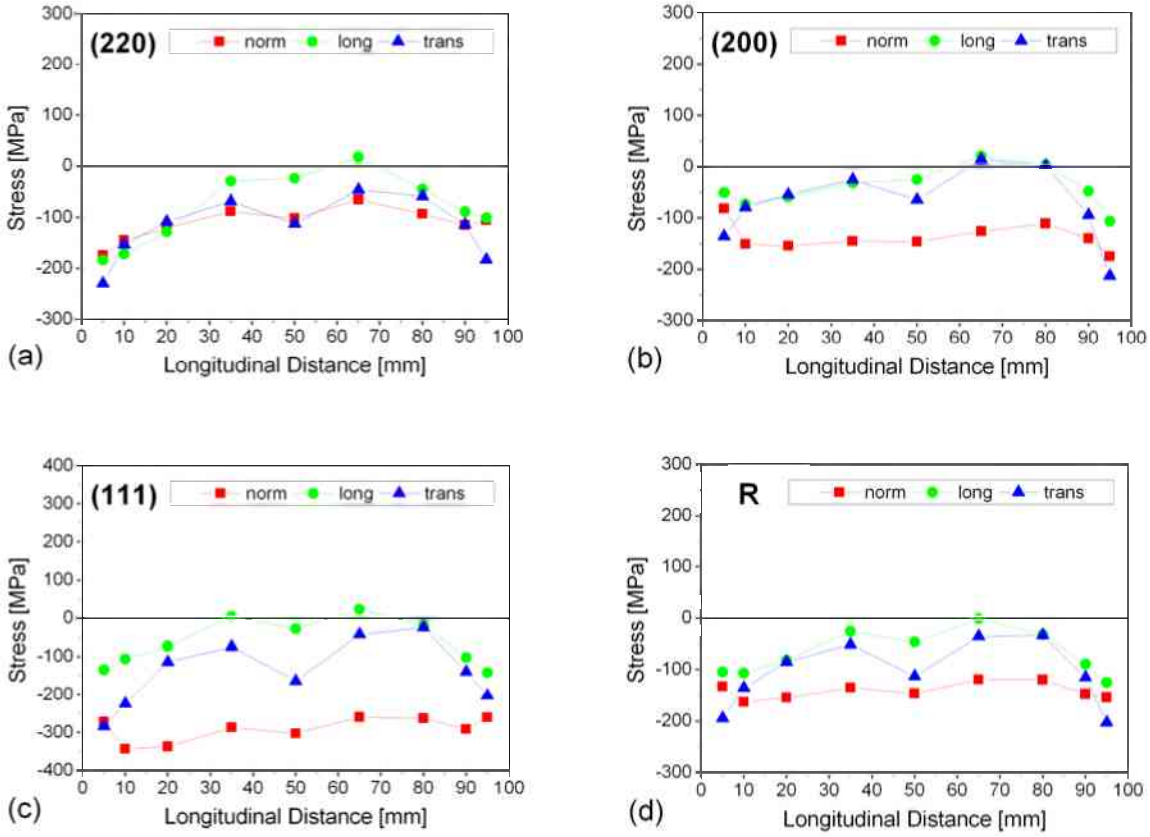

Figure 73: Residual stresses within an aged model plate (100 × 60 × 6 mm^3) cut from the pre-forged material determined with the (a) (220), (b) (200), and (c) (111) reflection and (d) Rietveld type analysis of all four reflections. The reference cube had a size of 4 × 5 × 6 mm^3, and was measured with a 2 × 2 × 2 mm^3 gauge volume.

6.7.1.5 Discussion of the Measurements on the Model Plates

In the end, only the results of the model plate **B** were considered as appropriate to optimise the FE model of the turbine disc. The model plate **A** was cut from the pre-forged material and therefore the grain size did not match the grain size of the forged disc. As no other differences between plate **A** and **B** such as chemical composition, texture or the amount of precipitates could be determined, the differences of the measured stress states were attributed to the different grain sizes.

The residual stress state within plate **B** was evaluated three times. Once, the reference cube with a size of 4.0 × 4.1 × 4.2 mm^3 was measured with a gauge volume of 2 × 2 × 2 mm^3 and once, with a gauge volume of 3 × 3 × 3 mm^3. Later, the reference cube was further cut up into small cubes and reassembled to be measured with a gauge volume of 3 × 3 × 3 mm^3. The measurements with the large gauge volume led to comparable stress results for the (311) reflection, which strongly indicated that the original cube size was sufficiently small to fully relax the macrostresses. Therefore, the stress results illustrated by the full symbols in Figure 66 were employed to evaluate and optimise the FE model.

6.7.2 Turbine Discs – Quenched Condition

6.7.2.1 Radial Symmetry

At first, the aim was to characterise the overall stress state within a water-quenched disc and to draw a comparison with the corresponding FE calculation. The first task was to clarify the angular homogeneity of the residual stress state within one disc. Therefore, the measurement locations were placed along a line parallel to the radius at relatively large distances at three cross sections of the disc within the disc B3. As a reference value the average of the lattice distances in three directions of one cube ($4 \times 5 \times 6$ mm^3) cut at the location A (see Figure 60) was used. The residual stresses determined with the (311) reflection are shown in Figure 74.

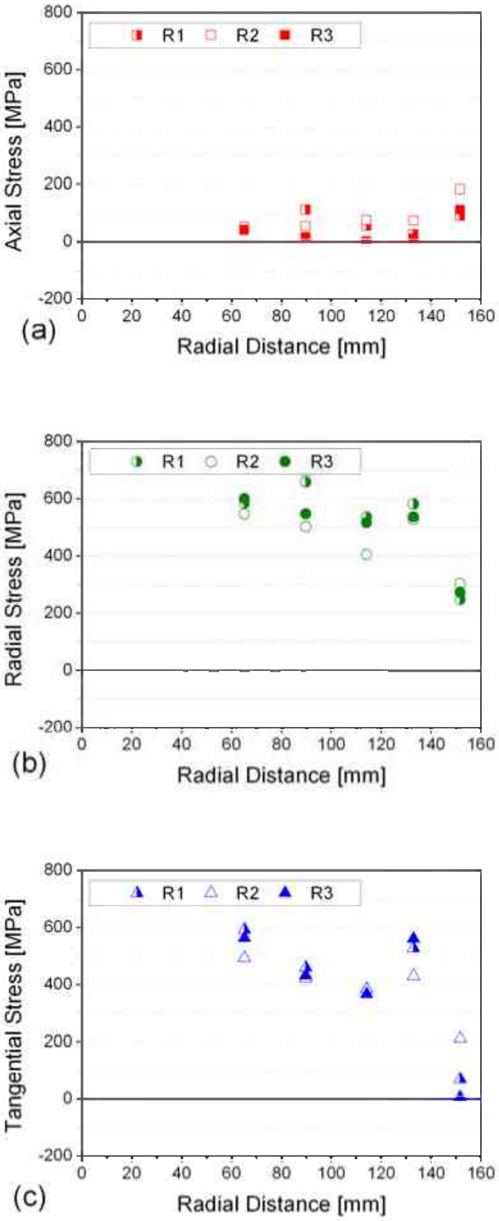

Figure 74: Residual Stresses along three radii in a water-quenched turbine disc. (a) axial, (b) radial and (c) tangential stress component. For the measurement the (311) reflection was used. The typical measurement error is 50 - 60 MPa, which cannot be resolved in the graph as it is in the size of the symbols.

The results along the radii illustrate that the stress state indeed seems to be quite symmetric despite the fact that the disc was put into the water in an upright position, leading to a quench-induced asymmetry. This was a first check whether a 2D finite element simulation is sufficient to model the whole disc.

However, two of the three scans show some ambiguity concerning the axial stress component. According to the finite element simulations the axial component should be zero over large parts of the cross section except for the rim region. Nevertheless, axial stresses of up to 100 MPa were determined in the thin section of the disc B3, which is above the average measurement error of ±55 MPa. This result provoked further examinations.

6.7.2.2 Homogeneity of the Stress State Between Different Discs

In order to verify the homogeneity of the stress state between different discs two more water-quenched discs of the same lot as disc B3 were examined. Again the peak (311) was used. For the discs B3 and B4 the same reference cube with a size of $4 \times 5 \times 6$ mm^3, cut from location "R" (Figure 60), was used. For disc B5 three reference cubes were cut directly at the location of the measurements (along scan B: R = 102 mm). They had a size of $4.0 \times 4.1 \times 4.2$ mm^3. For all three discs the alignment is based on the location of the edge at point **X** shown in Figure 9. Then the scan line was assumed to be parallel to the disc radius.

The stresses calculated from the measured strains in the discs B3, B4, and B5 are compared in Figure 75. Although, some differences in the residual stress values can be observed, the tendencies of the residual stresses and the magnitudes of the levels are equal. Therefore, one disc is regarded as representative for the residual stress state within discs with the same geometry that were quenched in water. The results of the scans along the horizontal line of the disc can be summarized as follows:

- There is a stress maximum of about 600 MPa for the radial and tangential component at approximately R = 140 mm.
- The axial component has its maximum at approximately 150 mm, where the radial and tangential stresses start to decrease rapidly towards the rim.
- There seems to be a decay of the radial and tangential component in the thinner section of the disc between R = 90 mm and R = 130 mm. However, the amount of this decrease in stress is different for the different discs and is not even obvious for all measurements.
- The radial stress component exceeds the tangential component by approximately 100 MPa in most examined locations within the disc.
- The axial component remains on the same level close to zero stress except for the rim region.
- The measurement error derived from the peak fitting procedures of the reflection (311) was 50 - 60 MPa for the stresses in the disc and 20 - 30 MPa for stresses in the model plates.

The stresses in disc B4 are generally higher than in the other discs, which can most likely be attributed to the fact that the reference value was determined on a cube taken from disc B3. Obviously, the reference cube has to be taken from the same disc to avoid erroneous stress results, although the discs from the same lot seem to be homogeneous concerning their microstructure, their chemistry and their deformation history.

As the scan along a radius follows a horizontal line the measurement points are not located in the middle of the particular section of the disc. Yet, the line of the maximum stress is located in the middle of the cross section of the disc according to finite element simulations. Therefore, the stress values determined by neutron diffraction only represent the maximum stress levels at a radius of approximately 150 mm but around R = 100 mm, the gauge volumes are situated below the maximum stress level.

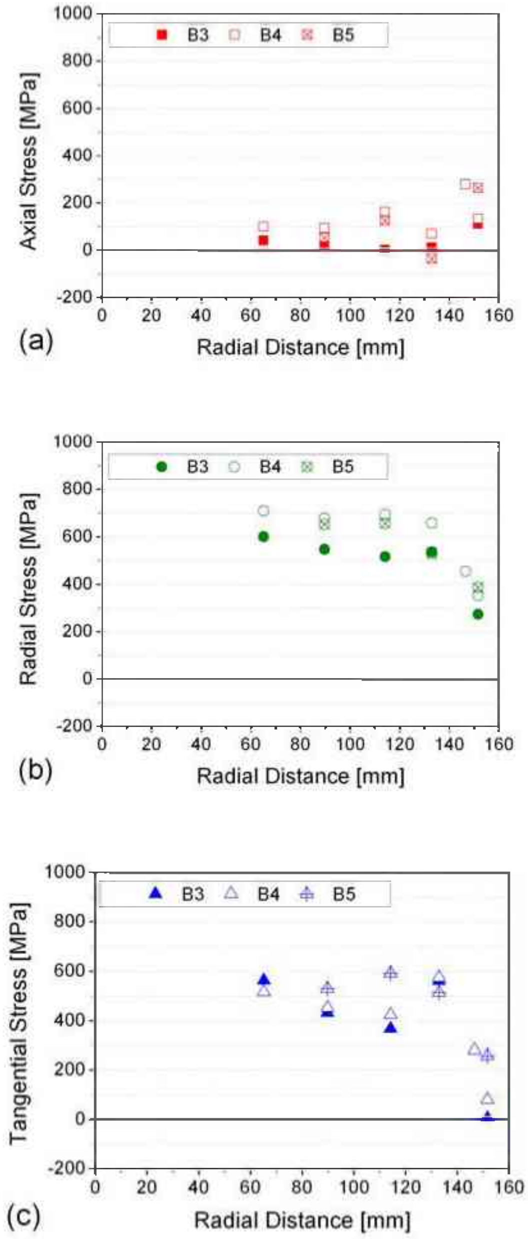

Figure 75: Residual stresses along the radius within three different water-quenched discs B3, B4, and B5; (a) axial, (b) radial and (c) tangential stress component. The typical measurement error is 50 - 60 MPa, which cannot be resolved in the graph as it is in the size of the symbols.

6.7.2.3 Residual Stress Along the Thickness of the Disc

The fact that the residual stresses determined by the measurements do not show a pronounced decrease in the thin section of the disc, motivated a more detailed examination of the stress along the thickness of the disc. As the stress gradient is relatively steep in the thin section, it is most likely that a slight misalignment can lead to large differences in the absolute stress values. Therefore, the alignment was then based on intensity curves determined directly at the edge of the scan line.

Altogether, four different scan lines parallel to the disc axis were examined: At R = 89 mm, R = 102 mm (Scan B), R = 123 mm (Scan C), R = 146 mm (Scan A), and R = 152 mm. Initially, the disc radii R = 89 mm (Figure 76) and R = 152 mm (Figure 77) were analysed at three measurement locations with gauge volumes of $3 \times 3 \times 30$ mm^3 and $3 \times 3 \times 14$ mm^3, respectively. However, the data provided by these scans proved to be too sparse to illustrate the actual distribution of the stress along the thickness. In addition, the positioning accuracy is crucial and, in some cases, was found to be insufficient when the number of performed intensity scans was too low.

The scan in at a disc radius of R = 89 mm and R = 102 mm is shown in Figure 76. It illustrates that the calculated stress results at different radii (R1 - R3) and within different discs are comparable. The stress curves of the disc B5 seem to be shifted to the top edge, which most likely indicates some uncertainty of the sample alignment, but in this case the maximum stress level is unaffected.

Near the rim of the disc at a disc radius of R =152 mm the residual stresses along the three radii R1, R2 and R3 are very similar (Figure 77). The results of the disc B5 showed a significant offset compared to the results of the discs B3 and B4. Most likely this can be attributed to a shift of the strain components against each other due to some misalignment of the sample. Here, the effect of the positioning uncertainties of the disc B5 prevails the effect of a reference value from another disc for B4.

Later the number of points on the scan line was increased to 6 and the gauge volume was reduced to $2 \times 2 \times 30$ mm^3 and $2 \times 2 \times 14$ mm^3, respectively. Additionally, the edge of the disc was determined directly at the radial position of the particular measurement. This was done by recording the neutron intensity curves (cf. Chapter 6.4.1) at the disc radii of R = 102 mm, R = 123 mm and R = 146 mm of the disc B5. Figure 78 shows the strain curves for the three principal directions. At the radius R = 146 mm the strain curves are slightly shifted against each other, which indicates uncertainties of the alignment. However, at R = 123 mm the location of the strain curves are not shifted (Figure 78b) and consequently the resulting residual stresses lead to zero axial stresses and the stress maxima of the radial and tangential component are very similar (Figure 79).

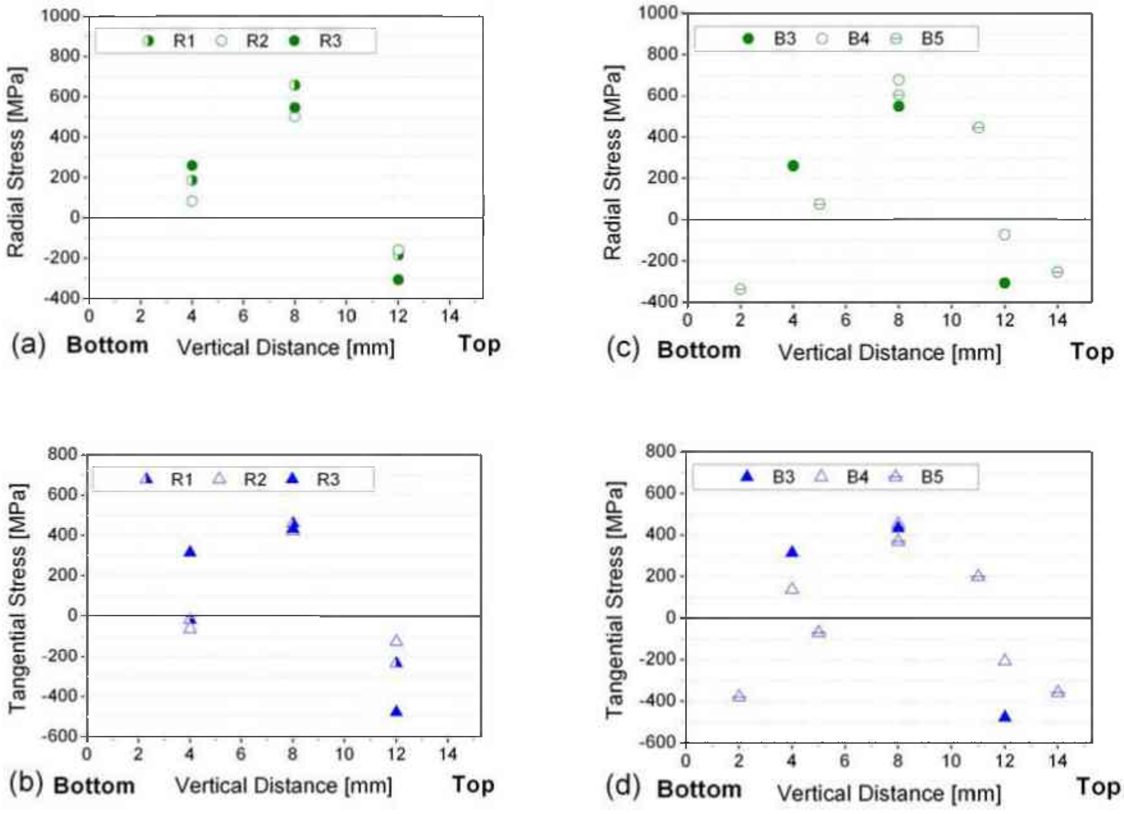

Figure 76: Residual stresses determined by neutron diffraction at a disc radius of R = 89 mm: (a) radial and (b) tangential component in the turbine disc B3 for three radii R1, R2, and R3; and (c) radial and (d) tangential component in three different discs B3, B4, and B5. The typical measurement error is 50 - 60 MPa, which cannot be resolved in the graph as it is in the size of the symbols.

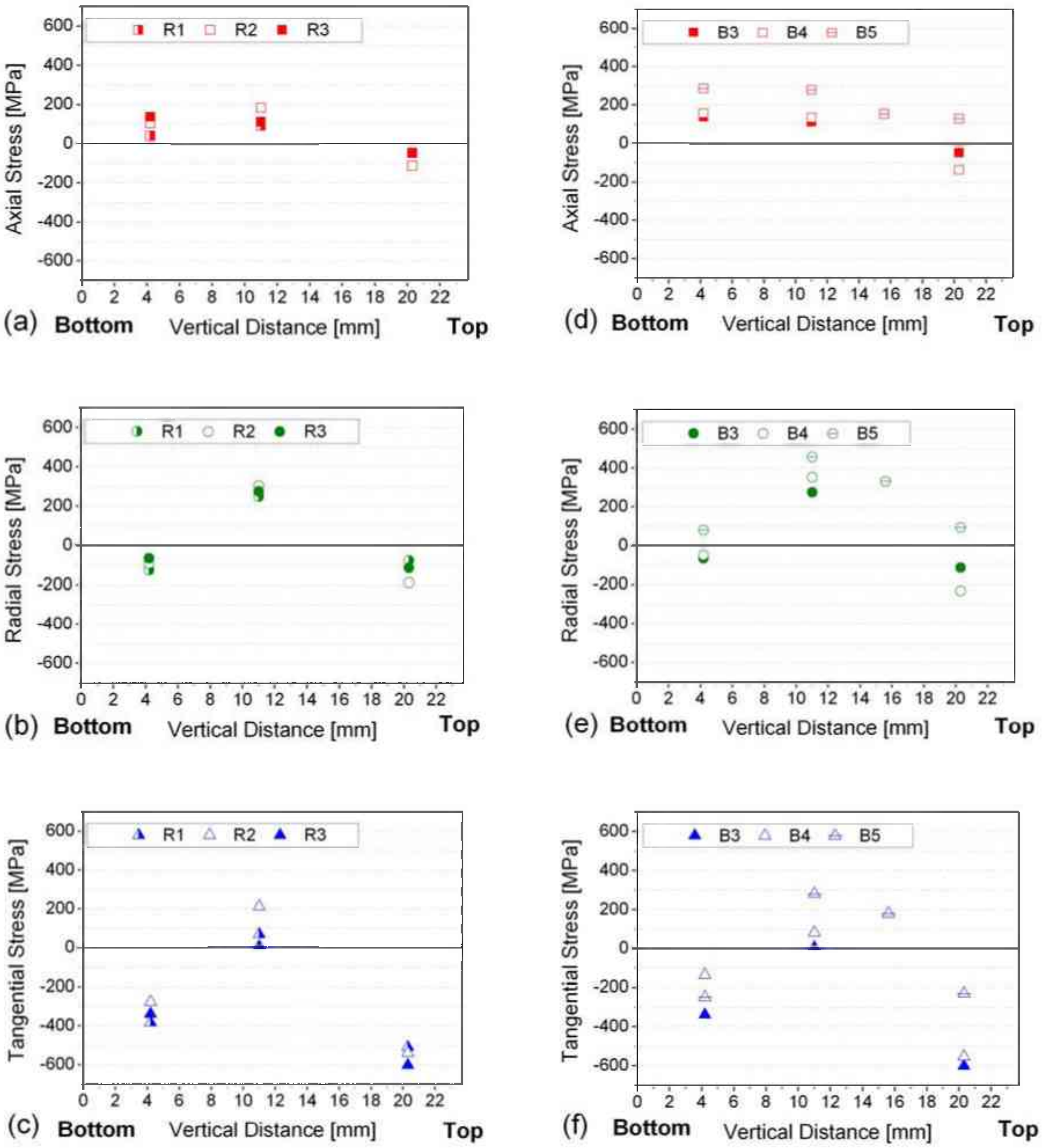

Figure 77: Residual stresses determined by neutron diffraction at a disc radius of R = 152 mm: (a) axial, (b) radial, and (c) tangential component in the turbine disc B3 for three radii R1, R2, and R3; and (d) axial, (e) radial, and (f) tangential component in the discs B3, B4 and B5. The typical measurement error is 50 - 60 MPa, which cannot be resolved in the graph as it is in the size of the symbols.

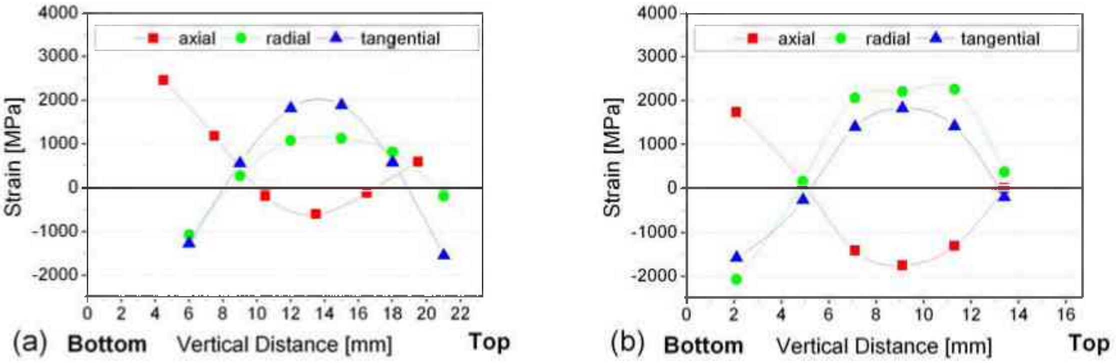

Figure 78: Residual strains determined by neutron diffraction in the turbine disc B5 along a scan line parallel to the disc axis at a disc radius of (a) R = 146 mm and (b) R = 123 mm.

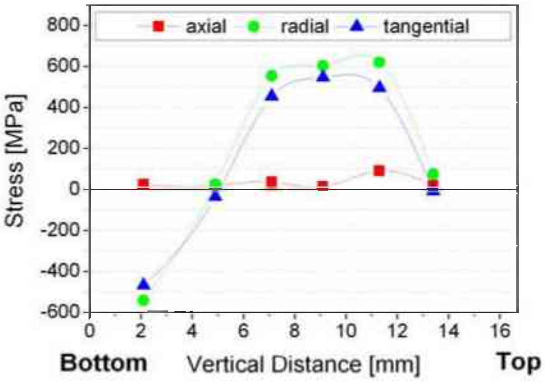

Figure 79: Residual stress state determined by neutron diffraction in the turbine disc B5 along a scan line parallel to the disc axis at a disc radius of R = 123 mm. The measurement error was between 50 MPa and 60 MPa.

The results of the scans along the thickness of the disc can be summarized as follows:

- The maximum stress level in the thin section of the disc (R ≈ 100 mm) reached approximately 600 MPa for the radial component and 400 MPa for the tangential component.
- The course of the radial and tangential stress component follows a parabolic shape for each scan.
- The results at the three radii within the disc B3 are comparable. This does also apply to the stress results determined within the discs B3, B4 and B5 at a disc radius of R = 89 - 102 mm.
- The results of disc B3 and disc B4 are comparable.
- The axial stress was close to zero in the scans at R = 89 mm, R = 102 mm, and R = 123 mm.
- Along R = 146 mm and R = 152 mm all the stress components showed an influence of the rim, which resulted in a strong decrease of the radial and tangential stress and an increase of the axial component.

Remaining deviations from the predictions made with DEFORM calculations caused the examination of the disc B5 with another diffraction peak to compare the results with the previous measurements that were all conducted with the peak (311) as it is generally recommended for macrostress determinations.

The results of the scans along R = 146 mm and R = 102 mm with the peak (220) are shown in Figures 80 - 81. Contrary to (311) the axial stress along scan B (R = 123 mm) is now negative, but the radial and tangential components show the same trend and the magnitudes are similar. Again, the radial component exceeds the tangential one. The results along scan A (R = 146 mm) are more surprising as the axial stress is zero in the centre but showed an asymmetric trend across the thickness of the disc. Again, this result can most likely be attributed to a small shift of the individual strain components against each other due to some misalignment of the disc. Figure 80a shows that the locations of the maxima of the strain components are not identical.

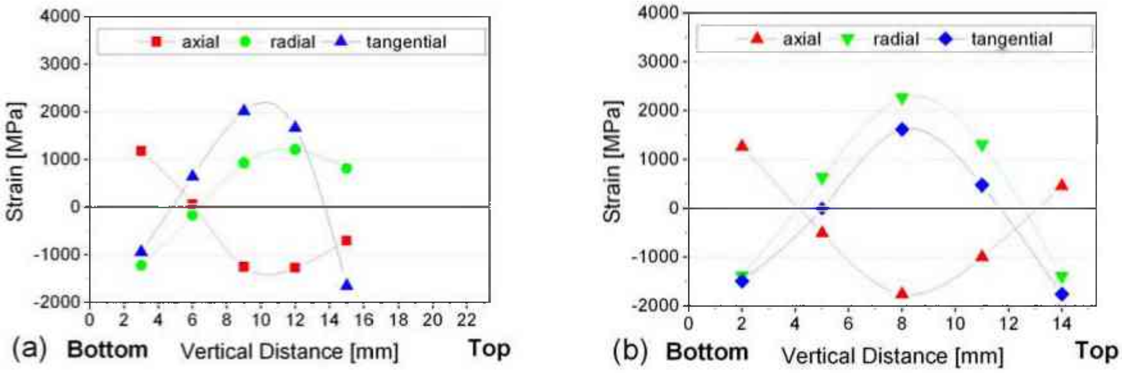

Figure 80: Residual strain determined with the peak **(220)** in the water-quenched disc B5 at two disc radii: (a) R= 146 mm and (b) R = 102 mm.

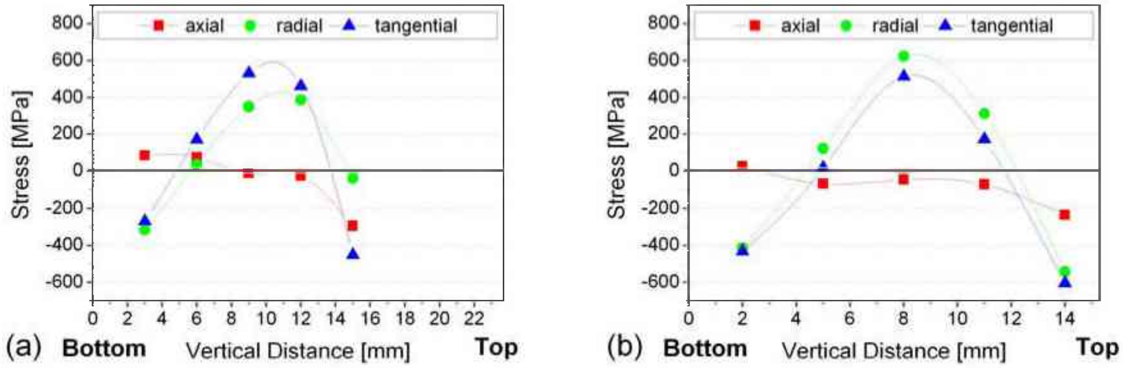

Figure 81: Residual stress determined with the peak **(220)** in the water-quenched disc B5 at two disc radii: (a) R= 146 mm and (b) R = 102 mm.

As the calculated stresses have no axial component in the disc except for the region near the rim, it is striking that only the stresses along R3 are actually reflecting this two-axial stress state (Figure 74). The others show positive axial components, whose magnitude is well above the measurement error of approximately 55 MPa. However, the simulation program DEFORM offers the possibility to extract elastic strain as well. Comparing these strain curves to the strain values derived from the measurements in disc B3 suggests that the disc was slightly misaligned. For an estimation of the trend of the strain along the thickness of the disc the number of measurements is far to small. Nevertheless, there are some hints further pointing to the explanation of a misalignment.

Eventually, a scan with higher resolution (gauge volume $1 \times 1 \times 30$ mm^3) was performed on the disc B2. This scan at the thinnest section of the disc (R ≈ 89 mm), where the thickness is 15.4 mm according to FE simulations, showed that the curve of the FE results can be followed more or less. For this scan a gauge volume of $1 \times 1 \times 30$ mm^3 was used and a step size of 0.5 mm. Contrary to the measurements presented above, the sample edge was determined directly at the disc radius R = 89 mm (Figure 82). This assured good positioning accuracy of the gauge volumes with respect to the sample edge even if the whole disc was not perfectly vertically aligned as shown in Figure 63.

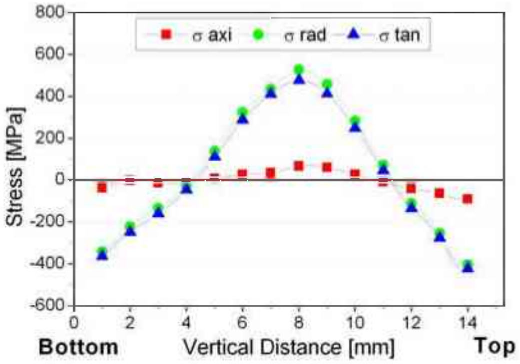

Figure 82: Residual stress in the water-quenched disc B2 determined with the peak (311)and a gauge volume of 1x1x30 mm³ at a disc radius of R= 100 mm.

6.7.3 Residual Stresses in the Turbine Disc – Annealed Condition

The turbine disc B4 was annealed and subsequently cooled on air and consequently renamed D4. The reference value was determined on a cube ($4 \times 5 \times 6$ mm³) cut from the edge of the disc. For all measurements a gauge volume with a 3×3 mm² cross section was chosen. The radial and tangential strains shown in Figure 83 illustrate that the residual strains were much lower than in the water-quenched turbine disc, where the residual strains reached up to +2000 µε and –1500 µε, respectively. Although the temperature difference was equal, as both discs were cooled down from a starting temperature of 960 °C, the residual strains after air-cooling appear to be negligible. Taking the measurement uncertainty from the peak fitting procedure into account, the results show that in fact, the scatter of the tangential strains along the different radii exceeded the magnitude of the error of the strain values, which was typically $\Delta\varepsilon = 10^{-4}$. Consequently, the reduced cooling velocity proved to have a large effect on the residual stress state within the disc. Yet, any influence of the changed microstructure caused by the annealing process could not be verified.

Finally, the residual stresses after air-cooling proved to be too low to be determined with the desired accuracy. This observation confirmed the initial approach that only water-quenched samples can be examined satisfyingly with neutron diffraction, although some production steps of commercial turbine discs involve air-cooling as well. Consequently, only water-quenched samples were employed to evaluate the finite element model.

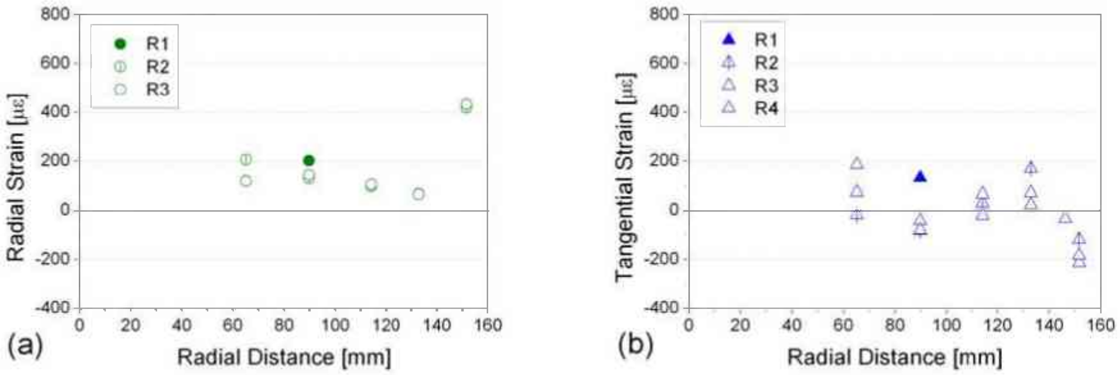

Figure 83: Residual Strains in an air-cooled, annealed turbine disc D4. R1, R2, R3, and R4 stand for the different radii where neutron measurements were performed. The typical measurement error was approximately 10^{-4}.

6.7.4 Residual Stresses in the Turbine Disc – Machined Condition

The water-quenched and machined turbine disc E3 was examined by neutron diffraction. It was machined at the Department for Mechanics A at the Technical University in Munich (Germany) to the shape shown in Figure 10. The residual stress state in this machined condition was determined along three scan lines parallel to the disc axis, because the stress gradients along the thickness are more important for the distortion due to material removal. Unfortunately, no reference cube could be examined due to limited beam time and so plane stress conditions were assumed in order to determine the residual stresses. As the machined disc is very thin (7.5 mm) compared to its diameter (approximately 160 mm), the assumption of plane stress conditions seemed well justified.

Figure 84 illustrates the residual stresses that remained in the disc after the machining procedure assuming plane stress conditions. The radial component did not exceed 100 MPa, but was still positive as in the as-forged condition. The tangential component varied between 0 MPa and –200 MPa for the Scans B and C, which were placed in the thin section of the disc (Figure 10). For scan A (at the rim) plane stress conditions did not correspond to the real stress state, because significant tensile axial stresses prevail near the rim according to finite element simulations. In the as-forged condition, the tangential stress component drops very quickly to large compressive stresses near the edge (Figures 74 - 75) and so the obtained values are very sensitive to the actual lateral position of the gauge volume. The position of scan A (R = 155 mm) is in fact the location where the tangential component turns to be negative. So even small changes of the scan radius of 0.5 mm or 1 mm can result in different stress results of several 100 MPa.

The fact does not change if plane stress conditions are imposed on the strain results. However, a direct comparison of the residual stresses in the as-forged and machined disc by calculating the stress difference does not make sense because of the largely position sensitive stress state. Due to the machining process, it cannot be guaranteed that the same position is examined in the as-forged and machined geometry. Figure 85 presents the deviatoric components of the residual stresses in the thin section of the disc in the as-forged and the machined geometry. This excluded the fact that plane stress condition had to be assumed for the machined condition and the as-forged stresses were based on an unstressed reference value. Nevertheless, the following conclusions can be drawn from the residual stresses in the machined disc: The removal of the material did relieve a great amount of stresses. Compared to the as-forged geometry the radial stresses drop from a level of about 500 MPa to about 100 MPa and the tangential stresses are more or less zero in the machined disc. In the rim part the tangential stresses are still negative.

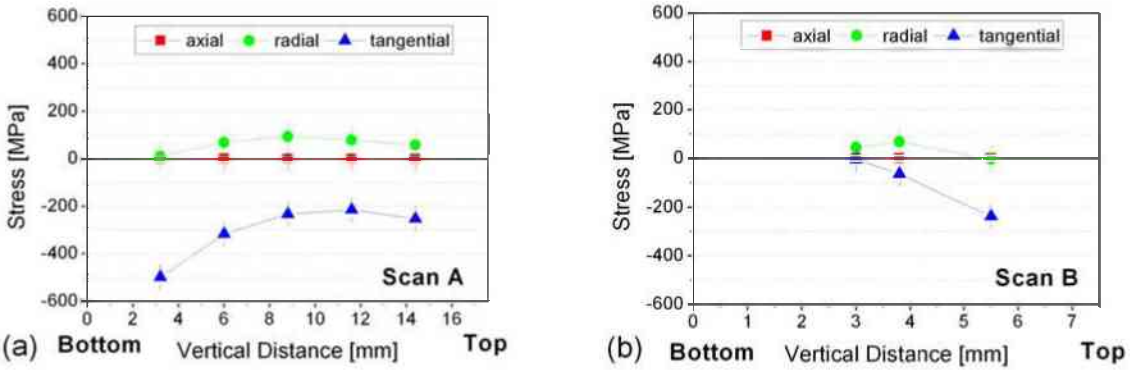

Figure 84: Residual stress state determined in the machined disc E3 along scan lines parallel to the disc axis at a radius (a) 155 mm (b) 104 mm.

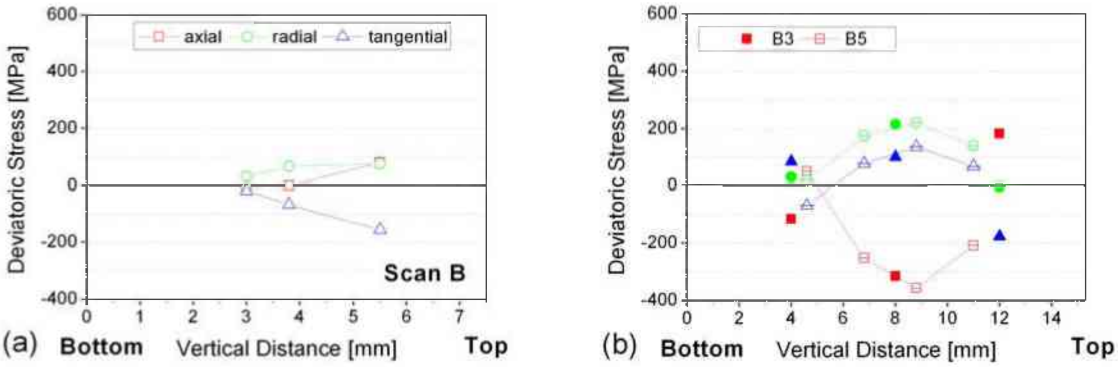

Figure 85: Deviatoric Stresses determined in (a) the machined, water-quenched disc E3 and in (b) two water-quenched non-machined discs: B5 (crossed symbols) and B3 (full symbols).

7 In-situ Tensile Tests

In-situ tensile tests were carried out to study the behaviour of diffraction lines under deformation within forged IN718 material. The general recommendation to use the (311) reflection for macrostress determination in cubic materials was verified for IN718. The elastic constants for IN718 were measured directly and compared to the literature data [86], which are based on the average of single crystal elastic constants for pure nickel and γ' precipitations. Initially, the tests were regarded to offer the possibility of a correction for microstresses, which can influence considerably the stress results determined by single peak diffraction [95]. The fact that the measured strains resulted in non-zero axial stresses in the turbine disc as well as the plate was attributed to the presence of significant microstrains, which adulterated the strain results. Thus, a major focus of the tensile test experiments was to extract microstrains from measured strains and to evaluate the influence of these microstrains on the results obtained from large engineering parts, where macrostresses have to be determined.

Microstrains of type II are also referred to as intergranular strains, they are dependent on the intrinsic elastic and plastic anisotropy of the material. The elastic anisotropy determines how the load is shared among the grain orientations and which orientation yields first. As the polycrystal is loaded into the plastic regime, certain grains are aligned such that the resolved shear stress reaches the critical value for slip before it is reached in other grains. Once slip has been initiated in certain grains, further deformation is accommodated plastically with little increase in the load supported by the grain. As these grains deform plastically, part of the elastic load they would have carried is transferred to the rest of the polycrystal because they remain at a stress corresponding to the critical resolved shear stress, while plastically hard grains are increasingly strained elastically [73. 94]. By measuring the lattice spacing of specific grain orientations as the polycrystal is loaded, these effects are first observed as deviations from the linear response under load and finally as residual strains after unloading. Thus residual intergranular strains are a consequence of plastic deformation.

The tensile tests were performed in a strain control mode by increasing the macrostrain stepwise and holding it constant during the diffraction measurements. The macroscopic load versus elongation curves were recorded by a load cell and an extensometer mounted directly on the cylindrical samples. Figure 86 shows a typical macroscopic stress-strain curve. The open symbols indicate the stress and strain levels at the measurement points. In the plastic regime the specimens were unloaded several times at different degrees of plastic deformation to record the remaining lattice strains in the unloaded condition. At very small deformations the increments between the unloadings were set very close in order to gain enough data points for a possible correction for residual microstrains. The maximum deformation was limited to 12% due to the maximum available extension of the extensometer and the diameter of the tensile test samples. Machining problems did not allow to the production of samples with a diameter below 5 mm. Initially, the load was fully removed after each loading cycle, but in a second series of measurement a nominal load of 500 N was used as the zero point to preclude any slight movement of the sample on loading or unloading. The unloading and reloading was performed stepwise for sample B5-2 only, due to the limited measurement time.

Altogether five samples were machined from a forged turbine disc and used for the in-situ tensile tests. Additionally, two samples of pure nickel were loaded in the same way to evaluate the influence of the coherent precipitates on the loading behaviour.

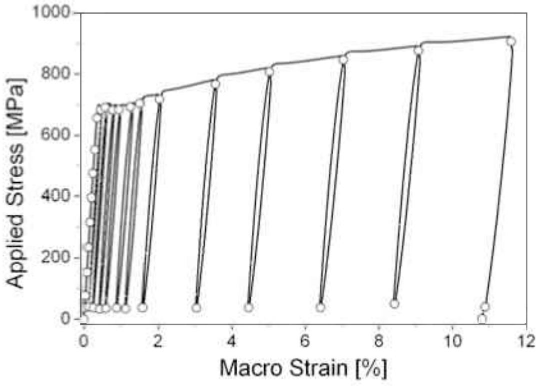

Figure 86: Macrostress strain curve indicating the measurement points of a sample machined from the forged, water-quenched IN718 turbine disc, receiving no further heat treatment.

7.1 Tensile Tests with Synchrotron Radiation at BW5 / HASYLAB

The in-situ tensile tests were performed at the beam line BW5 at the HASYLAB at DESY in Hamburg, Germany, using a small screw-driven tensile device. The tensile test specimens "B5-2" and "B5-5" were irradiated with a parallel, monochromatic photon beam with an energy of approximately 100 keV, a wavelength of λ = 0.12 Å and a cross section of 1 x 1 mm^2. As the average grain size of the tensile samples was the same as depicted in Figure 2 (Chapter 3), the irradiated volume encloses more than 10^6 grains, which should guarantee good statistics. Within 10 s, eight complete diffraction rings could be recorded on an image plate, which enabled the simultaneous measurement of the strain parallel and one of the strain components perpendicular to the loading direction (Figure 87). The results on the sample B5-2 were already presented on the TMS Annual Meeting 2005 (Appendix **C**).

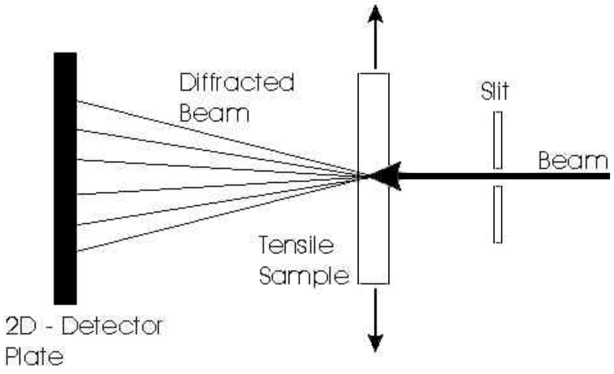

Figure 87: Schematic diagram of the set-up of the tensile test at BW5.

Figure 88a shows the diffraction ring pattern of the undeformed tensile sample with a random texture, which is illustrated by the even intensity of the diffraction rings in Figure 88a. After 12% deformation a weak texture can be observed in the diffraction pattern in Figure 88b.

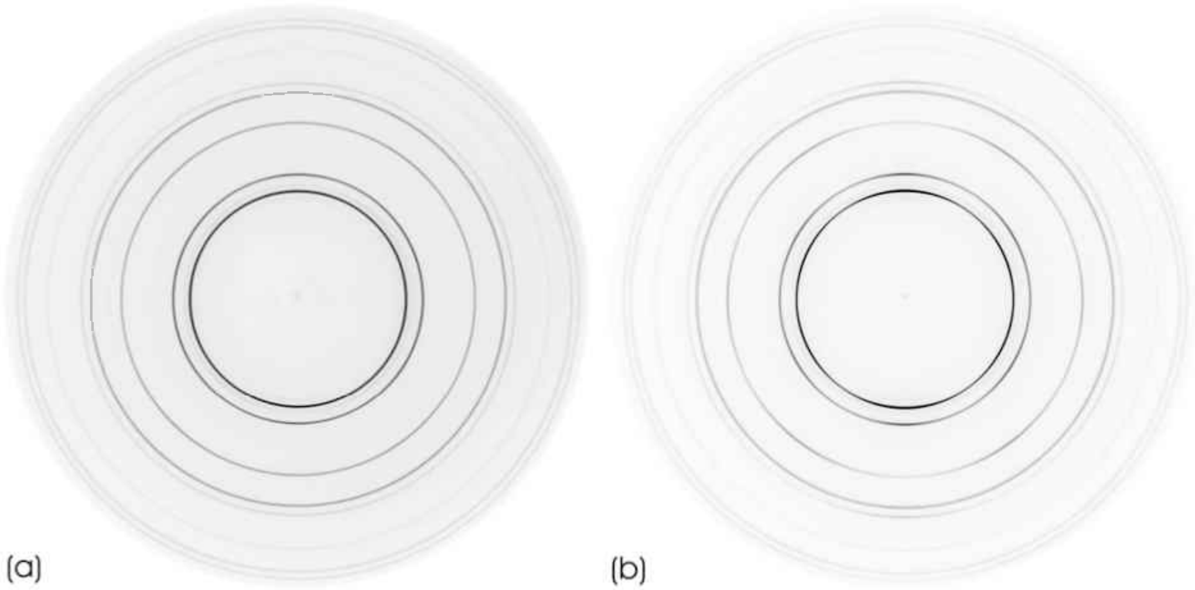

Figure 88: Typical 2D plot of the diffraction rings of an IN718 tensile sample. (a) in the initial condition prior to loading showing no angular dependency of the diffraction ring intensities; and (b) after 12% of macroscopic straining, where some increase or decrease of the initial peak intensities can be observed.

7.2 Tensile Test with Neutrons at ARES

One tensile test with the sample "B5-3" was performed at ARES (GKSS, Geesthacht, Germany), using the same tensile test device. Here, only the (311) reflection parallel to the loading direction was recorded. Due to the low flux compared to the synchrotron radiation an exposure time of 15 min was necessary for each measurement point to obtain reasonable statistics. The gauge volume was 3 x 3 x 3 mm^3.

7.3 Calculation of Stress and Strain

The applied stress was calculated relative to the initial cross section and thus represents the engineering stress, not the true stress, in this case the engineering stress is a good approximation of the true stress as the samples were not elongated up to necking. The macrostrains were determined relative to the gauge length of the extensometer which was 20 mm.

Different strategies can be found in literature for the determination of the lattice strains. Some authors use the lattice spacing at zero stress as a reference [96] and some the lattice spacing at a certain load, which they use as zero point [76]. Here, the intercept from the linear fit to the elastic response of the initial loading was used [77, 79]. This method is more precise, because all the data in the elastic regime is used to determine the zero lattice spacing. The lattice strains were determined using Equation 27 and d_0 was found by extrapolation of the initial elastic response to zero for each (hkl).

The intercept obtained from the linear fit to the linear elastic response during the initial loading gives the reference lattice spacing d_0^{hkl} for each reflection (hkl) at zero stress, which is shown in Figure 89.

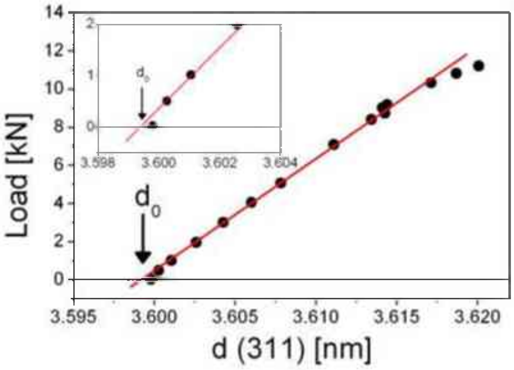

Figure 89: Initial loading curve of the sample B5-5 showing the reaction of the (311) refection parallel to the applied stress. The intercept with the horizontal axis is taken as the reference value d_0^{hkl} for the lattice strain calculation.

Below the yield point, the slope of the applied stress vs. strain reflection was referred to as the diffraction elastic constant. The ratio of axial to transverse slopes gives the Poisson's ratio.

The intergranular strains ε^{int} were derived from the difference between the measured lattice strain response ε^{lat} and the extrapolation of the linear response σ_{app}/E_{hkl}, plotted as a function of plastic strain [77]. Additionally, the measured strains in the unloaded condition were plotted against the plastic strain. Theoretically, no difference between the residual strain in the unloaded and the intergranular strain in the loaded condition is expected.

$$\varepsilon_{hkl}^{lat} = \varepsilon_{hkl}^{\text{int}} + \frac{\sigma_{app}}{E_{hkl}} \tag{27}$$

7.4 Results of Tensile Tests Conducted on IN718 Samples

7.4.1 Elastic Response

In Figure 90 the response of the first four reflections, determined in-situ at BW-5, are plotted against the applied stress. The average measurement errors were determined to be 30 με for (311), 50 με for (220), 75 με for (200), and 50 με for (111). In all cases, the data deviate from the initial elastic line as the amount of plastic deformation increases. Parallel to the loading direction (Figures 90a-d) the deviation is largest for the (200) reflection and almost negligible for the (311) and (111) reflections. The (220) refection is the only reflection that shows a significant compressive deviation. Transverse to the loading direction (Figures 90e-h) only the (200) and to a lesser degree, the (311) reflection show a significant tensile deviation from the elastic response. There is some indication of a compressive deviation for the (220) reflection but the results of the two samples are ambiguous. The (111) reflection shows a large scatter of the data in the transverse direction, but the deviation from linearity is almost negligible. The macroscopic yield limit is 700 MPa, but it can be seen that the non-linear behaviour of the lattice strain response starts before macroscopic yield at approximately 600 MPa for most reflections.

The elastic constants obtained from the linear least square fits to the initial loading in the elastic regime are summarized in Table 8 and Table 9. The measured constants are compared to calculated "Diffraction Elastic Constants" (DECs), which are 10% to 17% higher than the measured values depending on the reflection. These deviations are above the errors of the least square fit to the elastic response. According to Dye et al [86] the calculation of the DECs for IN718 is based on an average between single crystal elastic constants for pure nickel and γ' precipitates. Although this approximation does not correspond to the composition of IN718, Dye et al. claimed to achieve a good fit of the measured DEC values of IN718 as well as of the superalloy termed Waspaloy. The values for the Poisson's ratio determined from the slopes in the loading direction and transverse to the loading direction, shown in Table 8, are well below the data predicted by the Kröner model [86]. This can most likely be attributed to the larger scatter of the data in the transverse direction for all reflections.

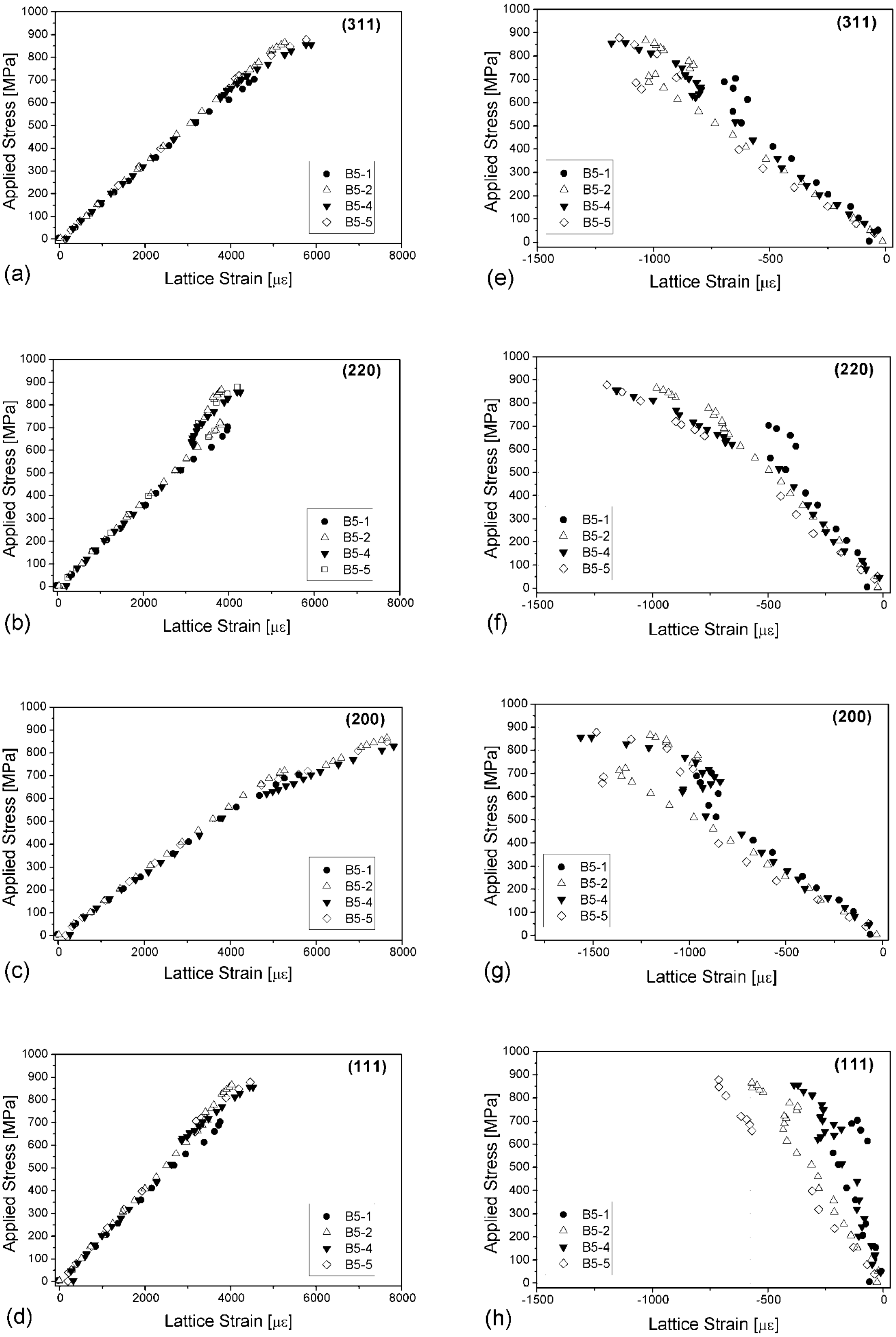

Figure 90: The lattice strain evolution (a)-(d): parallel to the stress axis and (e)-(h): perpendicular to the applied stress as measured with the (311), (220), (200), and (111) reflections at BW5. The average measurement errors were determined to be 30 με for (311), 50 με for (220), 75 με for (200), and 50 με for (111), but are not shown in the graphs for the sake of clarity.

Table 8: Young's Moduli determined via synchrotron measurements from the slope of the elastic response of four samples machined from a water-quenched turbine disc. The standard errors from the regression analyses of the least square fit to the elastic response were typically between 1.0 and 2.0 GPa. Also quoted are the values based on a calculation using the Kröner model and single crystal constants as given by Dye *et al.* [86]. The deviations between calculated and measured values are given in percent.

E_{hkl} [GPa]	Measured				Kröner	Deviation [%]			
	B5-1	**B5-2**	**B5-4**	**B5-5**		**B5-1**	**B5-2**	**B5-4**	**B5-5**
(311)	171.0	168.3	163.8	168.7	195	12.3	13.7	16.0	13.5
(220)	189.6	187.3	180.3	187.6	215	11.8	12.9	16.1	12.7
(200)	144.7	142.1	134.3	139.9	168	13.9	15.4	20.1	16.7
(111)	211.7	205.9	196.1	209.0	237	10.7	13.1	17.3	11.8
bulk	200.0	195.0	184.7	191.0	204	2.0	4.4	9.5	6.4

Table 9: Poisson's ratio determined via synchrotron measurements from the slopes of the elastic response in the loading and transverse direction. Also quoted are the values based on a calculation using the Kröner model and single crystal constants as given by Dye *et al.* [86]. The deviations between calculated and measured values are given in percent.

ν_{hkl}	Measured				Kröner	Deviation [%]			
	B5-1	**B5-2**	**B5-4**	**B5-5**		**B5-1**	**B5-2**	**B5-4**	**B5-5**
(311)	0.2669	0.2437	0.2148	0.2718	0.319	16.3	23.6	32.7	14.8
(220)	0.2339	0.1849	0.1659	0.2200	0.299	21.8	38.2	44.5	26.4
(200)	0.3045	0.2751	0.2361	0.3073	0.345	11.8	20.3	31.6	11.0
(111)	0.1915	0.1347	0.0668	0.1779	0.277	30.9	51.4	75.9	35.8
bulk	-	-	-	-	0.3	-	-	-	-

Figure 91 shows the results of the lattice strain measurements of the sample B5-3 that was examined with neutron diffraction at ARES. Here, the average error of the lattice strain determination was 80 με. Parallel to the loading direction the behaviour of the reflection (311) agreed with the observations of the synchrotron measurements. The Young's modulus determined from the slope of the elastic regime of the sample B5-3 was found to be E_{311} = 179 GPa.

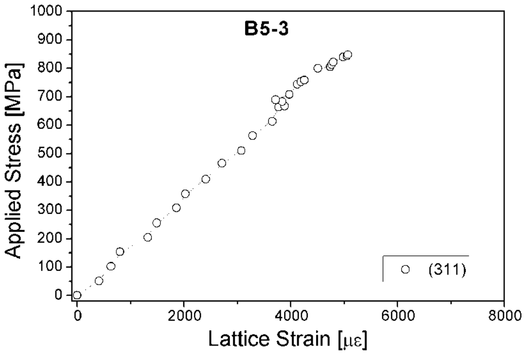

Figure 91: The lattice strain evolution parallel to the stress axis of the sample B5-3 as measured with the (311) reflection at ARES.

Altogether, the results of four samples (B5-1, B5-2, B5-3, and B5-5) show excellent reproducibility of the experiments. Only the results of the sample B5-4 are set apart (cf. Figure 90h, Tables 8 - 9), which could not be resolved even after considering all possible sources of error that are stated below. However, the general trend of all measurements is in accordance with theoretical EPSC model simulations for fcc systems [76, 97] and other measurements of nickel alloys [79], where (200) is the most compliant and (111) the stiffest lattice plane.

The fact, that all measured data were below the calculated values suggested the presence of a systematic error. The following potential sources of a systematic measurement error were considered:

a) Determination of the synchrotron wavelength and the distance between sample and detector.

b) Distance between the sample and the detector differs for the calibration sample Al_2O_3 and the tensile sample.

c) False indication of the load cell.

d) Systematic change of the slope between the 1st, 2nd and 3rd loading.

e) Misalignment of the tensile sample.

Addressing these in order:

a) The synchrotron wavelength was determined along with the distance between the sample and the detector via two measurements of a Al_2O_3 calibration sample. NIST Standards gave the lattice distances of the calibration sample and the relative distance between the two positions of Al_2O_3 was measured. As distances can only be determined with an uncertainty of ± 1mm, it is possible that the relative distance of the two positions was 399 mm or 401 mm instead of 400 mm. However, such a change proved to have a vanishing effect on the Young's modulus well below the uncertainty of the regression analysis.

b) The distance between the sample and the detector was determined to be 1270.5 mm for B5-4 and B5-5. If the calibration sample was positioned at exactly the same location as the tensile sample, this would result in a lateral uncertainty of the distance of ± 1 mm. The effect of a variation of the distance on the Young's modulus is, however, very small as can be seen in Table 9 for the sample B5-5. Therefore, this uncertainty cannot be regarded as the main source for the deviation between the measured and the calculated Young's moduli.

Table 9: Young's Moduli determined from the slope of the elastic response of the sample B5-5 machined from a water-quenched turbine disc, where the sample position was varied between 1270.5 ± 1 mm.

	E_{hkl} [GPa]			**ν**		
	-1 mm	**0**	**+ 1 mm**	**-1 mm**	**0**	**+ 1 mm**
(311)	168876	168671	168891	0.27212	0.2718	0.27217
(220)	187616	187634	187614	0.21969	0.22008	0.2197
(200)	139919	139916	139927	0.30708	0.3073	0.3071
(111)	208968	209009	208969	0.17818	0.17786	0.17812

c) Table 7 shows that the macroscopically determined values for the Young's modulus were also below the expected value of 204 GPa. However, tensile tests performed in Leoben at a large, commercial tensile test machine using the same extensometer clamped onto the sample resulted in Young's modulus data of 202 and 206 GPa. Additionally, the yield point of the stress-strain curves recorded in Leoben corresponded to the one recorded at BW5, which further indicates that the strain measurement is correct (Figure 92). As the tensile test device was designed to test Mg-alloys, incorrect force indications – especially for high values – were regarded as a source for too low stress values. Although most likely this error of indication was not linear, the measured stresses were multiplied with a constant factor to give the expected macroscopic Young's modulus of 204 GPa for the macroscopic stress strain curve. As a consequence, the E_{hkl} values of the single reflections were shifted to steeper values as well. This is illustrated in Figure 93, where the line illustrates the Kröner values and the symbols the measured slopes. Compared to the other possible sources of error, this influence of the load cell on E_{hkl} was significant and was therefore regarded as one main reason for a systematic error. Appling the idea of an erroneous load cell shifts the E_{hkl} values closer to the expected Kröner values but still there are deviations larger than the statistical error, as illustrated in Figure 93.

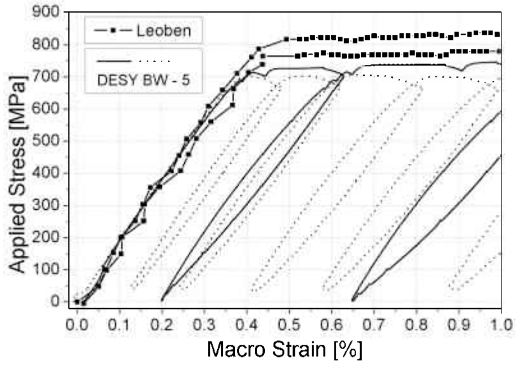

Figure 92: Macroscopically determined stress strain curves for IN718 recorded at a commercial tensile test machine in Leoben and at a small device used at DESY BW5. Both measurements used the same extensometer, clamped directly onto the sample.

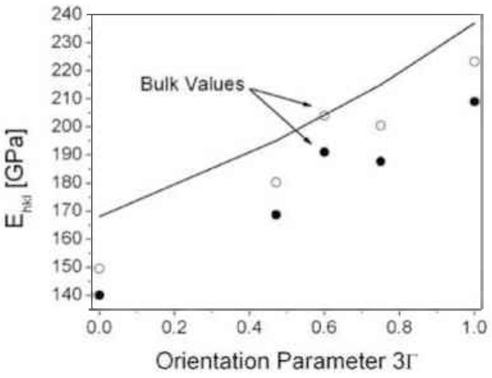

Figure 93: Young's moduli determined for the sample B5-5 depicted as a function of the orientation parameter $\Gamma = (h^2k^2+k^2l^2+l^2h^2)/(h^2+k^2+l^2)$. Full symbols: original data; open symbols: stress adapted; Line: Kröner Model. The Young's modulus obtained from the macroscopic stress-strain curve and its adapted value, which equal literature data, are indicated by "Bulk Values" and the arrows. The uncertainty of the regression analysis did not exceed 2 GPa, which cannot be resolved in the graph as it is in the size of the symbols.

d) In Table 10 there are considerable differences in the slopes between the initial loading cycle and the 2nd, 3rd, and 4th loading of the sample B5-2. This was also observed by Djapic *et al.* [98] for Udimet 720. However, Djapic claims that (311) is hardly affected by cyclic loading and that E_{311} remains almost unaffected. This observation cannot be confirmed by the present data, as neither of the reflections shows a steady increase or decrease. For this reason, the data in Table 10 are considered as the scatter of the Young's modulus data for the present experimental set-up. It was not interpreted as a material effect as the elastic response is known to be very insensitive to aging treatments and grain size differences, whereas the measurement of the Young's modulus via the slope is generally considered error-prone. Incorrect Young's modulus data can particularly be caused by a small misalignment of the sample axis. As a result the determined strains will not fully correlate with strains in the loading and transverse direction. When this tilt between the sample axis and the loading direction changes due to the release of the load, and the sample is reloaded again with another angle the result is a different slope of the elastic response for each loading cycle. As the sample B5-2 was totally unloaded after each loading cycle, the sample was completely loose and is then slightly different aligned upon re-loading. The samples B5-4 and B5-5 were unloaded to 500 N only, in order to avoid a complete loosening of the sample. Yet, the Young's modulus could only be determined for the initial loading, because limitations of the beam time only allowed measurements in the loaded condition and at 500 N.

Table 10: E_{hkl} values determined for the initial and following loadings of the sample B5-2, the average (av) of all four slopes and its corresponding standard deviation (values in brackets) are quoted as well.

E_{hkl} [GPa]	Measured					Kröner	Deviation [%]
	1st	2nd	3rd	4th	av		
(311)	168.3	176.1	173.4	169.8	171.9 (4)	195	11.8
(220)	187.3	203.0	210.0	203.6	200.9 (10)	215	6.6
(200)	142.1	145.2	138.7	135.0	140.2 (4)	168	16.5
(111)	206.0	224.8	219.0	212.6	215.6 (8)	237	9.0

e) Table 10 also shows the average of the slopes of the first four loadings and the corresponding standard deviation, which was interpreted as the measurement uncertainty. Although the standard deviation was much larger than the error of the regression analysis, the Kröner values were still not within the measurement uncertainty. The fact, that the apparent Young's moduli did not agree with the Kröner values within the statistical error and the fact that all measured slopes were below the expected values, gave rise to the idea of a misalignment of the tensile sample as the main cause for the disagreement. A tensile sample is misaligned if its axis is not exactly parallel to the direction of the tensile load. Due to these uncertainties the Kröner values (Tables 8, 10) were used to calculate the residual stresses within the studied turbine disc and the model plates.

7.4.2 Deviation from Linearity

One way to determine the intergranular effects is to calculate the difference between the measured strain response and the extrapolation of the initial linear response. A material that is elastically and plastically isotropic would exhibit zero intergranular residual stress for all stress values. The results for two IN718 samples calculated according to Equation (7) are shown in Figures 94 - 96. In the plastic region the load is no longer evenly distributed between the grains due to slip, which results in a non-linear behaviour for all sets of grains. It is remarkably pronounced for the (200) peak, which shows tensile intergranular strains in accordance to model calculations and other measurements on fcc materials published in literature [75, 76, 94, 95, 99]. The behaviour of (220) is opposite to that of (200) in the loading direction as well as perpendicular to it and, in a sense, balances the (200) effects. The deviations for the (111) and (311) reflections are much smaller and comparable with the uncertainty of the peak determination (app. ± 80 $\mu\varepsilon$) in the loading direction. This behaviour of the four reflections is consistent with measurements on other nickel-based alloys, for example, Monel 400 [75] and Inconel 600 [79]. Concerning the magnitude of the intergranular strains the results of the two samples do not fully agree.

In the loading direction the (200) strains of B5-2 exceed those of B5-5 by approximately 500 $\mu\varepsilon$, but the (220) strains match perfectly. According to the sample B5-2 (Figure 94a) grains with (311) plane normals oriented parallel to the applied load accumulate no intergranular strains at all, but for the sample B5-5 (Figure 94a) the deviation from linearity can reach up to 250 $\mu\varepsilon$.

Transverse to the loading direction the intergranular strains split into positive values for (200) and (311) for both samples and negative values for (111) and (220) for B5-5, only (Figures 94b, 95b). The results of B5-2 indicate zero intergranular strains for (111) and small negative strains (-200 $\mu\varepsilon$) for (220). Below 2% plastic strain, tensile shifts occur for all reflections in sample B5-2 transverse to the loading axis, which might be attributed to statistical errors.

The in-situ tensile test performed with neutrons on the sample B5-3 recorded the (311) lattice strains parallel to the loading direction. The determined deviation from linearity of the (311) lattice planes showed negative values reaching up till – 500 $\mu\varepsilon$ for plastic strains below 5% and zero deviation for larger plastic strains as illustrated in Figure 96.

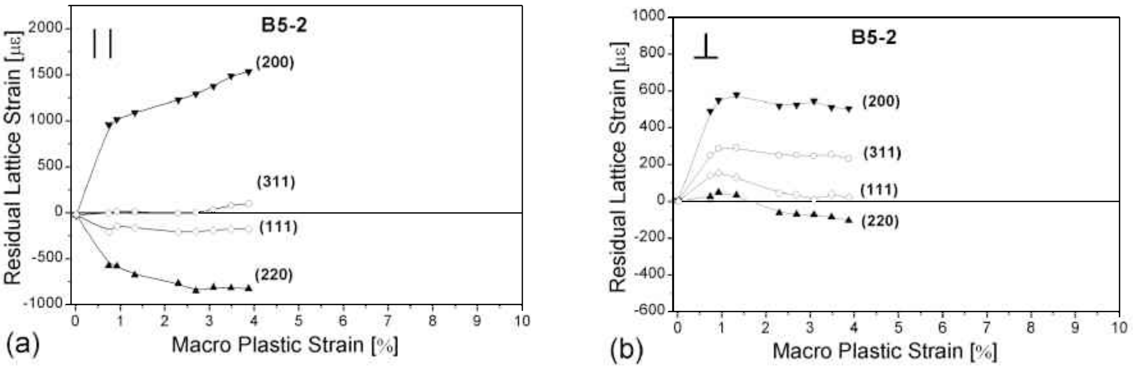

Figure 94: Intergranular strains as a function of macroscopic plastic strain (a) parallel and (b) transverse to the loading direction for the sample B5-2.

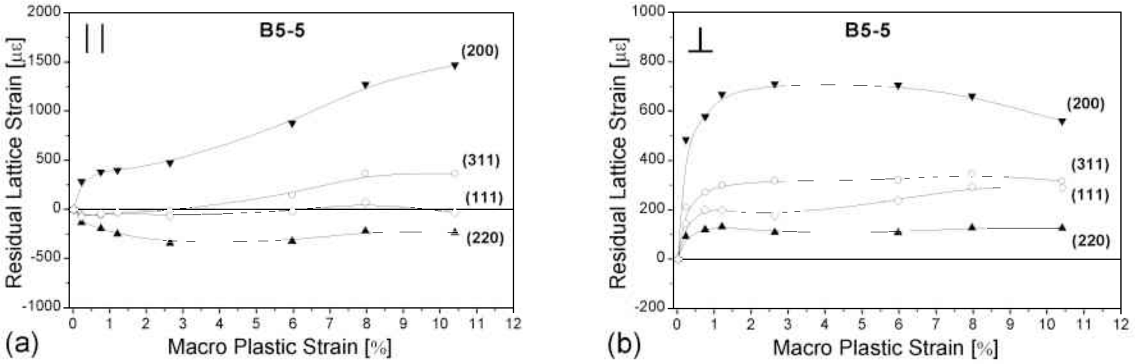

Figure 95: Intergranular strains as a function of macroscopic plastic strain (a) parallel and (b) transverse to the loading direction for the sample B5-5.

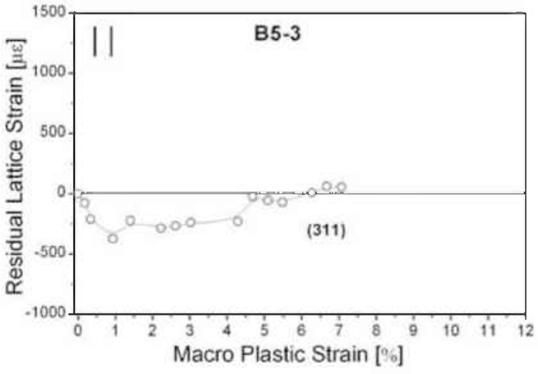

Figure 96: Intergranular strains as a function of macroscopic plastic strain parallel to the loading direction for the sample B5-3.

7.4.3 Residual Microstrains

Alternatively, the intergranular strains can be defined as the lattice strain after removal of the external load. Ideally, the lattice strain under load is equal to the residual strain after unloading. But the hysteresis in each unloading/loading cycle observed for sample B5-2 (Table 10) indicates that slip is occurring during unloading. Consequently, the strain in the unloaded condition differs from the strain under load.

Figures 97 - 99 show the residual lattice strains in each set of lattice planes after unloading of the tensile specimens B5-2 and B5-5 as a function of the macroscopic plastic strain.

In the loading direction the residual lattice strains of the sample B5-2 showed small negative intergranular (111) and the (311) strains (Figure 97a). The sample B5-5 exhibit the expected behaviour (Figure 98a) with zero intergranular strains for the (111) reflection and the slightly positive (311) strains. Compared to the deviation from linearity, the intergranular (200) strains in B5-5 (Figure 98a) are reduced and the compressive intergranular strains of the reflection (220) move closer to zero. The residual strains for the sample B5-2 (Figure 97a) showed the same behaviour for the (200) and (111) reflections, but the residual strain of (220) was identical with (111), and (311) surprisingly moved from zero deviation to tensile residual strains.

Transverse to the loading direction the signs of the residual strains were reversed to the signs of the deviation from linearity for the reflections (311), (111) and (220); a result which totally opposes all the tensile residual strains for the sample B5-2. Only grains with (200) plane normals oriented perpendicular to the applied load showed positive residual strains of 500 to 600 µε for both samples.

The different trends of the two samples regarding the residual lattice strains can be partly attributed to the fact that B5-5, compared to B5-2, was not fully unloaded but remained at a load of 500 N.

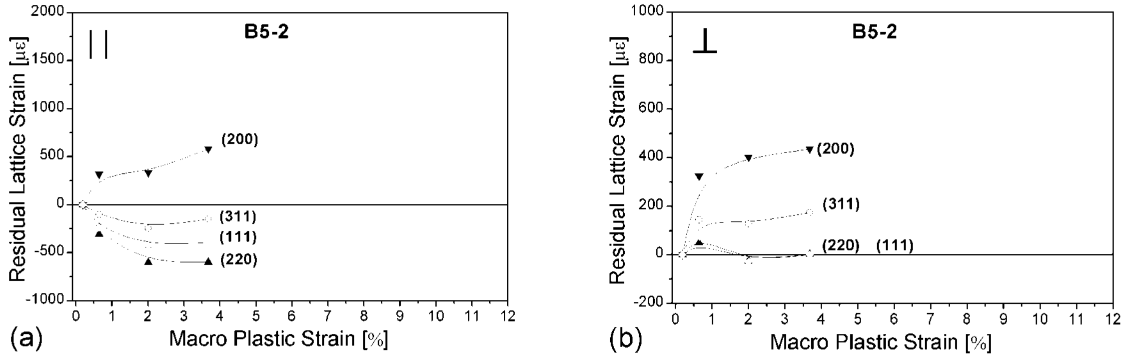

Figure 97: Residual lattice strains of the sample B5-2 after complete removal of the macroscopic load as a function of the plastic strain prior to unloading, (a) parallel and (b) transverse to the loading direction.

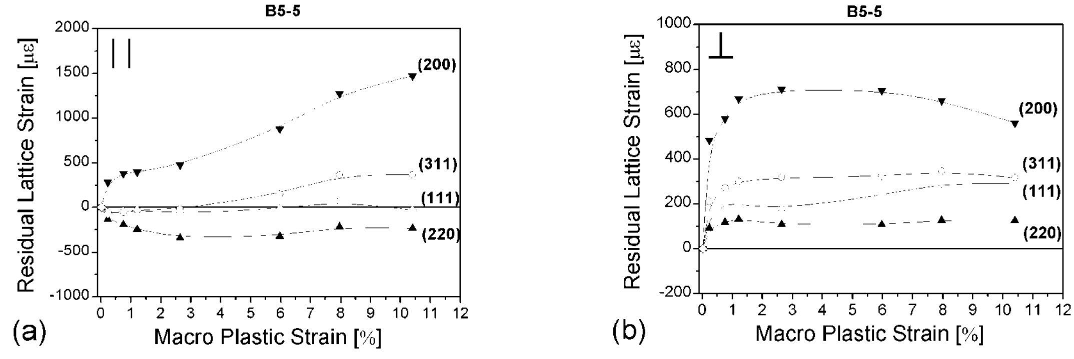

Figure 98: Residual lattice strains of the sample B5-5 at a load of 500 N as a function of the plastic strain prior to unloading, (a) parallel and (b) transverse to the loading direction.

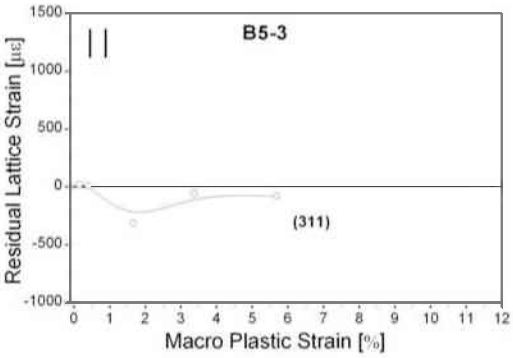

Figure 99: Residual lattice strains of the sample B5-3 after complete removal of the macroscopic load as a function of the plastic strain prior to unloading.

7.4.4 Discussion

The first aim of the tensile tests was to confirm the general recommendation to use the (311) reflection for measurements in fcc materials like the nickel-based alloy IN718. Studies presented in literature often favour (311) [54, 43], but (111) has also been used [79] for macrostress analysis. The tensile tests performed in this work displayed zero or minimal microstrains for both (311) and (111) reflections, which is reflected in an almost perfectly linear response even in the plastic regime. In the loading direction the deviation from the linear elastic response was negligible for (311) and in the unloaded condition the (111) residual strains were even smaller. Perpendicular to the loading direction it was more difficult to draw conclusions from the residual lattice strains or the deviations from linearity, as the scatter of the data was much higher. Still the microstrains measured for the (311) and (111) reflections were small. This is in accordance with the results of a number of investigations, e.g. Refs. [79, 95]. Consequently, the recommendation to use (311) could be confirmed with the present tensile tests, although the (111) reflection seems to fulfil the demand for minimal accumulation of microstrains as well. This result is in accordance with Dye et al [86], who found that (111) and (311) were equally suitable for macro stress determination in Ni superalloys. In the end, the (311) reflection was used at ARES as its diffraction angle was close to 90° and thus could guarantee much smaller measurement uncertainties than (111).

Secondly, the DECs for IN718 were investigated and compared to the calculated values based on single crystal data of pure Ni and γ' given by Dye et al [86], which did not correspond to the composition of IN718. The values for E_{hkl} determined from the regression analysis of the initial loading curves showed a qualitative agreement with the results of the Kröner calculation, but were 11 - 20% below the calculated DECs. Due to the fact that the slope of the macroscopic stress strain curve at BW5 was also below the expected value, a false indication of the load cell was regarded as one source for the inferior DEC data, as depicted in Chapter 7.4.1. A correction of the force indication shifts the values closer to the calculated data. The remaining deviations still exceed the uncertainty of the regression analysis as well as the standard deviation of the average slope of all loading cycles, which can be interpreted as the actual measurement error (Table 10). Few published studies on fcc materials compare the measured and calculated DEC values and no in-situ tensile test on IN718 have been published up to now. As the few publications on steel [100] or other nickel-based alloys [79] claim that the Kröner values are within the statistical error of the measured DECs, the single crystal elastic constants used in the present work might not be appropriate. Yet, other diffraction studies on IN718 use either the macroscopic data, because they apply a Rietveld fit to the entire spectrum [62], or like [88] and [101] refer to exactly the same publication by Dye et al [86], which is based on the average of γ and γ' single crystal constants. The only explicit data that can be found in literature are: E_{311} = 194 GPa, ν_{311} = 0.310, E_{111} = 246 GPa, ν_{111} = 0.258 [86]; and E_{311} = 209 GPa, ν_{311} = 0.29 [88]. Consequently, the remaining deviation from the calculated values was presumably caused by a slight misalignment of the tensile sample. This idea was supported by the analysis of the intergranular strains and their differences in the loaded and unloaded condition. When the unloading is ideally elastic the deviation from linearity under load should be equal to the residual strain after removal of the load. In reality, the residual strains are expected to be slightly smaller but the opposing signs observed in Figures 94 - 99 cannot be explained by an elastic unloading. The observed results can only be explained by the fact that the slope of the unloading curves was totally different from the initial loading curve. As the slope of the loading and unloading curves is known to exhibit no strong changes even if a pronounced hysteresis is present, the change of the slope during unloading cannot primarily be interpreted as a material effect. So changes of the alignment of the sample axis are seen as the cause of the obtained E_{hkl} values and the partly conflicting results on the intergranular strains. A tensile sample that is not perfectly aligned with the loading direction will not be loaded along its axis and thus strains recorded parallel to the loading direction are not uniaxial tensile strains, but have a shear component as well. The same argument applies for the transverse direction, which additionally exhibits a larger scatter due to a stronger potential texture influence.

Finally, the measured intergranular strains in the plastic regime were intended to be used for a correction of the measured strains for microstrain contributions. This was done successfully by Holden *et al.* for a bent Inconel 600 tube [79, 95] and for a bent Monel400 tube [75]. On the one hand, the inconsistent results of different tensile samples made of the same material rendered the determination of a correction factor very complicated. And on the other hand, the plastic strain in the model plate and in the turbine disc were found to be too small to require a significant correction of the measured strains. Also Holden *et al.* [95] admitted that no correction was needed for a slightly bent tube.

8 Texture Measurements

Any texture within the studied components would impede the residual stress analysis. As the turbine disc has undergone large deformations during forging, it was not clear if the microstructure was fully recrystallised and entirely random in the water-quenched condition.

8.1 Neutron Diffraction

The global texture was examined with neutron diffraction at the instrument TEX-2 at GKSS (Germany). There, it was possible to obtain pole figures from the whole sample. The sample, cut from the middle of the water-quenched turbine disc, was nearly perfectly cubic with a edge length of 2 cm. Figure 100 shows the resulting (111) and the (200) pole figures. No significant texture can be observed in the material, as the maximum intensities are hardly above 1 mrd (multiples of random distribution). Consequently, the material could be regarded as perfectly random.

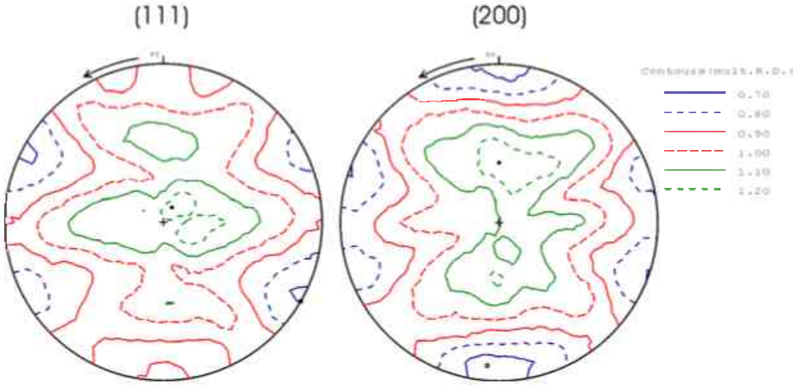

Figure 100: Pole figures determined with neutron diffraction at TEX-2 (GKSS, Germany) in a sample that was cut from the thin section of the as-quenched turbine disc made of IN718.

8.2 Electron Back Scatter Diffraction (EBSD)

In addition to the measurements on TEX-2, the texture at the scale of the grain size was examined with EBSD, scanning an area of 120 µm x 120 µm. The pole figures for a sample machined from the rim part of the water-quenched turbine disc are shown in Figure 101. The fact that even in near-surface regions the maximum intensities were hardly above 4 mrd, further approved the observations of the global texture. These examinations showed that the turbine disc exhibits a fully recrystallised microstructure and no preferred crystallographic directions can be observed. Hence, any texture influence on the residual stress analysis within the studied components could be excluded.

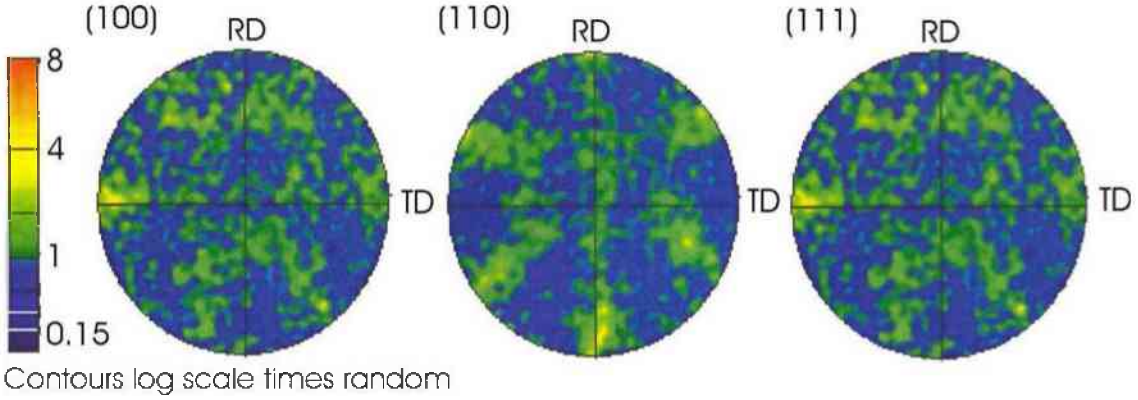

Figure 101: Pole figures determined with EBSD on a sample machined from the forged and water-quenched turbine disc.

9 Small-Angle Neutron Scattering (SANS)

Small-angle neutron scattering (SANS) measurements were conducted on differently annealed IN718 samples to clarify the presence of γ' and γ'' precipitates in the studied components. Although the γ'' precipitation is known to be sluggish [25], some authors observed small particles even in the water-quenched condition [38, 21]. Neutron diffraction measurements at ARES were not appropriate to identify coherent precipitates as no peak separation was observed. The SANS method can detect very small particles within a matrix, analyse the size distributions and appraise the corresponding volume content, provided the character of the particles is known. The measurements were performed with the instrument SANS-2 at GKSS, using selector-monochromated neutrons with a mean wavelength of λ = 0.57 nm and a wavelength spread of $\Delta\lambda/\lambda$ = 10%. The neutron beam impinging on the samples had a diameter of 3 mm. The scattering vectors q were determined from q = 0.02 to 2.5 nm^{-1} ($q = 4\pi\sin(\theta)/\lambda$, where 2θ is the scattering angle) resulting in the scattering curves shown in Figure 102.

For the interpretation of the SANS results, the particles were assumed to be γ'' precipitates, because they represent the main strengthening phase in IN718 and their volume content far exceeds the volume content of γ'. The size of the precipitates was calculated presuming spherically shaped particles and a scattering length difference of $0.50 \cdot 10^{10}$ cm^{-2}. The resulting particle density, volume content, and particle size are given in Table 8. The employed scattering length difference was very small and therefore very sensitive to the chemical composition of the particles. However, the exact chemical composition of the γ'' precipitates in the studied IN718 material was not measured. This uncertainty of the chemical composition of the precipitates causes an uncertainty of the volume fraction which is above the measurement errors given in Table 8. Still, the SANS measurements could prove that only after an annealing treatment significant amounts of precipitates can be observed. The sample number 3, which was annealed at 720°C for 30 min did not show any significant difference to the as-quenched sample, which served as a reference (Figure 102). The reference sample and the sample number 3 are not listed in Table 8, because the corresponding scattering curves, recorded within the available measurement time, did not allow a quantitative evaluation and strongly suggested that no precipitates are present. For all other samples the volume content of the measured particles was approximately 5%, using a scattering length difference of $0.50 \cdot 10^{10}$ cm^{-2}. Consequently, the assumption of a precipitation-free material was justified for the residual stress analysis within water-quenched components.

Table 11: SANS results for selected samples giving the volume fraction f, the number of particles n, the location of the maximum volume content R_{max}, the particle interference c_{HS}, and the quality of the fit χ^2. The difference of the scattering lengths was assumed to be 0.50 ·1010 cm^{-2}. The measurement error is given in brackets.

Sample	Heat Treatment	n [10^{18} cm^{-3}]	f [vol %]	$R_{\max}$ [nm]	C_{HS}	χ^2
2	8 h/720 °C	1.09(7)	5.6(4)	3.3	1.81(5)	2.6
4	20 h/720 °C	0.21(1)	5.2(3)	5.7	1.79(9)	7.6
9	8 h/750 °C	0.19(1)	4.9(3)	5.6	1.81(14)	6.2
10	8.5 h/680 °C	21(2)	4.6(3)	1.2	1.88(4)	1.7

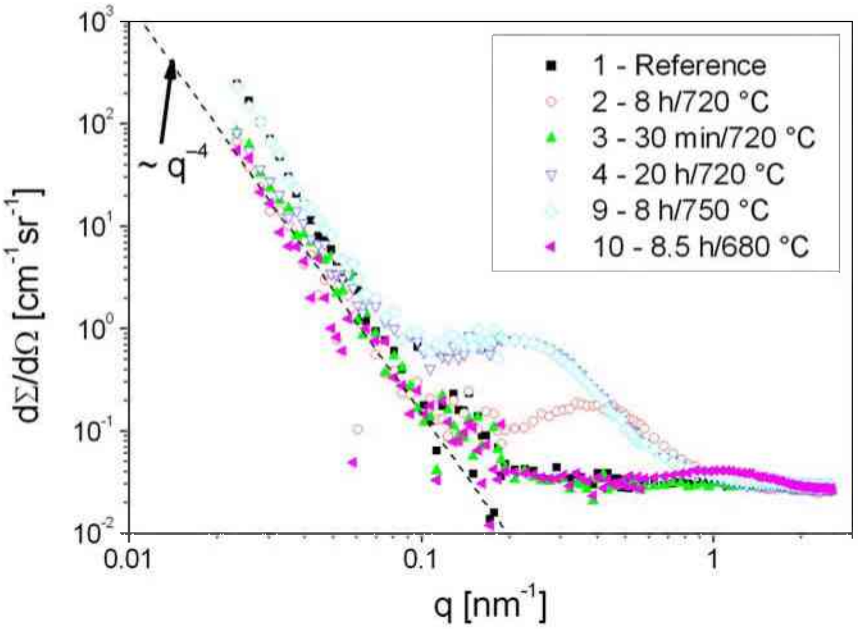

Figure 102: SANS scattering curves for all investigated samples made of IN718.

10 Comparison of Simulated and Measured Results

The simulation of the model plate and the turbine disc showed that the heat transfer coefficient was the key parameter for a correct finite element model. Various parameter variations were performed by modifying the heat transfer coefficient as a function of the surface temperature. In the following sections simulated residual stresses are compared to the values determined by neutron diffraction.

10.1 Model Plate

The measured longitudinal stresses gradually increase towards the middle, and the measured transverse stresses gradually decrease to a local minimum in the middle. Constant heat transfer conditions proved to be inadequate to reflect this trend because they led to fairly constant stresses along the length of the model plate. Figure 103 shows the longitudinal and transverse stress components that were determined with the (311) reflection with a gauge volume of a 3 x 3 x 3 mm^3, together with the results of four different simulations. Constant heat transfer coefficients did result in a very steep increase of the stress components near the rim but over the majority of the plate's length the stress components are fairly constant (cf. Chapter 6.6.3.1). The stresses determined by neutron diffraction, as illustrated in Figure 103, do not at all correspond to these simulated stresses using constant heat transfer coefficients. The residual stresses from a simulation with the initial heat transfer function h_s (cf. Figure 27) represent a first optimisation regarding the shape of the stress curves. The longitudinal stress increases steadily towards the middle, where the transverse stress component exhibits a local minimum. Yet, the level of the longitudinal stress component is well below the values determined by neutron diffraction and the difference between the longitudinal and transverse stress component should be larger according to the experimental results. An increase in the stress level and a larger difference between the stress components could be achieved with the heat transfer functions h_2, h_9 and h_{13}. These three modifications of h_s represent the best compromise to fit both: the experimentally determined stresses and the measured cooling curves.

Figure 104a again shows h_s and its modifications h_2, h_9 and h_{13}, which represent:

- an increase in the maximum value h_{max} from 17000 W/(m²K) (h_s) to 28000 W/(m²K) (h_2).
- a decrease in the temperature for maximum heat transfer T_{max} of 400 °C (h_2) to 250 °C (h_9).
- a smoother increase of h for decreasing temperatures combined with a lower maximum heat transfer value h_{max}, but no variation of the temperature for maximum heat transfer T_{max} = 400 °C: h_2 to h_{13}.

Figure 104b illustrates the temperature gradient in the model plate that builds up between the central point P2 and the near-surface point P1. The simulated temperature difference is too large for all four functions. This can be attributed to the combination of a steep increase in the heat transfer coefficient at relatively high temperatures (between 400 °C and 600 °C) and low heat transfer values above 600 °C.

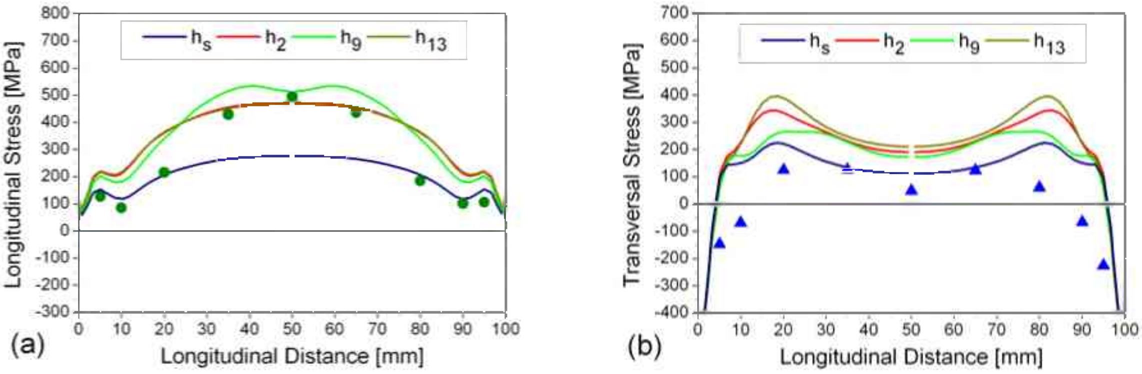

Figure 103: (a) Longitudinal and (b) transverse residual stresses in the model plate as determined by neutron diffraction (symbols) and finite element simulations (lines). The simulations were performed with the temperature dependant heat transfer functions h_s, h_2, h_9, and h_{13}.

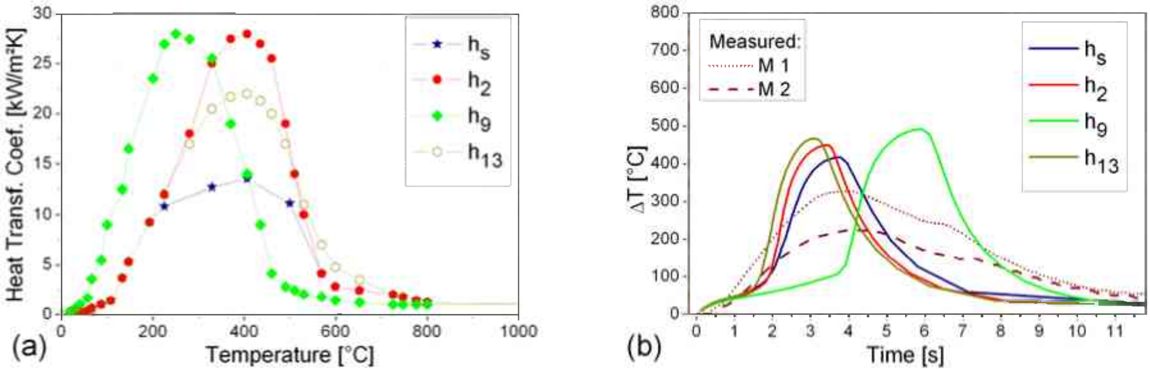

Figure 104: (a) Functions for temperature dependant heat transfer coefficients that resulted in stress levels equal to the measured stresses. (b) The temperature difference between the two points P1 and P2 as a function of time for the measured and simulated cooling curves (see text).

The two functions h_2 and h_{13} effectively lead to very similar temperature and stress results with only slightly higher transverse stresses for the simulation with h_{13}. This result illustrates that a reduced maximum heat transfer together with an increased Leidenfrost temperature T_{Le} generates similar residual stress states. They only differ regarding the final plastic strain, which is slightly higher for h_{13} in the normal and transverse direction. Consequently, the transverse stress component is slightly higher for the heat transfer h_{13} compared to h_2. The function h_9 represents a reduction of the temperature where maximum heat transfer takes place. Surprisingly, the value of the longitudinal and transverse stress component is fairly equal to the results of h_2 and h_{13}. In fact, the shape of the experimentally determined longitudinal component is reflected best by the simulation with h_9 and also the transverse component fits well to the experimental values. However, the temperature gradient does not correspond to the measured result as shown in Figure 104b because the cooling is considerably delayed. The fact that the residual stresses are nevertheless very high can be attributed to the extremely steep increase of the heat transfer function from T_{Le} to T_{max}, which obviously overlaps the effect of a reduced temperature for the maximum heat transfer (see Chapter 5.6).

10.2 Turbine Disc

The residual stresses within the turbine disc determined with neutron diffraction along the radius and along a scan through the thickness of the disc are given in Figures 105 - 107. In contrast to the model plate, simulations using constant heat transfer coefficients could reflect the general shape of the experimentally determined stress distribution. However, the maximum stress level was too low and the gradient of the simulated, parabolic shaped stress curves along the thickness were not steep enough for a good agreement with the measured values. Increasing the heat transfer value up to $h = 10000$ W/(m²K) did improve the fit of the simulated stresses with the measured stresses, but deteriorated the fit of the measured cooling curves with the measured temperatures.

Therefore, the turbine disc was simulated with a selection of the heat transfer functions that were employed for the initial parameter study of the model plate. Figures 105 - 107 show the stress results of the simulations with the functions h_s, h_2 and h_{13} together with the experimentally determined stresses of the disc B3 (cf. Figure 74, 76, 79). The function h_9 which led to satisfying stress results for the model plate was not employed for a simulation of the turbine disc because the cooling curves of h_9 did not fit the experimentally determined curves.

Along the radial scan given in Figure 105 the results of h_{13} correspond best to the measured stresses. The agreement is very good for the tangential component and for the radial component near the rim. Yet, in the thin section of the disc around a disc radius of 100 mm the divergence between the measured and the simulated stresses is quite striking. For all simulation results the local stress minimum is very pronounced, but for the experimental values it is not obvious and sometimes cannot be found at all.

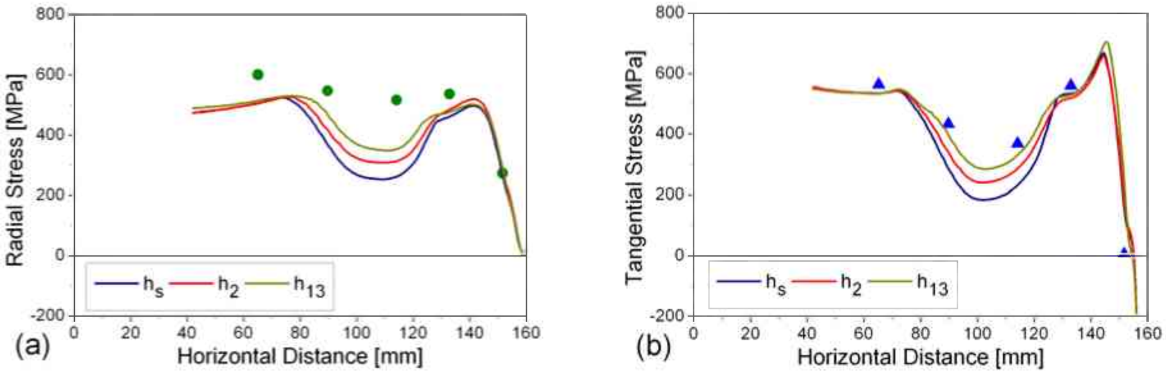

Figure 105: (a) Radial and (b) tangential residual stresses in the turbine disc along the radius determined by neutron diffraction (symbols) and finite element simulations (lines). The simulations were performed with the temperature dependant heat transfer functions h_s, h_2 and h_{13}.

Figure 106 shows the scan parallel to the disc axis at a radius of 100 mm. Compared to the radial scan in Figure 105 the differences are less pronounced. The maximum stress level of the radial component increases from 400 MPa for h_s to 500 MPa for h_{13} and the stress gradient becomes steeper for both components.

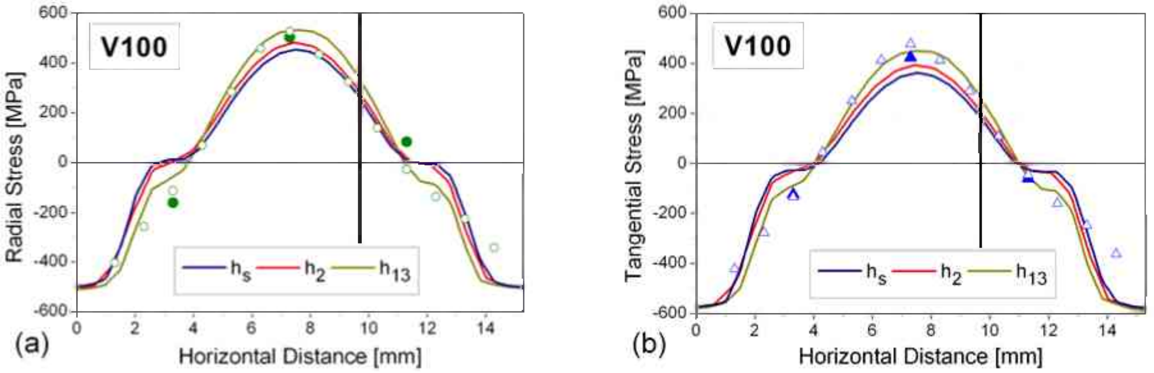

Figure 106: (a) Radial and (b) tangential residual stresses in the turbine disc parallel to the disc axis at a disc radius of R =100 mm determined by neutron diffraction (symbols) and finite element simulations (lines). The simulations were performed with the temperature dependant heat transfer functions h_s, h_2 and h_{13}.

In both cases the scans parallel to the disc axis illustrate that the parameter variations show differently pronounced regions with a decreased gradient or “shoulder” of the stress curves. Initially, the number of measurement points was too low to evaluate such details of the stress curve, but a detailed neutron diffraction scan at a disc radius of 100 mm did not reveal any shoulder in the real disc. As this reduced stress gradient is least pronounced for the simulation with the function h_{13} it seems to represent the best fit to the real heat transfer conditions.

The scan at a disc radius of R = 123 mm shows very little difference between the various simulations because of the steep stress gradient in this part of the disc (Figure 107). Over a length of 10 mm along the radius the stress components increase by about 150 MPa. Due to the similarity of the simulation results, this scan is not appropriate to test different parameters of the finite element model, but proved to be very useful to judge the experimentally determined stress values. Significant deviations between simulated and measured values at R = 123 mm can clearly be attributed to some uncertainty in the measurement. While the axial and tangential elastic strains fit perfectly to the simulated values (Figure 108), the measured radial strain exceeds the simulated strain by $0.5 \cdot 10^{-3}$. This strain difference corresponds to a stress of approximately 100 MPa. The misfit of the radial strain component is most likely caused by a slight misalignment of the disc regarding the radial position. Difficulties of the radial positioning can be attributed to the flashes caused by the forging process, which were different in size along the circumference of the disc and complicated the determination of the outer edge as well as the clamping of the sample. The strain results in Figure 108 suggest that the radial strain was determined at a larger disc radius than the tangential and axial strains. Consequently, strains from different locations inside the disc are combined to calculate the residual stress, which naturally leads to erroneous results.

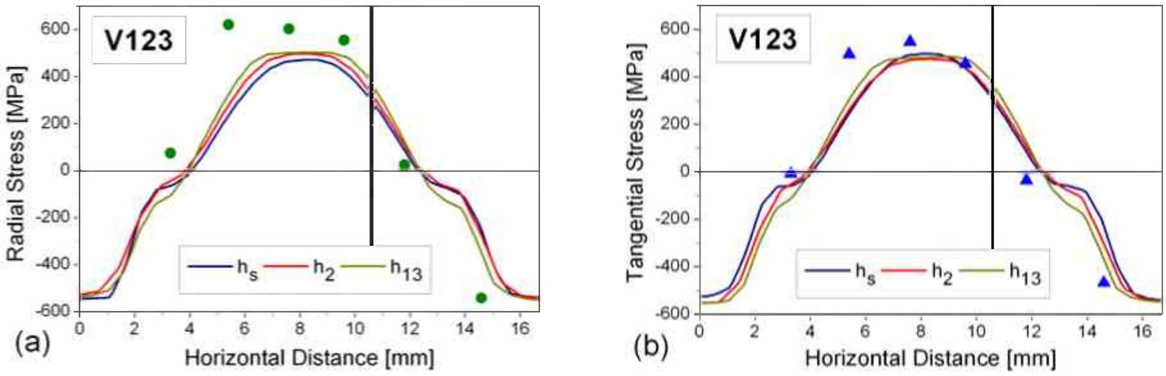

Figure 107: (a) Radial and (b) tangential residual stresses in the turbine disc parallel to the disc axis at a disc radius of R =123 mm determined by neutron diffraction (symbols) and finite element simulations (lines). The simulations were performed with the temperature dependant heat transfer functions h_s, h_2 and h_{13}.

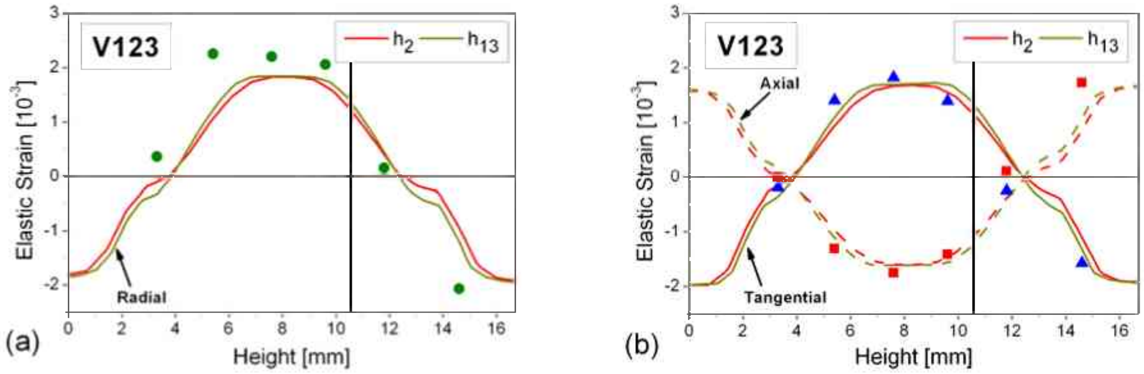

Figure 108: (a) Radial and (b) axial and tangential residual strain in the turbine disc parallel to the disc axis at a disc radius of R = 123 mm as determined by neutron diffraction (symbols) and finite element simulations (lines). The simulations were performed with the temperature dependant heat transfer functions h_2 and h_{13}.

For the radial scan a comparison of the simulated elastic strains and the measured strains instead of the residual stresses revealed additional information. Figure 109 illustrates that optimising the heat transfer coefficient does improve the fit to the measured values, but still some experimental data points deviate considerably from the finite element results. For a closer investigation of possible reasons for such large differences, the elastic strains simulated with h_2 were also extracted parallel to the horizontal scan. The dotted and dashed lines represent the simulated elastic strains at an offset of 1 mm to the top and bottom side of the disc, respectively. These curves illustrate that even minor imperfections of the positioning can be the source for significant deviations of the experimental values. As the radial scan can be compared to a contour line, it is very sensitive to the positioning if the stress gradient is very steep. This is the case in the thin section of the disc, because the stress changes by 150 MPa over a length scale of only 1 mm. Close to the rim of the disc the scan line is located at the maximum of a broad stress curve, where minor imperfections of the location do not lead to significantly different values. As the disc has to be mounted three times to determine all three strain components, it is possible that at least the values of one strain component do not represent the strain at the scan line. Consequently, strains from different locations inside the disc are combined which of course leads to erroneous stress results. Therefore, the positioning can be regarded as a main reason for the presence of axial stresses in the disc, which opposes the simulation results and analytic calculations.

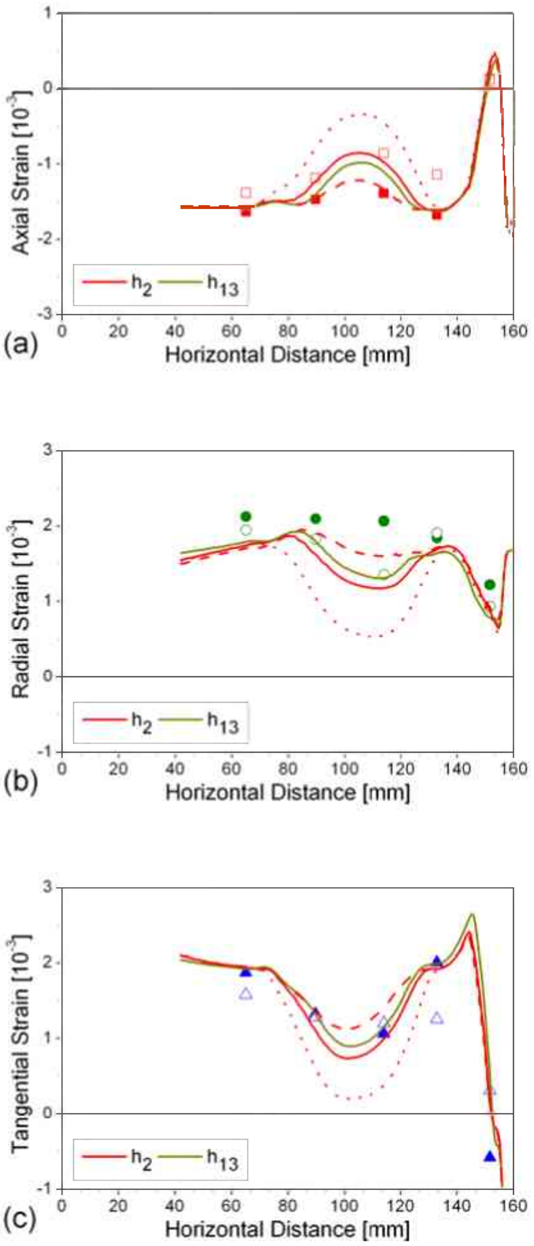

Figure 109: (a) Axial, (b) radial and (c) tangential residual strain in the turbine disc along the disc radius as determined by neutron diffraction (symbols) and finite element simulations (lines). The simulations were performed with the temperature dependant heat transfer functions h_2 and h_{13}. The dotted and the dashed lines represents the simulated strains at an offset of 1 mm closer to the bottom side (dotted) and 1 mm closer to the top side (dashed). The filled and open symbols represent two independent measurements.

11 Discussion and Summary

The focus of this doctoral thesis was to use two independent approaches for the determination of the residual stresses in a forged turbine disc made of IN718. The neutron diffraction method was used to evaluate the stress state at different locations inside the disc and thus provides the basis for a validation of the finite element model. Contrary to other studies in literature the whole tri-axial stress state was determined with both approaches and the results were compared. Previous investigations by other authors have either concentrated on the neutron diffraction measurements and have not presented corresponding finite element simulation data [102 - 104] or they have focused on the calculation and the experimental quenching conditions and lack any measured stress values [64]. Hossain *et al.* [51] studied the quenching of a steel sphere, published one of the few studies that present the finite element results along with measured stresses and also state the employed simulation parameters in detail. Regarding thermal residual stresses there are very limited publications on nickel-based alloys and commercial components. Most of the publications concentrate on the deformation behaviour in tensile testing conditions or examined the stresses in welded specimens. Currently, there are only two publications [54, 43] that have studied the residual quenching stresses in samples made of IN718. Dye *et al.* [43] examined a small cylinder and Rist *et al.* [54] investigated a commercial, water-quenched turbine disc along several scan lines. Both studies used the set up at ENGIN-X which employs the time-of-flight (TOF) method. Although ENGIN-X enables the simultaneous measurement of two strain components, Rist *et al.* did not determine the whole stress tensor for all scans but only compared the measured strains to the simulated strains. Presenting merely strain data can conceal experimental uncertainties and, moreover, it is the stress state not the strain that is required to solve engineering problems as for example the optimisation of a machining sequence to minimize distortion. Therefore, the current work gives the whole stress tensor for all measurement locations within the examined model plates and turbine discs. However, it is still assumed that the principal stress axes coincide with the specimen axes and thus, the shear stresses can be neglected.

The limited number of published studies that do compare simulated and measured values have taken the simulated or the experimental results for granted [43, 50, 54]. Contrary to these publications, the current work performed a critical investigation of the measured results regarding the repeatability of the experimental values, before they were used as a basis to test the finite element model. Measurements at different angular positions of the disc and repeated scans inside the model plate confirmed the general shape of the stress curves, but also revealed a certain scatter of the data. Furthermore, the results of the turbine disc exhibited positive axial stresses, partly reaching up to 150 MPa, and also for the model plate positive normal stresses up to 100 MPa were found. Yet, the presence of axial and normal stresses opposes the simulation results independently of the chosen input parameters. For both parts (disc and model plate) the axial and normal stresses should be zero according to analytic calculations of plates and discs that are thin compared to their lateral extension. Only near-rim positive axial or normal stresses are required to compensate the negative transverse and tangential stresses. Besides, the deviation from zero stress was above the measurement error of ± 50 MPa which is based on the uncertainty of the peak determination. Thus, the experimentally obtained axial stresses were regarded as a systematic measurement artefact. Consequently, the following potential influencing factors have been outlined and investigated in detail:

a) Chemical differences along the disc radius similar to welded specimens that results in a lateral difference of the unstrained lattice parameter.

b) Presence of texture and consequently differences of the unstrained lattice parameter in the three main stress directions.

c) Influence of the γ' and γ'' precipitates after water-quenching.

d) Choice of too large reference cube sizes and/or an inappropriate choice of the gauge volume for the reference value.

e) The chosen lateral resolution was insufficient to reflect details of the stress gradient and only shows a blurred picture of the stress curve.

f) The adequacy of the (311) reflection for macrostresses analyses.

g) Erroneous diffractometric elastic constants E_{hkl} and ν_{hkl} were used to calculate the stresses.

h) Presence of significant microstrains.

i) Uncertainties of the sample positioning.

a) - b) - c) The experimental results presented in Chapters 6 - 9 showed that no chemical gradient is present in the disc and no texture could be found by neutron diffraction nor by EBSD. There was no influence of the precipitates, as examinations with SANS did not observe any precipitates in the water-quenched condition. Consequently, the assumption of a homogenous material appears to be well justified.

The reference cube was measured in three perpendicular directions to evaluate any minor variations in the unstrained lattice parameter, which can indicate small localised texture effects. The fact that no systematic differences in the lattice parameter in the three main directions could be observed strongly suggests that no localised texture is present in the forged material. The threefold measurement of the reference cube can nevertheless be recommended, because the measurement itself seems to be very sensitive to the positioning. Even small irregularities of the microstructure can affect the intensity curve, which is used to align the cube, and thus can result in an off-centred position.

d) The optimum size for the reference sample depends on the size of the studied component and the prevailing stress state. Originally, the reference cube size for the disc was chosen to be $4 \times 5 \times 6$ mm^3 and was reduced to $4.0 \times 4.1 \times 4.2$ mm^3 for the model plate and detailed scans of the disc at R = 100 mm. This reduction of the size had no effect on the obtained stress results. Additionally, one reference cube with a size of $4 \times 4.1 \times 4.2$ mm^3 was further cut up into smaller sub-cubes, that were reassembled to increase the neutron intensity and measured with a gauge volume of $3 \times 3 \times 30$ mm^3. This further reduction of the reference cube size did not cause significantly different stress values either. Therefore, the chosen cube size of $4 \times 4.1 \times 4.2$ mm^3 was regarded as sufficiently small to enable the relaxation of the macrostress field of the studied components.

Essentially, two gauge volume sizes were employed in the current work: 2×2 mm^2 and 3 x 3 mm^2. For a precise determination of the unstrained lattice parameter it seems preferable to chose a gauge volume that captures the whole reference sample, because then the maximum number of grains can fulfil the diffraction condition. At first, this observation was surprising as the grain size was very small and thus the number of grains within the small gauge volume ($2 \times 2 \times 2$ mm^3) was already as high as $122 \cdot 10^{-6}$. Yet, in the model plate the $2 \times 2 \times 2$ mm^3 gauge volume led to normal stresses reaching up to 100 MPa. With the larger gauge volume the maximum normal stress was only ± 50 MPa, which correlates better to the analytic calculations.

e) The measured lattice parameter always represents the weighted average of all grains within the gauge volume that fulfil the diffraction condition; contrary to the simulation data that correspond to exactly one point within the component. This is irrelevant, as long as the stress gradient is very low or exhibits a linear increase. In this case, the average will lead to the same stress value as the point data. For the model plate a weighted average of the finite element stress data was calculated to simulate a neutron measurement and the obtained stress values were below the point data. However, all the measured values tend to be higher than the simulated results and so the direct comparison of the point data extracted from the simulation and the neutron data are no source of error.

The lateral resolution of the through thickness scan in the turbine disc was not very high due to the relatively large cross section of the employed gauge volumes (2×2 mm^2 or 3×3 mm^2). Initially, an overlap of the examined area was avoided and thus, only three locations were examined along the thickness of the disc. Of course this number is insufficient to elaborate the shape of the stress curve. In the course of the work, this proved to be necessary as the simulated results mainly differ regarding details of the stress gradient along the thickness. For this reason, a detailed scan at a disc radius of R = 100 mm was performed with a higher lateral resolution using a cross section of 1×1 mm^2.

f) The choice of the (311) reflection for macrostress analysis was verified with an in-situ tensile test experiment. This showed that the (311) reflection also deviates from the linear elastic response and accumulates microstrains. Still, compared to other reflections the amount of microstrains in the (311) and also in the (111) lattice planes are small and both reflections proved to be adequate to determine macrostresses. At ARES the (111) reflection had to be discharged as the measurement error was unacceptably high due to the low diffraction angle.

g) The calculated diffractometric elastic constants are based on single crystal values for pure Nickel and for γ'. This does not correspond to the composition of quenched IN718, which primarily consists of a solid solution nickel matrix without any γ' or γ'' precipitates. Unfortunately, there are no alternative data published in literature and all published studies that state E_{hkl} and ν_{hkl} values for IN718 refer to the same publication [43].

h) Despite the fact, that the (311) reflection only accumulates very low microstrains, there are studies [79, 85, 95] showing that a correction for microstrains is essential to extract the macrostress field. Holden *et al.* [79] studied a severely bent tube made of Inconel 600 and found that the strains determined with the (200) reflection had to be corrected as well as the strains determined with (111). This correction was based on the knowledge of the prevailing plastic strain in the tube and the corresponding residual lattice strains determined by in-situ tensile tests. In the current work, the plastic strain could be extracted from the finite element simulations and the lattice strains at different amounts of plastic strain were obtained from the in-situ tensile tests as described in Chapter 7. However, the plastic strains that build up in the turbine disc during the quenching process proved to be much lower (max. $\varepsilon_{pl} = 0.3\%$) than the plastic strains reported for the bent tube ($\varepsilon_{pl} = 9\%$) in Ref. [79]. Therefore, the correction factors determined for the studied components were very low. This is in accordance to studies on a slightly bent tube ($\varepsilon_{pl} = 7\cdot10^{-3}$) [95] that reports identical stress results for (200) and (111) within the experimental uncertainty. Furthermore, the residual lattice strains did not exhibit different signs for the (200) and the (220) reflections, which opposes findings of micro-plasticity. Comparisons with other in-situ tensile tests on similar materials led to the conclusion that the results were slightly erroneous due to imperfections of the sample alignment. Nevertheless, the tensile test results could be used to discharge the idea of significant microstrain influences on the obtained stress results, because the residual lattice strains for the prevailing plastic strains were very low compared to the measured strains. It seems that a correction for microstrains is only necessary if considerable plastic strains in the order of 9% exist in the component. This does not apply to the studied turbine disc.

i) The need for a precise transformation of the measurement locations between the specimen and the instrument coordinate system is well known. To this end, the intensity curves were recorded to determine the sample edge, which is generally accepted as the most accurate method. Despite all these effort for a precise alignment of the sample, the measured elastic strain curves sometimes seem to be shifted against the simulated elastic strain curves. The location of the strain maximum was not affected by the choice of the heat transfer function, so any influence of the simulation parameters can be excluded. The direct comparison of the elastic strains was only possible in the course of the work, when a 3D version of DEFORM was released that enabled the extraction of elastic strains. Solely for this reason, some simulations of the disc were repeated with DEFORM3D, despite the axi-symmetric shape of the disc. Finally, the comparisons showed that it is necessary to determine the edge of the turbine disc separately for each measurement location. Obviously, even thorough positioning of the disc could not ensure a perfectly parallel alignment of the sample axes and the instrument axes. In contrast to the present work, Rist *et al.* [54] obtained a two-dimensional cross-sectional profile of the disc surface, accurate to within 10 μm, prior to the neutron measurement on ENGIN-X (ISIS, Great Britain). If such equipment is available, it is not necessary to determine the intensity curve at numerous positions.

Summarising, the alignment of the component and the precise determination of the reference value proved to be the most important factors for a correct evaluation of the residual stress state in the quenched turbine disc at the instrument ARES. The majority of the studies that present residual stress measurements were performed on TOF instruments, for example ENGIN-X. The advantage of the TOF method compared to the single peak diffraction is the fact, that several reflections are recorded simultaneously. In addition, TOF instruments are often equipped with highly sophisticated equipment to ease the sample positioning. At SMARTS (Los Alamos National Laboratory, USA) two theodolithes are used and at ENGIN-X (ISIS, Great Britain) a device to digitalise the three-dimensional contour of a sample with a spherical contact probe is installed. Although, the recording of the neutron intensity as a function of the lateral position is still regarded as the most accurate method to determine the edge of a sample, the additional equipment at ENGIN-X and SMARTS most likely reduces the number of necessary intensity curves and thus contributes to an accurate alignment. The good correlation of simulated results and neutron measurements reported in literature [54, 43] can presumably be attributed to the accurate sample alignment. Consequently, the positive normal and axial stresses as well as the sometimes large deviations from simulated stress results are mainly attributed to non-perfect alignment of the sample and/or the reference sample.

Erroneous reference measurements could be identified by a comparison of the deviatoric stresses or strains, which eliminate the influence of the reference value. For example, the deviatoric stresses and strains of the model plate were equal for the repeated measurements of the reference sample with different gauge volume sizes. This illustrates, that the deviatoric stresses can be regarded as an additional aid to judge questionable measurement results, even if the whole stress state is required in the end.

After this thorough scrutiny of the experimental results, the simulation model was verified and improved. A geometrically simple part (a cuboid plate) proved to be a good choice to test the finite element model, because geometric effects of the disc contour on the shape of the residual stress state could be excluded. At the same time, the smaller thickness leads to a faster cooling of the plate, which seems to be responsible for a stronger influence of h on the predicted stress distribution. Additionally, more detailed measurements were possible due to the considerably reduced diffraction paths. The elaborate parameter study of the heat transfer h showed that a temperature dependent function of h has to be applied to model the real water quenching process. This observation is in contrast to Hossain *et al.* [51] and [61], who claimed to achieve satisfying fits with constant heat transfer values. Dye *et al.* [43, 62] and Rist *et al.* [54], who examined a cylinder and a turbine disc respectively, both made of IN718, effectively also used constant heat transfer conditions for the finite element simulation, as h = 20000 W/(m^{2}K) down to 100 °C. However, the resulting simulated residual stresses partly deviated by 250 MPa from the stresses determined by neutron diffraction. In the current work, the general correlation between measurement and simulation is much better due to the in-depth studies of the heat transfer. In the end, three of the empirically defined heat transfer functions resulted in residual stresses and cooling curves that represent a good fit to the measured stresses and temperatures in the model plate. Furthermore, the up-sizing of the optimised finite element model was verified. As most forged components that exhibit severe distortion problems during machining are even larger than the examined turbine disc, the finite element model has to be able to reflect the residual stresses in larger geometries, too. If the same heat transfer functions can be employed for the simulation of the small model plate and the turbine disc, it seems justified that the model can as well be applied for larger components. Often these forged parts are too large to be measured by neutron diffraction and so a verification of the finite element calculation with smaller samples is essential.

There are still some minor deviations between the measured temperatures and stresses in the model plate and the turbine disc, but the key parameters of the heat transfer function that describes water quenching could be narrowed down. At high temperatures the heat transfer coefficient h has to be about 1000 W(m^{2}K) down to the Leidenfrost temperature T_{Le}, which is between 500 °C and 800 °C. Then h increases to a maximum value at T_{max}, which is between 250 °C and 400 °C. The maximum value of h is obviously less important than the shape of the increase between T_{Le} and T_{max}, which should fairly smooth. The upper bound for this gradient could be defined as $(\Delta h/\Delta T)$ = 70 W/m^{2}K^2.

Actually, components are not machined in the water quenched condition, but in the aged condition. Yet, all the verifications were performed for water-quenching. The experimental study of an aged model plate and a solution annealed turbine disc showed that the residual stresses in any condition other than as-quenched are too low to be resolved with neutron diffraction. Therefore, no simulation data were presented for solution annealing or aging. The fact that, the finite element model is able to reflect the residual stresses caused by water quenching, implies that the model also correctly simulates lower stresses evolving during aging.

12 Conclusions

The main achievement of this doctoral thesis was the development of a finite element model that reflects the real residual stress state in a quenched large-scale component. This finite element model was required to determine the distortion during a machining process of components with a given residual stress field. For the experimental verification of the simulated residual stresses the neutron diffraction method was used. In order to avoid any cross-couplings, these two approaches for residual stresses analysis were treated strictly independently. For example, no plane stress conditions were assumed neither in the FE model nor for the determination of experimental stress values. After a detailed parameter study, a satisfying agreement between the experimental and calculated stresses could be achieved. The heat transfer coefficient proved to be the key parameter of the FE model and had to be defined as a function of the surface temperature. Based on empiric definitions of the heat transfer function, the key figures such as the Leidenfrost temperature, the temperature and value of the maximum heat transfer were specified.

Furthermore, the experimentally determined residual stresses were examined in detail. Multiple measurements within the turbine disc and the model plate were conducted to investigate the homogeneity of the stress state as well as the repeatability of the stress measurement itself. The scatter of the experimental strain and stress values showed that, in fact, the repeatability was not entirely satisfying. Besides, the neutron measurements resulted in tri-axial stress states at some locations, where two-axial stress conditions prevail according to FE simulations. In the end, the alignment of the components and the reference cuboids could be identified as the major source of the scatter in the measured results as well as for the presence of tri-axial stresses. Influences from microstrains, texture, chemical gradients or coherent precipitates could be discarded.

The novelty of the current work was the systematic study of two methods for residual stress analysis: the neutron diffraction method and the finite element simulation. Despite the general agreement on the requirement for experimental verifications of finite element simulations, there are currently no publications on thermal residual stresses that present critical inquiries and comparisons of both approaches. Either the experimental data or the simulation parameters are taken for granted.

This doctoral thesis presents a finite element model, which can be used for future simulations of quenching stresses in components made of IN718. Furthermore, the up-sizing of the model was successfully demonstrated with the comparison of results of a small model plate and the results obtained on relatively large turbine disc. This verification was essential, as often commercial components are too large to be measured on instruments for neutron stress analysis.

13 Reference

[1] S. Denis, P. Archambault, E. Gautier, A. Simon, G. Beck: *Prediction of Residual Stress and Distortion of Ferrous and Non-ferrous Metals: Current Status and Future Developments*; **JMEPEG**, 11, (1), (2002), p. 92 - 102.

[2] M. Stockinger: Mikrostrukturelle *Simulation des Gesenkschmiedens von Nickelbasis-Legierungen*; Thesis, **Technical University of Graz**, Austria, (2003).

[3] G. Wasle: *Cogging – Physikalische und numerische Simulation der Primärumformung von Nimonic 80a*; Theisis, **Technical University of Graz**, Austria, (2003).

[4] F. Renou-Devy, P. Mosser, A. Benallal: *Modélisation des contraintes résiduelles développées lors da la trempe à l'huile d'un disque de turbine en* astroloy; **Traitement Thermique**, 288, (1996), 33 - 39.

[5] S. Tin, P.D. Lee, A. Kermanpur, M. Rist, M. McLean: *Integrated Modeling for the Manufacture of Ni-based Superalloy Discs From Solidification to Final Heat Treatment*; **Met. Mat. Trans. A**, 36, (2005), 2493 - 2504.

[6] K. Karhausen, R. Kopp: *Model for Integrated Process and Microstructure Simulation in Hot Forming*; **Steel Research 63**, 6, (1992), 247 - 255.

[7] R. Srinivasan, V. Ramnarayan, U. Deshpande, V. Jain, I. Weiss: *Computer Simulation of the Forging Fine Grain IN-718 alloy*; **Met. Trans.**, 24A, (1993), 2061 - 2069.

[8] J.M. Zhang, Z.Y. Gao, J. Y. Zhuang, Z.Y. Zhong: *Mathematical Modelling of the Hot-deformation Behaviour of Superalloy IN718*; **Met. Mat. Trans.**, 30A, (1999), 2701 - 2712.

[9] M. Salio, T. Berruti, G. de Poli: *Prediction of Residual Stress Distribution After Turning in Turbine Disks*; **Int. J. Mech. Sci.**, 48, (2006), 976 - 984.

[10] I.C. Noyan, J. B. Cohen: *Residual Stress*; **Springer-Verlag**, New-York, Berlin, Heidelberg, London, Paris, Tokyo, (1987).

[11] K.C. Mills: *Recommended Values of Thermophysical Properties for Selected Commercial Alloys*, Woodhead Publishing Limited, Cambridge, U.K , (2002).

[12] A.J. Allen, M.T. Hutchings, C.G. Windsor, C. Andreani: *Neutron Diffraction Methods for Study of Residual Stress Fields*; **Advances in Physics**, 34, (1985), 445 - 473.

[13] M.E. Fitzpatrick, A. Lodini: *Analysis of Residual Stress by Diffraction using Neutron and Synchrotron Radiation*; **Taylor & Francis**, London, (2003).

[14] Ch. T. Sims, N. S. Stoloff, W.C. Hagel: *Superalloys II*; **Wiley**, New York, Chichester, Brisbane, Toronto, Singapore, (1987).

[15] J. Tockner, W. Horvath, and J. Fladischer: *Simulationsunterstützte Optimierung des Umformens auf Spindelpressen*, **BHM**, 146 (9), (2001), 392 - 395.

[16] W. Horvath, W. Zechner, J. Tockner, M. Berchthaler, G. Weber, E.A. Werner: *The Effectiveness of Direct Aging on Inconel 718 Forgings Produced at High Strain Rates as Obtained on a Screw Press*, **Superalloy 718, 625, 706 and Derivates** (Ed: E.A. Loria), TMS (The Mineral, Metals & Materials Society), (2001), 223 - 228.

[17] E.F. Bradley: *Superalloys – A Technical Guide*; **ASM International**, Metals Park, OH, USA, (1988).

[18] E.A. Loria: *Recent Developments in the Progress of Superalloy 718*, **JOM**, 6, 33 - 36.

[19] D.D. Krueger: *The Development of Direct Age 718 for Gas Turbine Engine Disk Applications*, **Superalloy 718 – Metallurgy and Applications** (Ed: E.A. Loria), TMS (The Mineral, Metals & Materials Society), (1989), 279 - 296.

[20] Y.S. Song, M.R. Lee, J.T. Kim: *Effect of Grain Size for the Tensile Strength and the Low cycle Fatigue at Elevated Temperature of Alloy 718 Cogged by Open Die Forging Press*, **Superalloy 718, 625, 706 and**

Derivates 2005 (Ed: E.A. Loria), TMS (The Mineral, Metals & Materials Society), (2005), 539 - 549.

[21] L. Geng, Y.-S. Na, N.-K. Park: *Continous Cooling Transformation Beha vior of Alloy 718*, **Mat. Letters**, 30, (1997), 401 - 405.

[22] M.C. Chaturvedi, Ya-fang Han: *Strengthening Mechanisms in Inconel 718 Superalloy*, **Metal Science**, 17, (1983), 145 - 149.

[23] L. Wenchang, X. Furen, Y. Mei, C. Zonglin, W. Shaogang, L. Weihong: *Quantitative Phase Analysis of Inconel 718 by X-ray Diffraction*, **J. Mat. Sci. Letters**, 16, (1997), 769 - 771.

[24] D. Mukherji, R. Gilles, B. Barbier, D. Del. Genovese, B. Hasse, P. Strunz, T. Wroblewski, H. Fuess, J. Rösler: *Lattice Misfit Measurement in Inconel 706 Containing Coherent γ' and γ'' Precipitates*, **Scripta Mat.**, 48, (2003), 333 - 339.

[25] S. Azadian, L.-Y. Wei, R. Warren, *Delta Phase Precipitation in Inconel 718*, **Mat. Char.**, 52, (2004), 7 - 16.

[26] W.C. Liu, F.R. Xiao, M. Yao, Z.L. Chen, Z.Q. Jiang, S.G. Wang: *Relationship Between the Lattice Constant of γ Phase and the Content of δ Phase, γ'' and γ' Phases in Inconel 718*, **Scripta Mat.**, 27, (1997), 59 —64.

[27] H. Yuan, W.C. Liu: *Effect of the δ Phase on Hot Deformation Behaviour of Inconel 718*; **Mat. Sci. Eng. A**, 408, (2005), 281 - 289.

[28] W. Gailian, W. Cuiwei, Z. Maicang, D. Jianxin, X. Xishan, J. Radavich, B. A. Lindsley, G. Shen: *The Microstructural Changes and Their Effect on CCGR After Long Time Thermal Exposure in DA718 and STD718*, **Mat. Sci. Eng. A**, 358, (2003), 71 - 75.

[29] M. Sundararaman, P. Mukhopadhyay, S. Banerjee: *Deformation Behaviour of γ'' Strengthened Inconel 718*; **Acta metal.**, 36, (4), (1988), 847 - 864.

[30] A. Royer, P. Bastie, M. Veron: *In-situ Determination of γ' Phase Volume Fraction and of Relations Between Lattice Parameters and Precipitate Morphology in Ni-based Single Crystal Superalloy*; **Acta. mat.**, 46, (15), (1998), 5357 - 5368.

[31] A. Jacques, F. Diologent, P. Bastie: *In-situ Measurement of the Lattice Parameter Mismatch of a Nickel-base Single-crystalline Superalloy Under Variable Stress*; **Mat. Sci. Eng. A**, 387 - 389, (2004), 944 - 949.

[32] C. Slama, M. Abdellaoui: *Structural Characterization of Aged Inconel 718*, **J. Alloys Comp.**, 306, (2000), 277 - 284.

[33] F.X. Kayser, C. Stassis: *The Elastic Constants of Ni_3Al*, **Phys. Stat. Sol. (a)**, 64, (1981), 335 - 342.

[34] M. Durand-Charre: *The Microstructure of Superalloys*; **Gordon and Breach Science Publishers**, Amsterdam, (1997).

[35] Xishan Xie, J. Dong, G. Wang, W. You: *The Effect of Nb, Ti, Al on Precipitation and Strengthening Behaviour of 718 Type Superalloys*, **Superalloy 718, 625, 706 and Derivates 2005** (Ed: E.A. Loria), TMS (The Mineral, Metals & Materials Society), (2005), 287 - 298.

[36] Xishan Xie, G. Wang, J. Dong, Ch. Xu, Wei-Di Cao, R. Kennedy: *Structural Stability Study on a Newly Developed Nickel-base Superalloy - Alvac 718Plus*; **Superalloy 718, 625, 706 and Derivates 2005** (Ed: E.A. Loria), TMS (The Mineral, Metals & Materials Society), (2005), 179 - 191.

[37] G. A. Rao, M. Kumar, M. Srinivas, D.S. Sarma: *Effect of Standard Heat Treatment on the Microstructure and Mechanical Properties of Hot Isostatically Pressed Superalloy Inconel 718*, **Mat. Sci. Eng. A**, 355, (2003), 114 - 125.

[38] L. Renhof, Ch. Krempaszky, E. Werner, M. Stockinger: *Analysis of Microstructural Properties of IN718 After High Speed Forging*; **Superalloy 718, 625, 706 and Derivates 2005** (Ed: E.A. Loria), TMS (The Mineral, Metals & Materials Society), (2005), 261 - 270.

[39] 'R.B. Li, M. Yao, W.C. Liu, X.C. He: *Isolation and Determination for δ, γ' and γ'' Phases in Inconel 718 Alloy*, **Scripta Mat.**, 46, (2002), 635 - 638.

[40] http://www.deform.com

[41] A.J. Brand, K. Karhausen, R. Kopp: *Microstructural simulation of nickel base alloy Inconel 718 in production of turbine discs*; **Mat. Sci. Tech.**, 12, (1996), 963 - 969.

[42] Internal Report provided by Bohler Schmiedetechnik GmbH & Co KG.

[43] D. Dye, K.T. Conlon, R.C. Reed: *Characterisation and Modelling of Quenching - Induced Residual Stresses in the Nickel-based Superalloy IN718*, **Met. Mat. Trans A**, 35A, (2004), 1703 - 1713.

[44] J.B. Henderson, A. Strobl: *Measurement of the Thermophysical Properties of Molten Metal Alloys*, TPS No I-1E, **Netzsch Thermische Analyse**, (1995).

[45] G. Pottlacher, H. Hosaeus, B. Wilthan, E. Kaschnitz, and A. Seifter: *Thermophysikalische Eigenschaften von festem und flüssigem Inconel 718*; **Thermochimica Acta**, **2002**, 382, 255.

[46] C. H. Gür, A. E. Tekkaya: *Numerical Investigaion of Non-homogenous Plastic Deformation in Quenching Process*, **Mat. Sci. Eng. A**, 319 - 321, (2001), 164 - 169.

[47] A. Buczek, T. Telejko: *Inverse Determination of Boundary Conditions During Boiling Water Heat Transfer in Quenching Operation*, **J. Mat. Proc. Tech.**, 155 - 156, (2004), 1324 - 1329.

[48] Ph. Le Masson, T. Loulou, E. Artioukhine, Ph. Rogeon, D. Carron, J.-J. Quemener: *A Numerical Study for the Estimation of a Convection Heat Transfer Coefficient During a Metallurgical „Jominy End-quench Test"*, **Int. J. Therm. Sci**, 41, (2002), 517 - 527.

[49] Ch. Heming, H. Xieqing, W. Honggang: *Calculation of the Residual Stress of a 25 Steel Cylinder with a Non-linear Surface Heat-transfer coefficient Including Phase Transformation During Quenching;* **J. Mat. Proc. Tech.**, 89 - 90, (1999), 339 - 343.

[50] S. Sen, B. Aksakal, A. Ozel: *Transient and Residual Stresses in Quenched Cylindrical Bodies*, **Int. J. Mech. Sci.**, 43, (2000), 2013 -2029.

[51] S. Hossain, M.R. Daymond, C.E. Truman, D.J. Smith: *Prediction and Measurement of Residual Stresses in Quenched Strainless-steel Spheres*, **Mat. Sci. Eng. A**, 373, (2004), 339 - 349.

[52] San Guay Chen, Cheng-I Weng, Jehnming Lin: *Inverse Estimation of Transient Temperature Distribution in the End Quenching Test*; **J. Mat. Proc. Tech.**, 86, (1999), 257 - 263.

[53] B. Liščić, H.M. Tensi, W. Luty: *Theory and Technology of Quenching*, **Springer-Verlag**, Berlin, Heidelberg, 1992.

[54] M.A. Rist, S. Tin, B.A. Roder, J.A. James, M.R. Daymond: *Residual Stresses in a Quenched Superalloy turbine Disc: Measurements and Modelling*, **Met. Mat. Trans. A**, 37A, (2006), 459 - 467.

[55] D. Li, M.A. Wells: *Effect of Subsurface thermocouple Installation on the Discrepancy of the Measured Thermal History and Predicted Surface Heat Flux During a Quench Operation*, **Met. Mat. Trans B**, 36B, (2005), 343 -354.

[56] P. Archambault, A. Azim: *Inverse Resolution of the Heat Transfer Equation: Application to Steel and Aluminium*, **JMEPEG**, 4, (1995), 730 - 736.

[57] http://www.sensotec.at

[58] S. Nukiyama: *The Maximum and Minimum Values of the Heat Q Transmitted from Metal to Boiling water under Atmospheric Pressure*, **J. Heat Mass Transfer**, 9, (1966), 1419 - 1433.

[59] M. Muster, L. Maibücher, R. Weber, R. Jeschar: *Einfluss einer Zweiphasenströmung auf die Kühlwirkung beim Abschrecken heißer Metalloberflächen in Tauchbädern*; **Gaswärme Int.**, 5, (2005).

[60] P. Di Marco, W. Grassi: *Overview and Prospects of Boiling Heat Transfer Studies in Microgravity*; **Int. Symp. IN SPACE 97**, Tokyo, Japan, (1997).

[61] S. Hossian, C.E. Truman, D.J. Smith, M.R. Daymond: *Application of Quenching to Create Highly Tiraxial Residual Stresses in Type 316H Stainless Steel*, **Int. J. Mech. Sci.**, 48, (2006), 235 - 243.

[62] D. Dye, B.A. Roder, S. Tin, M.A. Rist, J.A. James, M.R. Daymond: *Modelling and Measurement of Residual Stresses in a Forged IN718 Superalloy Disc*, **Superalloys 2004** (Ed: K.A. Grenn, T.M. Pollock, H. Harada, T.E. Howson, R.C. Reed, J.J. Schirra, S. Walston), TMS 2004, (2004), 315 - 322.

[63] R. Becker, M. E. Karabin, J. C. Liu, R. E. Smelser: *Distortion and Residual Stress in Quenched Aluminium Bars*; **J. Appl. Mech.**, 63, (1996), 699 - 705.

[64] M. deOliveira, J. Ward, D.R. Garwood, R.A. Wallis: *Quenching of Aerospace Forgings From High Temperatures Using Air-assisted, Atomized Water Sprays*, **JMEPEG**, 11, (2002), 80 - 85.

[65] C. Krempaszky, E.A. Werner, M. Stockinger: *Residual Stresses in IN718 Turbine Disks*, **Superalloys 718, 625, 706 and Derivates 2005**, (Ed: E.A. Loria), The Min., Met. & Mat. Society (TMS), Warrendale, PA, USA, (2005), 527 - 538.

[66] K. Arimoto, G.Li, A. Arvind, W.T. Wu: *Heat Transfer Coefficient vs. Workpiece Surface Temperature*; **SFTC Paper** #344 "The Modelling of Heat Treating Process".

[67] H. Chandler: *Heat Treater's Guide*, **ASM International**, Materials Park, Ohio, USA, (1995), 88 - 89.

[68] R. B. Von Dreele: *Neutron Diffraction*; **Materials Science and Technology: A Comprehensive Treatment**, Vol. 2B, Characterisation of Materials, Pt. II, (Ed. R.W. Cahn, P. Haasen, E.J. Kramer), (Vol. Ed. : E. Lifshin), Wiley – VCH, Weinheim, (2005).

[69] V. Hauk: *Structural and Residual Stress Analysis by Nondestructive Methods: Evaluation - Application - Assessement*; **Elsevier**, Amsterdam, (1997).

[70] F.A. Kandil, J. D. Lord, A.T. Fry, P.V. Grant: *A Review of Residual Stress Measurement Methods – A Guide to Technique Selection*; **NPL Report MATC(A)04**, NPL Materials Centre, Teddington, Middlesex, UK, (2001).

[71] A. Pyzalla: *Determination of the Residual Stress State in Components Using Neutron Diffraction*; **J. Neutron Research**, 8, 2000, 187 - 213.

[72] G.A. Webster, R.C. Wimpory: *Non-destructive Measurement of Residual Stress by Neutron Diffraction*; **J. Mat. Proc. Tech.**, 117, (2001), 395 - 399.

[73] M- T- Hutchings, P.J. Withers, T.M. Holden, T. Lorentzen: *Introduction to the Characterization of Residual Stress by Neutron Diffraction*; **Taylor & Francis Group**, Boca Raton, FL, (2005).

[74] A.J. Allen, M.T. Hutchings, C.G. Windsor: *Neutron Diffraction Methods for the Study of Residual Stress Fields*; **Advances in Physics**, 34, (4), (1985), 445 - 473.

[75] T.M. Holden, A.P. Clarke, R.A. Holt: *Neutron Diffraction Measurements of Intergranular Strains in Monel 400*, **Met. Mat. Trans. A**, 28A, (1997), 2565 - 2576.

[76] B. Clausen, T. Lorentzen, M.A.M. Bourke, M.R. Daymond: *Lattice Strain Evolution During Uniaxial Tensile Loading of Stainless Steel*, **Mat. Sci. Eng.**, A259, (1999), 17 - 24.

[77] J.W.L. Pang, T. M. Holden, J.S. Wright, T.E. Mason: *The Generation of Intergranular Strains in 309H Stainless Steel Under Uniaxial Loading*, **Acta Mater.**, 48, (2000), 1131 - 1140.

[78] J. Böhm, A. Wanner, R. Kampmann, H. Franz, K.-D. Liss, A. Schreyer, H. Clemens: *Internal Stress Measurements by High-energy Synchrotron X-ray Diffraction at Increased Specimen-detector Distances*; **Nuclear Inst. Meth. Phys. Res. B**, 200, (2003), 315 - 322.

[79] T.M. Holden, R.A. Holt, A.P. Clarke: *Intergranular Strains in Inconel-600 and the Impact on Interpreting Stress Fields in Bent Stream-generator Tubing*, **Mat. Sci. Eng.**, A246, (1998), 180 -198.

[80] H.J. Stone, T.M. Holden, R.C. Reed: *Determination of the Plane Specific Elastic Constants of Waspaloy Using Neutron Diffraction*, **Scripta Mat.**, 40, 3, (1999), 353 - 358.

[81] G.E Dieter: *Mechanical Metallurgy*; SI Metric Ed., **McGraw-Hill** Series in Materials Science and Engineering, (2001).

[82] H. Behnken, V. Hauk: *Berechnung der röntgenographischen Elastizitätskonstanten (REK) des Vielkristalls aus den Einkristalldaten für beliebige Kristallsymmetrie*, **Z. Metallkde**, 77, 9, (1986), 620 - 626.

[83] F. Bollenrath, V. Hauk, H. Müller: *Zur Berechnung der vielkristallienen Elastizitätskonstanten aus den Werten der Einkristalle*, **Z. Metallkde**, 58, 1, (1967), 76 - 82.

[84] J.T. Lenkkeri: *Measurements of Elastic Moduli of Face-centred Cubic Alloys of Transition Metals*, **J. Phys. F: Metal Phys.**, 11, (1981), 1991 - 1996.

[85] T.M. Holden, R.A. Holt, G. Dolling, B.M. Powell, J.E. Winegar: *Characterization of Residual Stresses in a Bent INCOLOY-800 Tubing by Neutron Diffraction*, **Met. Trans. A**, 19A, (1988), 2207 - 2214.

[86] D. Dye, S.M. Roberts, P.J. Withers, R.C. Reed: *The Determination of the Residual Strains and Stresses in Tungsten Inert Gas Welded Sheet of IN718 Superalloy Using Neutron Diffraction*, **J. Strain Analysis**, 35, 4, (2000), 247 - 259.

[87] J. Schröder, T.M. Holden, J.H. Root, C.A. Hubbard, T.A. Dodson: *Residual Stress Investigations in an Inertia Friction Welded Sample*; **Residual Stresses**, Proc. of the European Conf. on Residual Stress, (Ed. V. Hauk, H.P. Hougardy, E. Macherauch, H.-D. Tietz), DGM Informationsgesellschaft Verlag, Oberursel, (1992), 341 - 349.

[88] D. Dye, K.T. Conlon, R.C. Reed: *Characterization and Modelling of Quenching-induced Residual Stresses in the Nickel-based Superalloy IN 718*, **Met. Mat. Trans.**, 35A, (2004), 1703 - 1713.

[89] P. Staron, H.-U. Ruhnau, M. Marmotti, P. Mikula, R. Kampmann: *The New Diffractometer ARES for the Analysis of Residual Stresses*; **Physica B**, 276 - 278, (2000), 158 - 159.

[90] A.D. Kravitz, R.A. Winholtz: *Use of Position-dependent Stress-free Standards for Diffraction Stress Measurements*, **Mat. Sci. Eng. A**, 185 (1994), 123-130.

[91] T.M. Holden, R.A. Holt, C.N. Tomé: *Intergranular Strains in Inconel-600 Generator Materials*; **Physica B**, 241 - 243, (1998), 1246 - 1248.

[92] G.A. Alers, J.R. Neighbours, H. Sato: *Temperature Dependant Magnetic Contributions to the High Field Elastic Constants of Nickel and an Fe-Ni Alloy*; **J. Phys. Chem. Solids**, 13, (1960), 40 -55.

[93] H.J. Stone, T.M. Holden, R.C. Reed: *On the Generation of Microstrains During the Plastic Deformation of Waspaloy*, **Acta mater.**, 47, 17, (1999), 4435 -4448.

[94] D. Dye, H.J. Stone, R.C. Reed: *Intergranular and Interphase Microstresses*, **Current Opinion in Solid State and Material Science**, 5, (2001), 31 - 37.

[95] T.M. Holden, C.N. Tomé, R.A. Holt: *Experimental and Ttheoretical Studies on the Superposition of Intergranular and Macroscopic Strains in Ni-based Industrial Alloys*, **Met. Mat. Trans. A**, 29A, (1998), 2967 - 2973.

[96] R. Lin Peng, M. Odén, Y.D. Wang, S. Johansson: *Intergranular Strains and Plastic Deformation of an Austenitic Stainless Steel*, **Mat. Sci. Eng.**, A334, (2002), 215 - 222.

[97] D. Dye, H.J. Stone, R.C. Reed: *A Two Phase Elastic-plastic Self-consistent Model for the Accumulation of Microstrains in Waspaloy*, **Acta mater.**, 49, (2001), 1271 - 1283.

[98] L. Djapic, A.N. Ezeilo, G.A. Webster: *The Effect of Cyclic Deformation on the Elastic Constants in a Nickel Superalloy*, **Physica B**, 213 & 214, (1995), 797 - 799.

[99] T. Lorentzen, M. R. Daymond, B. Clausen, C.N. Tomé: *Lattice Strain Evolution During Cyclic Loading of Stainless Steel*; **Acta Mat.**, 50, (2002), 1627 - 1638.

[100] M.R. Daymond, C.N. Tomé, M.A.M. Bourke: *Measured and Predicted Intergranular Strains in Textured Austenitic Steel*, **Acta mater.**, 48, (2000), 553 - 564.

[101] D. Dye, K.T. Conlon, R.C. Reed, K.E. James, A.M. Korsunsky: *Diffraction Strain Measurements for the Characterization of Residual Stresses in Welds for Gas Turbine Applications*; **6th Int. Trends in Welding Research Conf. Proc.**, April 2002, ASM Int., (2003)

[102] M. Rogante, P. Battistella, F. Rustichelli: *Residual Stress Measurement by Neutron Diffraction in AA6082 Extruded Samples Submitted to Different Quenching Rates*; **J. Alloys Comp.**, 378, (2004), 335 - 338.

[103] A. Pyzalla, W. Reimers, K.-D. Liss: *A Comparison of Neutron and High Energy Synchrotron Radiation as Tools for Texture and Stress Analysis*; **Mat. Sci. Forum**, Trans Tech Publications, Switzerland, 347 - 349, (2000), 34 - 39.

[104] M.L. Martinez-Perez, C.R. Borlado, F.J. Mompean, M. Garcia-Hernandez, J. Gil-Sevillano, J. Ruiz-Hervias, J.M. Atienza, M. Elices, Ru Lin Peng, M.R. Daymond: *Measurement and Modelling of Residual Stresses in Straightened Commercial Eutectoid Steel Rods*; **Acta Mat.**, 53, (2005), 4415 - 4425.

Appendix A

Electrolytic Etching

250 ml	10 % Oxalic Acid
250 ml	Distilled Water

Voltage: 2V

Flux: 5 C/m^2

Time: 10 s (depends of the thickness of the sample)

Immersion Etching

40 ml	HCl
50 ml	Distilled Water
5 ml	Perhydrol H_2O_2
5 ml	HF

Time: 2 – 5 min

Preparation for EBSD

Grinding: till grain 4000

Polish:	MOL[*]	3 μm	4 min
	NAP[*]	1 μm	3 min
	DUR[*]	Si-Oxide	15 min with polishing liquid MASTERMET[+]

Ultrasonic cleaning for 5 min with alcohol.

[*] Proper name of the polishing cloths produced by the company STRUERS.

[+] Proper name of the company STRUERS.